



**POLITECNICO**  
**MILANO 1863**

DEPARTMENT OF MECHANICAL ENGINEERING  
DOCTORAL PROGRAMME IN MECHANICAL ENGINEERING

---

**DESIGN, SIMULATION AND TESTING OF A  
COUPLED PLATE-CAVITY SYSTEM TARGETED FOR  
VEHICLE INTERIOR NOISE ANALYSIS AND CONTROL**

Doctoral Dissertation of:  
**Ling Liu**

Supervisors:  
Prof. Roberto Corradi (POLIMI)  
Prof. Zhushi Rao (SJTU)

Co-supervisor:  
Prof. Francesco Ripamonti

Tutor:  
Prof. Andrea Matta

The Chair of the Doctoral Program:  
Prof. Daniele Rocchi

2021 – Cycle 32



Dissertation Submitted to Shanghai Jiao Tong University  
for the Degree of Doctor of Philosophy

**Design, Simulation and Testing of a  
Coupled Plate-Cavity System targeted for  
Vehicle Interior Noise Analysis and Control**



<b>Candidate:</b>	Ling Liu
<b>Student ID:</b>	017020910031
<b>Supervisor:</b>	Prof. Zhushi Rao (SJTU) Prof. Roberto Corradi (POLIMI)
<b>Academic Degree Applied for:</b>	Doctor of Engineering
<b>Speciality:</b>	Mechanical Engineering
<b>Affiliation:</b>	School of Mechanical Engineering
<b>Data of Defence:</b>	July, 2021
<b>Degree-Conferring-Institution:</b>	Shanghai Jiao Tong University





# **DESIGN, SIMULATION AND TESTING OF A COUPLED PLATE-CAVITY SYSTEM TARGETED FOR VEHICLE INTERIOR NOISE ANALYSIS AND CONTROL**

## **ABSTRACT**

Nowadays, people are paying more and more attention to the acoustic comfort of vehicles, as well as the health issues caused by noise. The various types of vehicles including automobiles, trains, aircrafts and ships are all being requested for a better acoustic design, where the vehicle interior noise analysis and control are important. Computer-Aided Engineering (CAE) tools are now popularly used for these purposes, but engineers are always doubtful about their reliabilities. Besides, the currently available vibroacoustic methods are still far from satisfactory in terms of capability, accuracy or efficiency, especially for the analyses in mid-frequency range. New methods and codes are continuously developed, but they are hard to find suitable benchmark cases for assessment and validation. Therefore, to facilitate the CAE analysis of vehicle interior noise, this thesis presents a benchmarking and testing tool called *Noise-Box*.

The Noise-Box includes the test equipment and its numerical models, so that it can provide both reference measurements and reference computations. The test equipment, designed as a plate-cavity system that is easy to model and analyse, can perform vibroacoustic tests that can be accurately reproduced by numerical models. Its ability to measure sound transmission loss and test noise control measures is also considered. The numerical models that simulate the test equipment, should accurately predict its behaviour. Three numerical methods are used in order to cover a wide frequency range. While Finite Element Method (FEM) and Statistical Energy Analysis (SEA) are respectively for the low- and high-frequency ranges, Wave Based Method (WBM) is applied and developed for its potential to fill the mid-frequency gap. Commercial software is used for the FEM, and self-developed codes are provided for the SEA and the WBM. Concerning the demand for 2D benchmark cases in developing new numerical techniques, validated 2D models of FEM and WBM are provided for the additional reference results.

To obtain such a tool, this work designs, constructs and characterizes the test equipment, and builds, validates and updates the numerical models. It is a big challenge to reach the

agreement between the numerical models and the test system, and this thesis has overcome the difficulties through the following efforts:

(1) When the plate-cavity coupled Noise-Box is designed towards the ideal conditions, its modelling considers the uncertainties in materials, manufacture and assembly. Especially, the plate edge conditions are modelled by elastic restraints to handle the uncertainty, where the stiffnesses can be updated based on test results.

(2) The Noise-Box is comprehensively and accurately characterized through experiments. Experiments are performed to the plate, the cavity and the plate-cavity system, respectively, covering different issues. Particularly, the modal parameters of the three situations are all precisely estimated through Experimental Modal Analysis (EMA), so that they can be the reliable reference for FE model updating, where the plate edge conditions are characterized.

(3) The numerical modelling techniques are strictly verified. Since the FEM results are important reference, both for updating the physical parameters of the real system and for validating the self-developed codes of WBM, the FE modelling techniques are first validated by benchmark cases, removing any doubt in element types, mesh control and boundary conditions. Then, the FE models are updated, and the updated models match well with the test system. Based on the FEM results, the WB models are also validated, during which the efficiency of WBM is demonstrated. The SEA models are built for the Noise-Box system to investigate the structure-borne noise and the airborne noise, respectively, and their validations are based on the open source software “SEAlab”.

Finally, with its characteristics well-informed and its matched numerical models prepared, the benchmarking and testing tool Noise-Box, is ready for application. The thesis lastly has an initial test on this tool for structure-borne and airborne noise investigations, where the solutions from the test equipment and the numerical models are presented and compared.

It is considered that this dissertation has the following innovative contributions:

- Proposes a modified weighted residual formulation to WBM, extending the availability of the method for elastically restrained plates;
- Introduces a way to employ EMA for vibroacoustic systems, through which the modal parameters of both plate- and cavity-controlled modes are identified with good accuracy;
- Presents a novel benchmarking and testing tool that can benchmark different techniques for vibroacoustic analysis and test the measures for interior noise control.

**KEY WORDS:** FEM, WBM, SEA, EMA, sound transmission loss, vibro-acoustics

# **PROGETTAZIONE, SIMULAZIONE E TEST DI UN SISTEMA ACCOPPIATO PIASTRA-CAVITA' PER L'ANALISI E IL CONTROLLO DEL RUMORE ALL'INTERNO DI UN VEICOLO**

## **SOMMARIO**

Al giorno d'oggi, si presta sempre più attenzione al comfort acustico dei veicoli, nonché ai problemi di salute causati dal rumore. I vari tipi di veicoli tra cui automobili, treni, aerei e navi richiedono quindi una migliore progettazione acustica, dove l'analisi e il controllo del rumore interno al veicolo sono importanti. Gli strumenti di Computer-Aided Engineering (CAE) sono ora comunemente usati per questi scopi, ma gli ingegneri restano comunque ancora scettici sulla loro affidabilità. Inoltre, i metodi vibroacustici attualmente disponibili sono ancora poco soddisfacenti in termini di capacità, accuratezza o efficienza, soprattutto per le analisi a medie frequenze. Nuovi metodi e codici vengono continuamente sviluppati, ma è difficile trovare casi di riferimento adatti per la loro validazione e valutazione. Pertanto, per facilitare l'analisi CAE del rumore interno ai veicoli, questa tesi presenta uno strumento di benchmarking e test chiamato *Noise-Box*.

L'attività svolta sulla *Noise-Box* include sia prove sperimentali sia modelli numerici, in modo che si possano fornire sia misure di riferimento che calcoli di riferimento. Grazie al banco prova realizzato, progettato come un sistema piastra-cavità facile da modellare e analizzare, si possono eseguire prove vibroacustiche che possono essere accuratamente riprodotte da modelli numerici. Inoltre, il banco può essere utilizzato per misure di transmission loss e per testare diverse strategie di controllo del rumore. I modelli numerici sviluppati riproducono in modo accurato il comportamento vibroacustico del banco. Sono stati utilizzati tre diversi metodi numerici per coprire un'ampia gamma di frequenze: il metodo degli elementi finiti (FEM) e la Statistical Energy Analysis (SEA) sono stati adottati rispettivamente per gli intervalli di bassa e alta frequenza, mentre il Wave Based Method (WBM) è stato applicato per colmare il divario alle medie frequenze. Per il FEM è stato utilizzato un software commerciale, mentre SEA e WBM sono stati implementati in codici sviluppati autonomamente. Per rispondere alla richiesta di casi di riferimento 2D nello sviluppo di nuove tecniche numeriche, vengono forniti modelli validati sia FEM che WBM.

In questo lavoro si è progettato, si è costruito e si è caratterizzato il banco prova. Inoltre, sono stati implementati e validati diversi modelli numerici. Nello specifico:

(1) Il sistema accoppiato piastra-cavità, Noise-Box, è stato progettato per condizioni ideali; la sua modellazione considera le incertezze nei materiali, nella fabbricazione e nell'assemblaggio. In particolare, le condizioni al contorno della piastra sono modellate da vincoli elastici per gestire l'incertezza, dove le rigidità possono essere aggiornate in base ai risultati dei test.

(2) La Noise-Box è stata caratterizzata in modo completo e accurato attraverso prove sperimentali. Sono stati eseguiti esperimenti rispettivamente sulla piastra, sulla cavità e sul sistema accoppiato piastra-cavità. I parametri modali per le tre configurazioni sono stati stimati mediante Analisi Modale Sperimentale (EMA), in modo che questi parametri possano essere un riferimento affidabile per l'aggiornamento del modello FEM e, nello specifico, per l'identificazione delle condizioni al contorno della piastra.

(3) Le tecniche di modellazione numerica sono state rigorosamente verificate. Poiché i risultati FEM sono un riferimento importante, sia per l'aggiornamento dei parametri fisici del sistema reale che per la validazione dei codici auto-sviluppati del WBM, le tecniche di modellazione a elementi finiti sono state prima convalidate tramite casi di riferimento, rimuovendo ogni dubbio su tipi di elementi, controllo della mesh e condizioni al contorno. Quindi, sono stati messi a punto i modelli FEM del sistema Noise Box. Sulla base dei risultati FEM, sono stati validati anche i modelli WB, dimostrandone l'efficienza. I modelli SEA, implementati per il sistema Noise-Box, studiano rispettivamente il rumore structure-borne e airborne e la validazione di questi modelli si basa su un software open source "SEAlab".

Infine, note le sue caratteristiche e validati i modelli numerici, lo strumento di benchmarking e di test (Noise-Box) è pronto per l'applicazione. In conclusione, la tesi riguarda la progettazione, la simulazione e la caratterizzazione sperimentale di un banco prova dedicato a indagini sul rumore airborne e structure-borne.

Si ritiene che questa tesi fornisca i seguenti contributi innovativi:

- propone una formulazione modificata del WBM ai residui pesati, estendendo la disponibilità del metodo per piastre vincolate elasticamente;
- introduce un modo per impiegare l'EMA per i sistemi vibroacustici, attraverso il quale i parametri modali dei modi controllati sia dalla piastra che dalla cavità sono identificati con buona accuratezza;
- rende disponibile un nuovo strumento di benchmarking e test che permette di confrontare diverse tecniche per l'analisi vibroacustica e testare diverse strategie per il controllo del rumore interno.

## Contents

ABSTRACT .....	I
SOMMARIO .....	III
Contents .....	V
List of Symbols .....	IX
Chapter 1 Introduction and state of the art .....	1
1.1 Introduction.....	1
1.2 State of the art .....	3
1.2.1 Benchmarks for vibroacoustic problems .....	3
1.2.2 Simplified systems for vehicle interior noise analysis and control.....	5
1.2.3 Plate-cavity system model updating and EMA .....	8
1.2.4 Numerical methods for vibroacoustic analysis.....	10
1.3 Objective and scope .....	18
1.4 Outline of the dissertation .....	20
Chapter 2 Fundamentals in a plate-cavity system.....	23
2.1 Problems in a plate-cavity system.....	23
2.2 Flexural vibration of thin plate.....	23
2.2.1 Two-dimensional thin plate model .....	25
2.2.2 One-dimensional thin plate model.....	28
2.3 Interior acoustic problem .....	29
2.3.1 Three-dimensional interior acoustic model .....	30
2.3.2 Two-dimensional interior acoustic model .....	31
2.4 Coupled vibroacoustic problem .....	31
2.4.1 Three-dimensional vibroacoustic model.....	31
2.4.2 Two-dimensional vibroacoustic model.....	33
2.5 Sound transmission loss of isotropic panels.....	34
2.6 Summary .....	39
Chapter 3 Design and construction of plate-cavity coupled Noise-Box .....	41
3.1 Set-up principle .....	41
3.2 Design of Noise-Box test bench.....	43
3.2.1 Cavity acoustic design and optimization .....	43
3.2.2 Construction and mould design .....	45
3.2.3 Installation and functioning design.....	46
3.2.4 Overview of the final design .....	47
3.3 Construction of Noise-Box test bench .....	49

3.4 The plate-cavity coupled Noise-Box .....	50
3.5 Summary .....	51
<b>Chapter 4 Numerical investigation using finite element method .....</b>	<b>53</b>
4.1 General procedures for FEM .....	53
4.2 FEM for flexural vibration of thin plate .....	56
4.2.1 Problem definition .....	57
4.2.2 ANSYS model .....	59
4.2.3 COMSOL model.....	60
4.2.4 Analytical solutions .....	60
4.2.5 Numerical results .....	61
4.2.6 One-dimensional plate model validation .....	74
4.3 FEM for acoustic cavity .....	75
4.3.1 Problem definition .....	75
4.3.2 Three- and two- dimensional FE models .....	76
4.3.3 Numerical results .....	77
4.4 FEM for plate-cavity system .....	81
4.4.1 Problem definition .....	81
4.4.2 COMSOL model.....	82
4.4.3 Numerical results .....	82
4.4.4 Two-dimensional plate-cavity model validation.....	85
4.5 Summary .....	87
<b>Chapter 5 Noise-Box test system characterization .....</b>	<b>89</b>
5.1 Noise-Box cavity characterization .....	89
5.1.1 Experimental set-up .....	89
5.1.2 Numerical model and predicting approach .....	90
5.1.3 Modal characteristics of Noise-Box cavity .....	91
5.1.4 Sound absorption of the room inside Noise-Box .....	92
5.1.5 Diffuseness of the sound field inside Noise-Box.....	95
5.1.6 Model update and frequency response analysis.....	98
5.2 Test panel characterization .....	102
5.2.1 EMA of mounted test panel .....	102
5.2.2 Free panel geometric and material properties .....	112
5.2.3 Mounted panel edge conditions .....	122
5.3 Plate-cavity system characterization .....	126
5.3.1 Improved EMA for plate-cavity system.....	127
5.3.2 Comparison between coupled and uncoupled situations .....	136
5.3.3 Plate-cavity system model updating .....	139
5.3.4 Influence of cavity on plate vibration .....	143
5.4 Summary .....	146
<b>Chapter 6 Numerical investigation using wave based method .....</b>	<b>149</b>
6.1 General procedures for WBM .....	149
6.2 WBM for flexural vibration of thin plate .....	150

6.2.1 Field variable expansion.....	151
6.2.2 Weighted residual formulation for boundary conditions.....	153
6.2.3 Model solution and postprocessing .....	156
6.2.4 Harmonic analysis on the mounted test panel .....	156
6.2.5 Validation for one-dimensional plates.....	159
6.3 WBM for acoustic cavity .....	160
6.3.1 Field variable expansion.....	160
6.3.2 Weighted residual formulation for boundary conditions.....	161
6.3.3 Harmonic analysis on the Noise-Box cavity .....	162
6.3.4 Validation for two-dimensional cavities.....	164
6.4 WBM for plate-cavity system .....	166
6.4.1 Field variable expansion.....	166
6.4.2 Weighted residual formulation for boundary conditions.....	167
6.4.3 Harmonic analysis on the Noise-Box test system.....	168
6.4.4 Validation for two-dimensional plate-cavity systems .....	175
6.5 Summary .....	177
<b>Chapter 7 Numerical investigation using statistical energy analysis.....</b>	<b>179</b>
7.1 General procedures for SEA .....	179
7.2 SEA for plate-cavity system under force excitation.....	181
7.2.1 Evaluation of SEA parameters .....	182
7.2.2 Matrix form equation and solution .....	184
7.2.3 Results and discussion .....	184
7.3 SEA for plate-cavity system under acoustic excitation.....	187
7.4 Summary .....	190
<b>Chapter 8 Structure-borne and airborne interior noise investigation .....</b>	<b>191</b>
8.1 Structure-borne noise investigation.....	191
8.1.1 Experimental set-up and results.....	191
8.1.2 Numerical results of FEM and WBM.....	196
8.1.3 Numerical results of SEA .....	201
8.2 Airborne noise investigation .....	203
8.2.1 Experimental set-up.....	203
8.2.2 Experiment and results .....	205
8.2.3 Analytical predictions.....	209
8.2.4 Numerical simulations and results.....	212
8.3 Summary .....	214
<b>Chapter 9 Conclusions and future perspectives .....</b>	<b>217</b>
9.1 Conclusions.....	217
9.2 Future perspectives .....	222
<b>Bibliography.....</b>	<b>225</b>
<b>Appendix A: CAD drawings .....</b>	<b>239</b>
A.1 Assembly drawing.....	239

A.2 Exploded drawing.....	240
A.3 Noise-Box concrete walls.....	241
A.4 Noise-Box steel mounting frame.....	242
A.5 Clamped panel.....	243
A.6 Free panel.....	244
A.7 Steel clamping frame.....	245
<b>Appendix B: Panel transmission loss approximate predictions.....</b>	<b>247</b>
B.1 Sharp's prediction scheme.....	247
B.2 Davy's prediction scheme.....	248
B.3 BS EN ISO 12354-1 (2017) prediction scheme.....	248
<b>Acknowledgements .....</b>	<b>251</b>
<b>List of publications .....</b>	<b>253</b>



## List of Symbols

### Abbreviations

1D	One-dimensional
2D	Two-dimensional
3D	Three-dimensional
BEM	Boundary Element Method
CAE	Computer-Aided Engineering
DEM	Discontinuous Enrichment Method
DOF	Degrees of Freedom
EMA	Experimental Modal Analysis
EFEA	Energy Finite Element Analysis
FRF	Frequency Response Function
FE	Finite Element
FEA	Finite Element Analysis
FEM	Finite Element Method
FSI	Fluid-Structure Interaction
PUFEM	Partition of Unity FEM
SEA	Statistical Energy Analysis
SmEdA	Statistical modal Energy distribution Analysis
SPL	Sound Pressure Level
TL	Transmission Loss
UWVF	Ultra Weak Variational Formulation
VTOR	Variational Theory of Complex Rays
WB	Wave Based
WBM	Wave Based Method
WBEM	Wave Boundary Element Method

### Symbols

$a$	shorter lateral dimension of a rectangular plate (m)
$A_R$	total sound absorption of a room (m <sup>2</sup> )
$A_{jk}$	structural accelerance between point $j$ and $k$ (m <sup>2</sup> /s/N)
$b$	longer lateral dimension of a rectangular plate (m)
$c$	speed of sound (m/s)
$c_w$	damping coefficient (per unit length) for the plate transverse displacement along edge (N·s/m <sup>2</sup> )
$c_\theta$	damping coefficient (per unit length) for the plate rotation along edge (N·s/rad)
$C_{jk,r}$	modal residue of mode $r$ in the transfer function between points $j$ and $k$ in the FRF model
$d$	decay rate (dB/s)
$D$	plate bending stiffness (N·m)
$E$	Young's modulus (N/m <sup>2</sup> )
$Er_f$	error or difference in calculated natural frequencies for the same case or similar cases (Hz)

---

$f_{2D}$	natural frequency of 2D acoustic model (Hz)
$f_{3D}$	natural frequency of 3D acoustic model (Hz)
$f_a$	acoustic natural frequency (Hz)
$f_c$	critical frequency of an elastic structure (Hz)
$f_m$	central frequency of a one-third octave band (Hz)
$f_r$	natural frequency of mode $r$ in the modal model (Hz)
$f_{sch}$	Schroeder frequency (Hz)
$F$	3D: normal point force (N); 2D: normal line force (N/m)
$F_k$	normal point force at Point $k$ (N)
$F_c$	concentrated force at plate corners
$h$	plate thickness (m)
$H_{lk}$	transfer function in a plate-cavity system between sound pressure $p_{cl}$ in the cavity and normal point force $F_k$ on the plate (Pa/N)
$H_0^{(2)}$	zero-order second kind Hankel function
$k$	acoustic wavenumber (1/m)
$k_b$	structural bending wavenumber (1/m)
$k_w$	spring constant (per unit length) for the plate transverse displacement along edge (N/m <sup>2</sup> )
$k_x, k_y, k_z$	wavenumber in $x$ , $y$ or $z$ direction (1/m)
$k_\theta$	spring constant (per unit length) for the plate rotation along edge (N/rad)
$k_{\theta_x}$	spring constant (per unit length) for the rotation along shorter edge of the test panel (N/rad)
$k_{\theta_y}$	spring constant (per unit length) for the rotation along longer edge of the test panel (N/rad)
$l$	length of 1D structure (m)
$L'$	total length of all edges of a volume (m)
$L_p$	sound pressure level in 1/3-octave band (dB)
$L_x, L_y, L_z$	length in $x$ , $y$ or $z$ direction for the rectangular that encloses a convex geometry (m)
$L_\theta$	differential operator related to the rotational displacement of plate
$L_m$	differential operator related to the bending moment of plate
$L_{ms}$	differential operator related to the twisting moment of plate
$L_F$	differential operator for the concentrated force $F_c$
$L_R$	average sound pressure level in the receiving room (dB)
$L_S$	average sound pressure level in the source room (dB)
$L_Q$	differential operator related to the effective shear force in plate
$\bar{m}$	prescribed plate bending moment per unit length (N)
$\bar{m}_{ns}$	prescribed torsional moments per unit length (N)
$M$	modal overlap factor
$M_n$	plate bending moment per unit length (N)
$M_{ns}$	plate torsional moment per unit length (N)
$\mathbf{n}$	local normal vector of an area
$n$	modal density (Hz <sup>-1</sup> )
$n_{2D}$	mode order in 2D acoustic model
$n_a$	number of acoustic wave functions
$n_M$	number of microphones
$n_s$	number of structural wave functions
$n_y$	mode order in $y$ direction
$N_m$	mode count within a given band of frequency
$p$	acoustic pressure (Pa)
$\bar{p}$	prescribed acoustic pressure (Pa)
$\tilde{p}$	acoustic weighting function

$p_a$	acoustic wave function contribution (Pa)
$p_i$	acoustic pressure at a given position $r_i$ (Pa)
$p_A$	absolute pressure (Pa)
$\hat{p}_q$	particular solution function for acoustic pressure, due to the acoustic excitation $q$ (Pa)
$p_{cl}$	acoustic pressure at a given position $r_{cl}$ , especially for the cavity in a vibroacoustic system (Pa)
$p_{ref}$	reference sound pressure, $2 \times 10^{-5}$ (Pa)
$p_{rms}$	root-mean-square sound pressure (Pa)
$P_i$	power input to subsystem $i$ (W)
$P_{id}$	power dissipated by subsystem $i$ (W)
$P_{ij}$	power transmitted from subsystem $i$ to subsystem $j$ (W)
$P_{rms}$	root-mean-square power (W)
$q$	fluid volume flow rate ( $m^3/s$ )
$Q_n$	plate shear force per unit length (N/m)
$\bar{Q}$	prescribed plate shear force per unit length (N/m)
$\mathbf{r}$	position vector in the global coordinate system (m)
$\mathbf{r}'$	position vector in a local coordinate system (m)
$\mathbf{r}_c$	corner position vector (m)
$\mathbf{r}_q$	acoustic source position vector (m)
$\mathbf{r}_F$	force position vector (m)
$R$	sound reduction index (dB)
$R_u$	residual error function associated with a boundary condition for physical quantity $u$ (e.g., $w, \theta, m, Q, cw, cF, m\theta, Qw, p, v, Z, s$ )
$S$	area of a mounted test element ( $m^2$ )
$S'$	total surface air of a volume ( $m^2$ )
$S_m$	total area of a measurement surface ( $m^2$ )
$T$	truncation factor for determining the number of wave functions
$T_{60}$	reverberation time (s)
$T_A$	absolute temperature (K)
$TL$	transmission loss (dB)
$\bar{v}_n$	prescribed acoustic normal velocity (m/s)
$v_{rms}$	root-mean-square velocity (m/s)
$V$	volume ( $m^3$ )
$\mathbf{V}$	acoustic domain
$w$	transverse displacement (m)
$\bar{w}$	prescribed plate transverse displacement (m)
$\tilde{w}$	structural weighting function
$w_s$	structural wave function contribution (m)
$\hat{w}_a$	particular solution function for plate transverse displacement, due to the acoustic pressure loading from an acoustic wave function (m)
$\hat{w}_F$	particular solution function for plate transverse displacement, due to the mechanical force $F$ (m)
$\bar{Z}$	prescribed acoustic impedance ( $kg/m^2/s$ )
$\alpha$	sound absorption coefficient
$\bar{\alpha}$	average sound absorption coefficient
$\alpha_0$	angle between the $x'$ -axis of local coordinate system and $x$ -axis of the global coordinate system (rad)
$\alpha_{jk}$	structural receptance between points $j$ and $k$ ( $m/s^2/N$ )
$\beta_u$	activation coefficient for residual error function $R_u$
$\gamma_n$	direction normal to a surface boundary
$\gamma_s$	direction tangential to a surface boundary

$\zeta_a$	acoustic modal damping ratio
$\zeta_r$	non-dimensional damping ratio of mode $r$ in the modal model
$\zeta_s$	structural modal damping ratio
$\eta$	structural loss factor
$\eta_{id}$	damping loss factor of subsystem $i$
$\eta_{ij}$	coupling loss factor between subsystems $i$ and $j$
$\theta$	normal rotational displacement (rad)
$\bar{\theta}$	prescribed normal rotational displacement (rad)
$\theta_L$	the upper limiting angle for field incidence (rad)
$\theta_{in}$	angle of incidence (rad)
$\psi$	frequency spacing index
$\psi_s$	structural wave function
$\phi_a$	acoustic wave function
$\phi_{in}$	azimuth angle of incident wave (rad)
$\lambda$	acoustic wavelength (m)
$\lambda_b$	structural bending wavelength (m)
$\mu$	ratio between plate bending wavenumber $k_b$ and acoustic wavenumber $k$
$\nu$	Poisson's ratio
$\rho$	structural density (kg/m <sup>3</sup> )
$\rho_0$	air density (kg/m <sup>3</sup> )
$\sigma$	radiation efficiency of panel
$\sigma_T$	standard deviation of the reverberation times $T_{60}$ over different positions (s)
$\sigma_M$	standard deviation of the SPLs over different positions (s)
$\omega$	circular frequency (rad/s)
$\omega_r$	natural frequency of mode $r$ in the modal model obtained from experiment (rad/s)
$\omega_s$	structural natural frequency (rad/s)
$\tau$	transmission coefficient
$\tau_{ij}$	transmission coefficient between subsystem $i$ and subsystem $j$
$\Omega_a$	acoustic boundary surface
$\Omega_p$	acoustic boundary surface with prescribed pressure
$\Omega_s$	elastic structural surface
$\Omega_v$	acoustic boundary surface with prescribed normal velocity
$\Omega_Z$	acoustic boundary surface with prescribed acoustic impedance
$\Gamma$	boundary/edge of a surface structure
$\Gamma_{\bar{w}\bar{\theta}}$	plate edge with prescribed transverse displacement and normal rotation
$\Gamma_{\bar{w}\bar{m}}$	plate edge with prescribed transverse displacement and bending moment
$\Gamma_{\bar{m}\bar{Q}}$	plate edge with prescribed bending moment and effective shear force
$\Gamma_{\bar{\theta}\bar{Q}}$	plate edge with prescribed normal rotation and effective shear force
$\Gamma_{\bar{w}m^*}$	plate edge with prescribed transverse displacement and elastically restrained normal rotation
$\Gamma_{\bar{Q}m^*}$	plate edge with prescribed effective shear force and elastically restrained normal rotation
$\Gamma_{\bar{\theta}Q^*}$	plate edge with prescribed normal rotation and elastically restrained transverse displacement
$\Gamma_{\bar{m}Q^*}$	plate edge with prescribed bending moment and elastically restrained transverse displacement
$\Gamma_{m^*Q^*}$	plate edge with elastically restrained normal rotation and transverse displacement
$\Pi_{in}$	incident power (W)
$\Pi_{tr}$	transmitted power (W)

# Chapter 1 Introduction and state of the art

## 1.1 Introduction

With the development of human society and the improvement of living standard, the public are paying more attention to their living and working environment as well as transport comfort. Vehicle interior noise is an integral part for the transport comfort and has become a competitive selling point for vehicle manufacturers <sup>[1]</sup>. Though vehicles (e.g., automobiles, trains, trams, airplanes and ships) have continuously being quieter, customers are in the meantime more sensitive to noise and discomfort <sup>[2]</sup>. Besides, for vehicle users (passengers, drivers or stewards), the noise exposure is not only a travel experience but also a nonnegligible health issue <sup>[3,4]</sup>. It is reported that noise can cause the auditory effects such as hearing loss, tinnitus and hyperacusis, and the non-auditory effects like annoyance, hypertension, cardiovascular disease, impaired cognitive performance and sleep disturbance <sup>[5]</sup>. The non-auditory effects are hard to be noticed but also prevalent. Therefore, the mitigation or control of vehicle interior noise is essential for the vehicle manufacturers, the transport companies as well as the final users.

Vehicle interior noise is drawing extensive concern from researchers, and many efforts have helped the noise level reduce <sup>[1,2,6-10]</sup>. However, what has been accomplished so far is still far from satisfying. This is on one hand due to the more demanding request from the customers, and on the other hand related to the intrinsic complexity of the interior noise problem, which is associated with the multiple intricate noise sources and transfer paths <sup>[10-12]</sup>. Hence, analysing, predicting and controlling the vehicle interior noise are challenging tasks that will last for long, especially when the vehicles are now under the trends of lightweight design and new energy replacement due to the issues of fuel economy and emissions <sup>[13,14]</sup>.

Apart from finding techniques to mitigate/control the noise, it is also important that the technique itself as well as the developing processing of the technique is cost effective <sup>[15]</sup>. Inevitably, the vehicle manufacturers have to consider the costs of time and money for them to improve or develop their product, so the costs for developing the acoustic design or the noise mitigation/control strategy should be reasonable and match the product's value. Fortunately, the recently rapid-developing Computer-Aided Engineering (CAE) tools significantly save the costs of the product development in the design stage. The tools are able to simulate the dynamic and acoustic behaviours of the product with virtual prototypes, where the design modifications are easy to apply and the added costs are considerably lower

than the traditional physical prototypes. However, this advantage relies on the availability and reliability of the CAE tools for the considered problem.

In terms of the availability, vehicle interior noise is a typical vibroacoustic problem, so the CAE tools for vibroacoustic analysis can be used. Though the CAE tools are now widely used among vehicle industries, their capability with respect to the vibroacoustic simulations is limited <sup>[16]</sup>. One of the limitations, which is also a matter of concern to this thesis, is the so-called ‘mid-frequency gap’ <sup>[16]</sup>. This issue has been pointed out since 1990s, but has not yet been well solved and continuously puzzles the engineers and researchers. For vibroacoustic analysis, there have been three mature methods, i.e., Finite Element Method (FEM) <sup>[17]</sup>, Boundary Element Method (BEM) <sup>[18]</sup> and Statistical Energy Analysis (SEA) <sup>[19]</sup>. But they all have their own applicable or suitable frequency ranges. For FEM and BEM, the two element-based deterministic approaches, they are generally confined to the low frequency range, because the convergence issue requires the element size smaller than a certain portion of the characteristic wavelength <sup>[20,21]</sup>, which makes the numerical model size dramatically increases with frequency. For SEA, on the contrary, as a statistic approach, is applicable for the high frequency range, when the SEA hypotheses should be valid <sup>[22,23]</sup>. Consequently, there is the gap between the two frequency range, where using the element-based models are computationally intractable and using SEA is not useful. Recently, many new vibroacoustic analysis methods have been put forward for this problem <sup>[16,24]</sup>, such as hybrid FE-SEA method <sup>[25]</sup>, Energy Finite Element Analysis (EFEA) <sup>[26]</sup>, Wave Based Method (WBM) <sup>[27]</sup>, etc. But the problem is still not solved and more efforts are necessary.

With respect to the reliability, it is an important issue whenever we’re developing or using a predicting tool. It may draw some attention of the person who develops the tools but is easily overlooked by the users. Indeed, both developers and users need to be aware of the reliability, since it determines whether they can trust and rely on the results. In this regard, benchmarking is one of the most important ways to check the reliability. The importance and demand of benchmarks for vibroacoustic software has been raised for long <sup>[28–30]</sup>, as more and more in-house or commercial tools are developed but they can hardly find the common benchmark cases for validation or calibration. The lack of benchmarks does hamper the development of new predicting techniques, hinder the improvement of existing numerical methods and waste the time and effort of researchers and engineers. Thus, to facilitate the CAE analysis of vehicle interior noise, a benchmarking tool that can validate the associated vibroacoustic analysis is very useful and helpful.

In general, a benchmarking tool can possess only the reference computations, only the reference measurements, or both <sup>[29]</sup>, and the tool *Noise-Box*, which will be presented in this work, is expected to be the last case, having both the reference numerical and

experimental results. Hence, the Noise-Box is going to be a simplified system, whose numerical models are built for simulations and test bench is constructed for experiments. The benefit of such a Noise-Box is multi-fold. The reference computations present not only the results but also its modelling details and computational efficiency, enabling a more direct comparison with a new method. The reference measurements are capable of validating some problems that the results of the current CAE tools are not reliable and checking which models are closer the actual situation. Moreover, they can also help with the development of vehicle interior noise control measures. A new control strategy can first test through the Noise-Box virtual prototype and the Noise-Box test bench in lab before they are applied to a complex real vehicle. A real vehicle will have its own specialties, but some features and principles will hold, such as material properties (of acoustic treatments, panels, etc.), vibroacoustic mechanisms and active control logics. Besides, the realization in a simplified system makes the strategy more likely to be effective in the later formal test. So, it is more informative and cost-saving.

Therefore, targeted for vehicle interior noise analysis and control, this thesis presents a benchmarking and testing tool called *Noise-Box*. The tool is prepared with a test bench and its matched numerical models. The test bench should be designed as a simplified system satisfying the requirements of benchmark cases and fulfilling the expectation of investigating the general vibroacoustic problems among different vehicles. Then, the constructed system needs to be characterized and validated through experiments, specifying its geometry, material and physical parameters for numerical modelling and its critical features for some applications. On the other hand, regarding the numerical models, due to the limitations of currently available vibroacoustic tools, different numerical methods targeted for different frequency ranges are applied, trying best to cover the entire frequency range.

## **1.2 State of the art**

### **1.2.1 Benchmarks for vibroacoustic problems**

It is not uncommon that engineers or researchers seek benchmarks for analysing a certain type of problems, either on computations or measurements. The benchmarks are strong tools for validating a new developed code, an implemented simulation technique or a conducted experimental procedure. The demand for benchmarks in vibro-acoustics has been noticed since 1990s <sup>[29]</sup>, when many researchers started to develop new methods and new codes for vibroacoustic analysis. However, after more than 20 years, a well-known and authorized benchmark database is not yet established, though the outcomes of some

attempts are trackable online <sup>[31–33]</sup>. In 1995-2003, NASA had 4 workshops on the benchmark problems in aeroacoustics <sup>[31]</sup> and the numerical solutions worked out by researchers were finally presented as proceedings <sup>[34]</sup>. This campaign is shown beneficial in promoting the application and development of the numerical methods. Another attempt was the benchmark platform on computational methods for architectural or environmental acoustic <sup>[32]</sup>, which is seen last updated in 2015. The motivation of the platform is to compare different numerical methods (from different contributors) in terms of accuracy and efficiency, by analysing the same specified problems. Later, in about 2015, a more recent platform was built by European Acoustics Association for benchmark cases in computational acoustics <sup>[30,33]</sup>. Since it is a long term project, the platform is now working and being enriched by new benchmark cases. However, the benchmarks currently available on the website <sup>[33]</sup> are only a few. Nevertheless, the importance and significance of benchmarks should not be overlooked. As pointed out in <sup>[30]</sup>, the lack of common reference results does hinder the validation of new techniques. Without these references, researchers need extra time and efforts in finding suitable validation cases and reliable results, and may finally make a comparison that is not so appropriate due to the lack of knowledge about the reference analysis. One may argue that it can be validated by analytical solutions, but in fact, most technically relevant problems don't have analytical solutions, where numerical solutions or measurements are inevitably required, even for the reference results. Besides, while more and more new methods, codes and software are being rapidly developed nowadays, the new techniques also tend to be aimed at more complex problems, which are not suitable to be validated by the simple cases that have analytical solutions. Thus, the benchmarks obtained by numerical solutions or experimental measurements are even more necessary and demanding. To sum up, the general benchmarks, if available, will definitely benefit the related research and booster the developments of new techniques. On the other hand, the users of a CAE tool also need the benchmarks. The developers of a method may clearly know the specifics and limitations of a method (e.g., mesh quality, convergence requirement, boundary conditions modelling, excitation modelling, etc.), but it is often difficult for the users to manage all of them. Thus, the engineers who implement the tools or methods also need the benchmarks, for knowing that if they are using them in a right way. Developers and users, or researcher and engineers are also interested in the difference between different methods in accuracy, efficiency and robustness, and this can be available from benchmarks.

Therefore, both numerical and experimental benchmarks are important, but we currently lack these benchmarking tools. This situation is faced by various acoustic problems, as well as the interior vibroacoustic problems that are considered in this work. Thus, it is worthwhile to construct the Noise-Box for this purpose. What should be focused on next is



the selection of suitable structures, which refers to the design of Noise-Box. Concerning a benchmarking tool with computations and experiments, several criteria have been mentioned in <sup>[29]</sup> and they seem straightforward. One says that the test cases should be able to pinpoint the pitfalls in the numerical methods. This can be interpreted as representative. For instance, in testing a tool for vibroacoustic analysis, the case should demonstrate the coupling effect between structural and acoustic fields. The second criterion highlights that the structure should be easy to model and analyse. In other words, the geometry is simple, the boundary conditions can be modelled and the model size is not too big. Last but not least, all geometric, material and physical parameters should be specified. To satisfy these criteria, it is necessary to have a simplified system that can be used for vehicle interior noise investigations, when the methods to characterize this simplified system and obtain the matched numerical models should also bear in mind.

### **1.2.2 Simplified systems for vehicle interior noise analysis and control**

Vehicle interior noise is a complex problem, where the vehicle's complicated structure, working conditions and air volume inside are involved. When a different vehicle is considered, all these properties are changed, and so is the interior noise. Even in a specified vehicle, the interior noise is still hard to predict or control, since the noise sources are various because of different generation mechanisms and the transmission paths are intricate due to many connections and interactions. Nevertheless, some common features are shared and some investigation techniques can exchange. Generally speaking, a vehicle compartment is an enclosure surrounded by flexible walls and the noise inside is a combination of noises from structure-borne and air-borne paths. It is claimed that the structure-borne and airborne contributions need to be assessed separately <sup>[35]</sup>. The former results from the part of noise radiation by cabin vibration transmitted from sources through solid structures, while the latter means the part of noise, which is already transmitted into air or generated in air, transmitted through the cabin structure. Interior noise from different sound source or different path has different properties. The structure-borne noise is mainly low-to-mid frequency, and the airborne noise is predominant at higher frequencies <sup>[36,37]</sup>. With the trim panels and improvement of pass-throughs, seals, grommets, etc., the airborne noise can be significantly reduced <sup>[37,38]</sup>, but it is in many situations accompanied with an increasing of weight, which is contrary to trend of lightweight design for fuel-efficiency. The trade-off between weight and noise reduction may need some numerical methods to evaluate. The introduction of new material helps to address the problem but enhances the predicting difficulties. If stuck to the passive noise control, the reduction of structure-borne noise may involve modifying vehicle structure or adding vibration isolation. Whether the approach would work well needs to be tested or verified through simulations. Otherwise,

the active structural-acoustic control or the active noise control can be employed. The former applies mechanical inputs to the structure to reduce sound radiation or transmission, while the latter uses secondary sources to cancel or absorb the noise <sup>[39]</sup>. The active approaches are shown effective for low-frequency noises <sup>[1,40]</sup>. Apart from the transmission, the acoustic modes of the compartment also enhance the low-frequency noise levels, thus in an acoustic design, the low-frequency body booms are not trivial. To summarize, though the vehicle compartments are various, they possess some common components like panel, cavity, structure-borne interior noise, airborne interior noise and noise control measures.

Considering the complexity of vehicle interior noise, simplified systems are always used for an instructive investigation. Determined by the final goal of the investigation, different levels of simplifications are applied. Limited to the cases that are not targeted for the noise generation mechanisms, the simplification of a vehicle compartment can be classified into three levels. The first level considers only the simplification on the geometry, so the compartment is scaled smaller or reduced to a regular shape, but still surrounded by flexible thin walls <sup>[41–44]</sup>. In this case, the vibration only interacts with the acoustic field, but also transmits among panels. Hence, though the system is closer to a specific design, it is too complicated as a benchmark tool, since the connection between components is always hard to characterized. The second level simplifies it into a plate-cavity system <sup>[45–54]</sup>. The system consists of a rigid box with one flexible panel. Then, without the influence from other panels, it is easier to determine how the panel structure affects the acoustic field inside the box and reversely, how the cavity influences the panel vibration. The plate-cavity system has been widely used for vibroacoustic analysis. For the plate, its structure and boundary conditions are not limited. It can be simple as an isotropic thin plate objected to the clamped or simply-supported boundary conditions <sup>[45–48]</sup>, or complicated as a laminated plate with elastically restrained or non-uniform boundary conditions <sup>[49,50]</sup>. For the cavity, it can be rectangular shaped or irregularly-shaped (e.g. car-like shaped) <sup>[51,52]</sup>, and the wall impedance can also be changed <sup>[53,54]</sup>. The third level simplification considers no flexible structure but only the acoustic cavity inside <sup>[55–57]</sup>. Such a model isolates the cavity from the structure vibration and helps to determine its acoustic property affected by its geometry and wall impedance. This is preferred when the coupling effect between walls and cavity is negligible, and acceptable when the coupling effect is weak or not of interest. However, since the simplified system is for vibroacoustic analysis where structure cannot be absent, this simplification is not adopted. Therefore, the plate-cavity system is finally selected. Besides the advantages mentioned above, it is also available for the key components: panel, cavity, structure-borne interior noise, airborne interior noise and noise control measures, for interior noise analysis and control. Additionally, if the flexible panel is replaced by a thick rigid wall, it can also be used to investigate the uncoupled interior acoustic problems.

Under the level of plate-cavity system, the regularity of cavity shape is also an important issue. In the literature, it can be noticed that the shape of the cavity may determine whether the problem is available for an analytical solution. The analytical solutions have the advantage of explicitly displaying the dependence of model behaviour on the physical parameters and easily extracting the physical interpretation <sup>[58]</sup>. The more regular shape is more likely to obtain analytical solutions but the acoustic field will be less like a vehicle compartment. In fact, the plate-cavity system has been used for interior noise and vibroacoustic analysis since 1960s. At the beginning, the plate-cavity system was limited to a rigid rectangular box with one flexible plate and the problem was solved by analytical methods. Lyon <sup>[46]</sup> first used this model to study the noise reduction through the flexible plate by dividing the problem into three situations according to the resonant behaviour of the panel and interior volume at corresponding frequency. Almost at the same time, Dowell and Voss <sup>[45]</sup> investigated the effect of the cavity on the plate by describing the deflection of the plate as a series expansion. Pretlove <sup>[59,60]</sup> derived the exact solution to the free and forced vibration of the cavity backed flexible wall with the acoustic velocity potential expressed by Fourier series, and according to the results, concluded the two types of plate-cavity system: one with the acoustic stiffness much less than the plate, where the cavity has little influence on the plate dynamics; the other with the acoustic stiffness approaching or larger than the plate stiffness, when the effect of the cavity need to be considered. Later, the popular modal-interaction theory for vibroacoustic analysis was proposed by a series of efforts from different researchers <sup>[47,58,61,62]</sup>, where the coupling between cavity and structure is represented by the coupling coefficient. This coefficient is given by the uncoupled structural and acoustic mode shape functions, which are respectively used for the expansions of structural field and acoustic field. Although this theory can also be applied to irregular plate-cavity system other than the simplest rectangular plate-cavity system, the former one is hard to obtain analytical solutions, because no simple algebraic expression for the natural frequencies and mode shape functions of the uncoupled subsystems are available. Nevertheless, the research on the analytical solution or modelling for more complicated plate-cavity system is never stopped. The introduced complexity can come from the structure of the plate, like double-panel structure <sup>[53]</sup>, laminated structure <sup>[49,50]</sup>, orthotropic structure <sup>[63]</sup> or nonlinearity effective structure <sup>[64]</sup>. It can also be the boundary conditions of plate (e.g., elastic <sup>[65,66]</sup> or non-uniform <sup>[49]</sup> support) or of cavity (e.g., complex wall impedance <sup>[54]</sup>). It may even result from the geometry of the cavity, such as a trapezoid <sup>[51]</sup> or an irregular shape that can be divided to rectangular and right-angled trapezoid <sup>[66]</sup>. Regarding the last case, it is expected that an analytical method can be developed in future for the cavity with only one pair of parallel walls instead of two.

### 1.2.3 Plate-cavity system model updating and EMA

For accurate predictions of vehicle interior noise, the accurate numerical vibroacoustic models of the vehicle compartments are important. But there are always errors in the structural and acoustic modelling, and model updating is an effective way to improve the accuracy <sup>[67]</sup>. The errors can come from the modelling of geometry, material, damping, joints and boundary conditions. Since most parameters are sensitive in the low frequency ranges and FEM is commonly used, a majority of model updating techniques are based on FEM, where some intrinsic errors in the FE modelling will also present <sup>[68]</sup>. The target of a model updating is to correct the numerical model so that its predictions match its responses obtained through experiment. Hence, it is crucial that the FEM is applied correctly and precisely, minimizing the errors from the technique itself. It is also essential that the experimental results are trustable. Then, the numerical model can be updated by the comparison of FRFs <sup>[69–72]</sup>, natural frequencies or/and mode shapes <sup>[73–75]</sup>. As reviewed by Sehgal and Kumar <sup>[68]</sup>, the updating techniques can be classified as direct and iterative ones, and the model adjustment may focus on the matrix elements or the physical properties. Most of the direct techniques update the mass and stiffness matrices, which are difficult to translate to the physical parameters. The iterative techniques can update the physical parameters directly, but have the low-efficiency and divergence problems. In recent years, some of the updating techniques, which were proposed for structural dynamic models, have been applied to vibroacoustic problems <sup>[67,72,73,76,77]</sup>. It would be interesting to develop an efficient and automatic model updating technique for the vibroacoustic system, but it is out of the scope of this thesis. In this work, taking the advantage of the simplicity of the plate-cavity system, a knowledge-based method will be used. Natural frequencies are mainly used as updating reference while FRFs and mode shapes help to validate the results. By investigating the sensitivity of the model to the updating parameters, the next set of parameters are given manually. Finally, the updating will be stopped when good agreement between numerical and experimental results are seen for natural frequencies and FRFs. This is not automatically, but more efficient when the system is simple and well investigated, especially when not a few modes are considered and the model size is not small. In the iteration process, the updating direction of the model is under control.

In the plate-cavity system, the modelling errors are most likely to occur at the material properties, boundary conditions and damping of the plate and the sound absorption properties of the cavity surfaces <sup>[72]</sup>. Thus, the parameters related to these factors should present in the mathematical model of the system, especially for the plate boundary conditions. In the modelling of a plate, the ideal boundary conditions (simply supported, clamped and free) are often used, but they are hard to realize in real engineering practice. Even for a specially designed mounting in the lab, the ideal situations are still hard to reach

[78,79]. So, it is probably the Noise-Box will face this problem and a more realistic model should be applied to the plate. Another model, which is popularly investigated model recently, considers that the plate edges are elastically restrained against translation and rotation [80–83]. Such a model has the advantage of determining the edge conditions by the translational and rotational stiffnesses. For the test plates that are designed as clamped, the model that depicts the edges as rigidly supported but elastically restrained against rotation shows good performance in some research [67,84], where the characterized rotational stiffnesses indicate that the edges could be not only imperfectly clamped but also different in their stiffnesses. Therefore, this work will consider the general- and partial-elastically restrained edge conditions in the modelling of the plate. Especially for the latter case, the rotational stiffnesses of the plate edges will be updated so that the models can better match the Noise-Box test bench.

Regarding the experimental data for updating the models, Experimental Modal Analysis (EMA) will be applied, which is the major technique to obtain the modal parameters (i.e., natural frequencies, mode shapes and modal damping ratios). A comprehensive EMA includes the modal testing and the subsequent parameter identification. After the point-to-point FRFs are also obtained from the modal testing, the biggest challenge is to extract the system parameters from these FRFs, which is called *modal parameter estimation* (or identification) [85]. When a mathematical function is used to fit the measured FRF (for frequency domain, or Impulse Response Function for time domain), the process is referred to as curve fitting, which is usually done by minimizing the squared errors [86]. Determined by the number of modes and the number of FRF, the algorithms can be categorized into the SDOF method, global SDOF method, MDOF method and poly-reference MDOF method [87]. For a curve fitting, it is necessary to construct the mathematical model from modal parameters, so that the fitting can be performed and after which, the modal parameters are available. If the model expression is not available, it is optional to use the peak-picking approach for a rough estimation of natural frequencies, which may also yield good results if the structure is lightly damped and the frequency resolution is sufficient. When EMA is widely used for structures, the acoustic EMA is not so popular. One of the main reasons should be the characterization of the acoustic input. The commonly-used theoretical FRF of a closed acoustic system is between sound pressure and volume velocity (or acceleration). The volume velocity is hard to obtain from a usual loudspeaker [88,89], except a few specially designed loudspeakers [90,91]. Whether the input is available determines whether the theoretical FRF can be used as the fitting model. The FRFs in modal model formulation are straightforward for the uncoupled structures and acoustic cavities [86,87,90,91], since their system matrices are symmetric. However, for a vibroacoustic system, if the inputs and outputs are represented by measurable quantities (e.g., force, sound pressure, displacement,

etc.), it is inevitable that the system matrix is unsymmetric. Thus, it may be necessary to use the partial fraction expansion to formulate the transfer functions <sup>[92–94]</sup>. In fact, there are very few references talking about how to achieve the EMA of a vibroacoustic system and extract the modal parameters, and it is a problem to solve in this work.

## 1.2.4 Numerical methods for vibroacoustic analysis

The numerical predicting tools are now indispensable for industries. With these tools, the behaviour of products can be simulated in virtual prototypes instead of the physical ones, which significantly saves time and cost, and probably leads to a better design. However, a single reliable and practical approach to predict the vehicle interior noise for the whole frequency range is not available. Different approaches are suitable for different frequency ranges, and every approach has its own limitations, therefore it is currently widely accepted that different frequency ranges use different numerical methods. If the entire audio-frequency range is roughly divided into low, middle and high ranges, the difficulties in vibroacoustic analysis are especially present in the mid-frequency range, as it has been pointed out that FEM and BEM are available for the low frequency range and SEA is suitable for the high one.

### 1.2.4.1 Mid-frequency numerical methods

Since the mid-frequency difficulty was pointed out at 1990s, many new vibroacoustic methods have been raised and developed. As one of the targets of this thesis is to analyse the vibroacoustic system in the whole frequency range, various methods for the mid-frequency ranges have been reviewed in order to select one that is suitable to the Noise-Box. Meanwhile, attention is also paid to their development history, through which we can see how to make our benchmarks more useful.

The advance methods for mid-frequency problems can be classified into three categories:

- Extension of the deterministic approaches towards higher frequencies. This can be an enrichment to the FEM or BEM element-based method, such as Partition of Unity FEM (PUFEM) <sup>[95]</sup>, Wave Boundary Element Method (WBEM) <sup>[96]</sup>, Discontinuous Enrichment Method (DEM) <sup>[97]</sup>, etc. It can also be a different kind of deterministic approaches like Trefftz method <sup>[98]</sup>, which includes the WBM <sup>[27]</sup>, Ultra Weak Variational Formulation (UWVF) <sup>[99]</sup>, Variational Theory of Complex Rays (VTCR) <sup>[100]</sup>, etc. However, the above subdivision between the enriched element-based method and the Trefftz method is not always clear, especially when a Trefftz approach includes the division of the problem domain into elements <sup>[101]</sup>.
- Extension of the statistical approaches towards lower frequencies. The methods in this category are mostly based on the SEA, but try to detail the energy distribution

or relax the SEA assumptions, such as the EFEM [26] and Statistical modal Energy distribution Analysis (SmEdA) [102,103].

- Combination of the deterministic and the statistical approaches. The hybrid FE-SEA method [25], which models the long-wavelength deterministic components using FE and describes the short-wavelength statistical components as SEA subsystems, belongs to this category. Similarly, this category also includes hybrid BE-SEA [104], hybrid WBM-SEA [105], hybrid FE-EFEM [106] and so on.

The conventional FEM uses polynomials as shape functions for the field variables. Thus, when the field is becoming more oscillating as the frequency increases, the element size needs to be reduced, provided that the orders of the polynomials are fixed. For the approaches that enrich the FEM, they mostly enrich the field variable approximation with some *a priori* knowledge of the problem. With the enrichment, it is possible to have a coarser mesh, reducing the model size and computation burden. However, the enrichment may complicate the model construction or worsen the conditioning of the systems of equations. This will depend on the feature of the considered problem and how the enrichment is applied.

In the PUFEM [95], the enrichment is introduced by multiplying the polynomial shape functions with the locally defined basis functions that include *a priori* knowledge about the differential equation. The method illustrates high efficiency for some problems that are hard to tackle in the conventional FEM [95,107]. The WBEM [96] is very similar to PUFEM, but the enrichment is applied to the shape functions of those boundary elements. Differently, the DEM [97] enriches the standard polynomial field in each element by adding a non-conforming field that contains the homogeneous solutions of the differential equation. Then, the enrichment is enforced to be continuous at element interfaces by Lagrange multipliers. This method was proved an effective way to obtain accurate results under a coarse mesh [97] and considered having a better conditioning than the PUFEM [101].

The Trefftz method is a deterministic approach that is not element-based. It was firstly presented by Trefftz in 1926 [98], earlier than the invention of the FEM, but not so popular as the FEM. In fact, the Trefftz method needs much more *a priori* known information, which may have somehow prohibited its prevalence. The formulations of this method are usually classified into indirect and direct ones [98]. The indirect formulation expresses the solution as the weighted superposition of the functions that satisfy the governing equation of the problem, and then determines the unknown weighting parameters by enforcing the solution to satisfy the boundary conditions in a weak integral form. The direct formulation takes the function that satisfies the governing equation as the weighting function to form the weighted residual expression of the governing equation, and then transforms the

expression to a boundary integral equation. Later, the boundary integral equation can be solved numerically by a discretization similar to the BEM.

The indirect formulation is much more widely used. The WBM, the UWVF and the VTCR are all indirect Trefftz approaches. The WBM<sup>[27]</sup> is a typical indirect Trefftz method, whose modelling procedures follow the original definition. The functions used to approximate the solution are so-called wave functions. In the WBM, it is not always necessary to divide the problem domain or just a small number of large subdomains is adequate. However, for the requirement of convex subdomains, it may not so powerful when the problem geometry is too complicated. The UWVF<sup>[99]</sup> is developed under the framework of FEM by dividing the problem domain into elements. But in each element, discontinuous basis functions (plane wave, Bessel or evanescent wave basis functions<sup>[108]</sup>) are used instead of the polynomial shape functions. Then, the ultra weak variation formulation is derived using the solutions of the adjoint problem as the test functions, included the governing equation, the boundary conditions and the transmission conditions at element interfaces. Compared with the WBM, the UWVF is capable of more complex geometry (as well as the FEM), but the modelling process is more complicated. Moreover, it is not yet seen the method's application to coupled vibroacoustic problems, though it has been applied in acoustics<sup>[99]</sup> and elastic wave propagation<sup>[109]</sup>. Differently, the VTCR<sup>[110]</sup> first writes the variational formulation of the problem, and then uses complex rays to describe each subdomain, where two-scale approximations are used. Only the slowly-varying scale is discretized, which corresponds to the amplitudes of the waves. The rapidly-varying scale for spatial shape of the waves is expressed analytically. Finally, the solution yields the wave amplitudes that can reconstruct the field<sup>[24]</sup>. The VTCR has illustrated its efficiency for structural<sup>[111–113]</sup> and acoustic<sup>[114–116]</sup> problems, but its application to vibroacoustic problem is not yet found in literature.

The EFEA is similar to the SEA as an energy based approach, but it is also like the FEM, dividing the problem domain into finite elements. The primary variable of EFEA is defined as the energy density averaged timely over a period and spatially over a wavelength. Specifically, the method derives the governing differential equations in energy variables and uses the finite element formulation for numerical solution<sup>[16,117–119]</sup>. Compared to the SEA, it is similar in modelling the system by energy and power flow, but different in the type of variable expansion basis. The SEA uses the modal basis and yields a system of the lumped parameters of subsystems, while the EFEA is based on the wave basis and assembled by finite elements. As a result, the EFEA is able to provide a more detailed energy distribution. So far, the method has been successfully applied to many engineering problems for the structural, acoustic or vibro-acoustic analysis in the mid- to high-frequency range<sup>[11,119–121]</sup>.



The SmEdA <sup>[102]</sup> is also based on the energy conservation. But in comparison to SEA, it relaxes the assumption of modal energy equipartition. Thus, when describing the power exchange between subsystems, the method concerns the couplings between the subsystem modes. Hence, the method is applicable when the modal overlap is low, rendering its capability for mid-frequency problems. However, the method requires the eigenmodes and eigenfrequencies of uncoupled subsystems. When they're not available from analytical solutions, modal analysis may need to be performed via FEM, which will lower computation efficiency and hinder its availability to high frequencies. Nevertheless, it is possible to link SmEdA with SEA to cover a wide frequency range <sup>[102,103]</sup>.

The hybrid FE-SEA method <sup>[25]</sup> in the last category is one of the well-developed approaches for mid-frequency vibroacoustic problems. The method is available in the commercial software VA One, and has been applied to various vibroacoustic problems <sup>[122–126]</sup>, where the results demonstrated good accuracy. As indicated by name, the method combines the FEM and the SEA, where the FEM is used for the ‘deterministic’ subsystems and the SEA is for the ‘statistical’ subsystems <sup>[25]</sup>. Since the subsystems with short wavelengths, which should be meshed by fine elements in FE model, are considered as SEA subsystems that have only one degree of freedom, the total degrees of freedom of the entire model can be significantly reduced, making some problems intractable by FEM being solvable by hybrid FE-SEA method. Meanwhile, the long-wavelength subsystems that don't satisfy the SEA assumptions are still modelled by FEM. Therefore, it can be noticed that the hybrid FE-SEA method is extremely suitable for a complex system whose components have very different characteristic wavelengths. However, the dilemma could be the case when all components are falling into the mid-frequency region.

Throughout all the methods, it can be noticed that in general, a new method is developed for 1D or 2D problems before extended to 3D ones. Meanwhile, benchmarks are more from the traditional numerical solutions instead of the analytical ones. Hence, it is reasonable to provide numerical results of the Noise-Box as part of the benchmarks, and it would better also present the numerical benchmark cases for corresponding 2D problems, so that the users can get a first check on their approaches in 2D situations before moving to 3D cases.

#### 1.2.4.2 Selection of numerical methods

Combined the above mid-frequency approaches with FEM, BEM and SEA, a big family of numerical methods for vibroacoustic analysis is presented. Then, it's a matter of selecting numerical methods for a given vibroacoustic problem. There are three main considerations: geometry, solution frequency range, and application.

Geometry is one of the considerations, because different numerical approaches may have different requirements on their elements or subdomains. For example, in the element-based methods, it is an important step to check the element quality, where the requirements of the element are indicated, including aspect ratio, Jacobina ratio, skewness, etc; in the WBM, the subdomains are required to be convex and the better close to regular envelopes; and in the BEM, the elements are on the surfaces and need to be higher qualified to avoid singularity. In these cases, the geometry will influence the discretizing strategy and then determine the final model size.

The solution frequency range is undoubtedly an important consideration, due to the fact that no method can confidently solve the problem in the entire audio-frequency range. However, when it is always mentioning the frequency regions as low, middle or high, the division or border lines of these regions are actually undetermined and ambiguous. In fact, the low or high standard is relative and related to the dimension of specific system or component. In <sup>[16]</sup>, the three frequency ranges are determined by the number of waves within a given dimension, which is calculated by  $kl$ , where  $k$  is the wavenumber relevant to the frequency and  $l$  is the characteristic length. With this non-dimensional parameter  $kl$ , the low, mid and high frequency ranges are  $0 < kl < \sim 20\pi$ ,  $\sim 10\pi < kl < \sim 40\pi$  and  $kl > \sim 20\pi$ , respectively, and an example also shows [20,1000], [500,2000] and [1000,  $+\infty$ ) as the three ranges in Hz for a vehicle passenger compartment <sup>[16]</sup>. However, for complicated system,  $k$  and  $l$  are difficult to identify, and the classification is according to the estimate  $kl$  values or other empirical values. Thus, it can approximately know the corresponding frequency region of a given frequency range. When a wide frequency range including the three regions is considered, it is more often the extend the results of the selected method to a frequency range wider than the supposed region. Then, the results in the overlapping frequency region can be compared and finally decided.

The application indicates what kind of results is expected to obtain, so that the results will be useful in the application. The deterministic methods enable detailed modelling and provide response solutions (vibration or sound pressure) that are available for every analysed frequency at any point. On the other hand, the statistical methods give broadband and spatially averaged responses. Therefore, the former is more suitable for a system whose excitation is at discrete frequencies in the low- or mid- frequency and whose modelling or response matters at some specified points, while the latter is optimal for a system that cares about the frequency-averaged and spatial-averaged responses.

Since it is a target for this thesis to analyse the vibroacoustic system in the whole frequency range, several numerical methods are selected for different regions. Considering that the analysis object will be a plate-cavity system, which belongs to the interior vibroacoustic

problems, the FEM is used for the low frequency range. In the high frequency range, the study will concern about the average responses of the plate and the cavity, so the SEA is selected. Regarding the mid-frequency range, the WBM is finally chosen, due to the following considerations: the problem involves only two subsystems; both plate and cavity are of simply geometry; the boundary conditions of the plate and the cavity may need to be modelled and characterized; responses at some points of the cavity and the plate may be required.

#### 1.2.4.3 Finite element method

The FEM is the most commonly used numerical prediction technique. It is a deterministic and element based approach, and can be characterized by the following two features:

- transformation of the differential equations into a weak integral formulation;
- discretization of field variable(s) and geometry into finite number of small subdomains (called elements), and within the element, approximating the variable(s) and geometry in terms of shape functions and nodal variables.

These two points highlight the approximations in the modelling process and explain how the method works. Since no rigorous requirement about the problem equations and the field geometry, the FEM is highly adaptive and flexible. It can be and has already used for various kinds of problem and geometry, making it the most popular numerical prediction technique after its rapid development in the past half century. For dynamic problems, the field approximation is correlated with the element size. In the conventional FEM, polynomial shape functions are used. To limit the numerical errors, the maximum element size for a given frequency is provided<sup>[20,21]</sup>. Consequently, the number of elements and the corresponding model size increase with higher frequencies. Owing to the heavy computational load and long computational time for large FE models, FEM is practical in the low frequency range for most applications.

The FEM was invented a long time ago, and started to be popular in the 1960s, with the development of computers. It was originally developed to solve static structural analysis and later applied to vibroacoustic problems in the 1970s<sup>[16]</sup>. Nowadays, it is quite mature and available in many commercial CAE tools. In this thesis, two of them, i.e., ANSYS 17.2® and COMSOL 5.4®, will be used for the structural, acoustic and vibroacoustic analyses. Except the frequency limitation, the FEM has no problem on these analyses, even when the geometry is complicated. However, when the method is implemented by a CAE tool, there is always a question whether the particular problem is tractable by the code or whether the user uses the tool in a correct way. For instance, concerning the plate that is to be modelled in this work, the tools and their users' guides don't tell us how to model the

elastically restrained edges, which element type to select or whether the results are accurate. Therefore, even for well-developed tools, benchmarks are still important.

#### 1.2.4.4 Statistical energy analysis

The SEA is a statistical and energy based approach. The name itself features the method. *Statistical* indicates that the investigating system is a sample from the population of similar design construction. The dynamic parameters are described statistically. *Energy* is the primary variable of interest. The model is established based on the energy flow equilibrium between subsystems. Vibration or acoustic response is derived from the energy levels of subsystems. *Analysis* emphasizes that the SEA is a framework of study. The SEA parameters (e.g., modal density, damping loss factor, coupling loss factor, etc.), which are decisive in the SEA models, are dependent on the geometry, material and connection of subsystems, therefore needs particular evaluations <sup>[19]</sup>.

The SEA was introduced by Lyon and his colleagues <sup>[23,127–129]</sup> in the 1960s for the high-frequency vibroacoustic response of complex systems. The SEA is advocated for high-frequency problems under two considerations: one is the unaffordable computational demand of the traditional deterministic methods (i.e., FEM and BEM); the other is the unavoidable uncertainty inside the system <sup>[130]</sup>. The foundations (either the modal approach <sup>[19]</sup> or the wave approach <sup>[16]</sup>) are complicated, but the implementation is simple. The main question is whether the prediction is reliable, and the answer, to a great extent, depends on whether the inherent hypotheses are satisfied and whether the SEA parameters are correctly evaluated. Until now, the hypotheses are still open for discussion <sup>[22,23]</sup> and some of the SEA parameters (e.g., damping or coupling loss factors) are still hard for a precise evaluation in some structures <sup>[131]</sup>. Nevertheless, the SEA has been successfully applied to many vibroacoustic systems for different industries <sup>[132–135]</sup>. There are also several commercial solutions such as Actran SEA module, VA One SEA module, Wave6, etc. In fact, different solutions may use different formulations to evaluate the SEA parameters, resulting in different outcomes, where we once again see the significance of benchmarks. Since the plate-cavity system is simple and the SEA modelling is not difficult, this work will use self-developed codes for the SEA solution, so as to master all the details inside the model.

#### 1.2.4.5 Wave based method

The WBM is a deterministic approach but wave based. It is an indirect Trefftz method <sup>[98]</sup> and can be featured by the following two points:

- approximation of field solution using the weighted superposition of wave functions that satisfy the governing equations;
- transformation of the boundary conditions into a weak integral formulation.

The unknowns in the model are the contribution factors of the wave functions. Thus, the model size and convergence of WBM are associated with the number of wave functions. Though more wave functions are needed for higher frequencies, the number increases not so dramatically as the number of degrees of freedom in the FEM. Thus, the WBM is more efficient than the FEM, especially at higher frequencies, so it is considered a promising numerical technique for mid-frequency analysis.

The WBM was first proposed by Desmet<sup>[27]</sup> in the 1990s for coupled vibroacoustic analysis and then has been continuously developed. The development includes extending its applicable fields (e.g., acoustic<sup>[136]</sup>, structural<sup>[137]</sup> and poroelastic<sup>[138]</sup> problems), overcoming its limitations (e.g., hybrid FE-WBM<sup>[139]</sup>), promoting its computational efficiency (e.g., multi-level WBM<sup>[140]</sup>) and improving its convergent performance<sup>[141]</sup>. With respect to the structural problems, the WBM has been widely investigated for plate vibrations. Vanmaele<sup>[137]</sup> further studied the WBM for the Kirchhoff plate bending problem and proposed to use corner functions to address the convergence problem caused by the stress singularities. In the same work, the method was extended to membrane problems and flat plate assemblies. Then, Vergote<sup>[142]</sup> considered the WBM for plate with point connections to springs, dampers and masses, and Devriendt et al.<sup>[143]</sup> and Xia et al.<sup>[144]</sup> discussed the WBM for orthotropic plates. For plates under distributed excitations, Jonckheere et al.<sup>[145]</sup> proposed the way to apply the WBM by introducing the particular solutions for distributed loads derived by the Hankel-based or the Fourier-based approach. Recently, Klanner and Ellermann<sup>[146]</sup> developed the WBM for the vibrations of thick plates, and Chen et al.<sup>[147]</sup> extended the WBM for plates under thermal load. The WBM for plate problem is seen being completing. When the above researches have constructed the weighted residual formulation for the commonly-used prescribed edge conditions (i.e., clamped, simply supported, free or loaded and symmetric boundary conditions, Liu<sup>[148]</sup> introduced the formulation for the general elastically restrained edges. The extension to more general edge conditions is valuable, since in practice, the conditions tend to be intermediate between the classical ones and sometimes are more appropriate to be modelled as elastically restrained against translation and rotation<sup>[82,83,149]</sup>. However, the formulation proposed by Liu<sup>[148]</sup> is not sufficiently generalized, because it performs not so good for the classical boundary conditions and cannot deal with the types of edges that are partial elastically restrained, i.e., the edges only elastically restrained against rotation or translation. Note that these edge conditions are also popularly used, especially for the plate edges that are rigidly supported but elastically restrained against rotation<sup>[67]</sup> and the plate edges that

are resting on elastic supports (with only linear or rotation springs) <sup>[150]</sup>. Given all this, this thesis further improves the weighted residual formulation when implementing the WBM, making it available to any type of edge conditions.

As for the acoustic problems, the WBM is now available for interior, exterior and scattering problems. In the original work <sup>[27]</sup>, the WBM for 2D and 3D interior acoustic problems has been clearly introduced in detail, where the problem geometry is relatively simple, the excitation is a harmonic monopole source, and the boundary conditions include prescribed pressure, normal velocity and normal impedance. Most interior acoustic problems of simple geometry are solvable based on this originally-proposed methodology, as well as the Noise-Box cavity that will be investigated in the work. Nevertheless, the method was further developed to make it available for more general geometry and more stable convergence. This process concerns about the division and combination of subdomains in 2D <sup>[151]</sup> and 3D <sup>[152]</sup> situations, and function enrichment for corner singularities <sup>[153]</sup>. The WBM for exterior acoustic problem was first introduced by Pluymers <sup>[152]</sup>, where the 2D unbounded wave function sets were introduced, and further developed and then extended to 3D situation by Bergen <sup>[136]</sup>. Later, the cases with scatterers inside the acoustic field were also included <sup>[140,154]</sup>.

Concerning the vibroacoustic problems, the feasibility of the WBM for them relies on the feasibility of the WBM for the corresponding uncoupled structural and acoustic problems, since the coupling between the structural and acoustic fields are introduced quite straightforward in the WBM. The currently available cases mainly contains the coupling between thin plate and interior or exterior acoustic field <sup>[27,143,155,156]</sup>. Therefore, applying the WBM to the plate-cavity coupled Noise-Box will not be a big challenge, but it is still a novel thing for modelling the coupled system constituted by a plate with elastically restrained edges and a damped cavity. And it needs to make sure the convergence and conditioning are not worsened by the introduction of new weighted residual formulation in the structural field.

### **1.3 Objective and scope**

The objective of this dissertation is to present a plate-cavity coupled Noise-Box, which is aimed at benchmarking the numerical methods and CAE tools for vibroacoustic analysis, and meanwhile considered for its potential capability to test interior noise control measures. The Noise-Box is a comprehensive benchmarking and testing tool with a test system and some numerical models that can accurately predict its behaviour. To obtain such a tool, this work needs to design, construct and characterize the test system, and build, validate and

update the numerical models. The design and construction are based on the function of the Noise-Box and some background knowledge of plate-cavity systems. The outcome should be a simplified system that is easy to model and analyse, and available for structure-borne and airborne interior noise investigations. The characterization is intended for the parameters that determine the dynamic performance of the system and its components, e.g., the modal parameters, material properties, edge conditions of the plate; the modal parameters, wall impedance, sound field diffuseness of the cavity; and the modal parameters of the plate-cavity system. EMA is the main technique applied to identify the modal parameters, while the physical parameters (including material properties and boundary conditions) are determined through FE model updating. For the numerical models, three numerical methods are used due to the frequency limitation of the currently available vibroacoustic tools. While the traditional approaches FEM and SEA are for the low- and high- frequency ranges, respectively, the WBM is employed and developed for its potential to fill the mid-frequency gap. This work implements FEM in the commercial software (COMSOL and ANSYS), and develops the MATLAB codes for SEA and WBM. Concerning the demand for 2D benchmark cases in developing new numerical techniques, validated 2D models of FEM and WBM are provided for the additional reference results. This work finally uses the Noise-Box for structure-borne and airborne noise investigations, and checks the performance of the test system and the numerical models. The development of interior noise control measures is not covered in this dissertation, though it is one of the considerations in the design of Noise-Box.

The biggest challenge is the agreement between the numerical models and the test system. This actually related to many issues throughout the research:

- whether the test system can be comprehensively described by the mathematical models;
- whether the numerical methods are applied correctly and properly to the problems;
- whether the geometrical, material and physical parameters in the numerical models are consistent with the test system;
- whether the experimental results are reliable and precise, since the numerical models are updated based on the experimental data.

Therefore, this work should take them into consideration. For the first point, in the primary mathematical modelling of the plate-cavity system, the non-ideal edge conditions of the plate in a real system are considered, and they are modelled by elastic restraints. A lot of research has applied the elastically restrained edge conditions but seldom mentioned about how they are modelled in the FE models. So, this work will figure how to model them in COMSOL and ANSYS. Besides, since these conditions are currently not available in the WBM, the conventional WBM needs to be modified for this purpose. For the second point,

the numerical modelling techniques are validated through benchmark cases in the process, either by analytical solutions or cross validations between models. For the third point, model updating is performed based on the results of FE modal analysis and EMA. However, this is not an easy task, especially for the plate-cavity coupled case, where the FE modal analysis may face an ill-conditioned system matrix and the EMA of structural dynamics cannot directly applied. For the last, the uncertainties in the experiment are analysed and discussed.

## 1.4 Outline of the dissertation

To describe the plate-cavity coupled Noise-Box and its development, this dissertation is structured into 9 chapters, covering its design, simulation and testing.

*Chapter 2* introduces the basic theories and mathematical models that are involved in a plate-cavity system. They include the fundamentals of the flexural vibration of thin plate (with arbitrary edge conditions), the interior acoustic problem, the interior vibroacoustic problem and the sound transmission loss of panels. Since the numerical models will provide benchmark cases for the problems in a lower dimensional space, the mathematical models of 1D plate, 2D cavity and 2D vibroacoustic system are defined.

*Chapter 3* elaborates the design and construction of the plate-cavity coupled Noise-Box. It explains how the Noise-Box reaches the final design, starting from the original considerations about a benchmarking and testing tool for vehicle interior noise analysis and control. Finally, the Noise-Box test system is obtained with a 4-mm aluminium plate and a non-rectangular cavity surrounded by concrete walls.

*Chapter 4* investigates the Noise-Box via FEM, respectively for the plate, the cavity and the plate-cavity problems. For each problem, it first validates the modelling techniques that are employed in ANSYS® and COMSOL® by benchmark cases, removing any doubt in element types, mesh control and boundary conditions. Then, the sensitivity of some parameters inside the models is investigated. As a result, this chapter will get ready the FEM models, accompanied by a group of the initial predictions and some knowledge of the model parameter sensitivity.

*Chapter 5* characterizes the Noise-Box and its components through experiments and numerical simulations, where the FE models prepared in Chapter 4 are used for simulations. The Noise-Box cavity is characterized for its modal parameters, sound absorption and diffuseness. The mounted panel is identified for modal parameters, material properties, thickness and edge conditions. Lastly, modal parameters of the coupled plate-cavity system



are estimated, based on which, the edge conditions of the panel are updated again. EMA is the main technique employed in this chapter to identify the modal parameters, and how to use EMA for vibroacoustic problem is specially considered.

*Chapter 6* investigates the Noise-Box using WBM, respectively for the plate, the cavity and the plate-cavity problems, based on the mathematical models defined in Chapter 2. All the updated parameters are applied. The WBM for each problem is introduced and then implemented in MATLAB® by self-developed codes. A new weighted residual formulation is proposed, enabling the WBM for elastically restrained plates. The new formulation and codes are validated by comparing the results between WBM and FEM.

*Chapter 7* investigates the Noise-Box by SEA, for its responses under point force excitation and under acoustic excitation, respectively. The SEA method for each case is introduced and then implemented in MATLAB by self-developed codes. The new codes are validated with reference to the corresponding results by an open-source software named ‘SEAlab’.

*Chapter 8* experimentally and numerically investigates the structure-borne and airborne interior noises of the plate-cavity coupled Noise-Box. The introduced numerical techniques (i.e., FEM, WBM and/or SEA) and a given experimental approach to the test system are used for the same structure-borne or airborne noise investigation, when their results are converted to the same format for comparison.

Finally, *Chapter 9* draws the main conclusions and achievements of the dissertation, and proposes some future work for this research.



## Chapter 2 Fundamentals in a plate-cavity system

*This chapter introduces the fundamentals of the problems to be solved and investigated in later chapters, in the sequence of (1) uncoupled flexural vibration of thin plates, where the mathematical models for 2D and 1D plate are determined; (2) uncoupled interior acoustics, where the mathematical description for 3D and 2D acoustic cavity are provided; (3) coupled interior vibro-acoustics, where the 3D and 2D vibroacoustic problems are formulated; (4) sound transmission loss of panels, where different measurement and prediction methods are introduced.*

### 2.1 Problems in a plate-cavity system

The investigation of a plate-cavity system is to know the vibration of the plate and meanwhile the sound pressure inside the cavity. The results are expected to be dependent on the following factors:

- the thin plate with its thickness, material properties and edge conditions;
- the acoustic cavity with its fluid properties, and surrounding wall conditions;
- the fluid-structure interactions, including the acoustic field influenced by the motion of the plate and the plate vibration perturbed by the fluid pressure loading;
- the excitation type and waveform, e.g., mechanical point force, monopole sound source or incident sound wave excitation; sinusoidal, impulse or white noise signal.

Therefore, we need the accurate models of the plate, the cavity, the coupling between plate and cavity, and the interaction between the excitation and the plate-cavity system. Thus, in the following sections, the related fundamentals are introduced, as the basics for later design, simulation and testing. The analyses are currently limited to the frequency domain, targeting to obtain the frequency response functions, which provide significant information for the response of a linear system.

### 2.2 Flexural vibration of thin plate

A plate is a special case of solid whose thickness is so small compared to the other dimensions that it can be studied using the two-dimensional models that are described in terms of its mid-plane. Kirchhoff-Love plate theory is the classical one for plate bending problems, whose fundamental assumptions are <sup>[157]</sup>:

- The plate is made of elastic, homogeneous and isotropic material.

- The plate is flat before deflection.
- The deflection of the mid-plane is small in comparison with the thickness. Hence, the slope of the deflected mid-surface is small, and its square is negligible compared with unity.
- The straight lines normal to the mid-plane before deformation suffer no change in length and remain straight and normal to the mid-surface during deformation. This indicates that the normal strain may be negligible and the transverse shear strains can be omitted. This assumption is known as hypothesis of straight normals or Kirchhoff-Poisson hypothesis.
- The stress normal to the mid-plane, small compared to other stress components, may be neglected in the stress-strain relationships.
- The mid-surface is assumed to be unstrained under the small transverse displacement of the plate.

The assumptions indicate some important issues need extra attention when the theory is utilised to model a plate. For example, regarding the *Kirchhoff-Poisson hypothesis*, there is a doubt whether the *shear deformation effect* or the *thickness stretch effect* <sup>[158]</sup> is small enough to be negligible. Especially for the *shear deformation effect*, it is found becoming more and more important as the thickness of the plate increases. Therefore, the more sophisticated two-dimensional plate theories, referred to as *Shear Deformation Theories*, were proposed. They are based on the hypotheses more realistic than the *Kirchhoff-Poisson hypothesis*, and extendable to anisotropic homogeneous or arbitrarily laminated anisotropic plates. Among the several *Shear Deformation Theories*, the *First-order Shear Deformation Theory* (also called the *moderately thick plate theory* or Reissner-Mindlin plate theory) is most popularly used. With respect to the *hypothesis of straight normals*, this theory states that “*Normals to the mid-plane of the undeformed plate suffer no change in length and remain straight, but not necessarily normal to the deformed mid-surface.*” <sup>[158]</sup> In other words, the transverse shear strains are not equal to zero. As a result, when the Reissner-Mindlin plate theory is used for the plate flexural vibration, the rotary inertia and shear deformation take effects, while they are neglected in the Kirchhoff-Love plate theory. There are also higher order theories, but they are not in favour for isotropic homogeneous plates because of the higher algebraic complexity and computational efforts.

Owing to the assumptions, both the Kirchhoff-Love and the Reissner-Mindlin theories have certain geometrical and frequency limits for accurate results. In general, the Kirchhoff-Love theory is sufficiently accurate for ‘thin’ plates and for not very elevated frequencies, while the Reissner-Mindlin theory can be applied to moderately thick plates and higher frequencies. The geometrical limit is often provided by the ratio of the plate thickness  $h$  to

the smaller lateral dimension  $l$  (thickness-to-span ratio), and the frequency limit can be represented by the ratio of the bending wavelength  $\lambda_b$  to the plate thickness  $h$ . There is no precise definition of the limits, since it is related to the requirement of accuracy and the accuracy may also be affected by other factors like the boundary conditions, the ratio of lateral dimensions, etc. <sup>[159]</sup> However, it can be summarized from different literature <sup>[160–164]</sup> that the recommended limits for the Kirchhoff plate could be  $h/l < 1/20 \sim 1/10$  and  $\lambda_b/h > 6$ , and that the counterparts for the Mindlin plate may be  $h/l < 1/5$  and  $\lambda_b/h > 2$ . In <sup>[158]</sup>, it is proved that the Kirchhoff-Love theory is very accurate if  $h/l \leq 1/25$ , and that the Reissner-Mindlin theory yields excellent results for  $h/l \leq 1/10$ . Furthermore, Klanner investigated the useful ranges of validity for these two theories in his PhD thesis <sup>[159]</sup>, which may provide more detailed information. His investigation indicates that if the plate is thinner, the effects of the rotary inertia and shear deformation are smaller, and therefore the two theories reach more identical results.

Nevertheless, in this thesis as well as the fundamentals that will be introduced in the following subsections, the discussion is limited to thin plates, where the Kirchhoff-Love theory is applicable. Consequently, the assumptions, applicable ranges and limitations have been specified here before the theory is to be applied. Meanwhile, it is worthwhile to notice that the Kirchhoff plate theory underestimates deflections and overestimates natural frequencies for the moderately thick plates due to the neglect of shear deformation <sup>[162]</sup>. This may be informative when thicker plates or higher frequencies are considered.

In the following subsections, the 2D mathematic model for the flexural vibration of thin plate with arbitrary edge restraints is introduced at first. This model can represent a real finite plate that is vibrating in the 3D space. Meanwhile it is further used to build up the 3D coupled vibro-acoustic model in Section 2.4. Since the 2D coupled vibro-acoustic problem is also considered in this work, the 2D plate model is reduced to 1D in Section 2.2.2, so that the plate can couple with 2D acoustic fields.

### 2.2.1 Two-dimensional thin plate model

In this subsection, the flexural vibration problem is discussed for a general convex thin plate  $\Omega_s$ , as shown in Fig. 2-1. It is excited by the normal harmonic point force  $F e^{j\omega t}$  at  $\mathbf{r}_F(x_F, y_F)$  and vibrates transversely in the 3D space, without interaction with any fluid. Based on the Kirchhoff plate theory [40], the transverse displacement  $w(\mathbf{r})$  at  $\mathbf{r}(x, y)$  is governed by the equation

$$\nabla^4 w(\mathbf{r}) - k_b^4 w(\mathbf{r}) = \frac{F}{D} \delta(\mathbf{r}, \mathbf{r}_F), \quad \mathbf{r} \in \Omega_s, \quad (2.1)$$

with the flexural rigidity



Then, determined by the restraint, an edge ( $\mathbf{r} \in \Gamma$ ) may satisfy two of following boundary conditions:

$$(2.9)$$

$$L_\theta[w(\mathbf{r})] = \bar{\theta}, \quad (2.10)$$

$$L_m[w(\mathbf{r})] = \bar{m}, \quad (2.11)$$

$$L_Q[w(\mathbf{r})] = \bar{Q}, \quad (2.12)$$

$$L_m[w(\mathbf{r})] = -(k_\theta + j\omega c_\theta)L_\theta[w(\mathbf{r})], \quad (2.13)$$

$$L_Q[w(\mathbf{r})] = -(k_w + j\omega c_w)w(\mathbf{r}). \quad (2.14)$$

One condition should be Eq. (2.9), Eq. (2.12) or Eq. (2.14), associated with the translation. The other should be  $E w(\mathbf{r}) = \bar{w}$ , q. (2.10), Eq. (2.11) or Eq.(2.13), involving the rotation. Eqs. (2.9)-(2.12) are the prescribed boundary conditions, where  $\bar{w}$ ,  $\bar{\theta}$ ,  $\bar{m}$  and  $\bar{Q}$  are the corresponding prescribed values or functions. In the case of prescribed functions, they can be functions of the edge coordinates  $\mathbf{r}(x, y) \in \Gamma$  but not of the displacement  $w(\mathbf{r})$ . Eqs. (2.13) and (2.14) are the boundary conditions for the elastic ( $c_w = c_\theta = 0$ ) or viscoelastic restraints. A combination of Eqs. (2.13) and (2.14) leads to the general elastically restraint (shown in Table 2-1 for  $\mathbf{r}(x, y) \in \Gamma_{m^*Q^*}$ ). The model of this restraint type is shown in Fig. 2-1(b) at the edge  $\Gamma_i$ . As is illustrated, the restraint is modelled with linear and rotational springs and dampers for the translational and rotational displacements of the edge. The coefficients  $k_w$  and  $c_w$  are respectively the translational spring constant per unit length and the translational damping coefficient per unit length. Similarly, the coefficients  $k_\theta$  and  $c_\theta$  are respectively the rotational counterparts. The viscoelastic restraint can be considered as an extension of the elastic restraint, where the spring constant contains a frequency-dependent imaginary part, i.e.,  $k'_i = k_i + j\omega c_i$ ,  $i = w$  or  $\theta$ .

For all the possible combinations out of Eqs. (2.9)-(2.14), Table 2-1 lists the corresponding restraint types and their examples. The first four restraint types possess the prescribed boundary conditions, while the rest five types are partial- or general- elastically restrained. The illustrations of these two sets can be found in Fig. 2-1(a) and Fig. 2-1(b), respectively. When corners are presents as shown in Fig. 2-1(b), additional conditions for the corners may be indispensable for some situations <sup>[165]</sup>. The reason is related to the different normal ( $\gamma_n^+$  and  $\gamma_n^-$ ) and tangential ( $\gamma_s^+$  and  $\gamma_s^-$ ) directions between the two intersecting edges ( $\Gamma^+$  and  $\Gamma^-$ ), which results in a concentrated force  $F_c$  at the corner, in the process of incorporating the twisting moment to the effective transverse shear force <sup>[160]</sup>. The supplemented conditions are given by

- for rigidly supported corners  $\mathbf{r}_c \in (\Gamma_{\bar{w}\bar{\theta}} \text{ or } \Gamma_{\bar{w}\bar{m}} \text{ or } \Gamma_{\bar{w}\bar{m}^*})$ :

$$w(\mathbf{r}_c) = \bar{w}; \quad (2.15)$$

- for other corners  $\mathbf{r}_c \notin (\Gamma_{\bar{w}\bar{\theta}} \text{ or } \Gamma_{\bar{w}\bar{m}} \text{ or } \Gamma_{\bar{w}\bar{m}^*})$  when force conditions of the intersecting edges are known:

$$L_F[w(\mathbf{r}_c)] = L_{ms}^+[w(\mathbf{r}_c)] - L_{ms}^-[w(\mathbf{r}_c)] = \bar{m}_{ns}(\mathbf{r}_c^+) - \bar{m}_{ns}(\mathbf{r}_c^-), \quad (2.16)$$

where,  $L_F$  is the differential operator for the concentrated force  $F_c$ ;  $L_{ms}^+$  and  $L_{ms}^-$  are the differential operators for the torsional moment with respect to  $\gamma_n^+$ ,  $\gamma_s^+$  and  $\gamma_n^-$ ,  $\gamma_s^-$ , respectively; and  $\bar{m}_{ns}(\mathbf{r}_c^+)$  and  $\bar{m}_{ns}(\mathbf{r}_c^-)$  are the prescribed torsional moments next to the corner  $\mathbf{r}_c$  on edge  $\Gamma^+$  and  $\Gamma^-$ , respectively.

 Table 2-1. Restraint types and their boundary conditions <sup>[151,161,162]</sup>

Restraint type	Boundary conditions	Examples
Kinematic prescribed: $\mathbf{r} \in \Gamma_{\bar{w}\bar{\theta}}$	$w(\mathbf{r}) = \bar{w}$ , $L_\theta[w(\mathbf{r})] = \bar{\theta}$	Clamped: $\bar{w} = \bar{\theta} = 0$
Mechanical prescribed: $\mathbf{r} \in \Gamma_{\bar{m}\bar{Q}}$	$L_m[w(\mathbf{r})] = \bar{m}$ , $L_Q[w(\mathbf{r})] = \bar{Q}$	Free: $\bar{m} = \bar{Q} = 0$
Mixed prescribed type 1: $\mathbf{r} \in \Gamma_{\bar{w}\bar{m}}$	$w(\mathbf{r}) = \bar{w}$ , $L_m[w(\mathbf{r})] = \bar{m}$	Pinned: $\bar{w} = \bar{m} = 0$
Mixed prescribed type 2: $\mathbf{r} \in \Gamma_{\bar{\theta}\bar{Q}}$	$L_\theta[w(\mathbf{r})] = \bar{\theta}$ , $L_Q[w(\mathbf{r})] = \bar{Q}$	Symmetric: $\bar{\theta} = \bar{Q} = 0$
Rotational elastic type 1: $\mathbf{r} \in \Gamma_{\bar{w}\bar{m}^*}$	$w(\mathbf{r}) = \bar{w}$ $L_m[w(\mathbf{r})] = -(k_\theta + j\omega c_\theta)L_\theta[w(\mathbf{r})]$	Rigidly supported and elastically restrained against rotation: $\bar{w} = 0$ , $k_\theta \neq 0$
Rotational elastic type 2: $\mathbf{r} \in \Gamma_{\bar{Q}\bar{m}^*}$	$L_Q[w(\mathbf{r})] = \bar{Q}$ , $L_m[w(\mathbf{r})] = -(k_\theta + j\omega c_\theta)L_\theta[w(\mathbf{r})]$	Resting on a rotational spring: $\bar{Q} = 0$ , $k_\theta \neq 0$
Translational elastic type 1: $\mathbf{r} \in \Gamma_{\bar{\theta}\bar{Q}^*}$	$L_\theta[w(\mathbf{r})] = \bar{\theta}$ , $L_Q[w(\mathbf{r})] = -(k_w + j\omega c_w)w(\mathbf{r})$	Clamped by transversely elastic support: $\bar{\theta} = 0$ , $k_w \neq 0$
Translational elastic type 2: $\mathbf{r} \in \Gamma_{\bar{m}\bar{Q}^*}$	$L_m[w(\mathbf{r})] = \bar{m}$ , $L_Q[w(\mathbf{r})] = -(k_w + j\omega c_w)w(\mathbf{r})$	Resting on a linear spring: $\bar{m} = 0$ , $k_w \neq 0$
General elastic: $\mathbf{r} \in \Gamma_{\bar{m}^*\bar{Q}^*}$	$L_m[w(\mathbf{r})] = -(k_\theta + j\omega c_\theta)L_\theta[w(\mathbf{r})]$ , $L_Q[w(\mathbf{r})] = -(k_w + j\omega c_w)w(\mathbf{r})$	Elastically restrained against rotation and translation: $k_\theta \neq 0$ , $k_w \neq 0$

## 2.2.2 One-dimensional thin plate model

The 1D thin plate model is proposed for solving 2D problems. Besides, it can serve as an efficient tool to validate a developing approach before the approach is extended to the higher dimension. When reduced to one dimension, the Kirchhoff plate is similar to a thin beam based on the Euler-Bernoulli beam theory <sup>[161]</sup>, but the propagating waves are *plane* bending waves <sup>[58]</sup>, because the length in y direction (as shown in Fig. 2-2) is regarded as infinite. Correspondingly, the harmonic force excitation  $F e^{j\omega t}$  is a line force, where  $F$  is the amplitude per unit length. The other parameters  $\rho$ ,  $E$ ,  $\nu$ ,  $h$ ,  $\eta$ ,  $D$  and  $k_b$  are the same as they are defined in Section 2.2.1 for the 2D model. The governing equation is also identical to Eq. (2.1) with y removed:



$$\frac{d^4 w(x)}{dx^4} - k_b^4 w(x) = \frac{F}{D} \delta(x, x_F), \quad x \in (0, l). \quad (2.17)$$

Similarly, the operators  $L_\theta$ ,  $L_m$  and  $L_Q$  are respectively given by

$$x = 0: L_\theta = \frac{d}{dx}; \quad x = l: L_\theta = -\frac{d}{dx}, \quad (2.18)$$

$$x = 0: L_m = D \frac{d^2}{dx^2}; \quad x = l: L_m = -D \frac{d^2}{dx^2}, \quad (2.19)$$

$$x = 0: L_Q = D \frac{d^3}{dx^3}; \quad x = l: L_Q = -D \frac{d^3}{dx^3}. \quad (2.20)$$

Then, the possible boundary conditions are presented from Eq. (2.9) to Eq. (2.14), where  $\mathbf{r}$  represents the 1D vector  $\mathbf{r}(x)$ . Accordingly, the various restraint types for this 1D model are also listed by Table 2-1. Fig. 2-2 includes the illustration of the general elastic restraint type in the 1D model. The springs and dampers work the same as they are in the 2D model.

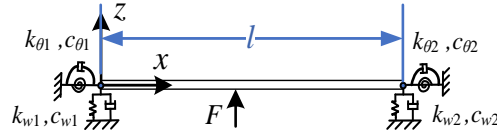


Fig. 2-2. 1D thin plate with general elastic edge restraints.

When compared with the Euler-Bernoulli beam model <sup>[58]</sup>:

$$\frac{d^4 w(x)}{dx^4} - \frac{\rho A \omega^2}{EI} w(x) = \frac{F}{EI} \delta(x, x_F), \quad x \in (0, l), \quad (2.21)$$

the 1D thin plate model represented by Eq. (2.17) is different in two folds: it uses the mass per unit area  $\rho h$  instead of the mass per unit length  $\rho A$ , and the bending rigidity is  $D = Eh^3/12(1-\nu^2)$  instead of  $EI = Eh^3/12$ . This is important if beam elements are used to model the 1D plate in FEM.

### 2.3 Interior acoustic problem

The uncoupled interior acoustic problem considers the steady-state pressure field inside a cavity domain, induced by a harmonic point source excitation. Meanwhile, if any wall of the cavity is vibrating, its velocity is prescribed without the fluid-structure coupling effect, in consistent with the word ‘uncoupled’. In this section, both the 3D and 2D acoustic models for the problem are introduced. Although for most cases, the 3D acoustic model is more appropriate, introducing the 2D model is worthwhile and even necessary. The 2D model requires relatively small amount of work to set up and significantly shorter time to solve and study. In the development of numerical techniques, its validity in 2D model is often an

important milestone before the extension to 3D. Meanwhile, for calculating the acoustic modes, a 2D model may be able to represent a 3D cavity if there are two opposite sides parallel.

### 2.3.1 Three-dimensional interior acoustic model

As shown in Fig. 2-3, consider a general convex cavity volume  $\mathbf{V}$ , under the harmonic monopole source excitation  $qe^{j\omega t}$ , where  $q$  (SI unit:  $\text{m}^3/\text{s}$ ) is the amplitude of the volume flow rate. The source is located at  $\mathbf{r}_q(x_q, y_q, z_q)$ , and the acoustic pressure  $p$  at any position  $\mathbf{r}(x, y, z)$  is unknown but satisfies the inhomogeneous Helmholtz equation<sup>[27]</sup>

$$\nabla^2 p(\mathbf{r}) + k^2 p(\mathbf{r}) = -j\omega\rho_0 q \delta(\mathbf{r}, \mathbf{r}_q), \mathbf{r} \in \mathbf{V}, \quad (2.22)$$

with the acoustic wavenumber

$$k = \frac{\omega}{c}, \quad (2.23)$$

where,  $\rho_0$  is fluid density and  $c$  is thermodynamic speed of sound of the fluid. In the case when air is the fluid (approximate to a perfect gas), the density can be expressed as a function of the absolute temperature  $T_A$  and absolute pressure  $p_A$ <sup>[166]</sup>:

$$\rho_0 = \frac{p_A M_d}{R_{\text{gas}} T_A}; \quad (2.24)$$

and the sound speed is dependent upon the absolute temperature  $T_A$ <sup>[166]</sup>:

$$c = \sqrt{\frac{1.4 R_{\text{gas}} T_A}{M_d}}. \quad (2.25)$$

In Eq. (2.24) and Eq. (2.25),  $M_d = 0.02897$  kg/mol is the molar mass of dry air and  $R_{\text{gas}} = 8.314$  J/(K·mol) is the universal gas constant.

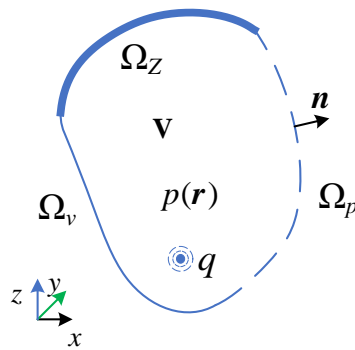


Fig. 2-3. A general convex acoustic cavity.

For a unique solution to Eq. (2.22), the conditions along the boundary  $\Omega_a = \Omega_p \cup \Omega_v \cup \Omega_z$  should be specified:

$$p(\mathbf{r}) = \bar{p}, \mathbf{r} \in \Omega_p, \quad (2.26)$$

$$-\frac{1}{j\omega\rho_0} \frac{\partial p(\mathbf{r})}{\partial n} = \bar{v}_n, \mathbf{r} \in \Omega_v, \quad (2.27)$$

$$-\frac{1}{j\omega\rho_0} \frac{\partial p(\mathbf{r})}{\partial n} = \frac{p(\mathbf{r})}{\bar{Z}}, \mathbf{r} \in \Omega_Z, \quad (2.28)$$

where,  $\mathbf{n}$  is normal direction of the boundary surface,  $\bar{p}$ ,  $\bar{v}_n$  and  $\bar{Z}$  are respectively the prescribed acoustic pressure, surface normal velocity and surface acoustic impedance, or their corresponding functions of the boundary coordinates  $\mathbf{r}(x,y,z)$ . The rigid/reflecting wall condition can be regarded as a special case of Eq. (2.27) with  $\bar{v}_n = 0$  or of Eq. (2.28) with  $\bar{Z} = \infty$ , simply applying the condition  $\partial p(\mathbf{r})/\partial n = 0$ .

### 2.3.2 Two-dimensional interior acoustic model

The 2D model is normally applied to the problems with a planar symmetry or a cylindrical symmetry. In this work, only the planar symmetry is considered, where the dimension  $y$  (as shown in Fig. 2-3) is extended to infinite. As a result, the coordinates are given by  $\mathbf{r}(x, z)$ . Correspondingly, the monopole excitation is a line source, where  $q$  is the amplitude of volume flow rate per unit length out from the source. Then, with the coordinate  $y$  eliminated, the governing equations and boundary conditions are the same as shown in Eqs. (2.22)-(2.28). However, if the sound wave is considered also propagating in the out-of-plane direction, i.e.,  $k_y \neq 0$ . The wavenumber shown by Eq. (2.23) should be replaced by

$$k = \sqrt{\frac{\omega}{c} - k_y^2}, \quad (2.29)$$

where,  $k_y$  is the out-of-plane wavenumber.

## 2.4 Coupled vibroacoustic problem

Regarding the coupled vibroacoustic problem, the plate introduced in Section 2.2 is now a boundary surface of the interior acoustic field considered in Section 2.3. From the above two sections, it can be noticed that there is no dramatic difference in mathematically modelling the 3D and the 2D problems. Similar modelling techniques can be applied to the vibroacoustic situation. In the following introduced 3D vibroacoustic model, the cavity and the plate are respectively 3D and 2D models, while in the 2D vibroacoustic model, the 2D cavity is coupled with the 1D plate.

### 2.4.1 Three-dimensional vibroacoustic model

As illustrated by Fig. 2-4(a), the plate-cavity system now has three possible excitations, i.e., the exterior sound wave excitation  $p_{\text{ext}}(\mathbf{r})$ , the point force excitation  $F$ , and the monopole

source excitation  $q$ . Though the three excitations are presented together in the mathematical model, only one excitation is considered to be effective in one case. The given excitation is still harmonic and the unknowns are the displacement field  $w$  of the plate and the pressure field  $p$  of the cavity.

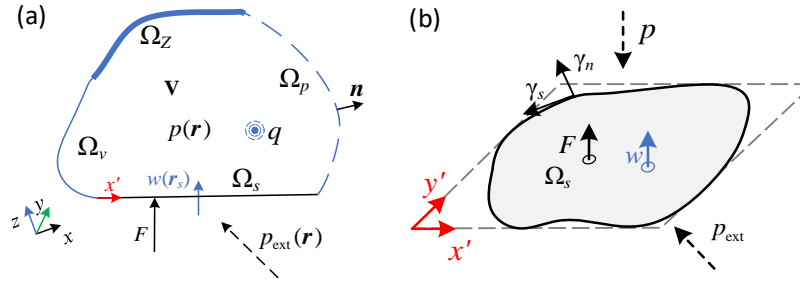


Fig. 2-4. Three-dimensional coupled vibroacoustic system: (a) acoustic field affected by plate vibration; (b) structural field influenced by acoustic pressure.

Concerning the acoustic field inside volume  $\mathbf{V}$ , it is like the uncoupled case governed by inhomogeneous Helmholtz equation Eq. (2.22), but the boundary  $\Omega_a$  has additional effect coming from the flexible plate  $\Omega_s$ . The boundary condition is given by

$$-\frac{1}{j\omega\rho_0} \frac{\partial p(\mathbf{r})}{\partial n} = -j\omega w(\mathbf{r}), \mathbf{r} \in \Omega_s. \quad (2.30)$$

In this boundary surface  $\Omega_s$ , the normal plate displacement  $w(\mathbf{r})$  is also unknown and meanwhile directly influenced by the acoustic pressure field coming from the cavity as shown in Fig. 2-4(b).

For directly utilizing the 2D plate model, a local coordinate system  $(x', y')$  is set up as shown by Fig. 2-4. It is defined in the mid-plane of the flat thin plate and any point in the plate is represented by  $\mathbf{r}'(x', y')$  in the local coordinate system. The coordinate transformation from the local system to the global system  $\mathbf{r}(x, y, z)$  be expressed in a bilinear parametric way as follows: <sup>[27]</sup>

$$\forall \mathbf{r}(x, y, z) \in \Omega_s : \begin{cases} x = u_x(x', y') = u_{x,0} + u_{x,x'}x' + u_{x,y'}y' \\ y = u_y(x', y') = u_{y,0} + u_{y,x'}x' + u_{y,y'}y' \\ z = u_z(x', y') = u_{z,0} + u_{z,x'}x' + u_{z,y'}y' \end{cases} \quad (2.31)$$

where,  $u_{i,0}$ ,  $u_{i,x'}$  and  $u_{i,y'}$  ( $i = x, y, z$ ) are constant values, depending on the position and orientation of the local system  $(x', y')$ .

Then, expressed in the local coordinate system, the governing equation of plate is given by

$$\nabla^4 w(\mathbf{r}') - k_b^4 w(\mathbf{r}') = \frac{F}{D} \delta(\mathbf{r}', \mathbf{r}'_F) + \frac{p_{\text{ext}}(\mathbf{r}')}{D} - \frac{p(\mathbf{r}')}{D}, \mathbf{r}' \in \Omega_s, \quad (2.32)$$

where,  $p(\mathbf{r}')$  is derived from  $p(\mathbf{r})$  based on Eq. (2.31). The edge conditions are identical to the uncoupled case as discussed in Section 2.2.1, since they are not affected by the fluid fields.

Finally, the 3D vibroacoustic problem is defined mathematically by combining the cavity governing equation Eq. (2.22) and the plate governing equation Eq. (2.32), utilizing the coordinate relationship Eq. (2.31), and accordingly applying the cavity boundary conditions Eqs. (2.26)-(2.28), (2.30) and the plate boundary conditions Eqs. (2.9)-(2.14).

## 2.4.2 Two-dimensional vibroacoustic model

As shown by Fig. 2-5, the considered 2D vibroacoustic problem is defined in the  $x$ - $z$  plane. Both the cavity  $\mathbf{V}$  and the thin plate  $\Omega_s$  are considered infinite length in the  $y$  dimension. This is consistent with the two subsystems in their uncoupled models. Correspondingly, the three possible excitations  $p_{\text{ext}}$ ,  $F$  and  $q$  are defined for unit length. Then, except the difference in dimension, all the others are the same as the problem in the 3D case. Therefore, the 2D model can be derived by a dimension reduction from the 3D vibroacoustic model.

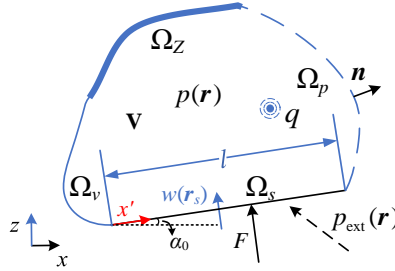


Fig. 2-5. Two-dimensional coupled vibroacoustic system.

In the global coordinate system  $(x, z)$ , any point at the plate-cavity system can be represented by  $\mathbf{r}(x, z)$ . A line source is exciting at  $\mathbf{r}(x_q, z_q)$ . Then, the governing equation of the interior acoustic field  $p(\mathbf{r})$  is given by Eq. (2.22) and the corresponding boundary conditions are provided by Eqs. (2.26)-(2.28) and (2.30). The local coordinate system built up for the flexible plate  $\Omega_s$  is  $(x')$ , with the local origin at one vertex the 1D plate line. Hence, any point in the plate can also be represented by  $\mathbf{r}'(x')$  and the line force  $F$  is imposed at  $\mathbf{r}'_F(x'_F)$ . Suppose that the origin  $\mathbf{r}'(0)$  is at  $\mathbf{r}(x_0, z_0)$  and that the angle between  $x'$ -axis and  $x$ -axis is  $\alpha_0$ , the relationship between the two coordinate systems can be expressed by

$$\forall \mathbf{r}(x, z) \in \Omega_s : \begin{cases} x = x_0 + x' \cos \alpha_0 \\ z = z_0 + x' \sin \alpha_0 \end{cases} \quad (2.33)$$

Using the local coordinate system, the plate's governing equation can be given by Eq. (2.32), or rewritten as follows:

$$\frac{d^4 w(x')}{dx'^4} - k_b^4 w(x') = \frac{F}{D} \delta(x', x'_F) + \frac{p_{\text{ext}}(x')}{D} - \frac{p(x')}{D}, \quad x' \in (0, l). \quad (2.34)$$

With the updated operator for  $x'$  given by Eqs. (2.18)-(2.20), the boundary conditions of the plate can be expressed as one of the restraint types listed in Table 2-1. The 2D vibroacoustic model is finally mathematically determined by combining all the equations mentioned in this subsection.

## 2.5 Sound transmission loss of isotropic panels

When airborne noise is considered, sound transmission of the intermediate structure (e.g., panel/partition) is important. The sound transmission ability can be evaluated by the transmission coefficient  $\tau$ , defined as the ratio of the transmitted power  $\Pi_{\text{tr}}$  to the incident power  $\Pi_{\text{in}}$ :

$$\tau = \frac{\Pi_{\text{tr}}}{\Pi_{\text{in}}}. \quad (2.35)$$

From another point of view, if the capability of the structure to avoid the power transmission is to be assessed, the *transmission loss*, TL (also referred to as ‘sound reduction index’,  $R$ ) is often used, which is defined by the logarithmic form of the power transmission coefficient:

$$\text{TL} = 10 \lg \frac{1}{\tau} = 10 \lg \frac{\Pi_{\text{in}}}{\Pi_{\text{tr}}} \quad [\text{dB}]. \quad (2.36)$$

Because  $\tau$  and thus TL depend on the direction of incidence (incident angle  $\theta_{\text{in}}$  and azimuth angle  $\phi_{\text{in}}$  as shown in Fig. 2-6), there are three terms about  $\tau$  or TL that are commonly referred to. They are respectively for normal incidence ( $\tau_N$  or  $TL_N$ ), diffuse field or random incidence ( $\tau_d$  or  $TL_d$ ) and field incidence ( $\tau_F$  or  $TL_F$ ). While the diffuse field incidence considers that the incident plane waves are coming from all directions with random phase and equal probability, the field incidence limits the incident angle to  $\theta_{\text{in}} \leq \theta_L$ . Precisely, it means that the field incidence transmission coefficient is obtained from<sup>[167]</sup>

$$\tau_F = \frac{\int_{\theta_{\text{in}}=0}^{\theta_{\text{in}}=\theta_L} \int_{\phi_{\text{in}}=0}^{\phi_{\text{in}}=2\pi} \tau(\theta_{\text{in}}, \phi_{\text{in}}) \sin \theta_{\text{in}} \cos \theta_{\text{in}} d\theta_{\text{in}} d\phi_{\text{in}}}{\int_{\theta_{\text{in}}=0}^{\theta_{\text{in}}=\theta_L} \int_{\phi_{\text{in}}=0}^{\phi_{\text{in}}=2\pi} \sin \theta_{\text{in}} \cos \theta_{\text{in}} d\theta_{\text{in}} d\phi_{\text{in}}}. \quad (2.37)$$

There is no rigorous justification of  $\theta_L$ , but it is found that  $\theta_L \approx 78^\circ$  makes the predictions agree well with the experimental results<sup>[58]</sup>. In this regard, the field incidence transmission loss  $TL_F$  is used in this thesis, representing the sound insulation characteristic of the considered thin isotropic panel.

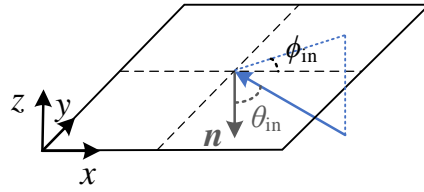
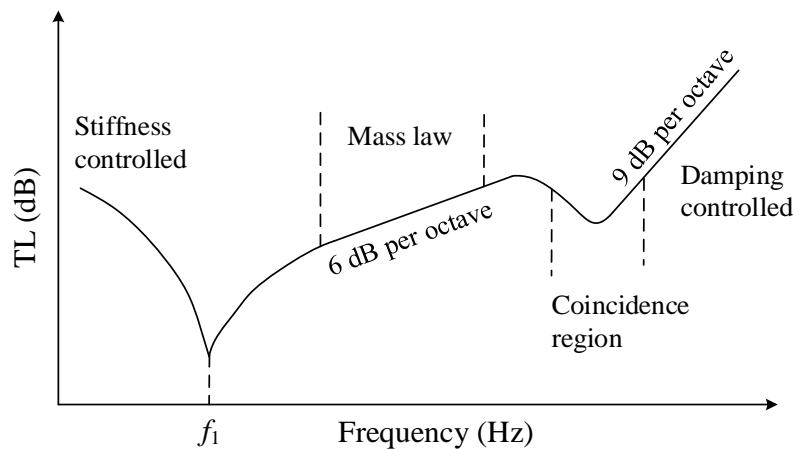


Fig. 2-6. Oblique incidence of plane wave.

Considering a single uniform isotropic panel with finite dimensions, the transmission loss is affected by four factors: size, stiffness, mass and damping <sup>[168]</sup>. A typical field incidence TL curve in the broad audio-frequency range is shown in Fig. 2-7 <sup>[169]</sup>. At very low frequencies below the frequency of first panel resonance  $f_1$ , the TL is stiffness controlled. It decreases as the frequency increases and the decreasing rate is reported to be -6 dB/octave <sup>[168,170]</sup>. If the stiffness of the panel increases, the TL within this region increases regardless of the mass or damping. Then, the first valley is seen at the first panel resonance. Since the panel is finite and bounded, several valleys may appear next to the first one, corresponding to the first several natural frequencies of the panel. In this region, the TL is partly influenced by the damping in the system and the region is sometimes called resonance controlled <sup>[168,170]</sup>. Subsequently, there is a relatively broad frequency region that is mass controlled. In this region, the relationship between TL and frequency  $f$  satisfies the mass law, where TL increases with  $f$  by 6 dB per octave and doubling the panel mass indicates a 6 dB increase in TL. Later, the frequency gradually enters the coincidence region. A sharp drop is seen just below the critical frequency  $f_c$ , which is the lowest coincidence frequency of the panel. Then, coincidence occurs and the panel radiates sound efficiently, leading to the locally small TL. The TL has been affected by the damping since the coincidence region. Finally, as the frequency further increases, the damping effect dominates and the TL increases at the rate of 9 dB/octave.


 Fig. 2-7. Typical TL of single-layer isotropic panels under field incidence <sup>[169]</sup>.

The specific function of TL (or denoted as  $TL_F$ ) versus  $f$  can be derived based on Eqs. (2.35)-(2.37), where  $\tau(\theta_{in}, \phi_{in})$  is calculated based on Eq. (2.35) with  $\Pi_{tr}$  and  $\Pi_{in}$  out of plane sound wave from a single direction  $(\theta_{in}, \phi_{in})$ . The analytical solution for a panel of finite size is not directly available but can be approximated by that for an infinite panel in practice, as long as the frequencies are above  $1.5f_1$  and the panel is limp. The transmission coefficient of an infinite isotropic panel is given by <sup>[169]</sup>

$$\tau(\theta, \phi) = \left| 1 + \frac{Z_b \cos \theta}{2\rho_0 c} \right|^{-2}, \quad (2.38)$$

where,  $Z_b$  is the bending wave impedance of the panel, expressed as

$$Z_b = j2\pi fm \left[ 1 - \left( \frac{f}{f_c} \right)^2 (1 + j\eta) \sin^4 \theta \right]. \quad (2.39)$$

In Eq. (2.39),  $m = \rho h$  is the panel surface density, and  $f_c$  is the critical frequency:

$$f_c = \frac{c^2}{2\pi} \sqrt{\frac{m}{D}}. \quad (2.40)$$

From Eq. (2.38), it can be noticed that  $\tau$  is independent of the azimuth angle  $\phi_{in}$ . This is reasonable since the formula is for the infinite panel. Thus, Eq. (2.37) can be simplified with angle  $\phi_{in}$  integrated separately. Furthermore, to ease the tedious calculation of Eq. (2.37), several approximate expressions are derived under different schemes. Meanwhile, the TL in the low frequency range  $f < 1.5f_1$  are also provided by incorporating the stiffness and natural frequencies or forced transmission of the partition. In <sup>[169]</sup>, the three schemes for approximate TL estimations respectively from Sharp, Davy and EN 12354-1(2000) are introduced. Since these schemes will be applied in later investigations on the test panel, their derived formulae are respectively listed in Appendix B: Panel transmission loss approximate predictions, where the Sharp's scheme and the Davy's scheme are excerpted from <sup>[169]</sup> and the EN 12354-1(2000) has been updated by ISO 12354-1(2017) <sup>[171]</sup>.

Apart from the theoretical calculations, the sound transmission loss (or airborne sound insulation of partitions) can also be measured in laboratory <sup>[172-175]</sup> or field <sup>[176,177]</sup>. In general, there are two standardized approaches. One is based on the difference of sound pressure levels (SPLs) in the two rooms separated by the partition <sup>[173,175,177]</sup>, while the other is distinguished from the former by directly measuring the sound intensity in the radiating side to obtain the sound power transmitted by the element <sup>[172,174,176]</sup>.

As for the measurement in laboratory, Fig. 2-8 shows the schematic test suites. Fig. 2-8(a) is for the first option based on SPLs (also referred to as two-room method). As the figure shows, the test partition is fixed in the window between two reverberation rooms. Then, the sound transmission loss  $TL$  is given by <sup>[173]</sup>



$$TL(f) = L_S(f) - L_R(f) + 10 \lg \frac{S}{A_R(f)}, \quad (2.41)$$

where,  $L_S$  and  $L_R$  are the average SPLs in the source room and the receiving room, respectively;  $S$  is the area of the test element that is exposed in the receiving room;  $A_R$  is the sound absorption of the receiving room with the test element in place.

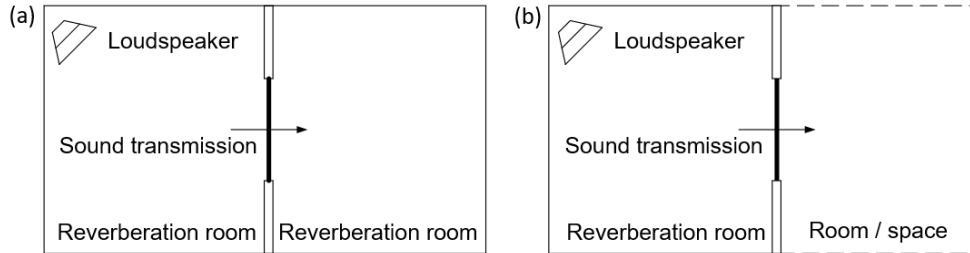


Fig. 2-8. The schematic diagrams and test suites for sound transmission loss measurement: (a) two-room method (or sound pressure measurement method); (b) sound intensity measurement method.

Fig. 2-8(b) is for the latter option using sound intensity. In this configuration, only one reverberation room is needed, serving as the source room. In the receiving side, it can be a not too reverberant room or space, though the ideal circumstance is a free field. The calculation of sound transmission loss is based on Eq. (2.36), where  $\Pi_{in}$  is evaluated from the measured average SPL in the source room considering that the sound field is diffuse, and  $\Pi_{tr}$  is determined by the product of the average normal sound intensity level over measurement surface and the area of the measurement surface. Hence, the intensity transmission loss  $ITL$  is obtained from <sup>[174]</sup>

$$ITL(f) = [L_S(f) - 6 + 10 \lg S] - [\bar{L}_m(f) + 10 \lg S_m], \quad (2.42)$$

where,  $\bar{L}_m$  represents the average normal sound intensity level over the measurement surface, and  $S_m$  is the total area of the measurement surface. Due to the bias between two methods <sup>[174]</sup>, the transmission loss measured by this method is named *intensity transmission loss* for distinction. In <sup>[169]</sup>, it is stated that the latter method is more accurate and is becoming more accepted recently. However, it is still unclear which method is better, but undoubtedly the latter approach is especially useful when the receiving room is not satisfying the reverberant requirement.

In the standard measurements <sup>[172–175]</sup>, there is always requirement on the volume of the reverberation room, whose minimum value is either  $50 \text{ m}^3$  or  $80 \text{ m}^3$ . However, non-standardized rooms can also be used for the TL measurement. Indeed, some small reverberation cabins have been developed for this purpose in the recent few decades. Featured by the small space occupancy and good mobility <sup>[88,178]</sup>, these cabins are appreciated for testing small elements. For example, Fig. 2-9 shows a small reverberation

cabin called *Alpha cabin*, which has been widely used in the automotive industry <sup>[179]</sup>. The cabin has a cavity volume of  $6.44 \text{ m}^3$ , and it is irregularly shaped with no walls parallel to each other for the utmost diffuseness in a limited space <sup>[180]</sup>. When used for TL measurement, the Alpha Cabin is coupled with an emission chamber to approximate the two-room method <sup>[173,175]</sup>, forming a system named *Isokell*, as shown by Fig. 2-10. This system is claimed to be well-performed from 125 Hz to 6300 Hz <sup>[179]</sup>. Besides, there are other proposals that use sound intensity method <sup>[172,174]</sup>. The small cabin (also referred to as PMA Soundbox) introduced by Vivolo <sup>[88]</sup> is constructed by five reinforced concrete walls, providing a reverberation room of  $0.83 \text{ m}^3$  volume. When used for sound transmission measurement, the small cabin was placed to an open field. For another case, the small mobile cabin used by Piollet et al. <sup>[178]</sup> is internally a  $0.8 \text{ m}^3$  volume surrounded by plywood walls. In this case, the small light cabin showed its convenience to move into an anechoic chamber, where the sound transmission loss measurements were performed following the ASTM E2249 (2002) standard. Therefore, small reverberation cabins can be used to characterize the sound TL of panels, using either the two-room or the one-room (i.e., sound intensity) approach. However, this needs special design of the cavity and attention to the effectiveness in the low frequency range.

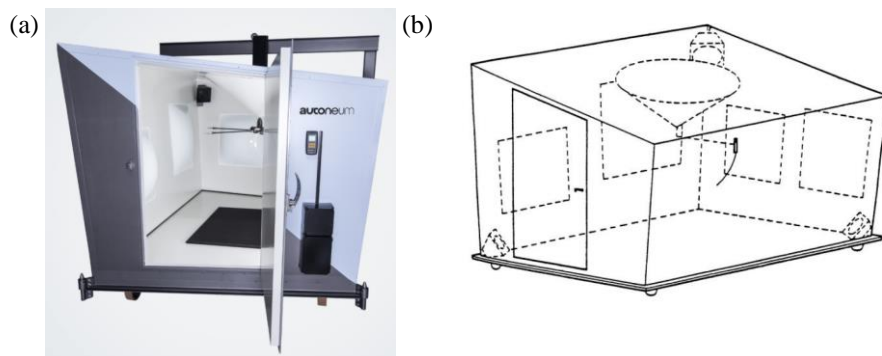


Fig. 2-9. Alpha Cabin: (a) a photo of test rig <sup>[179]</sup>; (b) a sketch of inner volume <sup>[180]</sup>.

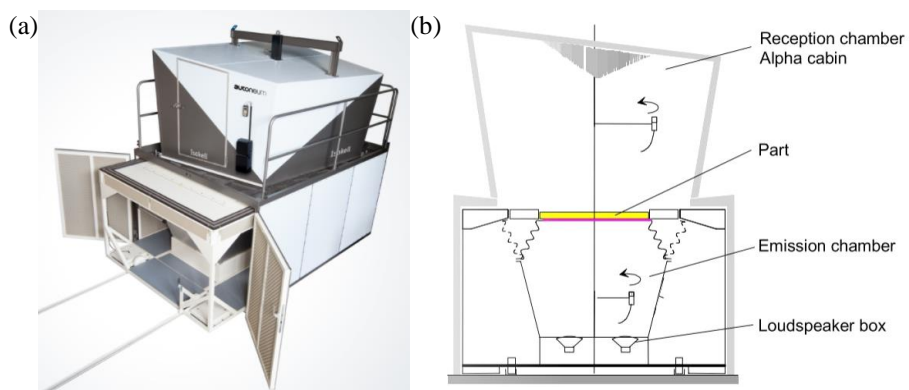


Fig. 2-10. Isokell: (a) a photo of the system <sup>[179]</sup>; (b) a sketch of its constitution <sup>[181]</sup>.

## 2.6 Summary

Four problems are involved in the plate-cavity system: flexural vibration of the plate, acoustic response of the cavity, plate-cavity coupled vibro-acoustics and sound transmission loss of the panel. This chapter introduces the fundamentals of these problems and the corresponding mathematic models or formulations for each of them. They are the basics for later chapters, including the background theory for the Noise-Box design, the differential equations to be solved using different numerical methods and the problems to be investigated through experiment.

Firstly, for the flexural vibration of a thin plate, Kirchhoff plate theory is introduced. Based on the theory, the mathematical model is proposed for a general convex plate under a harmonic point force excitation and with arbitrarily restrained edges. A wide range of restraint types are considered, and their boundary conditions are summarized in Table 2-1. It is worthwhile to mention that the model is feasible for various types of elastic or viscoelastic restraints. Secondly, for the interior acoustic problem, the mathematical model is given by considering a general convex acoustic cavity with various boundary conditions, and under a harmonic monopole source excitation. The fluid (air) properties are considered dependent on the ambient environment, especially the temperature. Thirdly, in the coupled vibroacoustic problem, the two uncoupled fields defined previously are considered interacting with each other. The acoustic field enriches the inhomogeneous part of the plate governing equation, while the structural field adds a flexible structural boundary surface. Corresponding to the three models mentioned above, three reduced models in 2D space are also provided by extending the  $y$  dimension to infinite.

Finally, the sound TL of isotropic panels is introduced. The figure of the typical TL curve for a field incidence indicates that a complete TL curve, as the frequency increases, will present the stiffness controlled, resonance controlled, mass controlled, coincidence and damping controlled regions. For an approximate prediction to the TL, three prediction schemes can be used, respectively from Sharp, Davy and ISO 12354-1. For measuring the TL in laboratory or field, two standardized approaches, respectively by sound pressure level and sound intensity level, are summarized. In addition, some alternative solutions using small reverberation cabins are reviewed.



## Chapter 3 Design and construction of plate-cavity coupled Noise-Box

*Noise-Box is a benchmarking and testing tool for vehicle interior noise analysis and control. It is going to be a simplified interior noise investigation system coupled by a plate and a cavity. The tool consists of a test bench and its numerical models. This chapter involves the design and construction of the test bench. The set-up principle is first introduced, explaining how it relates to a vehicle compartment, why it is originated as a plate-cavity system, and what functions it can perform. Then, the next section elaborates on its design process, including the determination of cavity shape and dimensions, the strategy for wall constructions, some details for experimental installation, etc. Finally, the complete plate-cavity coupled Noise-Box is presented.*

### 3.1 Set-up principle

The target of the design is to get a test bench that can benchmark the CAE tools for vehicle interior noise analysis and test the materials, structures or control strategies for vehicle interior noise mitigation. Under these instructions, Chapter 1 has raised some considerations through the literature review, where it is highlighted that

- the system should be representative, with access to panel, cavity, structure-borne noise, airborne noise and noise control measures;
- the system should be easy to model and analyse, with simple geometry and identifiable boundary conditions;
- all geometric, material and physical parameters should be specified.

In addition, through different types of simplified systems, the plate-cavity system of a rigid box with one flexible panel is selected. Therefore, the following work is to design a plate-cavity coupled Noise-Box based on the above three considerations.

However, there are still too many possibilities, especially for the shape of the cavity. Therefore, though the Noise-Box is considered for the vehicles in general, a passenger car is used as reference here for illustrating the correlation between the plate-cavity system and a vehicle compartment, and later for the geometric design of Noise-Box. The vehicle interior noise considers all noises transmitted into the cabin. The noise sources are various. For a road vehicle, they include the noises from power unit, tire-road interaction, intake system, exhaust system, wind and other ancillary components. The noise from these sources is transmitted inside the cabin through the structure-borne path or the airborne path, as

shown in Fig. 3-1. The panel-cavity system simplifies the car body and the acoustic field inside. The cavity represents the vehicle compartment, and the panel represents the vibrating car body. When the panel is excited by a mechanical force, the noise inside the cavity is structure-borne and the panel is the only transfer path. When there is a sound excitation outside, the interior noise is airborne and transmitted through the panel. The coupling between structure and enclosed acoustic field is revealed by the coupling between the panel and the cavity.

The panel-cavity simplification also enables the test bench to be more adaptable and multi-functional. On one hand, there are only two components inside the system, it is the simplest case for a vibroacoustic system, so it is the best option for benchmark cases of vibroacoustic problems, revealing the coupling mechanism or validating the numerical methods for interior noise prediction. On the other hand, various noise mitigation measures can be tested in such a test bench. For example, as shown in Fig. 3-2, structural optimized panel can be mounted for vibroacoustic test to validate its performance; soundproofing structure can cover the opening of the cavity to check its sound transmission loss; the wall impedance is changeable with acoustic treatment; and by placing sound sources inside it can help to develop the active noise control strategies.

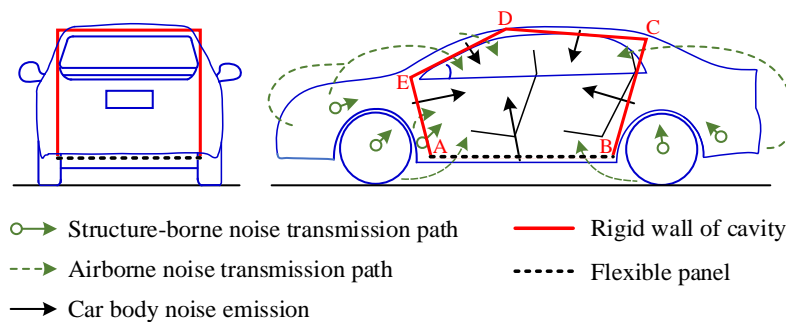


Fig. 3-1. Vehicle interior noise principle and the panel-cavity system.

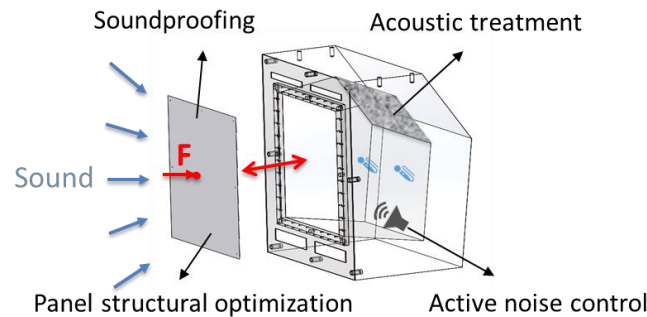


Fig. 3-2. Schematic diagram of the test bench for noise mitigation measures.

## 3.2 Design of Noise-Box test bench

### 3.2.1 Cavity acoustic design and optimization

To determine the shape and dimensions of cavity, two criteria are raised:

- the cavity should be easy to build, model and analyse;
- the acoustic field inside the cavity should be able to represent the acoustic field inside the vehicle compartment.

For the first criterion, simple geometry and physics are preferred. Flat walls are considered, and the walls (except the flexible panel) can be built by thick reinforce concrete to approximate the acoustically and mechanically rigid boundary conditions. With respect to the second criterion, the Noise-Box cavity is actually different from a real cabin of any vehicle. On one hand, the Noise-Box, as a test rig in lab, has to limit its size and weight. Accordingly, the cavity volume is smaller and the first natural frequency of the acoustic volume is higher. On the other hand, in accordance with the first criterion, the cavity is geometrically simpler and with fewer diffusers. Hence, the sound field diffuseness will not be as good as a real compartment. The design should try to optimize the diffuseness under the constraint of size. The methods used to design small reverberation cabins <sup>[88,182,183]</sup> are employed to the optimization. In fact, the methods are trying to make the cavity less dominant by a single acoustic mode by adjusting the mode shapes and natural frequency spacing. Moreover, increasing the diffuseness of the cavity sound field also helps to extend the function of the Noise-Box as a small reverberation cabin for TL measurement of panels, like the examples introduced in Section 2.5.

Considering an analogue to the vehicle compartments, a car-like shape is adopted. The preliminary shape was designed as shown in Fig. 3-1. In view of the diffuseness, a rectangular cavity was avoided and a pentagonal shape was used. Two side walls were simplified to be parallel to each other and perpendicular to the bottom panel. The bottom was selected as the flexible panel, which is rectangular shaped and larger than other rectangular walls. As the boundary conditions of the flexible panel may be one source of uncertainty to the system, the larger size can make it less significant. The simplification of two side walls is also reasonable. On one hand, the two sides of the car body are symmetric and close to vertical. On the other, the simplification makes it possible to build the corresponding two-dimensional (2D) model of the cavity <sup>[1]</sup>. In the numerical simulations, the 2D model is much more efficient than the three-dimensional (3D) one.

With the shape determined, the next is to settle the ratios of lateral dimensions. In the low frequency region, the modal density is low. The method to improve the diffuseness is to

optimize the geometry to achieve a homogeneous distribution of the natural frequencies. For rectangular reverberation rooms, the ratio 1:1.26:1.59 is recommended <sup>[173,184]</sup>, since it avoids modal degeneracy in the wide frequency range. Although cavity is not rectangular, the ratio was used as a start point for searching the optimized geometry. As shown in Fig. 3-3, the initial dimensions of the rectangular that encloses the cavity satisfy that the ratio  $L_x : L_y : L_z$  equals to 1.59:1.26:1. Then, the dimensions were adjusted as indicated by the arrows shown in Fig. 3-3, including  $L_x, L_y, L_z$  and the coordinates of corners A, B, C, D and E. For each case, the eigenfrequencies and mode shapes of the acoustic field in the low frequency range were computed and analysed in order to seek the best option.

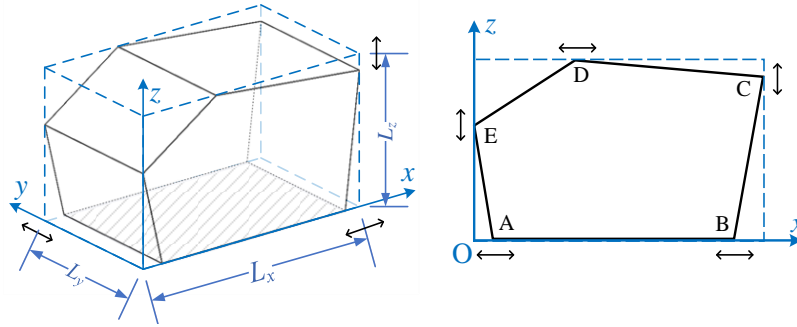


Fig. 3-3. Schematic diagram for optimizing the cavity geometry.

To quantifying the uniformity of the eigenfrequency distribution, the frequency spacing index ( $\psi$ ) proposed by Bolt <sup>[185]</sup> was used. This index evaluates the mean square of the deviations of the distances between subsequent modes, which is given by <sup>[182,185]</sup>

$$\psi = \frac{\sum_{i=1}^{n-1} \varepsilon_i^2}{(n-1)\bar{\delta}^2} + 1, \quad (3.1)$$

with

$$\bar{\delta} = \frac{1}{n} \sum_i^{n-1} \delta_i = \frac{1}{n} \sum_i^{n-1} (f_{i+1} - f_i), \quad (3.2)$$

$$\varepsilon_i = |\delta_i - \bar{\delta}|, \quad (3.3)$$

where,  $n$  is the total number of modes,  $\delta_i$  denotes the distance between  $(i+1)^{\text{th}}$  natural frequency  $f_{i+1}$  and  $i^{\text{th}}$  natural frequency  $f_i$ ,  $\bar{\delta}$  is the mean value of the distances  $\delta_i$ , and  $\varepsilon_i$  is the deviation of  $\delta_i$  from the mean value  $\bar{\delta}$ .

A smaller value of  $\psi$  means a better uniformity of the eigenfrequency distribution. In Eq. (3.1), the number  $n$ , which determines the upper bound frequency, is also important. One choice of the upper bound frequency is the low-frequency limit of the diffuse field. Blaszak <sup>[182]</sup> proposed to use the Schroeder frequency <sup>[186]</sup>



$$f_{\text{sch}} = 2000 \sqrt{\frac{T_{60}}{V}}, \quad (3.4)$$

where  $T_{60}$  is the reverberation time and  $V$  is the volume of the room.

However, since  $T_{60}$  is unknown in the design stage and the Schroeder frequency  $f_{\text{sch}}$  is too restrictive from the application point of view (maybe much higher than the upper bound of modal region), another commonly-used cut-off frequency was adopted. This cut-off frequency corresponds to the modal density of 20 modes per third-octave band and is given by <sup>[187]</sup>

$$f_{\text{cut}} = \frac{c}{\sqrt[3]{V/4}}, \quad (3.5)$$

where  $c$  denotes the sound velocity.

Due to the irregular shape of the acoustic field, the eigenfrequencies were computed using FEM. With all the eigenfrequencies below the cut-off frequency  $f_{\text{cut}}$ , the index  $\psi$  corresponding to each geometry was obtained. Fig. 3-3 shows the adjustments that were used to search the minimum index  $\psi$ , and the final geometry of the Noise-Box cavity is corresponding to this minimum  $\psi$ . However, as the index  $\psi$  doesn't bring complete information on the non-uniformity <sup>[182]</sup>, the designer still needs to check the exact eigenfrequency distribution in the process.

### 3.2.2 Construction and mould design

With the cavity design settled, the next step is to determine how to construct such a small room. Considering that it is a concrete box without a completely regular shape, the selected strategy is to pour the concrete into a shaped steel mould. Then, after the concrete dries up, the mould is taken off and the concrete box shows up. The designed steel mould is shown in Fig. 3-4.

As shown in Fig. 3-4(a), the mould has two parts: the inner part shapes the inner cavity; the outer part determines the shape outside. On the front is a steel frame that will be imbedded to the concrete for other purpose, which is introduced in Section 3.2.3. For pouring inside the concrete, four rectangular holes are kept in the steel frame as demonstrated in Fig. 3-4(b). Fig. 3-4(c) shows the way to place the mould in construction. Four square feet (Fig. 3-4(e)) are supporting the outer part and four cylindrical pillars (Fig. 3-4(d)) are holding the inner part. In order to enforce the strength of the concrete walls, a rebar cage was designed as shown in Fig. 3-4(f). It is to be put between the inner and outer parts before pouring process. From the outer part of the mould, it can be seen that the Noise-Box has two walls horizontal outside, while the walls on the back keep paralleling the inner

walls. The horizontal top and bottom are to help the front of the Noise-Box keep vertical when it is lifted up or placed on the floor. Meanwhile, paralleling to the inner walls lower the overall weight of the facility while the wall thickness has to be guaranteed. During the consideration of the outer shape, the centre of gravity was also checked to keep the facility stable and safe.

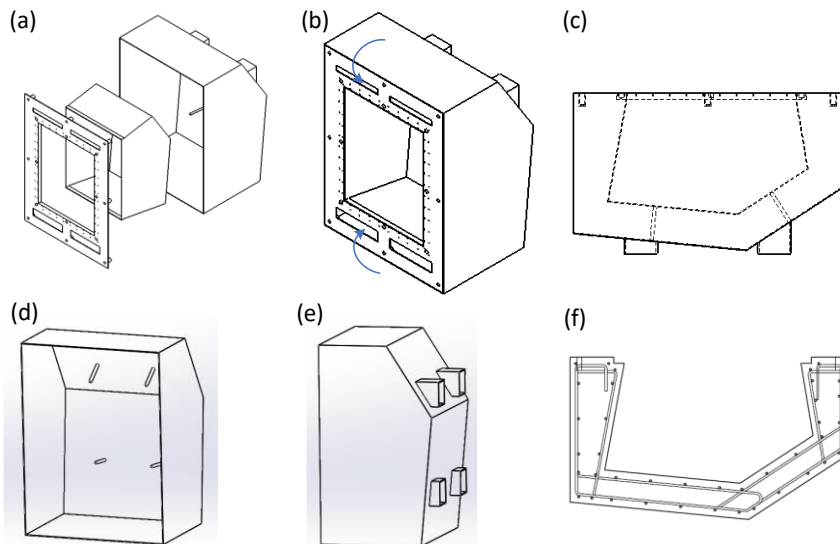


Fig. 3-4. Mould and skeleton design for the concrete construction of Noise-Box: (a) mould disassembly; (b) mould assembly; (c) placement mode for construction; (d) inner part holders; (e) outer part supports; (f) rebar cage reinforce.

### 3.2.3 Installation and functioning design

To ease the assembly and disassembly of the flexible panel as well as to stiffen the contact area, a steel frame is embedded to the concrete walls around the opening of the cavity, as shown in Fig. 3-5 (a). The steel mounting frame is able to mount the panel in two ways: rigidly supported and elastically supported. The two mounting types correspond to two different detail views of the circle area at the point B of Fig. 3-5(a). Fig. 3-5(b) shows the detail view for the rigid mounting. To approximate the clamped boundary conditions, a steel clamping frame is placed on the flexible panel and fixed with two circumferential rows of screws. Fig. 3-5(c) is the detail view of the elastic mounting. Different rubber mounts result in different restraint stiffness and damping. Soft material is needed for approximating the free boundary conditions. Nevertheless, to be exact, this design leads to (visco)elastic supports. Though two mounting strategies are considered in the design, this thesis focuses on the former strategy, and the latter is prepared as an option for future investigation.

Diffuse sound field is an ideal sound field that never exists but commonly used in research. In experiment, the diffuse sound field can be approximated by reverberation chamber.

Considering the investigation of airborne noise, where may need the diffuse sound field excitation, the test bench was designed to be able to mount on the window of the reverberation chamber. As shown in Fig. 3-6, with the help of a concrete frame, the flexible panel is excited by the diffuse sound field, while the test bench is outside the reverberation chamber. Therefore, thread holes for fastening the test bench to the concrete frame were designed approximate to the edges on the front. Meanwhile, thread holes for the eyebolts were prepared on the top concerning the lifting and moving of the test bench.

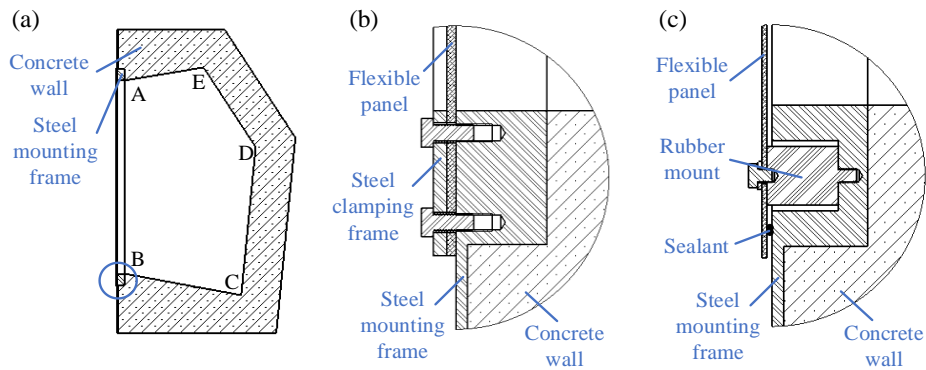


Fig. 3-5. Design for the mounting of flexible panel: (a) a steel mounting frame in the front; (b) realization of the rigid mounting; (c) realization of the elastic mounting.

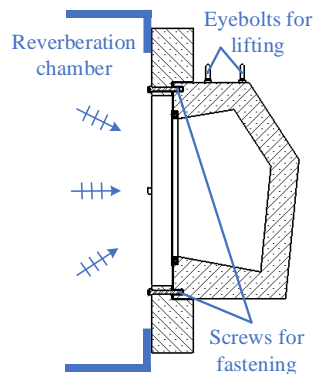


Fig. 3-6. Schematic diagram for the test under exterior diffuse sound field excitation.

### 3.2.4 Overview of the final design

Taken into account the issues of size, weight and manufacture, the final design was determined, as shown in Fig. 3-7. The equipment occupies around  $2 \text{ m}^3$  and weighs about 2.5 tons. The rigid walls are constructed out of reinforced concrete with the thickness no less than 200 mm. The cavity inside the facility is  $0.596 \text{ m}^3$ , shaped like a pentagonal prism. It is similar to the one shown in Fig. 3-3, but has a small flat step of 40 mm around the opening of the cavity, which is modified for the manufacture. All dimensions of the cavity are annotated in Fig. 3-3.

The shape was optimized according to Section 3.2.1. In the optimization, the air density and the sound speed were assumed to be  $\rho_0 = 1.2 \text{ kg/m}^3$  and  $c = 343 \text{ m/s}$ . For computing the frequency spacing index  $\psi$ , the cut-off frequency  $f_{\text{cut}} = 647 \text{ Hz}$  (based on Eq. (3.5)) was used. The natural frequencies were obtained from the modal analysis using the FEM by COMSOL. After the optimization, the final frequency spacing index is given by  $\psi = 1.57$ , smaller than the value ( $\psi = 1.71$ ) of a rectangular room with the same volume and the recommended ratios 1:1.26:1.59. Comparison of their eigenfrequency distributions is shown in Fig. 3-8, which also illustrates that the first eigenfrequency of the final design is around 160 Hz.

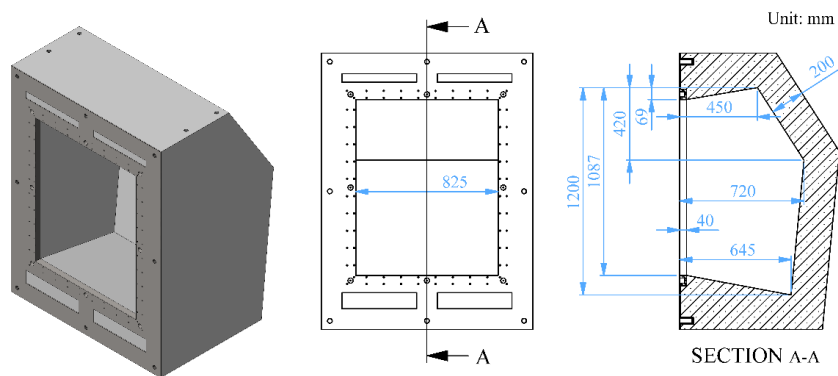


Fig. 3-7. Overview of the final design of Noise-Box and the cavity dimensions.

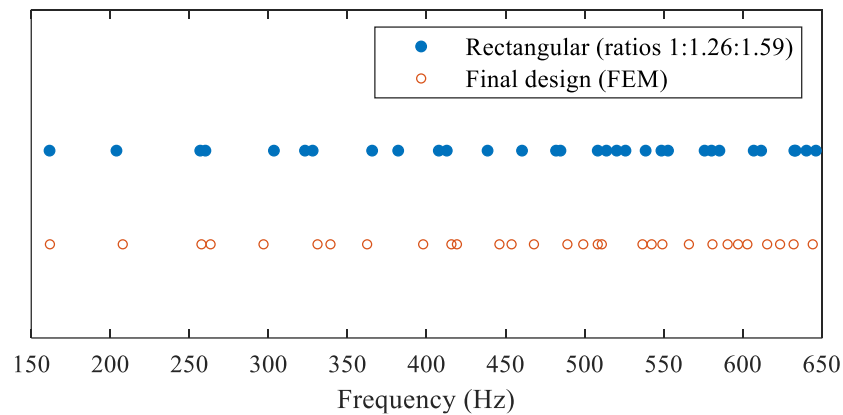


Fig. 3-8. Distribution of the cavity natural frequencies up to 650 Hz. Comparison between the rectangular cavity with the initial ratios 1:1.26:1.59 and the final design in simulation.

In addition to the dimensions of the cavity, as shown in Fig. 3-7, on the front steel mounting frame and around the opening of the cavity are 80 thread holes for the rigid mounting shown in Fig. 3-5(b), and 8 holes for the rubber mounts of the elastic mounting shown in Fig. 3-5(c). The other 8 thread holes around the outer edges of the steel mounting frames are for the fastening shown in Fig. 3-6.

### 3.3 Construction of Noise-Box test bench

Based on all the details considered in the design process, the manufacture started from the steel mounting frame in the front of the Noise-Box. The completed frame is shown in Fig. 3-9(a) with all the holes prepared. The two additional bars on top were used to aid the construction process. Mould and rebar cage (Fig. 3-9(b)-(c)) were then prepared for the concrete pouring in. After the concrete had been dry, the mould was taken off and the concrete Noise-Box was built. Fig. 3-9(d) showing the Noise-Box moving inside the lab and rotating to its vertical working condition. As can be observed from Fig. 3-9(e) the steel mounting frame has been embedded to the concrete box. Later, one hole through the back wall was kept in order to pass through the cables, as shown in Fig. 3-9(f). The hole is sized 20 mm. Finally, the surface finishes were done, because raw concrete surfaces tend to be porous and the steel part is easy to be corrupted. The inner and front wall surfaces were specially polished and painted. While the inner walls are intended to be highly reflected and acoustically rigid, the front wall is wanted to be flat and corrosion-resistant. Corresponding functional painting were used for these walls. Additionally, to isolate the Noise-Box from the laboratory floor, four isolators (VIBROSTOP MOPLA 5/BY 650) have been placed under the Noise-Box. The elastic constant of the isolator is 44.8 daN/mm. When holding the Noise-Box, its natural frequency is around 4 Hz, which is considered low enough to avoid affecting the experiments.

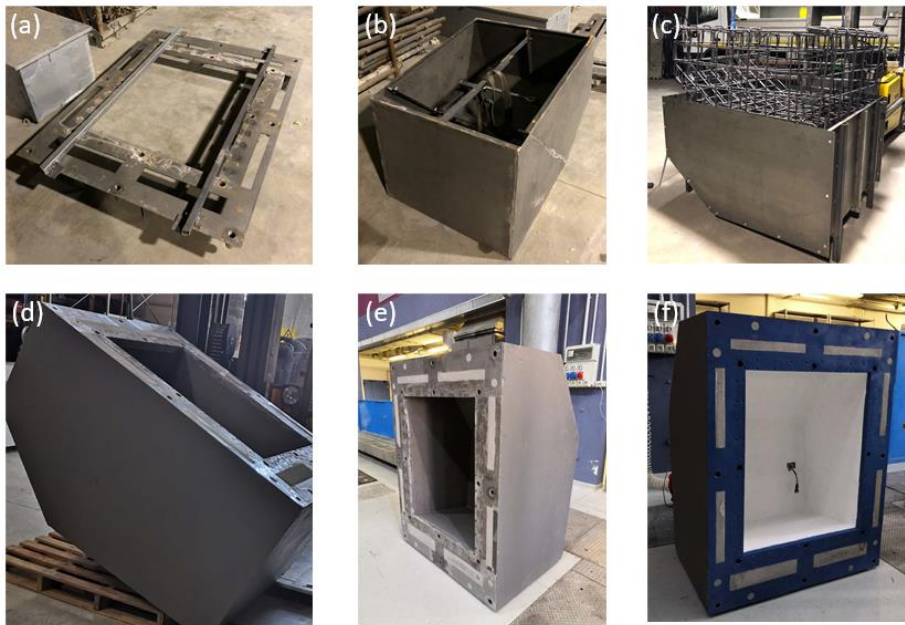


Fig. 3-9. The Noise-Box test bench built-up process: (a) steel mounting frame; (b) inner mould; (c) outer mould and rebar cage; (d) Noise-Box transportation; (e) Noise-Box before improvement; (f) Noise-Box after improvement

### 3.4 The plate-cavity coupled Noise-Box

The Noise-Box functions with the opening covered by a flexible panel when the system raises a plate-cavity problem. The plate can be of different structures and thicknesses, but this thesis considers only a flat thin plate made of aluminium. As for the two mounting approaches shown in Fig. 3-5, only the rigid mounting (Fig. 3-5(b)) is applied. Thus, the flexible region of the plate is overlapped with the opening of the cavity, whose dimensions are  $0.825 \text{ m} \times 1.018 \text{ m}$ . The selected thickness of the plate is  $4 \text{ mm}$ , so that the first several structural natural frequencies are not far away from the acoustic ones (as shown by Table 4-10). This was checked using the FEM introduced in Chapter 4. The plate was manufactured and its CAD drawing is shown in Appendix A.5. The plate was also proved thin enough to satisfy the Kirchhoff plate theory in the wide frequency range. The exact shape of the Noise-Box cavity is shown in Fig. 3-10. For modelling this cavity, the acoustic field can be of the exact geometry or simplified to a pentagonal prism, since the steps with  $40 \text{ mm}$  on the top and bottom are very small. However, it should be noticed that in the simplification, the plate-cavity coupling face is unchanged but the slopes of two walls are slightly modified, as shown in Fig. 3-11.

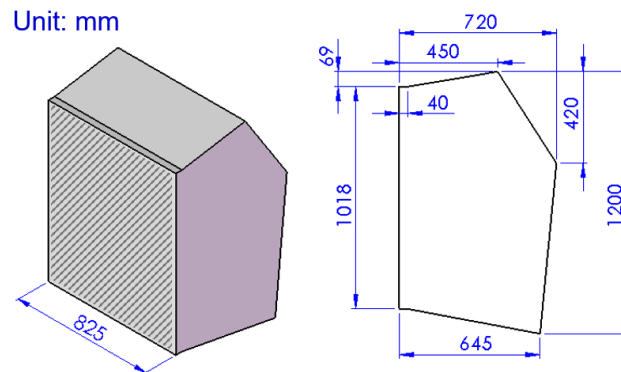


Fig. 3-10. The plate-cavity coupled Noise-Box and its exact cavity geometry.

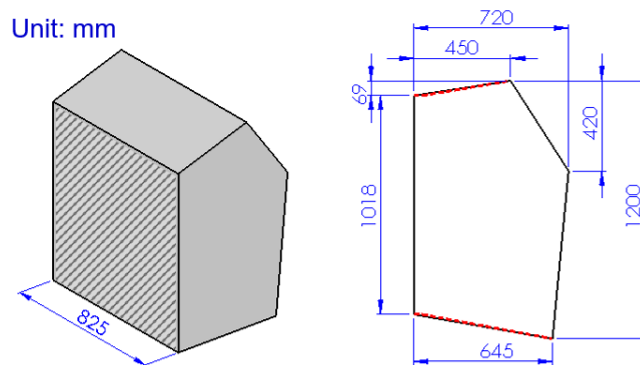


Fig. 3-11. The plate-cavity coupled Noise-Box and the simplified cavity geometry.

### 3.5 Summary

The Noise-Box targeted for benchmarking vehicle interior noise analysis and testing vehicle interior noise control strategies has been designed and constructed. It simplifies the vehicle cabin into a plate-cavity system composed of six rigid concrete walls and one flexible panel. The motivations of the simplification are introduced. That is, the plate-cavity system is available for the common components in the vehicle interior noise investigation, such as panel, cavity, structure-borne noise, air-borne noise and noise control measures; it is easier to model and analyse than other vibroacoustic system; its function can be extended without much modification.

Then, the design and construction of the Noise-Box are presented. The shape of the cavity is inspired from a real car compartment and simplified as a pentagonal prism. The two pentagonal side walls are parallel while the others are rectangular. This design enables the 3D numerical model to be reduced to 2D if necessary. The dimensional ratios of the cavity have been specially determined and optimized by the frequency spacing index to realize a more diffuse sound field under a limited acoustic volume. For constructing the Noise-Box walls, pouring concrete is used, with the aid of the customized mould and rebar cage. Besides, the front surface of the Noise-Box is embedded a steel frame for mounting purpose. On the frame, different holes are prepared for the rigid and elastic supports of the test element. Considering the possibility for exterior diffuse sound field excitation, the Noise-Box is also prepared for mounting to the window of a reverberation chamber. Finally, limited by size and weight, the final design as well as its dimensions are determined. All details are shown in Appendix A: CAD drawings.

After construction, the Noise-Box test bench is obtained. It occupies around  $2 \text{ m}^3$ , weighs about 2.5 tons and provides a cavity of  $0.596 \text{ m}^3$  surrounded by its concrete walls that are at least 200 mm thick. There is an opening of  $0.825 \text{ m} \times 1.018 \text{ m}$  in front of the test bench. The final plate-cavity coupled Noise-Box is assembled by mounting a 4-mm aluminium plate to the opening, and this is the system to be investigated in the following chapters.





## Chapter 4 Numerical investigation using finite element method

*This chapter uses FEM to solve the problems involved in the Noise-Box, corresponding to the plate, acoustic and vibro-acoustic problems that have been modelled in Chapter 2. The general steps of FEM are first illustrated. Then, commercial software that implements this method is used to analyse the three problems, respectively. After the FE models are proved accurate, the parameters or conditions that affect the numerical results are investigated. The target of this chapter is to obtain reliable FE models for the considered problems, and meanwhile to provide informative initial predictions.*

### 4.1 General procedures for FEM

Consider a generic problem defined by

$$\begin{cases} \mathbf{D}(u) = F_v & \mathbf{r} \in \Omega \\ \mathbf{C}(u) = \bar{F} & \mathbf{r} \in \partial\Omega \end{cases} \quad (4.1)$$

where,  $\mathbf{D}$  and  $\mathbf{C}$  are differential operators;  $u$  is the unknown variable;  $F_v$  and  $\bar{F}$  are load functions independent of  $u$ ;  $\mathbf{r}$  is the vector of global coordinates; the problem domain is denoted as  $\Omega$  with the boundary  $\partial\Omega$ .

There are generally seven basic steps to analyse it using FEM <sup>[188]</sup>:

(1) Writing the weak integral form of the problem

In this process, various methods can be used to construct the integral formulation, e.g., *method of weighted residuals* (including *collocation method*, *least-square method*, *Galerkin's method*, etc.), *variational method* and *Raleigh-Ritz's method*.

For Eq. (4.1), the weak integral formulation in Galerkin's form is given by:

$$\begin{cases} W(u, \delta u) = W_\Omega(u, \delta u) + W_{\partial\Omega_n}(u, \delta u) = 0 \\ \mathbf{C}_e(u) = \bar{F}_e \quad \mathbf{r} \in \partial\Omega_e \end{cases}, \quad (4.2)$$

where,  $W(u, \delta u)$  can be derived from  $\int_\Omega (\mathbf{D}(u) - F_v) d\Omega$  using the rules of integration by parts to reduce the order of differentiation and incorporating the natural boundary conditions over  $\partial\Omega_n$ . The essential boundary conditions over  $\partial\Omega_e$  are keeping enforced.  $\delta u$  is the test function in Galerkin's form. It is arbitrary but admissible variation of  $u$  under the enforced essential boundary conditions.

## (2) Meshing the problem domain into subdomains/elements

The elements are selected with certain shape, order, nodal arrangement and therefore shape functions. The meshing rule is provided considering the convergence, accuracy and model size. In this step, it is a common practice to associate the elements to the corresponding reference element(s), where the shape functions are known or can be derived a priori.

This step can be denoted as

$$\Omega \simeq \tilde{\Omega} = \bigcup_{e=1}^{n_e} \Omega^e, \quad (4.3)$$

where  $n_e$  is the total number of elements. As aforementioned, consider a reference element  $\Omega^r$  with a local coordinate system.  $\mathbf{r}'$  is the vector of local coordinates. The shape functions of the reference element are known as  $N_1^e(\mathbf{r}'), \dots, N_{nn_e}^e(\mathbf{r}')$ , with  $nn_e$  denoting the number of nodes in a single element. Then, by comparing  $\Omega^r$  and  $\Omega^e$  the local coordinates can always map to the global coordinates with

$$\mathbf{r} = \mathbf{T}\mathbf{r}' \quad (4.4)$$

where  $\mathbf{T}$  is the transformation matrix.

## (3) Approximating variable(s) and calculating elementary matrices

The variable(s) and geometry of each element are approximated using their nodal correspondences with the aid of shape functions, and the elementary matrices are calculated based on the weak integral formulation. In most cases, the elementary integrals need to be calculated numerically, and the Gauss quadrature rules are usually used in the numerical integration.

Thus, for each element  $\Omega^e$ , the nodal variables  $u_i^e$  and nodal coordinates  $\mathbf{r}_i^e$  are used (for iso-parametric elements):

$$u = \sum_{i=1}^{nn_e} N_i^e(\mathbf{r}') u_i^e, \quad (4.5)$$

$$\mathbf{r} = \sum_{i=1}^{nn_e} N_i^e(\mathbf{r}') \mathbf{r}_i^e. \quad (4.6)$$

By instituting Eq. (4.5) into Eq. (4.2) for  $\Omega^e$  and utilizing the relationship between  $\mathbf{r}$  and  $\mathbf{r}'$  indicated by Eqs. (4.4) and (4.6), the following expression is obtained:

$$\{\delta u^e\}^T ([\mathbf{A}^e] \{u^e\} - \{F^e\}) = 0, \quad (4.7)$$

where,  $[\mathbf{A}^e]$  is the elementary matrix, and  $\{F^e\}$  is the elementary load vector. With respect to the dynamic or acoustic problems in frequency domain, the elementary dynamic matrix

$[\mathbf{A}^e(\omega)]$  dependent on frequency can be expressed as a combination of the elementary mass  $[\mathbf{M}^e]$ , stiffness  $[\mathbf{K}^e]$  and damping  $[\mathbf{C}_d^e]$  matrices:

$$[\mathbf{A}^e(\omega)] = -\omega^2[\mathbf{M}^e] + j\omega[\mathbf{C}_d^e] + [\mathbf{K}^e]. \quad (4.8)$$

#### (4) Assembling the elementary matrices for global matrices

With this step, the continuity between elements is guaranteed. The assembling starts from the integral of Eq. (4.2) over  $\Omega$ . Thus,

$$W(u, \delta u) = \sum_{e=1}^{n_e} \{\delta u^e\}^T ([\mathbf{A}^e] \{u^e\} - \{F^e\}) = 0. \quad (4.9)$$

According to the elements' locations, Eq. (4.9) can be rewritten as

$$W(u, \delta u) = \{\delta u\}^T ([\mathbf{A}] \{u\} - \{F\}) = 0, \quad (4.10)$$

where,  $\{u\}$  is the vector of nodal variables,  $[\mathbf{A}]$  is the global matrix and  $\{F\}$  is the global load vector. Under the same situation in introducing Eq. (4.8), the global dynamic matrix  $[\mathbf{A}(\omega)]$  is a combination of the global mass  $[\mathbf{M}]$ , stiffness  $[\mathbf{K}]$  and damping  $[\mathbf{C}_d]$  matrices:

$$[\mathbf{A}(\omega)] = -\omega^2[\mathbf{M}] + j\omega[\mathbf{C}_d] + [\mathbf{K}]. \quad (4.11)$$

#### (5) Imposing constraints or essential boundary conditions

There are three basic techniques to do this: *Lagrange's multiplier method*, *partitioning method* and *penalty method*. After the essential boundary conditions in Eq. (4.2) is imposed. The problem is then well-posed and can be solved in the next step.

Implemented the arbitrariness of  $\delta u$ , Eq. (4.10) yields the system of equations for solution:

$$[\hat{\mathbf{A}}] \{\hat{u}\} = \{\hat{F}\}, \quad (4.12)$$

where, the head '^' denotes that the constraints have been imposed.

#### (6) Solution

The FE model are established after step (5), and the solving method relies on the specific analysis (e.g., stationary, modal, harmonic, random, transient, etc.) and the model size.

#### (7) Convergence study and postprocessing.

The last step is to make sure the results accurate and precise as expected, and to obtain other required physical indicators. In the convergence study, three types of errors should be noticed: modelling, discretization and numerical errors [188]. The modelling error comes when we try to describe the problem using a mathematical model. In other words, it happens before the numerical approach is applied, in the process of establishing the governing

equation(s) and boundary conditions. The latter two are directly related to the numerical technique. The error caused by the discretization of the problem domain is categorized as the discretization error, and the remaining is called numerical error including the round-off, truncation, integration, matrix-conditioning in normal numerical calculations. While the errors induced by FEM for dynamic/acoustic problems are discussed, they are also referred to as interpolation and pollution errors <sup>[20,21,152]</sup>. The former results from the polynomial approximation of variables in the elements, and the latter is due to the different wavenumbers between the FE model and the exact problem. Both are related to the element size, the analysis frequency and the order of the polynomial shape functions. The relationships are given by <sup>[20,21]</sup> and summarized in <sup>[152]</sup> and <sup>[159]</sup>. The errors increase if the elements enlarge or the frequency rises. Therefore, it is necessary to reduce the element size as the frequency increases. There is a rule of thumb stating that at least six elements per wavelength for linear elements or alternatively at least four elements for quadratic elements. However, this simple rule of thumb is proposed based on the interpolation error, while the pollution error is more complicated. In comparison, the interpolation error dominates at low frequencies, while the pollution error increases fast at high frequencies and becomes predominant. Nevertheless, the simple rule of thumb is adequate in general practice, since the FEM is hardly implemented to very high frequencies limited by the affordable computational burden. To ensure a reliable solution, it is recommended in both ANSYS® and COMSOL® by their user's manuals using at least either 10 linear or 5 quadratic elements per wavelength. This is the rule of thumb implemented in this thesis. Even so, finer mesh is considered for more accurate results or checking the convergence performance.

## **4.2 FEM for flexural vibration of thin plate**

The mathematical model based on the Kirchhoff-Love plate theory has been introduced in Section 2.2, where the governing differential equation and boundary conditions are provided. To analysis the flexural vibration of the plate with any restraint types (see Table 2-1), we can use FEM following the steps as mentioned in Section 4.1. The seven steps are also implemented in the commercial software, where the steps (1)-(2) are part of the preprocessing, and step (7) corresponds to the postprocessing. While commercial software is used to solve the problem, all the routine parts are done automatically by the computer and the interactions from users are to help clarify the problem and the meshing and solving strategies. Since the FE analyses in this thesis are achieved via commercial software, the implementation of the basic steps for a specific problem is not further introduced here and in the following sections. For different problems and different types of elements, the

elementary matrices are different, but the FE modelling procedures are the same. Concerning the formulating of thin plate elements, a comprehensive introduction can be found in <sup>[17]</sup>.

Before the FEM is used to analyse a plate, it is here to clarify the discrepancies between the FE model that should be built up based on the mathematical model introduced in Section 3.2 and the final FE models established the two commercial software environments. The discrepancies rely on the element types that are available in the software or the selection of element type in practice. In commercial software, shell elements are imbedded instead of plate elements. The shell elements are extensions of plate elements. In shells, the mid-surface can be curved and the membrane (or in-plane) forces or displacements are considered. If a shell is flat without in-plane force or motion, the model developed according to the shell theory is equivalent to the model from the corresponding plate theory. Therefore, it is feasible to use shell elements to model the plates in the software environments. Moreover, while in ANSYS, it is able to select either the thin shell element based on Kirchhoff-Love shell theory or the moderately-thick shell element based on Mindlin-Reissner shell theory, the former is not directly available in COMSOL. The difference between Kirchhoff-Love and Mindlin-Reissner theories has been discussed at the beginning of Section 2.2. As mentioned previously, the Mindlin-Reissner theory is more precise, considered the effects of rotary inertia and transverse shear strain. With respect to thin plates (or shells), the two plate (or shell) models are comparable, and the thinner the structure is (in terms of the thickness-to-span ratio  $h/L$ ), the better the models match. The two theories are compared for this issue using FEM in <sup>[159]</sup>, where plates with 230 different ratios of  $h/L$  from 1/500 to 1/10 are analysed to compare the first 100 bending modes, proving the foregoing statement and also showing that the relative error is meanwhile related to the frequency and boundary conditions. Nevertheless, for the considered plate in this section, the FE models based on these two theories will be considered in ANSYS, using the SHELL63 and the SHELL181 elements, respectively. In COMSOL, the default shell element is used, which is a second-order element and of the Mindlin-Reissner type.

#### 4.2.1 Problem definition

An aluminium thin plate, which will be mounted to the Noise-Box for experiment, is considered. The plate's 2D engineering drawing can be found in Appendix [A.5](#). With the perimeter clamped to the test bench, the vibrating part should overlap with the opening of the Noise-Box. Therefore, it is a rectangular plate with dimensions  $a \times b = 0.825\text{m} \times 1.018\text{m}$ , as shown in Fig. 4-1. The plate's thickness and material properties are given as

$$h = 0.004 \text{ m}, \rho = 2700 \text{ kg/m}^3, E = 70 \times 10^9 \text{ Pa}, \nu = 0.33. \quad (4.13)$$

Then, the plate is very thin, with the thickness-to-span ratio  $h/a = 0.0048 < 1/200 \ll 1/20$ . Regarding the condition  $\lambda_b/h > 6$ , the upper frequency limit is 67941 Hz. As discussed in Section 2.2, concerning this plate, the Kirchhoff-Love theory is very accurate. However, there is also a drawback that the plate may be sensitive to the membrane forces as  $h/a < 1/100$  [157]. Nevertheless, since it is assumed that no initial tension exists and the plate is vibrating under small deflection, the membrane forces can be considered negligible.

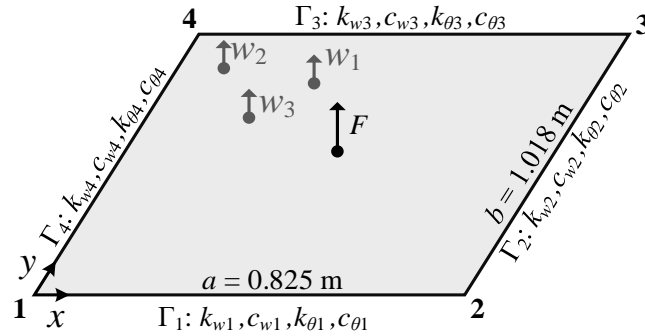


Fig. 4-1. Rectangular plate for FEA

Moreover, as Fig. 4-1 shows, the translational and rotational spring constants and damping coefficients for the four edges are given by  $k_{wi}$ ,  $k_{\theta i}$  and  $c_{wi}$ ,  $c_{\theta i}$  ( $\mathbf{r} \in \Gamma_i$ ,  $i = 1, 2, 3, 4$ ). This means that the elastically restrained or supported edge conditions will be considered. In other words, like the model introduced in Section 2.2 being available for any type of edge conditions, the FE modelling strategy introduced here is also adaptable to all those types. Although the plate edges are designed to be clamped when it is rigidly supported, the ideally clamped boundary conditions are hard to be guaranteed in practice. As can be found in the literature [48,67,78,84,189–193], it is very common to utilize a rigid mounting frame (as shown in Fig. 3-5(a)) to reach the fully clamped boundary conditions. However, the outcome is not always satisfying, especially for the first several modes. Some research [67,84,194] suggests that the conditions may be between the clamped and the simply supported, with an unknown rotational stiffness. This is also the case for the panel that will be examined in this work. The real boundary conditions can relate to the stiffness of the support, the local stiffness or bending rigidity of the plate, the perfectness of the attachment, meteorological conditions, etc. Similar difficulty is also faced when the simply supported boundary conditions are to be replicated in experiment. Some research finds good approximation with the plate simply bolted close to the edges [56,195,196], while others propose particular designs with shims [197], adapters [78], rollers [189], spring-steel-skirt [198] or v-grooves [199]. Therefore, the elastically restrained/supported models are helpful in case that the restraints/supports are not sufficiently rigid or free.

In this section, the plate will be considered for four types of edge restraints (see Table 2-1): clamped, simply supported, rigidly supported with elastic restraint against rotation, and general-elastically restrained against rotation and translation. The consideration of the third type also includes the influence of the rotational stiffness or damping. For each situation, modal analysis (and/or harmonic analysis) is performed, where we can see how the modal parameters (or the resonance frequencies and amplitudes) are affected. In the harmonic analysis, as indicated by Fig. 4-1, the harmonic point force is acting at point  $r_F$  (0.385m, 0.533m), with the amplitude  $F=1$  N, and the frequency responses are measured at  $r_1$  (0.31m, 0.8055m),  $r_2$  (0.11m, 0.8755m) and  $r_3$  (0.16m, 0.6555m), whose displacements are respectively provided by  $w_1, w_2$  and  $w_3$ .

#### 4.2.2 ANSYS model

In ANSYS, linear elements are used to discretize the plate domain: SHELL63 based on Kirchhoff-Love (thin shell) theory and SHELL181 based on Mindlin-Reissner (moderately-thick shell) theory. Both are four-node elements, and each node has six *degrees of freedom* (DOF): 3 translations and 3 rotations. Regarding the boundary conditions, the non-elastic or non-viscoelastic ones can be imposed by constraining the corresponding DOF along the plate edges, while the (visco)elastic ones can be simulated with the nodal-based spring-damper elements COMBIN14. Then, if an edge is elastically restrained, all nodes on the edges should be associated with one or two COMBIN14 elements, where one element for translational stiffness (and damping) or/and one element for rotational stiffness (and damping). Every COMBIN14 element is defined by one spring constant  $k_{\text{node}}$  (and one damping coefficient  $c_{\text{node}}$ ) with its DOF specified. One end of the COMBIN14 element is fixed, while the other is connecting to one of the nodes on the plate edges. Since the coefficients  $k_w, c_w, k_\theta,$  and  $c_\theta$  are defined per unit length and linear elements are used for the connected plate model, for an element edge with length  $l_e$ , the spring constant  $k_{\text{node}}$  and damping coefficient  $c_{\text{node}}$  allocated to its two ends are

$$k_{\text{node}} = \frac{k_i l_e}{2}, \quad c_{\text{node}} = \frac{c_i l_e}{2} \quad i = w, \theta. \quad (4.14)$$

Besides, if the plate is in the  $x$ - $y$  plane, the model size can be reduced by prescribing the 3 DOF – translations in  $x$  and  $y$  direction and rotation about  $z$ -axis – of all nodes to be zero.

Additionally, SHELL281 is also applicable to the plate bending problems. It is based on Mindlin-Reissner (moderately-thick shell) theory like SHELL181, but a quadratic element with 8 nodes, i.e., one mid-side node for each side of the element. Because ANSYS suggests not to define nodal-based elements at faces with mid-side nodes, SHELL281 is not used for simulating the cases associated to elastic restraints/supports but only for the clamped and simply supported cases, which are targeted to demonstrate the influence caused by the

element orders with the software unchanged or by the software environments (ANSYS and COMSOL) with the element type (quadratic element of the Mindlin-Reissner type) unchanged.

### 4.2.3 COMSOL model

In COMSOL, the model is built in 3D space under the ‘Shell’ physics. As set by default, the shell elements are quadratic and of the Mindlin-Reissner type. Meanwhile, the MITC interpolation is selected. It is claimed that the MITC formulation <sup>[200]</sup> enables the elements for both thin (Kirchhoff theory) and thick (Mindlin theory) shells. Unlike in ANSYS, the shell elements in COMSOL use the 3 DOF – shell normals in the  $x$ ,  $y$  and  $z$  directions – instead of the customary rotations against the  $x$ ,  $y$  and  $z$ -axes. Furthermore, the approach to modelling the elastic restraint/support is different. Instead of the spring-damper elements, edge loads are implemented based on Eq. (2.13) or Eq. (2.14). The geometry is meshed using the ‘Mapped’ method, hence the elements are rectangularly shaped.

### 4.2.4 Analytical solutions

Analytical solutions are available (based on the Kirchhoff-Love plate theory) for rectangular plates with simple boundary conditions, such as clamped, simply supported, free and their combinations <sup>[201]</sup>. As will be used to compare with the numerical results, the analytical formulae for the natural frequencies  $\omega_s$  and mode shapes  $W_{mn}(x,y)$  of uniformly clamped and simply supported plates are explicitly given as follows, where the indicators  $m$  and  $n$  are the mode order in the  $x$  and  $y$  directions, respectively.

(a) Simply supported plates:

$$\omega_s = \sqrt{\frac{D}{\rho h} \left[ \left( \frac{m\pi}{a} \right)^2 + \left( \frac{n\pi}{b} \right)^2 \right]}; \quad (4.15)$$

$$W_{mn}(x, y) = A_{mn} \sin\left(\frac{m\pi x}{a}\right) \sin\left(\frac{n\pi y}{b}\right). \quad (4.16)$$

(b) Clamped plates <sup>[201]</sup>:

$$\omega_s^2 = \frac{\pi^4 D}{a^4 \rho h} \left\{ G_x^4 + G_y^4 \left( \frac{a}{b} \right)^4 + 2H_x H_y \left( \frac{a}{b} \right)^2 \right\}, \quad (4.17)$$

with  $G_x$  and  $H_x$  are listed in Table 4-1, and  $G_y$  and  $H_y$  are determined by substituting  $y$  for  $x$  and  $n$  for  $m$ ;

$$W_{mn}(x, y) = A_{mn} X_m(x) Y_n(y), \quad (4.18)$$

where



$$X_m(x) = \sin \gamma \left( \frac{x}{a} - \frac{1}{2} \right) - (-1)^m \frac{\sin(\gamma/2)}{\sinh(\gamma/2)} \sinh \gamma \left( \frac{x}{a} - \frac{1}{2} \right), \quad (4.19)$$

with  $\gamma$  obtained as the  $m^{\text{th}}$  root of  $\tan(\gamma/2) - (-1)^m \tanh(\gamma/2) = 0$ , and  $Y_n(y)$  are obtained from replacing  $x$  by  $y$  and  $m$  by  $n$ .

Equations (4.17)-(4.19) were proposed by Warburton [202]. He used the Rayleigh method to obtain the solutions. As commented by Leissa in [201], the frequency values calculated from Eq. (4.17) yield the upper bounds and the accuracy will decrease for higher order modes.

Table 4-1. Frequency coefficients in Eq. (4.17) for clamped-clamped edges

$m$	$G_x$	$H_x$
1	1.506	1.248
2, 3, 4, ...	$m + \frac{1}{2}$	$\left(m + \frac{1}{2}\right)^2 \left[1 - \frac{2}{\left(m + \frac{1}{2}\right)\pi}\right]$

## 4.2.5 Numerical results

In the following cases, the computational results through all the introduced models are discussed and compared under different edge conditions. The maximum frequency is set as 1000 Hz. The mesh of the FE models is based on the rule of thumb, i.e., no less than either 10 linear or 5 quadratic elements per wavelength. Then, with bending wavelength calculated by

$$\lambda_b = 2\pi \left( \frac{D}{\omega^2 \rho h} \right)^{1/4}, \quad (4.20)$$

the element size is set as 0.02 m for linear elements and 0.04 m for quadratic elements. As an illustration, the FE model with 0.02m-sized elements (ANSYS example) and the FE model with 0.04m-sized elements (COMSOL example) are shown in Fig. 4-2.

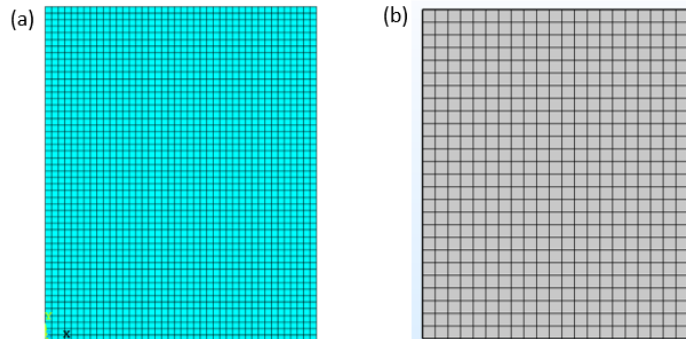


Fig. 4-2. FE models of the rectangular plate: (a) 0.02m-sized linear elements in ANSYS; (b) 0.04m-sized quadratic elements in COMSOL.

#### 4.2.5.1 Simply supported

At first, computations were conducted for the plate with simply supported edges to check the accuracy of different FE models. The natural frequencies were compared for the first 100 modes, of which those smaller than 1000 Hz are listed in Table 4-2. Mode shapes are indicated by  $m$  and  $n$ , which are the mode order (or the number of antinodes) respectively in the  $x$  and  $y$  directions. The analytical results based on Eq. (4.15) are used as reference, denoted as  $f_s^{(Ana)}$ . Then, the error in natural frequency for numerical prediction is defined by

$$Er_f^{(Num)} = f_s^{(Num)} - f_s^{(Ana)}, \quad (4.21)$$

where, ‘Num’ is given as ‘Com’, ‘S63’, ‘S181’ or ‘S281’, corresponding to results from the FE models of COMSOL, ANSYS SHELL63, ANSYS SHELL181 or ANSYS SHELL281, respectively.

Fig. 4-3 shows the errors of different numerical predictions vs the predicting mode order, where the 60<sup>th</sup> natural frequency is closest to 1000 Hz. Through the figure, it can be noticed that the ANSYS model using SHELL181 is problematic, its prediction has been obviously larger than the others since the 20<sup>th</sup> mode and the gap is even manifested as the frequency increases. This phenomenon is caused by the shear locking effect that occurs in FEA when linear elements of regular shape are used. Because the linear element cannot model the curvature inside under bending, a shear stress is introduced, making it appear to be stiffer. But beyond that, the other models yield rather accurate predictions below the upper limit 1000 Hz. When the element size meets the rule of thumb, the results from COMSOL and SHELL281 match very well, and both are very close to the analytical curve. However, if the element density is not sufficient, the COMSOL predictions are shown relatively more accurate than the other. The SHELL281 model tends to overestimate the natural frequencies as the frequency increases, while the SHELL63 model underestimates them. Although SHELL63 is also linear element, stress stiffening and large deflection capabilities are included in default, so unlike the SHELL181 model, the SHELL63 model does not overestimate the natural frequencies.

To sum up, in this case, by comparing the numerical results with the exact solution out of the analytical formula, we can conclude that

- the rule of thumb suggested by the CAE tools is credible;
- the COMSOL model and the ANSYS SHELL281 model yield very accurate predictions, where the former may be better if the elements are not sufficient;
- the ANSYS SHELL63 model yields acceptable accuracy, using instead linear elements and based on the Kirchhoff-Love shell theory.

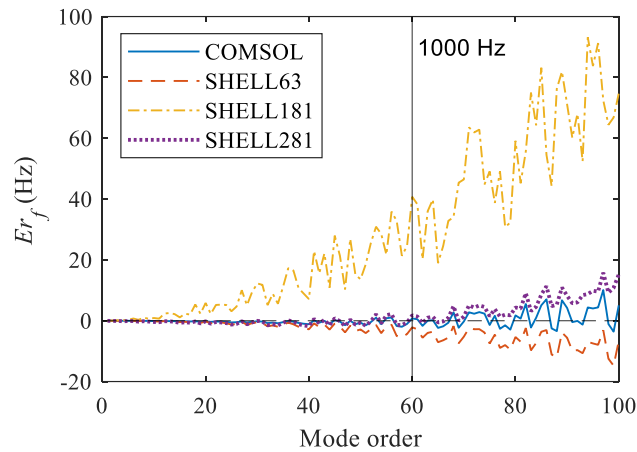


Fig. 4-3. Difference between numerical results and the analytical prediction of the first 100 natural frequencies of the simply supported plate

Table 4-2. Natural frequencies of the simply supported plate predicted by different models and the difference between numerical and analytical results.

Order	Mode		Analytic	COMSOL		SHELL63		SHELL181		SHELL281	
	$m$	$n$	$f_s$ (Hz)	$f_s$ (Hz)	$Er_f$ (Hz)	$f_s$ (Hz)	$Er_f$ (Hz)	$f_s$ (Hz)	$Er_f$ (Hz)	$f_s$ (Hz)	$Er_f$ (Hz)
1	1	1	23.8	23.8	-0.002	23.8	-0.003	23.8	0.000	23.8	-0.044
2	1	2	52.1	52.1	-0.008	52.1	-0.013	52.2	0.043	52.1	-0.085
3	2	1	66.9	66.9	-0.013	66.9	-0.017	67.1	0.124	66.9	-0.073
4	2	2	95.3	95.2	-0.027	95.2	-0.052	95.4	0.111	95.1	-0.195
5	1	3	99.3	99.3	-0.027	99.3	-0.036	99.6	0.292	99.2	-0.117
6	3	1	138.8	138.8	-0.049	138.8	-0.049	139.5	0.721	138.7	-0.109
7	2	3	142.5	142.4	-0.062	142.3	-0.122	142.7	0.278	142.2	-0.312
8	1	4	165.4	165.4	-0.063	165.4	-0.073	166.4	0.997	165.3	-0.163
9	3	2	167.1	167.1	-0.080	167.0	-0.130	167.8	0.630	166.8	-0.290
10	2	4	208.5	208.4	-0.116	208.3	-0.216	209.4	0.884	208.1	-0.416
11	3	3	214.3	214.2	-0.133	214.1	-0.263	215.0	0.667	213.8	-0.503
12	4	1	239.4	239.3	-0.119	239.3	-0.129	241.8	2.351	239.3	-0.169
13	1	5	250.4	250.3	-0.128	250.2	-0.148	252.9	2.522	250.2	-0.208
14	4	2	267.8	267.6	-0.160	267.5	-0.260	269.9	2.160	267.4	-0.380
15	3	4	280.4	280.2	-0.217	280.0	-0.467	281.5	1.093	279.7	-0.717
16	2	5	293.5	293.3	-0.201	293.2	-0.361	295.8	2.279	293.0	-0.521
17	4	3	315.0	314.7	-0.243	314.5	-0.493	317.0	2.027	314.3	-0.673
18	1	6	354.2	354.0	-0.194	354.0	-0.254	359.6	5.336	354.0	-0.234
19	3	5	365.4	365.0	-0.342	364.7	-0.732	367.7	2.278	364.5	-0.902
20	5	1	368.8	368.6	-0.197	368.5	-0.267	374.6	5.833	368.6	-0.187
21	4	4	381.0	380.7	-0.377	380.2	-0.827	383.3	2.223	380.1	-0.987
22	5	2	397.1	396.9	-0.269	396.6	-0.479	402.3	5.181	396.7	-0.429
23	2	6	397.4	397.1	-0.307	396.8	-0.567	402.6	5.283	396.8	-0.587
24	5	3	444.3	443.9	-0.391	443.5	-0.831	449.5	5.179	443.5	-0.781
25	4	5	466.0	465.4	-0.562	464.7	-1.272	469.1	3.098	464.7	-1.282
26	3	6	469.2	468.7	-0.498	468.1	-1.088	473.9	4.672	468.2	-1.048
27	1	7	477.0	476.7	-0.232	476.6	-0.412	487.0	10.028	476.8	-0.172
28	5	4	510.4	509.8	-0.585	509.1	-1.325	515.5	5.075	509.2	-1.185

Table 4-2 (Continued). Natural frequencies of the simply supported plate predicted by different models and the difference between numerical and analytical results.

Order	Mode		Analytic	COMSOL		SHELL63		SHELL181		SHELL281	
	<i>m</i>	<i>n</i>	$f_s$ (Hz)	$f_s$ (Hz)	$Er_f$ (Hz)	$f_s$ (Hz)	$Er_f$ (Hz)	$f_s$ (Hz)	$Er_f$ (Hz)	$f_s$ (Hz)	$Er_f$ (Hz)
29	2	7	520.1	519.7	-0.374	519.3	-0.834	529.5	9.446	519.5	-0.564
30	6	1	526.9	526.7	-0.184	526.4	-0.504	539.2	12.246	526.9	-0.034
31	6	2	555.2	554.9	-0.295	554.4	-0.805	567.0	11.785	554.9	-0.305
32	4	6	569.8	569.1	-0.788	568.0	-1.838	575.0	5.122	568.3	-1.508
33	3	7	592.0	591.3	-0.626	590.4	-1.546	600.8	8.874	590.9	-1.086
34	5	5	595.4	594.5	-0.840	593.4	-1.990	600.9	5.560	593.8	-1.550
35	6	3	602.4	602.0	-0.478	601.1	-1.298	613.6	11.182	601.7	-0.708
36	1	8	618.6	618.4	-0.140	617.9	-0.640	635.9	17.280	618.7	0.110
37	2	8	661.7	661.4	-0.323	660.5	-1.183	678.2	16.497	661.4	-0.313
38	6	4	668.5	667.8	-0.742	666.5	-2.002	679.2	10.708	667.4	-1.152
39	4	7	692.6	691.6	-1.005	690.0	-2.535	701.5	8.895	691.0	-1.565
40	5	6	699.2	698.1	-1.156	696.4	-2.826	706.3	7.114	697.4	-1.796
41	7	1	713.8	713.9	0.091	712.9	-0.869	736.7	22.921	714.4	0.581
42	3	8	733.6	732.9	-0.654	731.5	-2.104	749.1	15.566	732.7	-0.864
43	7	2	742.1	742.1	-0.051	740.8	-1.271	764.2	22.109	742.4	0.269
44	6	5	753.5	752.4	-1.087	750.6	-2.927	764.4	10.893	752.0	-1.527
45	1	9	779.1	779.3	0.221	778.1	-0.939	807.0	27.951	779.9	0.811
46	7	3	789.3	789.0	-0.303	787.4	-1.933	810.7	21.377	789.1	-0.163
<b>47</b>	<b>5</b>	<b>7</b>	821.9	820.5	-1.484	818.1	-3.834	832.3	10.316	820.2	-1.794
<b>48</b>	<b>2</b>	<b>9</b>	822.2	822.2	-0.022	820.6	-1.632	849.1	26.918	822.5	0.358
49	4	8	834.2	833.1	-1.134	830.8	-3.384	849.3	15.086	832.9	-1.324
<b>50</b>	<b>7</b>	<b>4</b>	855.4	854.7	-0.657	852.5	-2.877	869.0	13.643	854.8	-0.597
<b>51</b>	<b>6</b>	<b>6</b>	857.3	855.8	-1.523	853.3	-4.073	875.9	18.527	855.7	-1.683
52	3	9	894.1	893.6	-0.443	891.3	-2.773	919.7	25.597	893.9	-0.193
53	8	1	929.4	930.4	0.997	928.0	-1.403	960.3	30.887	931.5	2.127
54	7	5	940.4	939.2	-1.132	936.3	-4.102	968.9	28.528	939.5	-0.892
55	8	2	957.7	958.5	0.796	955.8	-1.914	979.4	21.696	959.5	1.796
56	1	10	958.4	959.5	1.060	957.1	-1.330	994.3	35.840	960.7	2.230
57	5	8	963.6	961.8	-1.752	958.5	-5.042	996.4	32.798	962.2	-1.372
58	6	7	980.1	978.1	-1.990	974.6	-5.460	1001.4	21.340	978.6	-1.450
59	4	9	994.7	993.6	-1.053	990.3	-4.383	1019.2	24.527	994.1	-0.553
60	2	10	1001.6	1002.3	0.747	999.4	-2.183	1042.3	40.747	1003.3	1.747

#### 4.2.5.2 Clamped

Secondly, the plate with clamped edges is analysed, with also the first 100 natural frequencies and mode shapes are compared. Table 4-3 lists natural frequencies that smaller than 1000 Hz. Similarly, the analytical results are used as reference, but in contrast to the simply supported case, Eq. (4.17) is an approximate solution and probably overestimates the true values. However, we can still use Eq. (4.21) with the same denotations to calculate the difference between numerical and analytical results.

Fig. 4-4 shows the comparison among different models. Through the figure, it can be seen that the three models, COMSOL, SHELL63 and SHELL281, agree very well in the first 30 modes, where the analytical results are seen overestimated. Afterwards, the three curves separate under the same trend as they are presented in the previous case (see Section 4.2.5.1, Fig. 4-3).

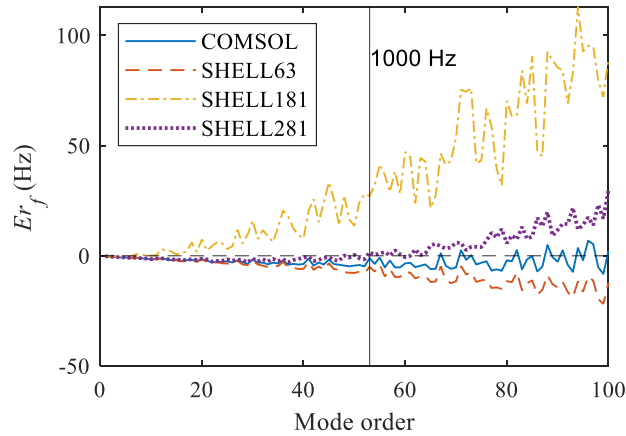


Fig. 4-4. Difference between numerical results and the analytical prediction for the first 100 natural frequencies of the clamped plate.

Table 4-3. Natural frequencies of the clamped plate predicted by different models and the difference between numerical and analytical results.

Order	Mode		Analytic	COMSOL		SHELL63		SHELL181		SHELL281	
	$m$	$n$	$f_s$ (Hz)	$f_s$ (Hz)	$Er_f$ (Hz)	$f_s$ (Hz)	$Er_f$ (Hz)	$f_s$ (Hz)	$Er_f$ (Hz)	$f_s$ (Hz)	$Er_f$ (Hz)
1	1	1	44.1	43.9	-0.188	43.9	-0.192	44.0	-0.137	43.9	-0.187
2	1	2	78.2	77.8	-0.413	77.8	-0.425	78.0	-0.245	77.8	-0.410
3	2	1	100.5	100.0	-0.495	100.0	-0.495	100.4	-0.105	100.1	-0.485
4	2	2	132.1	131.3	-0.779	131.2	-0.829	131.7	-0.389	131.3	-0.769
5	1	3	133.5	132.8	-0.745	132.8	-0.755	133.4	-0.105	132.8	-0.735
6	2	3	184.7	183.6	-1.075	183.5	-1.175	184.4	-0.345	183.7	-1.035
7	3	1	186.7	185.9	-0.845	185.9	-0.845	187.4	0.675	185.9	-0.825
8	1	4	208.6	207.4	-1.151	207.4	-1.161	209.2	0.649	207.4	-1.121
9	3	2	217.2	215.9	-1.299	215.8	-1.389	217.3	0.111	215.9	-1.259
10	2	4	258.1	256.4	-1.656	256.3	-1.806	258.1	0.064	256.5	-1.566
11	3	3	267.7	266.3	-1.354	266.1	-1.554	267.8	0.186	266.4	-1.244
12	4	1	301.8	300.6	-1.204	300.6	-1.224	304.7	2.936	300.6	-1.144
13	1	5	302.8	301.3	-1.492	301.3	-1.512	305.3	2.538	301.4	-1.422
14	4	2	331.9	329.9	-2.007	329.8	-2.157	333.9	1.913	330.1	-1.887
15	3	4	338.9	337.2	-1.659	336.9	-2.019	339.5	0.601	337.5	-1.429
16	2	5	351.3	349.0	-2.366	348.8	-2.596	352.8	1.424	349.2	-2.176
17	4	3	381.3	379.3	-1.997	378.9	-2.357	383.1	1.813	379.6	-1.747
18	1	6	416.0	414.2	-1.829	414.1	-1.919	422.0	6.021	414.3	-1.679
19	3	5	430.5	428.2	-2.272	427.7	-2.832	432.2	1.758	428.7	-1.832
20	5	1	445.6	444.1	-1.492	444.0	-1.642	453.0	7.318	444.3	-1.332

Table 4-3 (Continued). Natural frequencies of the clamped plate predicted by different models and the difference between numerical and analytical results.

Order	Mode		Analytic	COMSOL		SHELL63		SHELL181		SHELL281	
	<i>m</i>	<i>n</i>	$f_s$ (Hz)	$f_s$ (Hz)	$Er_f$ (Hz)	$f_s$ (Hz)	$Er_f$ (Hz)	$f_s$ (Hz)	$Er_f$ (Hz)	$f_s$ (Hz)	$Er_f$ (Hz)
21	4	4	450.9	448.7	-2.152	448.1	-2.782	453.3	2.388	449.2	-1.652
<b>22</b>	<b>2</b>	<b>6</b>	464.1	461.0	-3.027	460.7	-3.397	468.5	4.403	461.4	-2.667
<b>23</b>	<b>5</b>	<b>2</b>	475.8	473.1	-2.643	472.8	-2.973	481.9	6.147	473.4	-2.363
24	5	3	524.6	521.8	-2.813	521.2	-3.443	530.2	5.637	522.3	-2.283
25	4	5	540.8	538.3	-2.534	537.3	-3.504	543.9	3.036	539.2	-1.604
26	3	6	542.0	539.0	-3.047	538.1	-3.867	546.3	4.303	539.7	-2.257
27	1	7	548.2	546.1	-2.062	545.8	-2.342	560.0	11.788	546.4	-1.742
28	5	4	593.1	590.3	-2.889	589.2	-3.929	598.7	5.591	591.2	-1.909
29	2	7	595.9	592.3	-3.671	591.6	-4.311	605.5	9.569	592.9	-3.031
30	6	1	618.2	616.6	-1.620	616.1	-2.150	634.2	16.010	617.0	-1.220
31	6	2	648.5	645.3	-3.156	644.5	-3.966	656.1	7.614	645.9	-2.546
32	4	6	650.9	647.8	-3.121	646.4	-4.501	662.5	11.649	649.3	-1.551
33	3	7	673.1	669.2	-3.890	667.9	-5.130	681.9	8.870	670.5	-2.590
34	5	5	681.8	678.6	-3.128	677.1	-4.678	688.0	6.262	680.4	-1.378
35	6	3	697.0	693.5	-3.500	692.4	-4.680	710.1	13.020	694.6	-2.470
36	1	8	699.2	697.1	-2.099	696.4	-2.819	719.8	20.581	697.8	-1.489
37	2	8	746.9	742.8	-4.076	741.6	-5.256	764.6	17.774	743.9	-2.996
38	6	4	765.0	761.3	-3.694	759.6	-5.434	777.4	12.456	763.1	-1.904
39	4	7	780.8	776.8	-4.000	774.8	-6.020	790.1	9.350	779.3	-1.460
40	5	6	790.5	786.7	-3.728	784.5	-5.938	798.4	7.882	789.6	-0.838
41	7	1	819.5	818.2	-1.322	816.7	-2.812	840.0	20.438	819.1	-0.442
42	3	8	823.4	818.9	-4.500	817.0	-6.410	849.0	25.610	821.0	-2.410
43	7	2	849.9	846.8	-3.063	845.0	-4.863	865.2	15.277	848.0	-1.863
44	6	5	852.7	848.7	-3.988	846.2	-6.438	877.0	24.302	851.7	-0.958
45	1	9	869.2	867.4	-1.758	865.8	-3.368	902.5	33.312	868.5	-0.658
46	7	3	898.4	894.6	-3.780	892.3	-6.100	923.8	25.430	896.5	-1.930
<b>47</b>	<b>2</b>	<b>9</b>	916.8	912.7	-4.081	910.5	-6.241	930.6	13.809	914.5	-2.311
<b>48</b>	<b>5</b>	<b>7</b>	919.1	914.7	-4.456	911.6	-7.496	946.5	27.374	919.3	0.154
49	4	8	930.2	925.4	-4.792	922.5	-7.702	946.7	16.478	929.4	-0.882
<b>50</b>	<b>6</b>	<b>6</b>	960.3	955.8	-4.480	952.5	-7.800	973.9	13.590	960.8	0.500
<b>51</b>	<b>7</b>	<b>4</b>	966.0	961.8	-4.194	958.8	-7.224	990.3	24.246	964.9	-1.164
52	3	9	993.0	988.1	-4.831	985.1	-7.871	1020.9	27.949	991.3	-1.631

So far, the simply supported and clamped cases may prove that using the default shell elements in COMSOL and the SHELL63 and SHELL281 elements in ANSYS will obtain consistent results as long as the mesh density is sufficient and the frequency is not too high. In addition, the two cases also demonstrate the discrepancy in the values of natural frequencies between the simply supported and clamped boundary conditions, as shown by Table 4-2 and Table 4-3. The discrepancy is not so small and about 20 Hz for the first mode. The absolute discrepancy and relative difference (limited for the first 50 modes) are plotted in Fig. 4-5, where the clamped results are obtained from COMSOL and used as denominators in the calculation of relative values. By comparison, it can be observed that

the absolute value increases with the mode order while the relative value is decreasing. Meanwhile, it should be noticed that for most modes, the combinations of  $m$  and  $n$  are the same for the same mode order, but there are some modes whose combinations  $(m,n)$  are different between two cases. In Table 4-2 and Table 4-3, these modes are bolded, i.e., 6<sup>th</sup>-7<sup>th</sup>, 22<sup>nd</sup>-23<sup>rd</sup>, 47<sup>th</sup>-48<sup>th</sup>, 50<sup>th</sup>-51<sup>st</sup> modes.

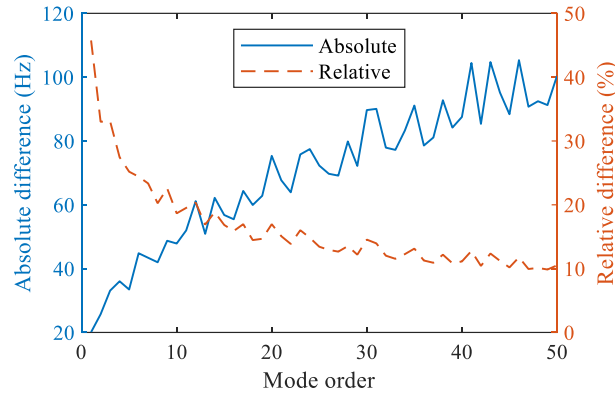


Fig. 4-5. Absolute and relative differences in natural frequencies between the simply supported and the clamped boundary conditions.

#### 4.2.5.3 Rigidly supported but elastically restrained against rotation

With the above validations of the FE models, the plate with the partial-elastically restrained edge conditions, i.e., rigidly supported but elastically restrained against rotation, is analysed via COMSOL using the default shell elements and via ANSYS using SHELL63, respectively. The modelling techniques are introduced in Sections 4.2.2-4.2.3. At the beginning, damping effect is ignored, and three rotational stiffnesses are considered:

$$c_{\theta} = 0, k_{\theta} = 10^3, 10^4 \text{ or } 10^5 \text{ N/rad.} \quad (4.22)$$

The first 50 modes are listed in Table 4-4. The difference in natural frequencies between SHELL63 model and COMSOL model is determined by

$$Er_f = f_{s,S} - f_{s,C}, \quad (4.23)$$

where,  $f_{s,S}$  and  $f_{s,C}$  denote the natural frequencies predicted by the SHELL63 ANSYS model and the COMSOL model, respectively. As can be seen from the table, though the modelling strategies of the elastic restraints are different in ANSYS and COMSOL. The difference between two predictions is very small, which is less than 1 Hz for the first 30 modes. The prediction from SHELL63 is slightly smaller, and as the frequency increases, the discrepancy enlarges, which are the same phenomena as we observed in the previous two cases. Accordingly, it is probably that the discrepancy is mainly raised by the shell elements that model the plate instead of the different strategies that model the edge conditions. To confirm the hypothesis that the results from SHELL63 model with finer mesh will better

matches the COMSOL results, an additional modal analysis was performed using 0.015m-sized SHELL63 elements for the case  $k_\theta = 10^4$  N/rad. The errors of the SHELL63 models before and after refinement are compared in Fig. 4-6, which validates the hypothesis. This further confirms that the COMSOL model has better convergence, while it can be indicated from Fig. 4-3 and Fig. 4-4.

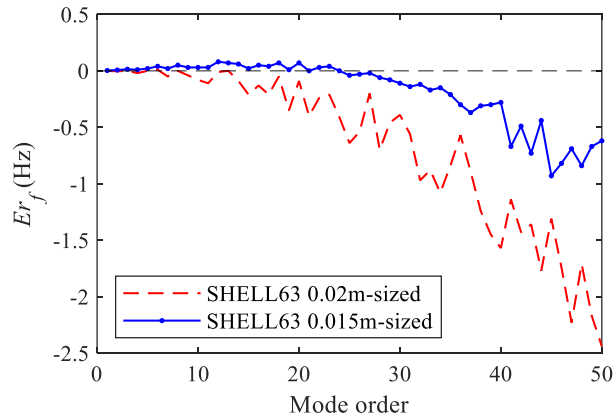


Fig. 4-6. Difference of natural frequencies between SHELL63 and COMSOL models for the plate with edge restraint stiffness  $k_\theta = 10^4$  N/rad.

For comparing changes of natural frequencies caused by different restraint stiffness  $k_\theta$ , all predictions from SHELL63 (0.02m-sized) and COMSOL models are subtracted by the analytical results of the simply supported plate ( $k_\theta = 0$ ):

$$\Delta f_s = f_{s,k_\theta} - f_{s,0}. \quad (4.24)$$

Included the clamped case  $k_\theta = \infty$ , the subtracted natural frequencies  $\Delta f_s$  are plotted for the plate with  $k_\theta = 0, 10^3, 10^4, 10^5$  or  $\infty$  N/rad in Fig. 4-7. The figure clearly demonstrates that the natural frequencies increase with the edge restraints becoming stiffer.

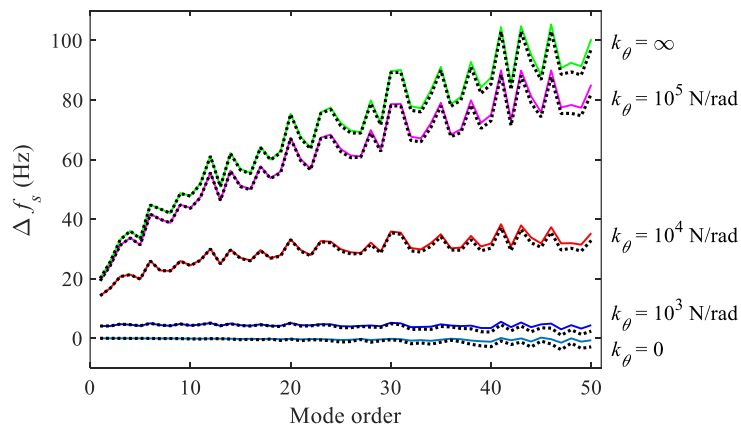


Fig. 4-7. Natural frequencies subtracted by the analytical prediction of the simply supported plate ( $k_\theta = 0$ ), respectively for the plate with  $k_\theta = 0, 10^3, 10^4, 10^5$  or  $\infty$  N/rad. Results are from two FE models: COMSOL (solid lines); SHELL63 (dotted lines).



Table 4-4. Natural frequencies of the plate with different rotational stiffness along the restrained edges, and the difference ( $Er_f$ ) between SHELL63 ( $f_{s,s}$ ) and COMSOL ( $f_{s,c}$ ) predictions.

Order	$k_\theta = 10^3$ N/rad					$k_\theta = 10^4$ N/rad					$k_\theta = 10^5$ N/rad				
	$m$	$n$	$f_{s,c}$ (Hz)	$f_{s,s}$ (Hz)	$Er_f$ (Hz)	$m$	$n$	$f_{s,c}$ (Hz)	$f_{s,s}$ (Hz)	$Er_f$ (Hz)	$m$	$n$	$f_{s,c}$ (Hz)	$f_{s,s}$ (Hz)	$Er_f$ (Hz)
1	1	1	27.9	27.9	0.006	1	1	38.1	38.1	-0.001	1	1	43.1	43.1	-0.004
2	1	2	56.2	56.3	0.010	1	2	68.9	68.9	-0.004	1	2	76.5	76.5	-0.010
3	2	1	71.7	71.7	0.009	2	1	87.6	87.6	0.000	2	1	98.2	98.2	-0.004
4	2	2	99.8	99.8	0.010	2	2	116.6	116.6	-0.020	2	2	129.0	128.9	-0.040
5	1	3	103.5	103.5	0.010	1	3	119.2	119.2	0.000	1	3	130.7	130.7	-0.010
<b>6</b>	<b>3</b>	<b>1</b>	143.8	143.8	0.010	<b>3</b>	<b>1</b>	164.8	164.8	0.010	<b>2</b>	<b>3</b>	180.6	180.5	-0.090
<b>7</b>	<b>2</b>	<b>3</b>	146.9	146.9	0.000	<b>2</b>	<b>3</b>	165.2	165.2	-0.050	<b>3</b>	<b>1</b>	182.4	182.4	0.000
8	1	4	169.6	169.6	0.010	1	4	188.0	188.0	0.000	1	4	204.2	204.2	-0.010
9	3	2	172.0	172.0	0.000	3	2	193.1	193.0	-0.040	3	2	212.0	211.9	-0.080
10	2	4	212.9	212.8	-0.030	2	4	233.0	232.9	-0.080	2	4	252.3	252.2	-0.140
11	3	3	218.9	218.9	-0.050	3	3	240.6	240.5	-0.110	3	3	261.7	261.5	-0.180
12	4	1	244.5	244.5	0.000	4	1	269.5	269.4	-0.010	4	1	295.0	295.0	-0.020
13	1	5	254.6	254.6	0.010	1	5	275.4	275.4	0.000	1	5	296.7	296.7	-0.020
14	4	2	272.7	272.6	-0.050	4	2	297.5	297.4	-0.090	4	2	324.0	323.9	-0.130
15	3	4	284.8	284.7	-0.130	3	4	307.4	307.2	-0.210	3	4	331.7	331.3	-0.330
16	2	5	297.7	297.6	-0.080	2	5	319.6	319.5	-0.130	2	5	343.5	343.3	-0.220
17	4	3	319.6	319.5	-0.140	4	3	344.6	344.3	-0.210	4	3	372.7	372.4	-0.330
18	1	6	358.4	358.4	-0.040	1	6	381.2	381.1	-0.050	1	6	408.0	407.9	-0.080
19	3	5	369.6	369.3	-0.240	3	5	393.3	392.9	-0.350	3	5	421.4	420.9	-0.510
20	5	1	373.9	373.9	-0.060	5	1	402.0	401.9	-0.090	5	1	436.0	435.9	-0.130
21	4	4	385.4	385.1	-0.280	4	4	410.7	410.3	-0.400	4	4	441.2	440.6	-0.570
<b>22</b>	<b>2</b>	<b>6</b>	401.5	401.3	-0.180	<b>2</b>	<b>6</b>	425.0	424.8	-0.240	<b>2</b>	<b>6</b>	454.0	453.7	-0.340
<b>23</b>	<b>5</b>	<b>2</b>	402.1	401.9	-0.160	<b>5</b>	<b>2</b>	430.0	429.8	-0.210	<b>5</b>	<b>2</b>	464.7	464.4	-0.300
24	5	3	449.0	448.7	-0.320	5	3	476.8	476.4	-0.410	5	3	512.7	512.1	-0.580
25	4	5	470.1	469.6	-0.500	4	5	495.9	495.3	-0.640	4	5	529.6	528.7	-0.890
26	3	6	473.2	472.8	-0.430	3	6	498.1	497.6	-0.540	3	6	530.6	529.8	-0.750
27	1	7	481.1	481.0	-0.170	1	7	505.6	505.4	-0.200	1	7	538.0	537.7	-0.260
28	5	4	514.7	514.2	-0.560	5	4	542.5	541.8	-0.700	5	4	580.3	579.3	-0.950
29	2	7	524.1	523.7	-0.380	2	7	549.2	548.7	-0.460	2	7	583.4	582.8	-0.600
30	6	1	532.1	531.8	-0.310	6	1	562.8	562.4	-0.390	6	1	605.5	605.0	-0.500
31	6	2	560.2	559.8	-0.460	6	2	590.7	590.1	-0.560	6	2	633.9	633.1	-0.740
32	4	6	573.6	572.8	-0.810	4	6	600.2	599.2	-0.970	4	6	637.5	636.3	-1.290
33	3	7	595.8	595.0	-0.730	3	7	621.8	620.9	-0.880	3	7	659.0	657.9	-1.140
34	5	5	599.3	598.4	-0.900	5	5	627.3	626.2	-1.080	5	5	667.5	666.1	-1.420
35	6	3	607.1	606.4	-0.710	6	3	637.4	636.5	-0.840	6	3	681.5	680.4	-1.100
36	1	8	622.9	622.4	-0.490	1	8	648.8	648.2	-0.570	1	8	686.9	686.2	-0.690
37	2	8	665.8	665.0	-0.780	2	8	692.1	691.3	-0.890	2	8	731.8	730.7	-1.110
38	6	4	672.8	671.7	-1.060	6	4	702.9	701.6	-1.240	6	4	748.4	746.8	-1.600
39	4	7	696.0	694.8	-1.260	4	7	723.4	721.9	-1.450	4	7	764.9	763.0	-1.860
40	5	6	702.7	701.3	-1.360	5	6	731.0	729.5	-1.570	5	6	774.2	772.2	-2.020
41	7	1	719.3	718.4	-0.980	7	1	752.1	750.9	-1.140	7	1	803.7	802.3	-1.420
42	3	8	737.3	736.1	-1.260	3	8	764.4	763.0	-1.430	3	8	806.8	805.0	-1.780
43	7	2	747.4	746.2	-1.180	7	2	780.0	778.6	-1.360	7	2	832.0	830.3	-1.700
44	6	5	757.2	755.7	-1.550	6	5	787.3	785.5	-1.770	6	5	834.7	832.5	-2.250
45	1	9	783.7	782.6	-1.160	1	9	810.9	809.6	-1.310	1	9	854.9	853.3	-1.540
46	7	3	794.2	792.7	-1.520	7	3	826.6	824.8	-1.740	7	3	879.2	877.0	-2.170
<b>47</b>	<b>5</b>	<b>7</b>	825.0	823.0	-1.990	<b>5</b>	<b>7</b>	853.8	851.6	-2.230	<b>2</b>	<b>9</b>	899.4	897.4	-2.040
<b>48</b>	<b>2</b>	<b>9</b>	826.6	825.1	-1.530	<b>2</b>	<b>9</b>	854.1	852.4	-1.710	<b>5</b>	<b>7</b>	900.5	897.7	-2.800
49	4	8	837.4	835.5	-1.940	4	8	865.6	863.4	-2.170	4	8	911.6	908.9	-2.690
<b>50</b>	<b>7</b>	<b>4</b>	859.8	857.8	-2.010	<b>6</b>	<b>6</b>	890.7	888.2	-2.440	<b>6</b>	<b>6</b>	940.5	937.4	-3.070

Next, the damping effect  $c_w \neq 0$  is considered. Based on the models with  $k_\theta = 10^4$  N/rad,  $c_\theta = 0, 0.1$  or  $1$  N·s/rad is introduced. The natural frequencies  $f_s$  and modal damping ratios  $\zeta_s$  of the first 50 modes are listed in Table 4-5. The case  $k_\theta = 10^4$  N/rad,  $c_\theta = 1$  N·s/rad is simulated both in COMSOL and ANSYS SHELL63 for modal analysis, validating that the two models yield consistent results in the damped situations. Meanwhile, a trend can be observed that the modal damping ratios are increasing with the frequency. To be more precise, the increase is not monotonous but with fluctuations related to the mode shape. For example, at the 17<sup>th</sup> mode, the damping ratio reaches a local maximum.

Then, the case  $k_\theta = 10^4$  N/rad,  $c_\theta = 1$  N·s/rad is further analysed in COMSOL. Comparison of the two cases in the table illustrates that the natural frequencies  $f_s$  have quite limited change and slightly increase as the damping coefficient  $c_\theta$  increases. Besides, the change of modal damping ratios  $\zeta_s$  is almost proportional to the variation of the rotational damping coefficient  $c_\theta$ . Furthermore, in order to demonstrate the damping effect on the frequency response of the plate, the FRFs  $w_1/F$  are calculated via COMSOL by frequency domain analysis for  $k_\theta = 10^4$  N/rad and  $c_\theta$  respectively equals to 0, 0.1 and  $1$  N·s·rad<sup>-2</sup>. The excitation is given by  $F = 1$  N at intervals of 1 Hz within 10-900 Hz. Fig. 4-8 shows the comparison of the frequency responses. Through the figure and the damping ratios  $\zeta_s$  in Table 4-5, it is found that the damping effect becomes noticeable from the frequency response function since  $\zeta_s \approx 0.01$ .

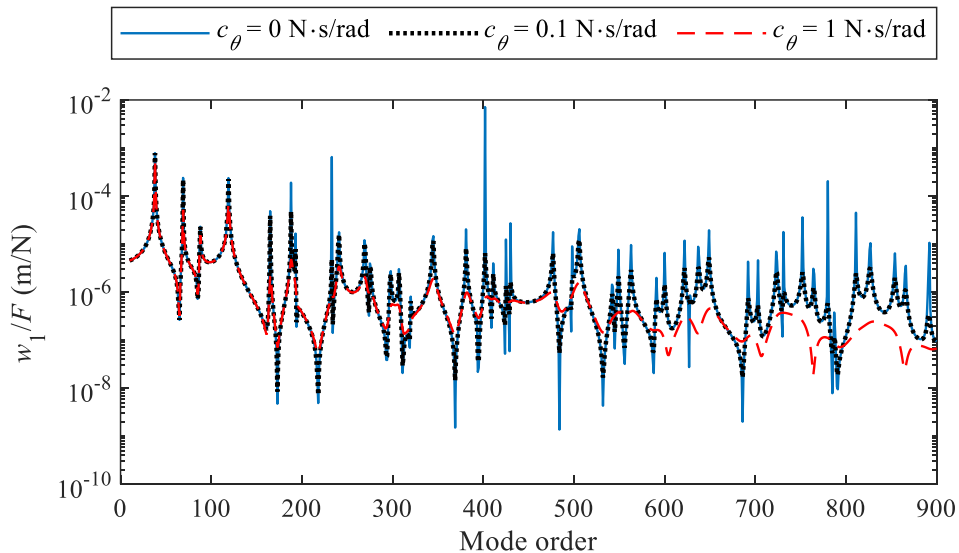


Fig. 4-8. FRFs of plate with  $k_\theta = 10^4$  N/rad and different  $c_\theta$ .

Table 4-5. Natural frequencies and modal damping ratios of plate with  $k_\theta = 10^4$  N/rad and different  $c_\theta$ .

Order	Mode		$c_\theta = 0.1 \text{ N} \cdot \text{s/rad}$				$c_\theta = 1 \text{ N} \cdot \text{s/rad}$	
			SHELL63		COMSOL		COMSOL	
	$m$	$n$	$f_s$ (Hz)	$\zeta_s$	$f_s$ (Hz)	$\zeta_s$	$f_s$ (Hz)	$\zeta_s$
1	1	1	38.1	2.55E-04	38.1	2.55E-04	38.1	2.55E-03
2	1	2	68.9	3.63E-04	68.9	3.63E-04	69.0	3.63E-03
3	2	1	87.6	4.87E-04	87.6	4.87E-04	87.7	4.87E-03
4	2	2	116.6	5.45E-04	116.6	5.46E-04	116.7	5.45E-03
5	1	3	119.2	5.11E-04	119.2	5.12E-04	119.2	5.11E-03
6	3	1	164.8	7.41E-04	164.8	7.41E-04	164.8	7.40E-03
7	2	3	165.2	6.41E-04	165.2	6.43E-04	165.3	6.41E-03
8	1	4	188.0	6.68E-04	188.0	6.68E-04	188.1	6.66E-03
9	3	2	193.0	7.69E-04	193.1	7.71E-04	193.2	7.68E-03
10	2	4	232.9	7.60E-04	233.0	7.62E-04	233.1	7.58E-03
11	3	3	240.5	8.22E-04	240.6	8.25E-04	240.8	8.21E-03
12	4	1	269.5	9.83E-04	269.5	9.83E-04	269.6	9.78E-03
13	1	5	275.4	8.21E-04	275.4	8.22E-04	275.5	8.17E-03
14	4	2	297.4	9.94E-04	297.5	9.96E-04	297.7	9.90E-03
15	3	4	307.2	8.99E-04	307.4	9.03E-04	307.6	8.97E-03
16	2	5	319.5	8.85E-04	319.7	8.88E-04	319.9	8.81E-03
17	4	3	344.3	1.02E-03	344.6	1.02E-03	344.9	1.02E-02
18	1	6	381.1	9.63E-04	381.2	9.64E-04	381.5	9.55E-03
19	3	5	392.9	9.90E-04	393.3	9.95E-04	393.7	9.85E-03
20	5	1	401.9	1.20E-03	402.0	1.20E-03	402.5	1.19E-02
21	4	4	410.3	1.06E-03	410.7	1.07E-03	411.1	1.06E-02
22	2	6	424.8	1.01E-03	425.1	1.01E-03	425.5	1.00E-02
23	5	2	429.8	1.20E-03	430.0	1.21E-03	430.5	1.19E-02
24	5	3	476.4	1.21E-03	476.8	1.22E-03	477.4	1.20E-02
25	4	5	495.3	1.12E-03	495.9	1.13E-03	496.6	1.12E-02
26	3	6	497.6	1.09E-03	498.1	1.09E-03	498.7	1.08E-02
27	1	7	505.4	1.09E-03	505.6	1.09E-03	506.2	1.08E-02
28	5	4	541.8	1.24E-03	542.5	1.24E-03	543.4	1.22E-02
29	2	7	548.7	1.13E-03	549.2	1.13E-03	550.0	1.11E-02
30	6	1	562.4	1.39E-03	562.8	1.40E-03	563.7	1.38E-02
31	6	2	590.1	1.39E-03	590.7	1.40E-03	591.8	1.37E-02
32	4	6	599.2	1.19E-03	600.2	1.20E-03	601.1	1.18E-02
33	3	7	620.9	1.18E-03	621.8	1.19E-03	622.8	1.17E-02
34	5	5	626.2	1.27E-03	627.3	1.28E-03	628.4	1.26E-02
35	6	3	636.5	1.39E-03	637.4	1.40E-03	638.6	1.37E-02
36	1	8	648.2	1.21E-03	648.8	1.21E-03	649.9	1.19E-02
37	2	8	691.3	1.23E-03	692.2	1.24E-03	693.4	1.21E-02
38	6	4	701.7	1.40E-03	702.9	1.41E-03	704.4	1.38E-02
39	4	7	721.9	1.27E-03	723.4	1.28E-03	724.8	1.25E-02
40	5	6	729.5	1.31E-03	731.1	1.33E-03	732.5	1.29E-02
41	7	1	751.0	1.56E-03	752.1	1.57E-03	753.9	1.54E-02
42	3	8	763.0	1.28E-03	764.5	1.29E-03	766.0	1.26E-02
43	7	2	778.7	1.56E-03	780.0	1.57E-03	781.9	1.53E-02
44	6	5	785.6	1.42E-03	787.3	1.43E-03	789.1	1.39E-02
45	1	9	809.6	1.31E-03	810.9	1.32E-03	812.7	1.29E-02
46	7	3	824.9	1.55E-03	826.6	1.56E-03	828.7	1.53E-02
47	5	7	851.6	1.37E-03	853.8	1.38E-03	855.8	1.34E-02
48	2	9	852.4	1.33E-03	854.1	1.34E-03	856.1	1.31E-02
49	4	8	863.5	1.34E-03	865.6	1.36E-03	867.6	1.32E-02
50	6	6	888.2	1.44E-03	890.7	1.46E-03	893.0	1.41E-02

#### 4.2.5.4 Elastically restrained against translation and rotation

As the last case considering the 2D plate model, the plate with general-elastically restrained edge conditions is analysed. The translational and rotational restraint stiffnesses are respectively given by  $k_w = 10^6 \text{ N/m}^2$  and  $k_\theta = 10^4 \text{ N/rad}$ . On one hand, this case is to validate the edge modelling strategy in the ANSYS and COMSOL FE models, referring to the translational stiffness. As shown by Table 4-6, the natural frequencies predicted by the two models agree well, and the difference is less than 1 Hz for the first 60 modes. The denotations  $f_{s,s}$ ,  $f_{s,c}$  and  $Er_f$  have been defined in Eq. (4.23), where  $f_{s,s}$  is for the ANSYS model with SHELL63 elements, and  $f_{s,c}$  is for the COMSOL model. On the other hand, the influence by the flexibility of the edge supports can be illustrated. Compared with the case  $k_\theta = 10^4 \text{ N/rad}$  in Section 4.2.5.3, the translational stiffness  $k_w$  in this case is reduced from  $\infty$  to  $10^6 \text{ N/m}^2$ . Correspondingly, the natural frequencies decrease. As illustrated by Table 4-6 and Table 4-4, the first natural frequency is reduced from 38.1 Hz to 35.3 Hz. For comparison, the variations are calculated for each mode and plotted in Fig. 4-9. The higher the mode order is, the larger the variation becomes. Moreover, the mode shape is visually changed more significant as the mode order increase. The first 4 mode shapes are compared in Fig. 4-10 as examples, where the displacement along the plate edges is clearly observed in the latter case.

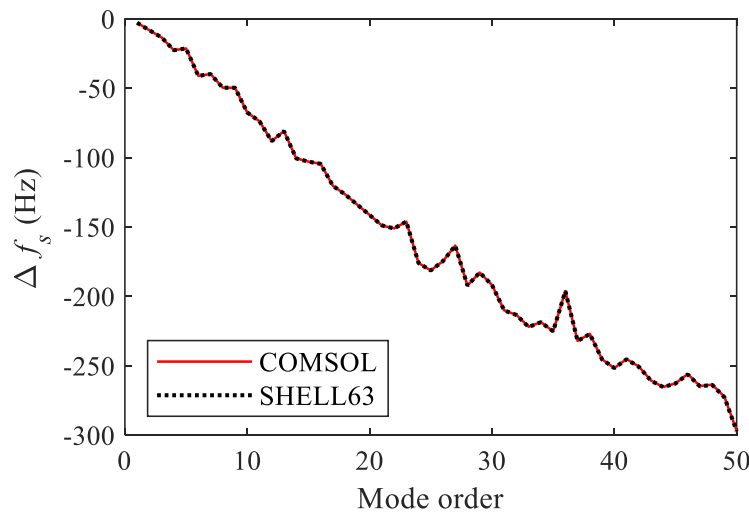


Fig. 4-9. Variation of natural frequencies between the plate with  $k_w = 10^6 \text{ N/m}^2$ ,  $k_\theta = 10^4 \text{ N/rad}$  and the plate with  $k_w = \infty$ ,  $k_\theta = 10^4 \text{ N/rad}$ .

Table 4-6. Natural frequencies of the plate with edges elastically restrained against translation ( $k_w = 10^6$  N/m<sup>2</sup>) and rotation ( $k_\theta = 10^4$  N/rad), and the difference ( $Er_f$ ) between SHELL63 ( $f_{s,s}$ ) and COMSOL ( $f_{s,c}$ ) predictions.

Order	$f_{s,c}$ (Hz)	$f_{s,s}$ (Hz)	$Er_f$ (Hz)	Order	$f_{s,c}$ (Hz)	$f_{s,s}$ (Hz)	$Er_f$ (Hz)	Order	$f_{s,c}$ (Hz)	$f_{s,s}$ (Hz)	$Er_f$ (Hz)
1	35.3	35.3	-0.001	21	261.9	261.9	0.020	41	506.9	506.8	-0.160
2	60.8	60.8	-0.002	22	274.0	274.0	-0.020	42	514.0	513.8	-0.190
3	74.3	74.3	0.000	23	283.9	283.9	0.000	43	519.4	519.3	-0.100
4	94.1	94.1	-0.012	24	300.9	300.8	-0.030	44	522.0	522.0	-0.050
5	97.9	97.9	-0.001	25	314.7	314.6	-0.060	45	548.3	548.1	-0.130
6	123.7	123.7	0.000	26	323.5	323.5	-0.030	46	570.6	570.4	-0.270
7	125.5	125.5	-0.030	27	342.2	342.2	-0.060	47	589.2	589.0	-0.210
8	138.4	138.4	-0.010	28	350.4	350.4	0.020	48	590.6	590.4	-0.200
9	143.5	143.5	-0.010	29	366.4	366.4	-0.030	49	593.3	592.9	-0.330
10	165.6	165.6	-0.030	30	371.0	371.1	0.020	50	593.9	593.7	-0.240
11	166.8	166.8	-0.040	31	380.6	380.6	-0.020	51	608.6	608.5	-0.080
12	181.4	181.4	0.000	32	386.9	386.8	-0.080	52	650.8	650.6	-0.180
13	194.5	194.5	0.000	33	399.9	399.8	-0.100	53	657.5	657.1	-0.420
14	197.0	197.0	-0.020	34	408.8	408.7	-0.040	54	678.6	678.0	-0.590
15	204.6	204.5	-0.050	35	412.2	412.2	-0.020	55	684.2	683.7	-0.460
16	215.2	215.2	-0.020	36	452.6	452.5	-0.090	56	690.5	689.9	-0.530
17	224.3	224.3	-0.050	37	460.1	460.0	-0.030	57	690.6	690.1	-0.440
18	254.7	254.7	-0.040	38	476.0	475.8	-0.170	58	718.3	717.9	-0.480
19	259.4	259.3	-0.010	39	478.1	478.0	-0.120	59	721.0	720.5	-0.440
20	260.8	260.7	-0.050	40	479.4	479.4	0.020	60	738.6	737.9	-0.650

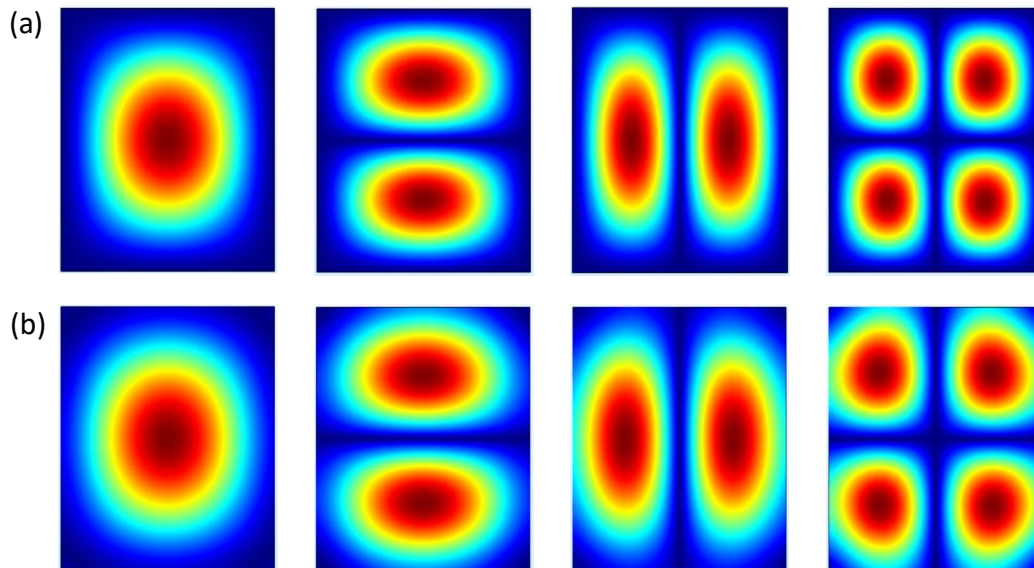





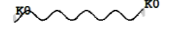




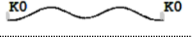
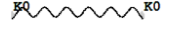
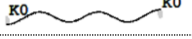
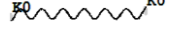
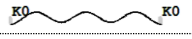
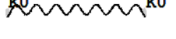
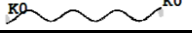

Fig. 4-10. The first 4 mode shapes of the plate with: (a)  $k_w = \infty$ ,  $k_\theta = 10^4$  N/rad; (b)  $k_w = 10^6$  N/m<sup>2</sup>,  $k_\theta = 10^4$  N/rad.

### 4.2.6 One-dimensional plate model validation

The 1D model assumes that the plate is extended to infinite in the direction perpendicular to the propagating plane bending wave. Using FEM, the plate can be modelled in two ways: one is similar to the 2D situation, continuously using shell elements but only one layer in the infinitely extended direction; the other is instead utilizing beam elements with area  $h$  and area moment of inertia  $I = h^3/12(1-\nu^2)$ , as discussed in Section 2.2.2.

For validating the equivalence of the two FE modelling approaches, a 1D thin plate bending problem is proposed for analysis. Based on the problem defined in Section 4.2.1, a reduced 1D problem is raised: referring to Section 2.2.2 and Fig. 2-2, now consider a thin aluminium plate with length  $l = 1.018$  m and boundary conditions  $c_{w1} = c_{w2} = c_{\theta1} = c_{\theta2} = 0$ ,  $k_{w1} = k_{w2} = 10^6$  N/m<sup>2</sup>,  $k_{\theta1} = k_{\theta2} = 10^4$  N/rad. Other parameters are the same as all the other cases discussed in this chapter, given by Eq. (4.13). Then, the problem is analysed via ANSYS. One FE model is built up by SHELL63 elements, and one FE model is established by BEAM3 elements. The maximum element size is set as 0.01m, so that the highest frequency can reach 2000 Hz. The results obtained through modal analysis are listed in Table 4-7 for the first 16 modes, including natural frequencies and the corresponding mode shapes. As expected, the two models yield good matching results.

Table 4-7. Natural frequencies and mode shapes of the 1D thin plate with  $k_{w1} = k_{w2} = 10^6$  N/m<sup>2</sup>,  $k_{\theta1} = k_{\theta2} = 10^4$  N/rad.

Order	Mode shape	SHELL63	BEAM3	Order	Mode shape	SHELL63	BEAM3
		$f_s$ (Hz)	$f_s$ (Hz)			$f_s$ (Hz)	$f_s$ (Hz)
1		18.2	18.2	9		587.0	586.8
2		48.3	48.3	10		738.2	738.0
3		88.4	88.4	11		908.7	908.4
4		133.9	133.9	12		1098.4	1097.8
5		186.9	186.9	13		1306.9	1306.2
6		255.3	255.3	14		1534.4	1533.3
7		344.7	344.6	15		1780.7	1779.3
8		455.6	455.5	16		2045.7	2043.9

### 4.3 FEM for acoustic cavity

The mathematical model for an uncoupled interior acoustic problem has been introduced in Section 2.3, where the governing differential equation and boundary conditions are provided. In this section, the corresponding problem to the Noise-Box is solved using FEM via COMSOL. Before the implementation to Noise-Box, a validation has been conducted over a rigid-walled rectangular cavity, by comparing the modal analysis results with the analytical solutions [166]. The validation proves the reliability of the tool for acoustic problem and the correct implementation by the user. For acoustic problem, the problem domain is discretized by acoustic/fluid elements, and the DOF of each node is acoustic pressure  $p$ .

#### 4.3.1 Problem definition

An air volume surrounded by rigid walls is considered. As shown by Fig. 4-11, geometry of the volume is the cavity of the Noise-Box, whose detailed dimensions are shown in Fig. 3-10. The cavity can also be simplified as a pentagonal prism as shown in Fig. 3-11. Influence of the simplification will be discussed. The meteorological conditions are changeable. The temperature is influential, determining the air properties according to Eqs. (2.24)-(2.25), which is also the definition of air material in COMSOL. Assumed that the static pressure remains 1 atm, then the air properties are given by  $\rho_0 = 1.2043 \text{ kg/m}^3$ ,  $c = 343.2 \text{ m/s}$  at  $20^\circ\text{C}$ , and given by  $\rho_0 = 1.1841 \text{ kg/m}^3$ ,  $c = 346.12 \text{ m/s}$  at  $25^\circ\text{C}$ . With respect to the boundary conditions, all the surrounding walls are assumed to be acoustically rigid  $\bar{v}_n = 0$  or with the same acoustic impedance  $\bar{Z} = \infty$ . Then, modal analysis can be conducted, obtaining the eigenfrequencies and eigenmodes of the system. Regarding the case with a harmonic monopole source excitation, the excitation and measurement positions are shown in Fig. 4-11. The unit input volume flow rate is given by  $q = 1 \text{ m}^3/\text{s}$  at intervals of 1 Hz within 100-700 Hz.

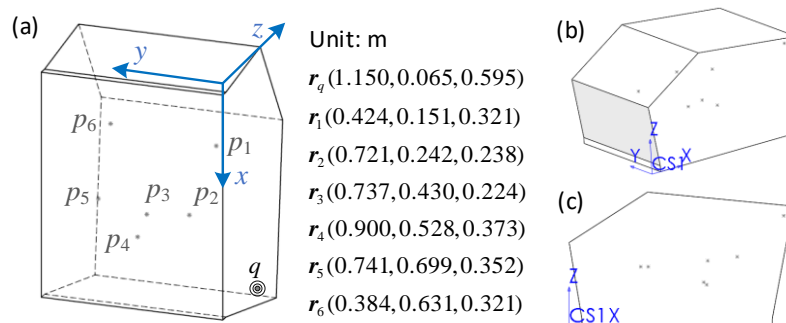


Fig. 4-11. Acoustic cavity for FEA.



In addition, the coordinate system is arranged consistent with the one utilized in Section 3.2.1, where the origin is at one corner of the enclosing rectangular and the  $x$ - $y$  plane overlaps with the mid-plane of the plate, as shown by Fig. 3-3. The coordinate system can ease the process to derive the 2D model (used for modal analysis), as illustrated from Fig. 4-11(b) to Fig. 4-11(c). Correspondingly, the enclosing rectangular shown in Fig. 3-3 is defined by  $L_x \times L_y \times L_z = 1.2 \text{ m} \times 0.825 \text{ m} \times 0.72 \text{ m}$ .

### 4.3.2 Three- and two- dimensional FE models

The FE models are built up in COMSOL as shown in Fig. 4-12. The default quadratic tetrahedral element is used in the 3D model, whose maximum element size is controlled as 0.056 m, corresponding to 6 elements per wavelength at 1000 Hz. The default quadratic triangular element is used in the 2D model with maximum element size 0.034m corresponding to 10 elements per wavelength at 1000 Hz.

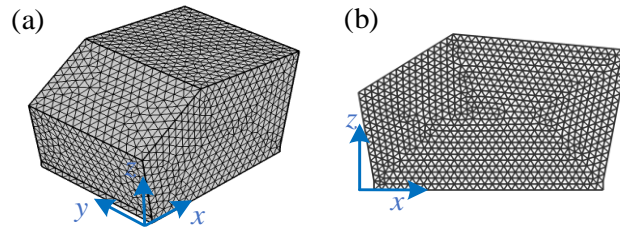


Fig. 4-12. Acoustic cavity FE models: (a) 3D; (b) 2D.

Thanks to the two parallel walls, the 2D model is available and can be used to represent the 3D cavity. In the modal analysis, if the cavity is considered as a rigid-walled cavity, its modes satisfy <sup>[1]</sup>

$$p(x, y, z) = p(x, z) \cos\left(\frac{n_y \pi y}{L_y}\right), \quad (4.25)$$

and its natural frequencies are given by

$$f_{3D} = \sqrt{f_{2D}^2 + \left(\frac{c}{2} \frac{n_y}{L_y}\right)^2}, \quad n_y = 0, 1, \dots, \quad (4.26)$$

where,  $n_y$  is the order of the standing wave in  $y$  direction,  $f_{3D}$  denotes the natural frequency of the 3D cavity,  $f_{2D}$  is the natural frequency of the 2D model,  $p(x, y, z)$  is the pressure distribution. Though it is optional to directly use the 3D model, the build-up and proof of the 2D model is meaningful, since using the 2D model significantly saves the computational time and memory, especially for the higher frequencies.



### 4.3.3 Numerical results

At first, modal analysis is performed. Under the temperature 20°C and the rigid-walled boundary condition  $\bar{v}_n = 0$ , the 2D acoustic model is validated by comparing the natural frequencies and mode shapes with the 3D analysis. Table 4-8 lists the natural frequencies of the acoustic cavity obtained from the 3D COMSOL model  $f_a$ , the natural frequencies obtained from the 2D COMSOL model  $f_{2D}$  and the natural frequencies of the cavity  $f_{3D}$  calculated by Eq.(4.26). The table verifies that  $f_a = f_{3D}$ , and correspondence of the mode shapes from 2D to 3D is indicated by Fig. 4-13 with the examples of the first 8 modes. Therefore, the 2D model can be used to predict the acoustic modes of the 3D cavity. Besides, the 2D model is more efficient. With only 3344 DOF, its solution time is 6 sec, while the 3D model has 78806 DOF and uses 146 sec.

Table 4-8. The first 38 natural frequencies of the uncoupled cavity at 20°C.

Mode order	COMSOL 3D $f_a$ (Hz)	COMSOL 2D*				Mode order	COMSOL 3D $f_a$ (Hz)	COMSOL 2D*			
		2D modes		$n_y$	$f_{3D}$ (Hz)			2D modes		$n_y$	$f_{3D}$ (Hz)
		Order	$f_{2D}$ (Hz)					Order	$f_{2D}$ (Hz)		
0	0	0	0	0	0	19	536.9	4	339.46	2	536.9
1	161.9	1	161.91	0	161.9	20	542.7	8	542.72	0	542.7
2	208.0	0	0	1	208.0	21	549.5	7	508.64	1	549.5
3	257.8	2	257.82	0	257.8	22	566.3	9	566.31	0	566.3
4	263.6	1	161.91	1	263.6	23	581.2	8	542.72	1	581.2
5	297.1	3	297.09	0	297.1	24	590.8	5	419.5	2	590.8
6	331.3	2	257.82	1	331.3	25	597.4	10	597.4	0	597.4
7	339.5	4	339.46	0	339.5	26	603.3	9	566.31	1	603.3
8	362.7	3	297.09	1	362.7	27	615.9	6	454.08	2	615.8
9	398.1	4	339.46	1	398.1	28	624.0	0	0	3	624.0
10	416.0	0	0	2	416.0	29	632.6	10	597.4	1	632.6
11	419.5	5	419.5	0	419.5	30	644.7	1	161.91	3	644.7
12	446.4	1	161.91	2	446.4	31	657.1	7	508.64	2	657.1
13	454.1	6	454.08	0	454.1	32	660.9	11	660.89	0	660.9
14	468.2	5	419.5	1	468.2	33	675.2	2	257.82	3	675.2
15	489.4	2	257.82	2	489.4	34	683.1	12	683.09	0	683.1
16	499.5	6	454.08	1	499.5	35	683.9	8	542.72	2	683.8
17	508.7	7	508.64	0	508.6	36	691.2	3	297.09	3	691.1
18	511.2	3	297.09	2	511.2	37	692.9	11	660.89	1	692.8

\* $f_{3D}$  is the natural frequency of the 3D cavity derived from the numerical result of 2D model using Eq.(4.26).

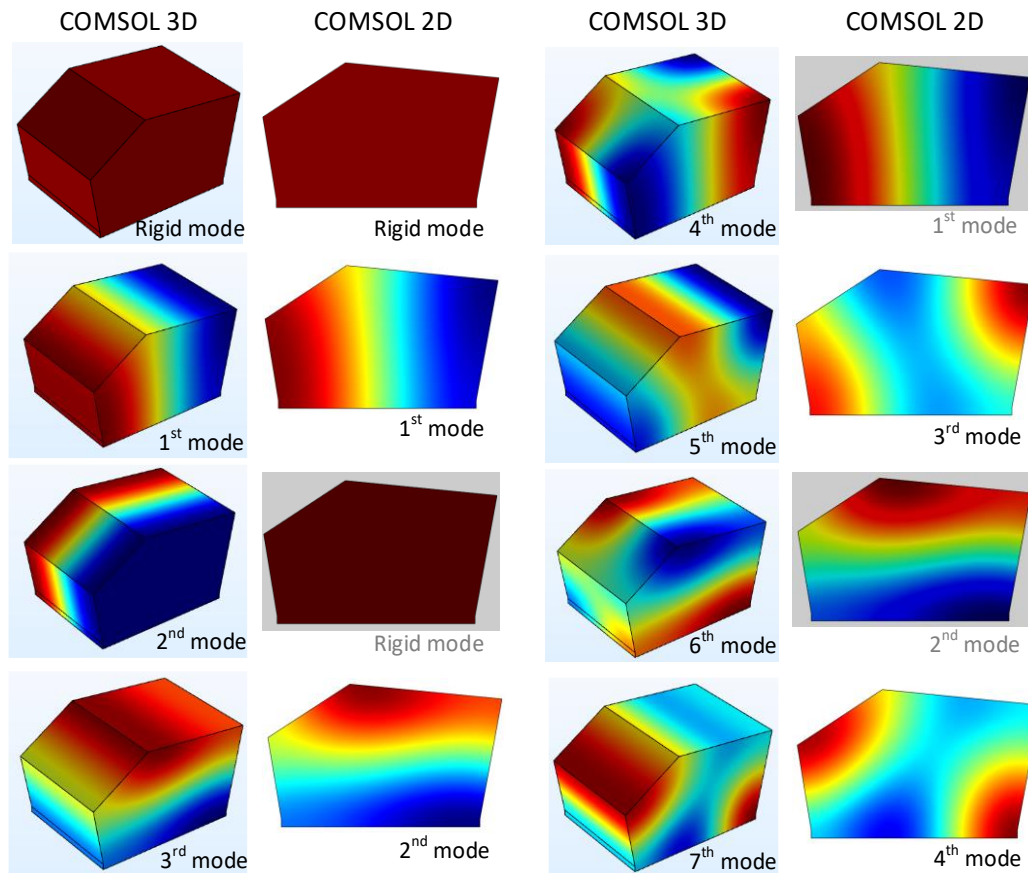


Fig. 4-13. First 8 mode shapes of the uncoupled 3D cavity and their counterparts in the 2D model.

Next, the influences of temperature, cavity shape simplification (see Section 3.4 from Fig. 3-10 to Fig. 3-11) and wall impedance are analysed respectively through modal analysis and harmonic excitation analysis, using the above case as reference. All analyses are performed on the 3D model. The four cases (including the reference one) are specified as follows:

- Case R(Reference): 20°C, exact geometry, reflecting walls  $\bar{v}_n=0$ ;
- Case T(Temperature): 25°C, exact geometry, reflecting walls  $\bar{v}_n=0$ ;
- Case S(Simplification): 20°C, simplified geometry, reflecting walls  $\bar{v}_n=0$ ;
- Case I(Impedance): 20°C, exact geometry, wall impedance  $\bar{Z} = 32233 \text{ Pa}\cdot\text{s/m}$ , corresponding to absorption coefficient  $\bar{\alpha} = 0.05$ .

Natural frequencies of the new cases T, S and I are listed in Table 4-9, up to 700 Hz. In Case I, when wall impedance is included, the system is damped and the modal damping ratios  $\zeta_a$  are listed alongside. It is shown that the wall absorption  $\bar{\alpha} = 0.05$  leads to a modal damping ratio between 0.005 and 0.02 for the first 38 modes. The modal damping ratio is mode-dependent but has a decreasing tendency as the frequency increases. To illustrate the

effect caused by the three factors Temperature, Simplification, Impedance on natural frequencies, their differences  $\Delta f_a$  to the reference case  $f_{a,R}$ , i.e.,  $f_a$  in Table 4-8, are plotted in Fig. 4-14. As shown by the figure, the temperature is most influential. With 5°C higher than Case R, Case T has higher natural frequencies and the difference is monotonously larger for higher mode orders. The influence on the frequency response, represented by the  $p_1/q$ , is similar. As shown by Fig. 4-15(a), the discrepancy is larger at higher frequencies. The next is the simplification. It enlarges the air volume, so the natural frequencies are smaller. However, the difference depends on how much the simplification affects the mode shape. For example, at the 3<sup>rd</sup> mode (as shown by Fig. 4-13), which is an axial mode in  $y$  direction, the simplification effect is negligible. Nevertheless, the FRFs  $p_1/q$  are close between Case S and Case R, as shown by Fig. 4-15(b). Therefore, the difference caused by the simplification is small in general, and it is acceptable to use the simplified cavity shape if necessary. The last is the wall impedance. Since the impedance  $\bar{Z}$  only contains real part, its influence on the natural frequencies very small, but the damping effect is not negligible. As indicated from Fig. 4-15(c), the amplitudes around natural frequencies are significantly reduced under the current damping ratios.

Table 4-9. Natural frequencies  $f_a$  of the uncoupled acoustic cavity in Case T, Case S and Case I, and modal damping ratios  $\zeta_a$  of Case I.

Order	Case T	Case S	Case I		Order	Case T	Case S	Case I	
	$f_a$ (Hz)	$f_a$ (Hz)	$f_a$ (Hz)	$\zeta_a$		$f_a$ (Hz)	$f_a$ (Hz)	$f_a$ (Hz)	$\zeta_a$
0	0	0	0	----	19	541.5	536.4	536.9	0.0084
1	163.3	161.1	161.9	0.0195	20	547.3	539.9	542.8	0.0073
2	209.8	208.0	208.0	0.0161	21	554.2	549.4	549.6	0.0077
3	260.0	257.7	257.8	0.0132	22	571.1	566.4	566.3	0.0069
4	265.8	263.1	263.6	0.0152	23	586.2	578.6	581.3	0.0083
5	299.6	296.3	297.1	0.0122	24	595.8	589.9	590.8	0.0085
6	334.1	331.2	331.3	0.0128	25	602.5	595.9	597.5	0.0062
7	342.4	338.6	339.5	0.0108	26	608.4	603.4	603.3	0.0079
8	365.7	362.0	362.7	0.0123	27	621.1	615.0	615.9	0.0073
9	401.5	397.4	398.1	0.0113	28	629.3	624.0	624.1	0.0054
10	419.5	416.0	416.0	0.0081	29	638.0	631.1	632.6	0.0072
11	423.1	418.2	419.5	0.0099	30	650.2	644.5	644.7	0.0062
12	450.2	446.1	446.4	0.0090	31	662.7	657.0	657.1	0.0064
13	457.9	452.9	454.1	0.0080	32	666.5	660.5	660.9	0.0059
14	472.2	467.1	468.3	0.0107	33	680.9	675.2	675.2	0.0063
15	493.6	489.4	489.4	0.0087	34	688.9	678.8	683.1	0.0055
16	503.7	498.4	499.5	0.0090	35	689.7	681.6	683.9	0.0070
17	513.0	508.5	508.7	0.0067	36	697.0	690.8	691.2	0.0065
18	515.5	510.8	511.2	0.0088	37	698.8	692.4	692.9	0.0068

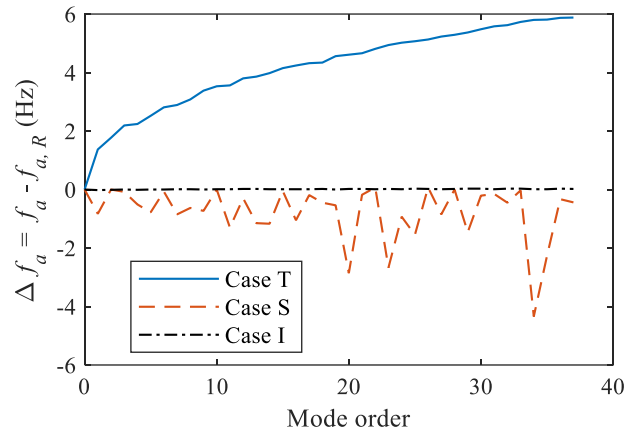


Fig. 4-14. Difference in natural frequencies between Case T, S or I and Case R.

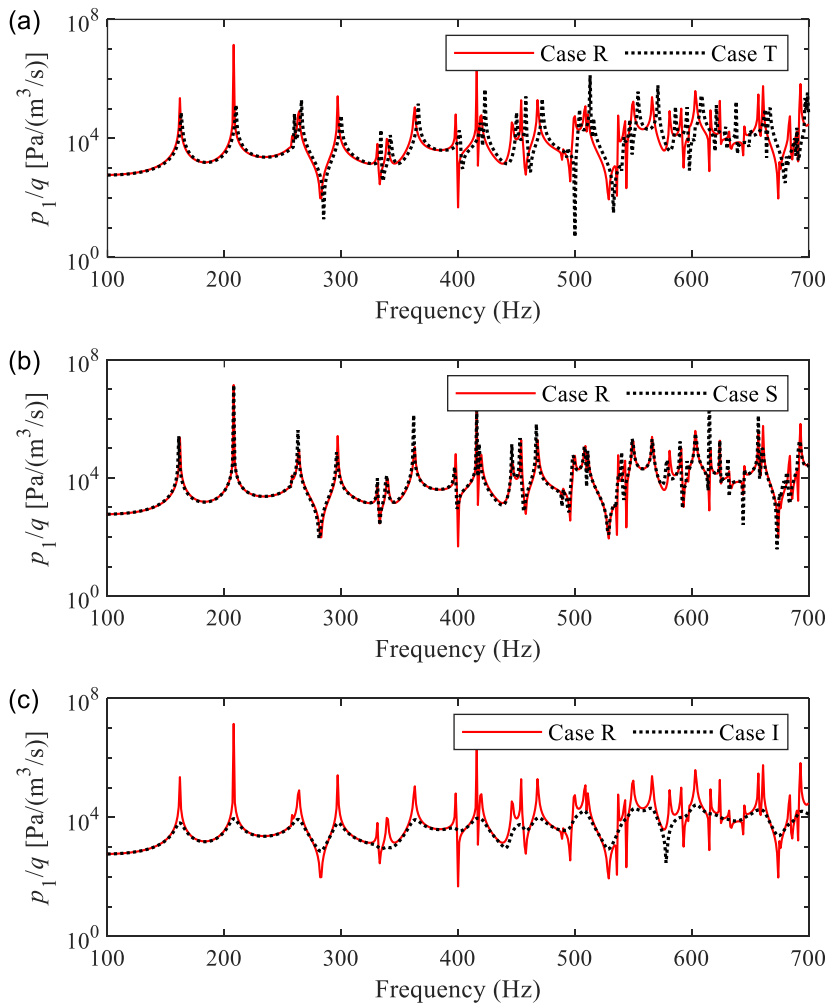


Fig. 4-15. Comparisons of FRFs  $p_1/q$  between Case R and (a) Case T; (b) Case S; (c) Case I.

## 4.4 FEM for plate-cavity system

The mathematical model of a coupled plate-cavity system has been introduced in Section 2.4, where the cavity is generally shaped. In this section, the problem is targeted to the Noise-Box and solved via FEM. FE modelling of the rectangular plate has been discussed in Section 4.2, and that of the Noise-Box cavity has been mentioned in Section 4.3. The complete modelling of the system involves coupling between the two components, i.e., the Acoustic-Shell Interaction or Fluid-Structure Interaction (FSI). In ANSYS, the strongly coupled FSI interface should be specified, while in COMSOL it is to define the acoustic-structure boundary. With the specification or definition, the normal velocity of the plate and the particle velocity of the fluid is matching on the coupled surface. Concerning the two-way coupling between two fields, a conforming mesh between the acoustic and structural elements over the coupled surface is recommended.

### 4.4.1 Problem definition

The plate-cavity coupled Noise-Box is shown as Fig. 4-16. The plate is the one discussed in Section 4.2, that is,  $a \times b = 0.825 \text{ m} \times 1.018 \text{ m}$ ,  $h = 4 \text{ mm}$ ,  $\rho = 2700 \text{ kg/m}^3$ ,  $E = 70 \text{ GPa}$ ,  $\nu = 0.33$ . The edge conditions are assumed to be ideally clamped. The cavity is the one considered in Section 4.3. Its geometry is defined in Fig. 3-10. The air inside is under temperature  $20^\circ\text{C}$  and the standard atmosphere  $1 \text{ atm}$ . Consequently, by  $\rho_0 = 1.2043 \text{ kg/m}^3$  and  $c = 343.2 \text{ m/s}$ . The walls except the flexible plate are acoustically rigid  $\bar{v}_n = 0$ . For this plate-cavity system, its modal property is to be analysed and then compared with the uncoupled plate and cavity modes. Later, its frequency response will be investigated. While three types of input are mentioned in Section 2.4, only harmonic point force excitation with amplitude  $F = 1 \text{ N}$  on the plate is applied in this section.

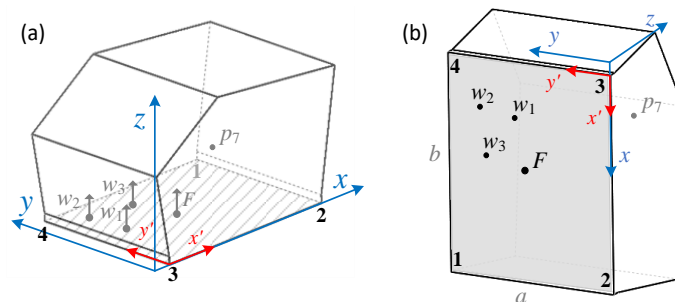


Fig. 4-16. Plate-cavity system for FEA.

The excitation  $F$  and measurement points  $w_1, w_2, w_3$  on the plate are at the same positions as the uncoupled plate in Section 4.2 (see Fig. 4-1). However, under the new coordinate

system shown by Fig. 4-16, their new coordinates are  $\mathbf{r}'_F$  (0.485m, 0.44m) and  $\mathbf{r}'_1$  (0.2125m, 0.515m),  $\mathbf{r}'_2$  (0.1425m, 0.715m) and  $\mathbf{r}'_3$  (0.3625m, 0.665m). The measurement inside the cavity for acoustic pressure  $p_7$  is located at  $\mathbf{r}_7$  (0.342m, 0.15m, 0.464m). The harmonic response analysis is performed every Hz within 10-700 Hz to obtain the FRFs  $w_1/F$  and  $p_7/F$ .

#### 4.4.2 COMSOL model

The 3D problem introduced above is solved using COMSOL. The bottom surface of the cavity shown by Fig. 4-16(a) is defined as shell with four edges fixedly constrained. Then, with the Multiphysics ‘Acoustic-Structure Boundary’ applied, the overall physics of the problem is settled. Later, the same rule of mesh as the previous two sections is used, where the maximum element sizes of the plate and the cavity are respectively set as 0.04 m and 0.056 m. Since the mesh of the plate should overlap with the bottom surface of the cavity, the element size gradually grows from the bottom part of the cavity to the top. However, due to the small difference between 0.056 m and 0.04 m, the meshed FE model of the plate-cavity system looks like that of the uncoupled cavity (see Fig. 4-12(a)). On the other side, the plate here is meshed by triangular elements instead of the rectangular ones in the uncoupled situation.

#### 4.4.3 Numerical results

Considering that the modification of mesh may affect the results, especially for the plate, where rectangular elements are replaced by triangular ones, the uncoupled natural modes and frequencies are analysed again based on the current mesh. Consequently, the difference between the coupled and uncoupled systems illustrated by the following comparison is raised solely by the coupling effect. Table 4-10 compares the coupled and uncoupled natural modes and frequencies. In the table, the modes of the plate are expressed in the same way as Section 4.2. Whereas, due to the different coordinate system in this section, the denotations are changed to  $n_x$  and  $n_y$ , respectively indicating the mode orders in  $x$  and  $y$  directions of the new coordinate system. With respect to the modes of the cavity, they are denoted by the orders in the 2D model  $n_{2D}$  and the orders in  $y$  direction  $n_y$ , expressed as  $(n_{2D}, n_y)$ . This part is in accord with Table 4-8. As for the coupled plate-cavity system, the natural modes and frequencies are highly related to the uncoupled plate and cavity. As shown by Table 4-10, the natural frequencies  $f_{sa}$  are close to either the structural frequency  $f_s$  or the acoustic frequency  $f_a$ . Correspondingly, the modes are plate-controlled, cavity-controlled or strongly influenced by both plate and cavity modes. For instance, the first 5 modes are plate-controlled. As they are shown in Fig. 4-17, the plate modes are like they are *in vacuo*, while the acoustic modes are slightly perturbed in the region close to the plate.

The 6<sup>th</sup> mode is cavity-controlled, where the plate mode is distorted to fit the acoustic mode. Under the plate-controlled modes, sometimes the plate vibration can excite a nearby cavity mode that matches itself, like in the 12<sup>th</sup> coupled mode, and vice versa for the cavity-controlled modes, such as the 15<sup>th</sup> coupled mode. There are also cases when the uncoupled plate and cavity natural frequencies are very close to each other. In these cases, the ‘frequency-splitting’ happens, where the coupled modes have one frequency above and one frequency below the uncoupled values, e.g., the 17<sup>th</sup> and 18<sup>th</sup> coupled modes.

Table 4-10. Natural modes and frequencies of the *in-vacuo* clamped plate, the rigid-walled cavity and the plate-cavity system coupled by them.

<i>In-vacuo</i> clamped plate			Rigid-walled cavity			Coupled plate-cavity		
Mode		$f_s$ (Hz)	Mode		$f_a$ (Hz)	Modes involved		$f_{sa}$ (Hz)
Order	$(n_y, n_x)$		Order	$(n_{2D}, n_y)$		Order	$(n_y, n_x)-(n_{2D}, n_y)$	
			0	(0,0)	0			
1	(1,1)	43.8				1	(1,1)-(0,0)	45.9
2	(1,2)	77.6				2	(1,2)-(0,0)	76.7
3	(2,1)	99.6				3	(2,1)-(0,0)	98.7
4	(2,2)	130.6				4	(2,2)-(0,0)	129.7
5	(1,3)	132.2				5	(1,3)-(0,0)	131.4
			1	(1,0)	161.9	6	(1,0)	162.2
6	(2,3)	182.5				7	(2,3)-(0,1)	181.2
7	(3,1)	184.7				8	(3,1)-(0,0)	183.6
8	(1,4)	206.0				9	(1,4)-(1,0)	205.2
			2	(0,1)	208.0	10	(0,1)	208.7
9	(3,2)	214.3				11	(3,2)-(2,0)	213.3
10	(2,4)	254.3				12	(2,4)-(1,1)	252.4
			3	(2,0)	257.8	13	(3,3)-(2,0)	258.5
11	(3,3)	264.0				14	(3,3)-(2,0)	263.3
			4	(1,1)	263.6	15	(2,4)-(1,1)	264.6
12	(4,1)	297.7				16	(4,1)-(2,1)	295.9
13	(1,5)	298.6	5	(3,0)	297.1	17	(1,5)-(3,0)	296.1
13	(1,5)	298.6	5	(3,0)	297.1	18	(1,5)-(3,0)	299.0
14	(4,2)	326.6				19	(4,2)-(2,1)	325.0
15	(3,4)	333.7				20	(3,4)-(4,0)	332.2
			6	(2,1)	331.3	21	(2,1)	332.3
			7	(4,0)	339.5	22	(4,0)	340.6
16	(2,5)	345.4				23	(2,5)-(2,1)	344.5
			8	(3,1)	362.7	24	(3,1)	363.1
17	(4,3)	374.9				25	(4,3)-(3,1)	373.6
			9	(4,1)	398.1	26	(4,1)	399.0
18	(1,6)	409.4				27	(1,6)-(4,1)	407.9
			10	(0,2)	416.0	28	(0,2)	415.5
			11	(5,0)	419.5	29	(3,5)-(5,0)	419.2
19	(3,5)	422.9				30	(3,5)-(5,0)	422.8



Next, if focusing on the plate-controlled modes, we can gain some knowledge about how the backed cavity alters the plate modes. As indicated from Table 4-10, 1<sup>st</sup> natural frequency of the plate is increased due to the Noise-Box cavity, while all the other natural frequencies are decreased. The variations are small for all, with the maximum absolute value around 2 Hz. By contrast, most of the cavity-controlled modes have the natural frequencies slightly larger than the uncoupled cavity.

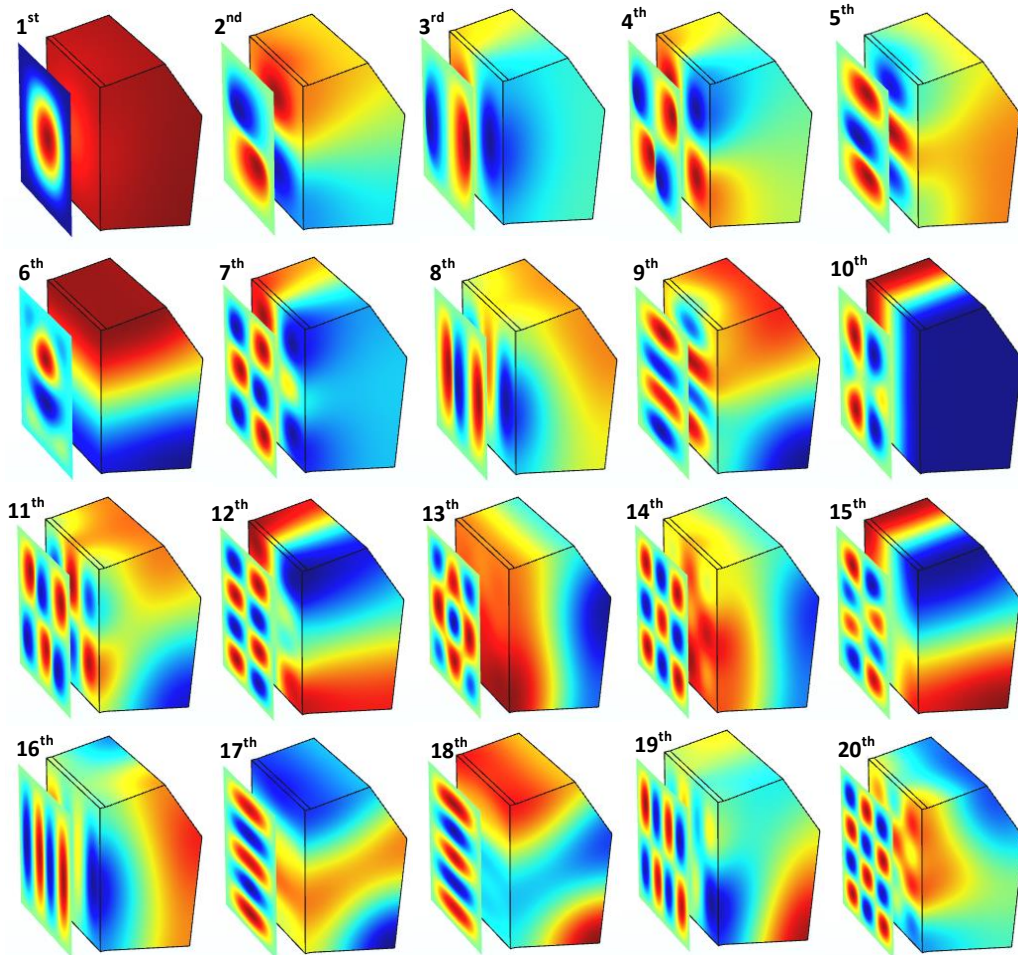


Fig. 4-17. Coupled modes of the plate-cavity system.

Fig. 4-18 shows the FRFs  $w_1/F$  and  $p_7/F$  of the plate-cavity system. Resonances are observed at the coupled natural frequencies either from the plate displacement or from the cavity pressure. For the plate, the FRFs are compared with (coupled plate) and without (*in vacuo* plate) the backed Noise-Box cavity. Tiny change of the natural frequencies related to the plate-controlled modes and additional emergence of the cavity-controlled modes are highlighted. In Fig. 4-18, some of the additional peaks are circled out for examples. Nevertheless, the two FRFs are not significantly different. Some of the cavity-controlled modes are even hard to be noticed in the coupled FRF  $w_1/F$ , such as the circled-out peaks



at 162 Hz and 363 Hz. By contrast, in the FRF  $p_7/F$  of the coupled cavity, both the plate-controlled and cavity-controlled modes can raise similarly influential resonance peaks. From another point of view, the FRF with output as the acoustic pressure at a measurement point inside cavity may be preferred to detect the resonance/natural frequencies of the coupled system.

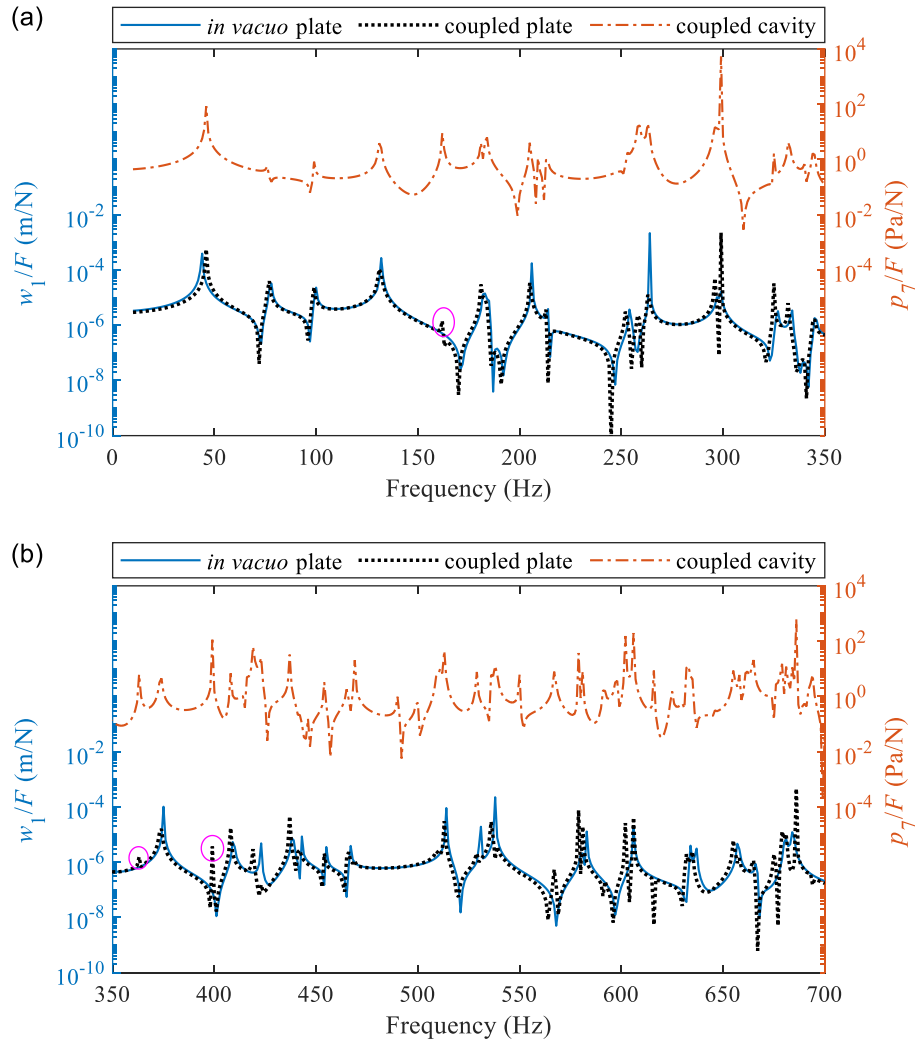


Fig. 4-18. FRFs of the plate-cavity system and the *in vacuo* plate. The input and output points are shown by Fig. 4-16.

#### 4.4.4 Two-dimensional plate-cavity model validation

The 2D vibroacoustic model has been introduced in Section 2.4.2. According to the description of the 2D model, the problem to be solved here is not able to build an equivalent 2D model, but a similar 2D vibroacoustic problem can be raised to test the 2D modelling strategies.

Fig. 4-19 shows the 2D vibroacoustic problem. Geometry of the cavity is the simplified Noise-Box geometry in  $x$ - $z$  plane (a pentagonal whose detailed dimensions shown by Fig. 3-11). The rigid walls can be assigned with different impedances  $\bar{Z}$ , and the bottom flexible can be of any type of edge conditions (see Table 2-1). Though, the 2D problem cannot replace the 3D one, it is very useful for code testing or parametric study owing to its small model size, low computation load, short computation time and simple physical interpretation. For instance, if this 2D problem is used to investigate the influence rules of the parameters  $\bar{Z}$ ,  $k_w$ ,  $k_\theta$ ,  $c_w$  and  $c_\theta$ , it will be much more efficient. In the following, it is to introduce the approach to FE model of the 2D vibroacoustic problem through a simple case that possesses the same materials and boundary conditions ( $k_w = k_\theta = \infty$ ) as the 3D system defined in Section 4.4.1. Besides,  $y$  dimension is eliminated,  $l = 1.018$  m, and  $F = 1$  N/m is forcing at  $x'_F = 0.485$  m.

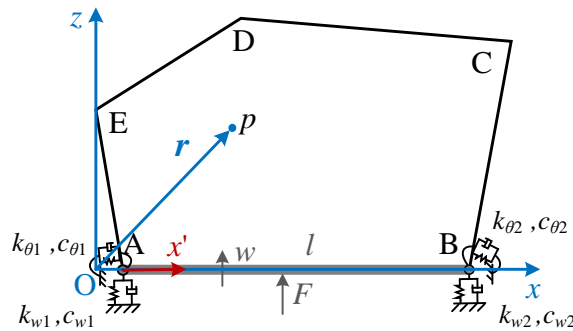


Fig. 4-19. Two-dimensional plate-cavity system for FEA.

This problem can be solved using FEM in ANSYS via two different modelling strategies. One is to use the reduced 3D FE model with only one layer of elements, where the plate is modelled using SHELL63 element and the cavity is modelled using FLUID30, the element for 3D acoustic fluid. The other option is to model the plate with BEAM3 element and the cavity with FLUID29, the element for 2D acoustic fluid. Both models are built with the conform element size 0.01 m. Modal analysis for the first 10 modes and harmonic analysis at 100 Hz are conducted.

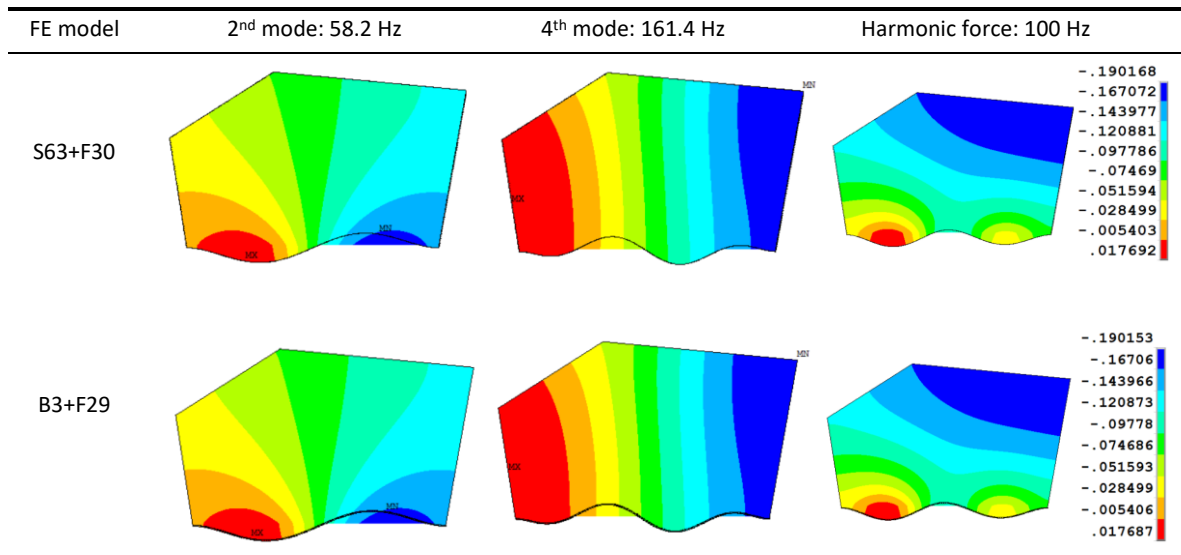
Table 4-11 shows the natural frequencies obtained from modal analysis. ‘S63+F30’ indicates the former model using SHELL63 and FLUID30 elements, and ‘B3+F29’ represents the latter option utilizing BEAM3 and FLUID29 elements. If compared with Table 4-8, where lists the natural frequencies of the 2D cavity, the 4<sup>th</sup>, 6<sup>th</sup>, 8<sup>th</sup> and 9<sup>th</sup> can be noticed as the cavity-controlled modes. Presented as examples for the plate-controlled and cavity-controlled modes of the 2D vibroacoustic problem, the 2<sup>nd</sup> and 4<sup>th</sup> mode shapes are shown in Table 4-12. Through the natural frequencies and mode shapes, it can be found that the two FE models yield good matching results. Additionally, the field response raised

by the force excitation at 100 Hz is provided in Table 4-12, further comparing and validating the two models. While both models are small-sized and efficient, the latter performs better in this aspect, since the acoustic elements are 2D, resulting in just one layer of nodes in y direction.

Table 4-11. The first 10 natural frequencies of the 2D plate-cavity system

Order	S63+F30	B3+F29	Order	S63+F30	B3+F29
	$f_{sa}$ (Hz)	$f_{sa}$ (Hz)		$f_{sa}$ (Hz)	$f_{sa}$ (Hz)
0	0	0	5	190.73	190.73
1	27.58	27.58	<b>6</b>	<b>258.82</b>	<b>258.82</b>
2	58.203	58.204	7	284.54	284.53
3	115.06	115.06	<b>8</b>	<b>297.16</b>	<b>297.16</b>
<b>4</b>	<b>161.36</b>	<b>161.36</b>	<b>9</b>	<b>339.69</b>	<b>339.69</b>

Table 4-12. The 2<sup>nd</sup> and 4<sup>th</sup> mode shapes of 2D plate-cavity system and the forced response at 100 Hz.



## 4.5 Summary

This chapter builds and validates the FE models for the plate bending problem, the interior acoustic problem and the plate-cavity vibroacoustic problem, respectively. The models are built in their designed geometries, with the commonly used parameters for the materials, and the assumed boundary conditions that are intended for investigation.

At the beginning, the seven steps for employing the method are illustrated. They are instructive, no matter using a commercial CAE tool or developing our own FEA program. When convergence issue is considered for the numerical technique, the rule of thumb for

element size is discussed. As the FEM is implemented in ANSYS or COMSOL, the thumb of rule recommended by them are adopted. They both recommend at least either 10 linear or 5 quadratic elements per wavelength.

The rectangular plate mounted on the Noise-Box is first analysed. Four types of boundary conditions are considered: simply supported, clamped, rigidly supported but elastically restrained against rotation, and elastically restrained against both translation and rotation. The methods to build the corresponding models in ANSYS and COMSOL are introduced, especially for the elastically restrained edges. Then, the models are validated and compared by their predicted natural frequencies. According to the results in simply supported and clamped cases, the COMSOL model with default element type has best performance for accuracy, and the ANSYS model with SHELL63 is a good option if it is necessary to use linear elements or Kirchhoff-Love shell elements. For the other two cases associated with elastic restraints, the COMSOL and ANSYS SHELL63 models yield consistent results, which increases the credibility of the results, as well as the modelling methods applied to the software. Besides, the numerical results are also compared among different boundary conditions, demonstrating how the natural frequencies of the plate will be influenced by the boundary conditions. Additionally, two FE modelling approaches for 1D plate are provided via ANSYS. One uses SHELL63 element and the other uses BEAM3 element.

Next, the uncoupled interior acoustic problem is solved in COMSOL, targeted to the Noise-Box cavity. This section first proves that the 2D FE model of the Noise-Box cavity is applicable to the prediction of the natural frequencies and modes of the 3D Noise-Box cavity, and it is much more efficient than the 3D FE model. Later, the research focuses on how the natural frequencies and frequency response are influenced by the change of temperature, the simplicity of cavity shape and the increase of wall absorption coefficient. The numerical results indicate that increasing temperature (from 20°C to 25°C) will increase the natural frequencies (by 1.4 Hz for 1<sup>st</sup> mode); the cavity simplification reduces the natural frequencies at some modes; and the wall absorption coefficient mainly enhances the damping effect.

For the coupled plate-cavity system, the 3D FE model is built in COMSOL. With the modal analysis results, the coupled natural frequencies and modes are compared with the uncoupled ones that are obtained previously. The natural frequencies of the system are very close to the natural frequencies of the plate or the cavity (within  $\pm 2$ Hz for most of them). It is also found that the Noise-Box cavity will increase the first natural frequency of the plate but decreases all the others. Additionally, two FE modelling approaches for 2D plate-cavity problem are provided via ANSYS. One uses SHELL63 and FLUID30 elements and the other uses BEAM3 and FLUID29 elements.

## Chapter 5 Noise-Box test system characterization

*This chapter is aimed at characterizing the Noise-Box test system through experiments. The complete work is divided into three parts. At first, the Noise-Box cavity is characterized for its modal property, sound absorption and sound field diffuseness. Secondly, for the mounted test panel, its modal parameters are identified through EMA, while its thickness, material parameters and boundary conditions are further characterized with the aid of additional tests and numerical simulations. Thirdly, the plate-cavity system is characterized by its coupled modal parameters. In each of the three parts, the corresponding FE model is updated based on the characterization results. Therefore, this chapter also provides the updated FE models that match the experimental results.*

### 5.1 Noise-Box cavity characterization

This section characterizes the modal property, the sound absorption and the spatial variation/diffuseness of the interior cavity of Noise-Box. The characterization includes two parts. One is the measurement over the physical test bench, and the other is the prediction by the numerical model. Indeed, both solutions have certain assumptions and simplifications. In order to have a better knowledge of the test bench, the two sets of results are obtained and compared. Meanwhile, the numerical model is updated according to some of the parameters obtained from the experiment.

#### 5.1.1 Experimental set-up

The same experimental set-up was used for the following three tests to characterize the cavity inside the Noise Box:

- experimental modal analysis,
- reverberation time measurement,
- inner pressure field spatial variation measurement.

Fig. 5-1 shows the photograph and schematic of the set-up. The opening of the Noise-Box is closed with a transparent plexiglass plate. The plate is 25 mm thick and fixed to the Noise-Box with 80 screws. At the right corner of the cavity is the loudspeaker (FaitalPRO 3FE22) that is used to excite the sound field. Six microphones (Brüel & Kjær Type 4188) are placed at six different positions inside the cavity. They are neither too close to each other nor too close to the walls. On the floor inside the cavity is also a thermo-hygrometer (INKBIRO IBS-TH1 Mini). It is 35 mm × 10.5 mm in white and used for monitoring the

temperature and humidity inside the cavity. As shown in the schematic, the signal generated by the waveform generator (KEYSIGHT 33500B) is output to two instruments. One is to the power amplifier (Brüel & Kjær Type 2716C) so as to provide a desired input to drive the loudspeaker. The other is to the acquisition system (NI cDAQ), so that the input signal is recorded. The signals from the microphones are also acquired with the aid of the sensor signal conditioner (PCB 483C).

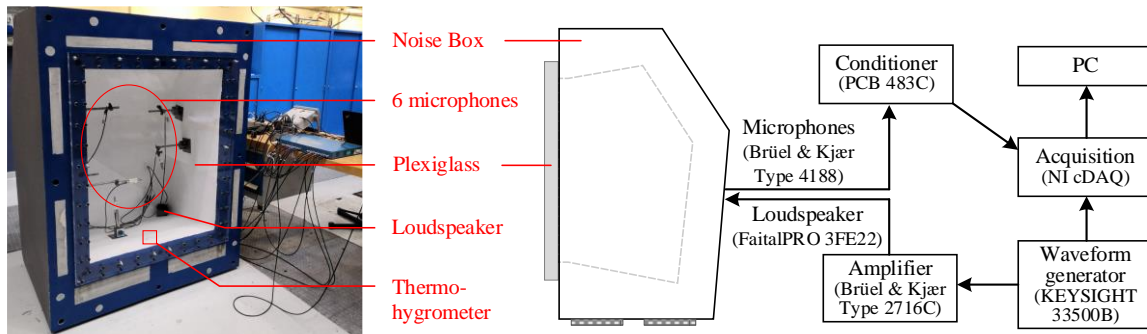


Fig. 5-1. Photograph and schematic of the experimental set-up for Noise-Box cavity characterization

### 5.1.2 Numerical model and predicting approach

The experimental tests can also be simulated using numerical models. Concerning the investigated approach FEM, the corresponding FE models have been introduced in Section 4.3 – FEM for acoustic cavity. As shown by Fig. 4-11,  $\mathbf{r}_q$  and  $\mathbf{r}_1$  to  $\mathbf{r}_6$  are respectively the position of the loudspeaker and the measuring locations of the 6 microphones. The meshed FE models are shown in Fig. 4-12. They are achieved in COMSOL. Both the 3D and 2D models can be used for modal analysis, predicting the natural frequencies of the Noise-Box cavity, while the 2D model is much more efficient and able to reach a very high number of modes. The 3D model can also be used to predict the frequency response at any point inside the cavity. All these results can be compared with the experimental measurements, and after which, the models can be further updated to match the experimental environment and the cavity boundary conditions (e.g., acoustic impedance of walls).

Regarding the prediction of FRFs from the 3D COMSOL model, the input source amplitude  $q$  can be the unit volume flow rate  $1 \text{ m}^3/\text{s}$  or instead use the value corresponding to a unit input power<sup>[203]</sup>

$$q = \frac{4\pi}{j\omega\rho_0} \sqrt{\frac{\rho_0 c P_{\text{rms}}}{2\pi}}, \quad (5.1)$$

with  $P_{\text{rms}} = 1 \text{ W}$ . The latter proposal is based on the fact that the input power to the loudspeaker is easier to obtain in the experiment. In COMSOL, the monopole source is able to prescribe the unit power input  $P_{\text{rms}} = 1 \text{ W}$  directly.

### 5.1.3 Modal characteristics of Noise-Box cavity

Experimental and numerical approaches are combined together to identify the modal characteristics of the interior acoustic field. The experimental modal analysis was performed using the experimental set-up shown in Fig. 5-1, where the loudspeaker was driven by a white noise signal up to 3000 Hz. According to the transfer functions between sound pressure measured by the microphones and the input signal, the first 31 natural frequencies of the interior acoustic field were identified by peak-picking method. They are listed as  $f_{\text{exp}}$  in Table 5-1. During the test, the temperature and humidity inside the cavity were recorded as  $(24.16 \pm 0.01)^\circ\text{C}$  and  $(75.5\% \pm 0.13\%)\text{RH}$ , respectively.

Table 5-1. Numerically and experimentally determined acoustic natural frequencies

Mode order	Experiment $f_{\text{exp}}(\text{Hz})$	COMSOL 3D $f_a(\text{Hz})$	COMSOL 2D $f_{3\text{D}}(\text{Hz})$	$\left  \frac{f_a - f_{\text{exp}}}{f_{\text{exp}}} \right  \times 100\%$
0	0	0	0	--
1	162.87	163.05	163.05	0.11%
2	208.93	209.47	209.47	0.26%
3	259.47	259.65	259.65	0.07%
4	265.53	265.45	265.45	-0.03%
5	300.03	299.19	299.19	-0.28%
6	333.67	333.61	333.61	-0.02%
7	342.60	341.86	341.86	-0.22%
8	366.07	365.23	365.23	-0.23%
9	401.40	400.94	400.93	-0.11%
10	418.93	418.95	418.95	0.00%
11	423.17	422.47	422.46	-0.16%
12	450.27	449.56	449.56	-0.16%
13	459.60	457.29	457.29	-0.50%
14	471.93	471.55	471.54	-0.08%
15	494.50	492.89	492.88	-0.33%
16	505.07	502.99	502.98	-0.41%
17	512.13	512.24	512.24	0.02%
18	516.40	514.82	514.81	-0.31%
19	542.70	540.74	540.73	-0.36%
20	549.40	546.57	546.56	-0.52%
21	551.87	553.42	553.42	0.28%
22	570.07	570.32	570.31	0.04%
23	586.90	585.34	585.33	-0.27%
24	594.73	594.99	594.97	0.04%
25	604.93	601.64	601.63	-0.54%
26	606.33	607.58	607.56	0.21%
27	623.00	620.20	620.19	-0.45%
28	630.93	628.44	628.42	-0.40%
29	638.83	637.07	637.05	-0.28%
30	651.63	649.25	649.23	-0.37%

Correspondingly, numerical modal analyses were conducted respectively based on the COMSOL 3D and COMSOL 2D finite element models, as shown by Fig. 4-12(a) and Fig. 4-12(b). According to the experimental temperature 24.16°C, the air density and acoustic speed were given by  $\rho_0 = 1.1875 \text{ kg/m}^3$  and  $c = 345.63 \text{ m/s}$ . For the results from COMSOL 2D model, Eq. (4.26) was used to calculate the eigenfrequencies from  $f_{2D}$  to  $f_{3D}$ . In order to distinguish the two sets of natural frequencies, the set of COMSOL 3D is denoted as  $f_a$  and the other is denoted as  $f_{3D}$ . The two sets of numerical results are listed in Table 5-1, and a good agreement can be observed between them, verifying the equivalence in accuracy for the two numerical models in modal analysis.

When the numerical results are compared with the experimental results, Table 5-1 shows that the relative prediction error in natural frequency is less than 0.6%. The good agreement indicates that the results from both the experiment and the simulation can be used to represent the modal characteristics of the Noise-Box cavity.

#### 5.1.4 Sound absorption of the room inside Noise-Box

Regarding the sound absorption of a room, two parameters are commonly used: the reverberation time  $T_{60}$  and the average absorption coefficient  $\bar{\alpha}$ . The two parameters are closely related to each other, and the relationship given by Sabine formula is <sup>[166]</sup>

$$T_{60} = \frac{0.161V}{\bar{\alpha}S'}, \quad (5.2)$$

where,  $V$  is the volume of the room,  $S'$  is the total surface area. With respect to the room inside Noise-Box, the reverberation time  $T_{60}$  was obtained from measurement, and the absorption coefficient  $\bar{\alpha}$  was derived according to Eq. (5.2), with the volume of the cavity  $V = 0.596 \text{ m}^3$  and surface area of the cavity  $S' = 4.26 \text{ m}^2$ . The considered frequencies are all the one-third octave bands within 141 - 7080 Hz.

The interrupted noise method was used to measure the reverberation time, following the instructions of ISO 3382-2 <sup>[204]</sup>. For each measurement, white noise covering the bands of interest was generated as input to build a steady-state acoustic field inside the cavity. The excitation had lasted for 10 seconds before it was stopped. Then, after the signal switched off, the responses were continuously recorded for 20 seconds, so that the cavity reached the background noise level for sure. Totally 20 measurements were performed, and the averaging of measurements was made in the preferred way <sup>[204]</sup>, where the ensemble average of the squared sound pressure decays is used. Due to the relatively low Sound Pressure Level (SPL) in the low frequency range, the T20 measurement method was used. In this case, the decay curves start at least 35 dB above the background noise for all the one-third octave bands of interest. The reverberation time is given by



$$T_{60} = 60 / d, \quad (5.3)$$

where  $d$  is the decay rate in decibels per second. It is determined from the slope of the least-squares fit line of the decay curve from 5 dB to 25 dB below the steady-state level. Fig. 5-2 shows an example (measured by  $p_1$ , 1000 Hz one-third octave band) in the data processing for applying the T20 measurement method.

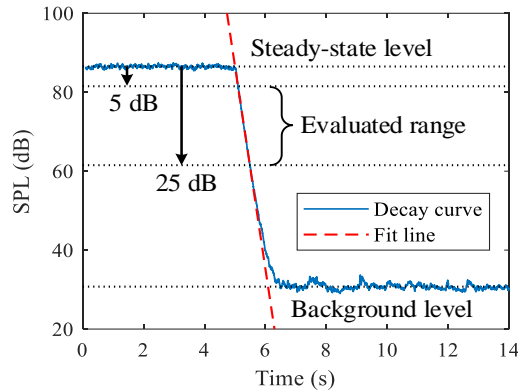


Fig. 5-2. Decay curve measured by  $p_1$  for 1000Hz 1/3 octave band, using the T20 measurement method.

For every 1/3 octave band whose central frequency is between 160 Hz and 6300 Hz, the reverberation time corresponding to each of the six microphones (from  $p_1$  to  $p_6$  as shown in Fig. 5-1 and Fig. 4-11) were obtained following the same procedures, respectively. The results are listed in Table 5-2, where  $f_m$  denotes the 1/3 octave mid-band frequency, and  $T_{60, M_i}$  denotes the reverberation time measured by  $i^{\text{th}}$  microphone (corresponding to  $p_1$  at position  $r_i$ ). The average and standard deviation of the reverberation time are calculated over the six microphone positions for each band using the equations

$$T_{60} = \frac{1}{n_M} \sum_{i=1}^{n_M} T_{60, M_i} \quad \text{and} \quad \sigma_T = \sqrt{\frac{1}{n_M - 1} \sum_{i=1}^{n_M} (T_{60, M_i} - T_{60})^2}, \quad (5.4)$$

with the number of microphone positions  $n_M = 6$ .

Fig. 5-3 shows the change of the reverberation time  $T_{60}$  with the increase of band frequency, where the standard deviation  $\sigma_T$  is also plotted using error bar. As the figure shows, except the first two bands, the reverberation time tends to decrease when the frequency increases, which indicates a higher energy dissipation.

In addition, the sound absorption coefficient  $\bar{\alpha}$  has also been calculated according to Eq. (5.2) and listed in Table 5-2. Fig. 5-4 shows the comparison between the absorption coefficient  $\bar{\alpha}$  of the Noise-Box and the corresponding upper limit of reverberation test room in ISO 3471 <sup>[184]</sup> and ASTM C423-17 <sup>[205]</sup>. It can be observed that the sound absorption of the Noise-Box interior is much smaller than the upper limit of the standard reverberation

room. On the other hand, the absorption coefficient  $\bar{\alpha}$  can be used to update the wall impedance of the numerical models. Under the assumptions that all the sound absorption is uniformly caused by the walls and the sound transmission through walls are negligible, the wall impedance of all the cavity boundaries can be updated with

$$Z = \rho_0 c \frac{1 + \sqrt{1 - \bar{\alpha}}}{1 - \sqrt{1 - \bar{\alpha}}} \quad (5.5)$$

Then, the updated numerical model can be used to analyse the frequency response of the cavity with the damping effect considered.

Table 5-2. Reverberation time  $T_{60}$  and average absorption coefficient  $\bar{\alpha}$  of Noise-Box for 1/3 octave bands

$f_m$ (Hz)	Reverberation time (sec)							$\sigma_T$	$\bar{\alpha}$
	$T_{60, M1}$	$T_{60, M2}$	$T_{60, M3}$	$T_{60, M4}$	$T_{60, M5}$	$T_{60, M6}$	$T_{60}$		
160	2.02	2.02	2.02	2.02	2.02	2.02	<b>2.02</b>	0.00	<b>0.011</b>
200	2.05	2.05	2.03	2.04	2.05	2.05	<b>2.04</b>	0.01	<b>0.011</b>
250	3.30	4.10	5.13	3.14	3.47	3.11	<b>3.71</b>	0.71	<b>0.006</b>
315	2.69	2.65	3.33	3.01	2.73	3.03	<b>2.90</b>	0.24	<b>0.008</b>
400	2.57	3.02	3.09	3.00	3.03	2.61	<b>2.89</b>	0.21	<b>0.008</b>
500	2.37	2.79	2.52	2.59	2.69	2.49	<b>2.58</b>	0.13	<b>0.009</b>
630	1.98	1.99	1.89	2.11	2.06	1.93	<b>1.99</b>	0.07	<b>0.011</b>
800	1.47	1.50	1.43	1.72	1.42	1.44	<b>1.50</b>	0.10	<b>0.015</b>
1000	1.17	1.23	1.15	1.28	1.21	1.19	<b>1.20</b>	0.04	<b>0.019</b>
1250	1.14	1.15	1.07	1.04	1.03	1.03	<b>1.08</b>	0.05	<b>0.021</b>
1600	1.10	1.12	1.12	1.15	1.09	1.07	<b>1.11</b>	0.03	<b>0.020</b>
2000	1.12	1.12	1.10	1.19	1.15	1.15	<b>1.14</b>	0.03	<b>0.020</b>
2500	1.07	1.06	1.03	1.08	1.12	1.02	<b>1.06</b>	0.03	<b>0.021</b>
3150	1.02	1.05	0.96	1.00	1.03	1.03	<b>1.02</b>	0.03	<b>0.022</b>
4000	0.86	0.92	0.90	0.92	0.84	0.92	<b>0.89</b>	0.03	<b>0.025</b>
5000	0.82	0.82	0.83	0.86	0.77	0.82	<b>0.82</b>	0.03	<b>0.028</b>
6300	0.69	0.72	0.71	0.71	0.67	0.70	<b>0.70</b>	0.02	<b>0.032</b>

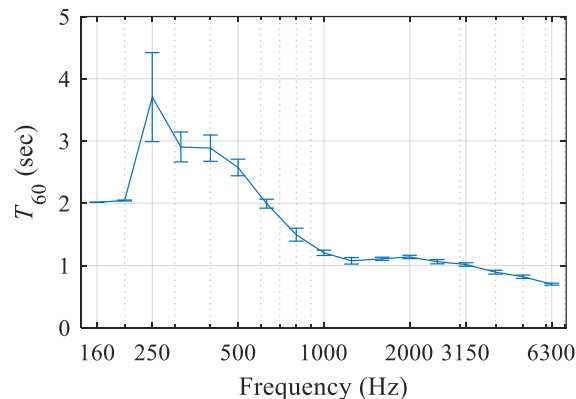


Fig. 5-3. Reverberation time  $T_{60}$  of the Noise-Box in 1/3 octave bands with the error bars representing the standard deviation  $\sigma_T$  over the 6 microphone positions.

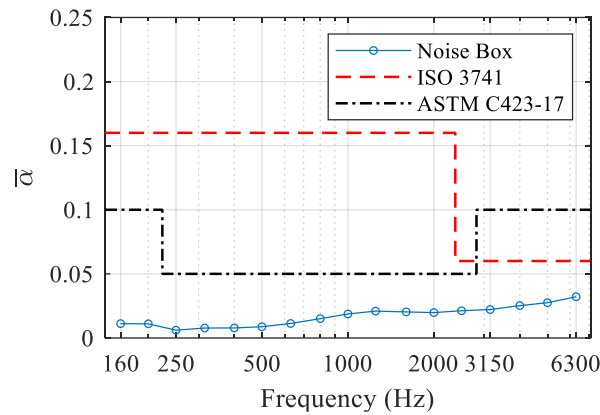


Fig. 5-4. Average absorption coefficient  $\bar{\alpha}$  of the Noise-Box for 1/3 octave bands and the corresponding upper limits of the ISO 3741 and the ASTM C423-17 for qualified reverberation rooms.

### 5.1.5 Diffuseness of the sound field inside Noise-Box

Fig. 5-5 shows the experimental transfer function between the sound pressure measured by one of the microphones ( $p_1$  in Fig. 4-11) and the input signal generated by the waveform generator (see Fig. 5-1). It could be noticed that the natural frequencies of the acoustic field start getting very close to each other above the defined cut-off frequency  $f_{\text{cut}} \approx 650$  Hz. As the frequency increases, the modal density and the modal overlap increase. Meanwhile, the sound field inside becomes more diffused or spatially uniform. Therefore, in the higher frequency range, the diffusivity characteristics of the inner acoustic field becomes more important. It determines whether or from which frequency we can consider the sound field inside to be uniform or use the Noise-Box as a reverberation room. It also relates to the division of solution frequency range for acoustic/vibroacoustic problems <sup>[16]</sup>.

There are several quantifiers for the field diffuseness <sup>[206]</sup>. Two quantifiers are used here to characterize the inner sound field of the Noise Box. One of the quantifiers is the mode count in 1/3 octave band or the modal overlap in 1/3 octave band. Regarding the higher modal overlap at higher frequencies, counting the modes with the experimental transfer function becomes impractical. Accordingly, the proven numerical models (as shown in Fig. 4-12 but smaller element size is used) were used to identify the modes by studying the eigenfrequencies in COMSOL. Since the increase of frequency requires a much larger model size (to keep at least 6 elements per wavelength) and much more extracting modes (up to 7080 Hz), the 2D model was used for saving simulation memory and time. Table 5-3 lists the mode count  $N_m$ , the modal density  $n$  and the modal overlap  $M$  in each 1/3 octave band centred from 160 Hz to 6300 Hz. The modal density  $n$  is defined as number of modes per Hz and computed with the mode count divided by the corresponding bandwidth. The

modal overlap  $M$  is evaluated with  $M = 2.2n/T_{60}$ , using reverberation time  $T_{60}$  from experiment (as listed in Table 5-2).

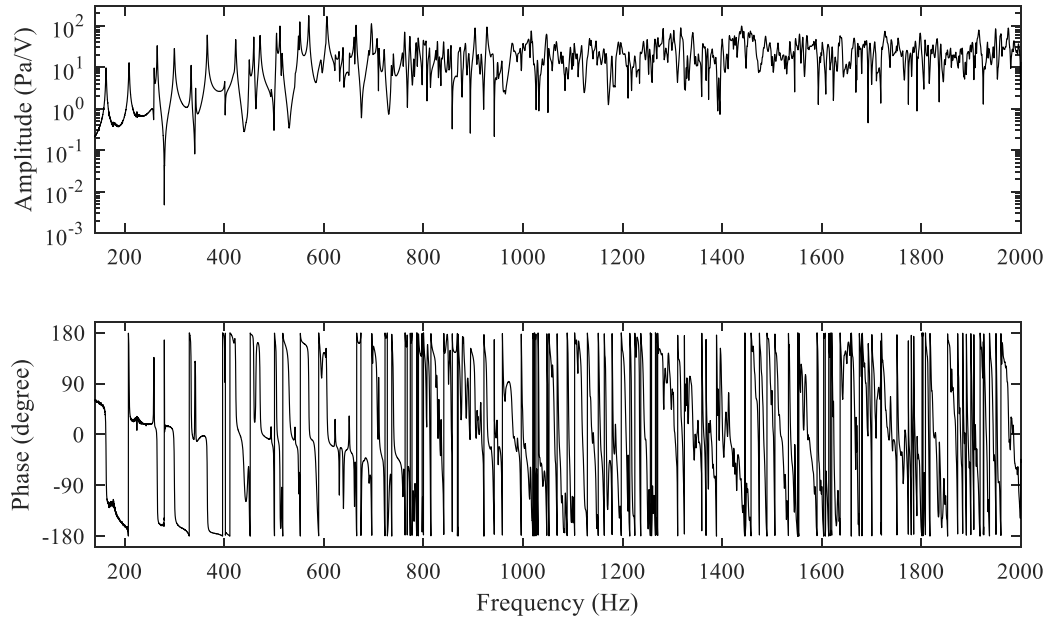


Fig. 5-5. FRF of the Noise-Box cavity in experiment (see Fig. 5-1), where the input is the voltage out of the waveform generator and the output is the sound pressure measured by the microphone whose position is corresponding to  $p_1$  in Fig. 4-11.

Table 5-3. Mode count, modal density and modal overlap in 1/3 octave bands of the Noise-Box

$f_m$ (Hz)	Mode count $N_m$	Modal density $n$ ( $\text{Hz}^{-1}$ )	Modal overlap $M$
160	1	0.027	0.03
200	1	0.022	0.02
250	2	0.034	0.02
315	3	0.041	0.03
400	4	0.043	0.03
500	10	0.087	0.07
630	17	0.116	0.13
800	31	0.169	0.25
1000	55	0.240	0.44
1250	106	0.366	0.75
1600	204	0.551	1.09
2000	392	0.852	1.65
2500	761	1.312	2.72
3150	1476	2.022	4.38
4000	2908	3.161	7.79
5000	5663	4.924	13.23
6300	11238	7.697	24.16

Then, the criteria are considered. The less rigorous one defines the limit to diffuse sound field as more than 20 modes per band. It can be observed from Table 5-3 that the cut-off frequency is between 630 Hz to 800 Hz. Thus, it is valid to use Eq. (3.5) to evaluate the cut-off frequency with  $f_{\text{cut}} = 650$  Hz. The restrictive one known as the Schroeder frequency corresponds to the modal overlap no less than 3. Table 5-3 indicates that the frequency is between 2500 Hz to 3150 Hz, which in conform with the calculation based on Eq. (3.4), where the Schroeder frequency  $f_{\text{sch}} = 2669$  Hz. There is a wide frequency range between  $f_{\text{cut}}$  and  $f_{\text{sch}}$ . It may be reasonable to consider this range as a transition between the modal region ( $f < f_{\text{cut}}$ ) and the highly diffuse Schroeder region ( $f > f_{\text{sch}}$ ). The parameters listed in Table 5-3 also provides a reference for considering whether to use FEM or Statistical Energy Analysis (SEA) methods to analyse the acoustic field. If  $M > 1$  is considered as a prerequisite for applying SEA, the frequency range will be larger than 1250 Hz.

The other quantifier is the sound pressure field uniformity. To evaluate the pressure field uniformity, in other words, is to check the spatial variation. In the experiment, sound pressures at the six microphone positions were measured while the inner acoustic field was at the steady state excited by the white noise input signal up to 8000 Hz. The SPLs among microphone positions are compared for each 1/3 octave band as shown in Fig. 5-6.

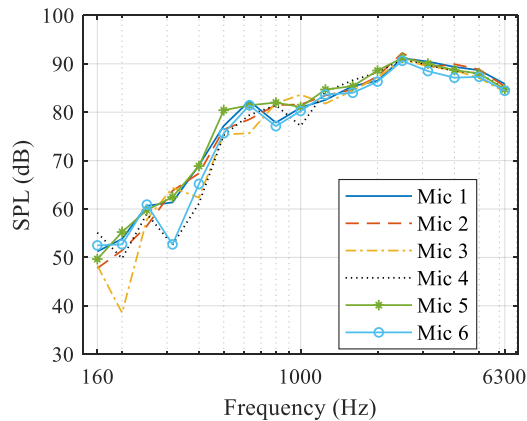


Fig. 5-6. SPLs at the 6 microphone positions inside Noise-Box for 1/3 octave bands.

Corresponding standard deviations  $\sigma_M$  over the six positions can be used for the quantification and these results for the Noise Box are shown in Fig. 5-7. The standard deviation  $\sigma_M \leq 1.5$  dB is acceptable in some cases for the sound field to be considered as uniform <sup>[206]</sup>, while the ISO 3471 <sup>[184]</sup> has a more precise limit to qualify the reverberation test room. Fig. 5-7 includes the maximum allowable lines from both the 1.5 dB limit and the qualification limit from the ISO 3471. However, it should be noticed that the provided qualification limit from the ISO 3471 is originally for the standard deviation over different source locations and also that the other matched requirements with respect to the

microphone and sound source positions are not able to fulfil due to the small size of the Noise Box. According to these criteria, it can be found from Fig. 5-7 that the starting frequency for the diffused field is between 1000 Hz to 1250 Hz, or between 2500 Hz to 3150 Hz. The limit frequency satisfied the ISO 3471 is consistent with the Schroeder frequency  $f_{sch} = 2669$  Hz. Therefore, it is believed that the sound field is sufficiently diffuse in the frequency range higher than the 2500 Hz 1/3 octave band. Nevertheless, it is also practical to consider the Noise Box as a small reverberation room when the frequencies are higher than the 1000 Hz 1/3 octave band.

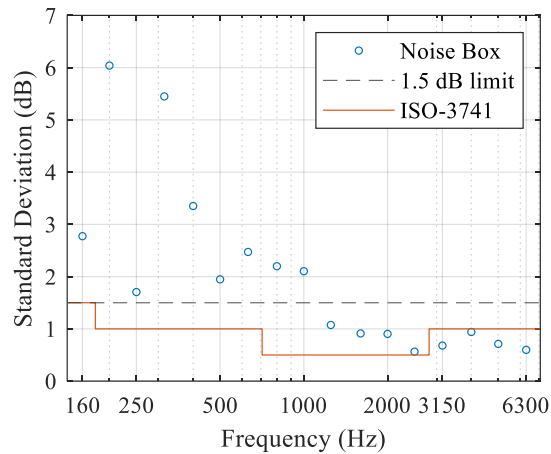


Fig. 5-7. Standard deviation of the SPLs over the 6 microphone positions inside Noise-Box for 1/3 octave bands and the corresponding suggested limits of 1.5 dB and of the ISO 3471 reverberation room qualification.

### 5.1.6 Model update and frequency response analysis

In the Experimental Modal Analysis (EMA), since the recorded signal was from the waveform generator, the obtained transfer function actually results from three component in series, i.e., the amplifier, the loudspeaker and the cavity, as shown in Fig. 5-1. Hence, the transfer functions have following relationship:

$$H_{EMA}(f) = H_{cavity}(f)H_{loudspeaker}(f)H_{amplifier}(f). \quad (5.6)$$

However, what is in interest is the frequency response of the cavity  $H_{cavity}$ , which is one of the characteristics of the test bench and meanwhile able to be compared with the numerical results. Considering the utilized numerical approach as well as the increase of modal overlap and sound field diffuseness/uniformity over frequency, this section focuses the frequency response analysis on the frequency range up to the cut-off frequency 650 Hz, covering the region dominated by the cavity modal properties.

Since  $H_{\text{loudspeaker}}$  and  $H_{\text{amplifier}}$  are not directly available, the frequency response of the cavity is at first predicted using the updated numerical model. The 3D FE model shown in Fig. 4-12 was updated with the wall impedance determined by Eq. (5.5). For each frequency, the value of the absorption coefficient  $\bar{\alpha}$  is shown in Fig. 5-4, and as is illustrated by the curve, the linear interpolation (with the frequency in log scale) is used for the frequencies between the adjacent central frequencies of the 1/3 octave bands. Frequency domain analysis was performed in COMSOL from 141 to 650 Hz at 1 Hz intervals. A monopole sound source with the root mean squared power  $P_{\text{rms}} = 1 \text{ W}$  was applied at the point  $q$  (shown in Fig. 4-11). Then, the sound pressures at the microphone positions ( $p_1$  to  $p_6$ ) were computed and the frequency response of the acoustic field was obtained.  $H_{\text{cavity}}$  is represented by the output sound pressure at one of the microphone positions over the input power in the sound source position. The estimated  $\hat{H}_{\text{cavity}}$  from simulation is shown in Fig. 5-8, using the response at  $p_1$  as an example. The experimental transfer function is also presented for comparison. The two curves have similar shapes, especially the peaks and valleys, which are partly due to the accurate predictions of natural frequencies, as proved in Section 5.1.3. However, the amplitude levels are different. Theoretically, this difference in response level should result from the frequency response of the loudspeaker and the amplifier in chain, between the power input to the acoustic field and the voltage generated by the waveform generator. Therefore, it is able to estimate the transfer function  $H_{\text{loudspeaker}} \cdot H_{\text{amplifier}}$  by estimating the difference.

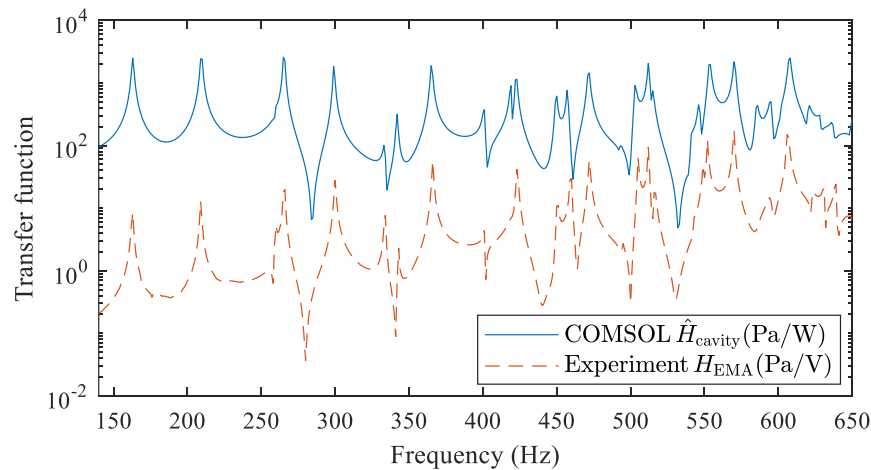


Fig. 5-8. Simulated transfer function of the cavity between  $p_1$  and the input power generated by  $q$  (see Fig. 4-11), and experimental transfer function of the system between  $p_1$  and the input voltage from the waveform generator (see Fig. 5-1)

Suppose that

$$H_{\text{LA}}(f) = H_{\text{loudspeaker}}(f)H_{\text{amplifier}}(f), \quad (5.7)$$

the experimental  $H_{\text{cavity}}$  is then given by

$$H_{\text{cavity}}(f) = H_{\text{EMA}}(f)H_{\text{LA}}^{-1}(f). \quad (5.8)$$

Conversely, the transfer function  $H_{\text{LA}}^{-1}$  is available if  $H_{\text{EMA}}$  and  $H_{\text{cavity}}$  are known, calculated by

$$H_{\text{LA}}^{-1}(f) = H_{\text{EMA}}^{-1}(f)H_{\text{cavity}}(f). \quad (5.9)$$

So far, six transfer functions  $H_{\text{EMA}}$  have obtained corresponding to the six microphones, but  $H_{\text{cavity}}$  are unknown. Only the simulation results  $\hat{H}_{\text{cavity}}$  have been estimated from the numerical model. In order to obtain  $H_{\text{LA}}^{-1}$ , the functions  $\hat{H}_{\text{LA}}^{-1} = H_{\text{EMA}}^{-1}\hat{H}_{\text{cavity}}$  are calculated and depicted in Fig. 5-9, respectively for the six microphones M1 to M6 (corresponding to  $p_1$  to  $p_6$ ). Considering that  $H_{\text{LA}}^{-1}$  is independent of the microphone positions and should change slowly and continuously with the frequency, a curve best fitting the six  $\hat{H}_{\text{LA}}^{-1}$  functions is computed and the fitting outcome is expressed as

$$10\lg(H_{\text{LA}}^{-1}) = -0.02715f + 28.77. \quad (5.10)$$

This fitting curve is plotted in companion with the  $\hat{H}_{\text{LA}}^{-1}$  functions in Fig. 5-9, showing how it follows the variation trend of every  $\hat{H}_{\text{LA}}^{-1}$  even if the  $\hat{H}_{\text{LA}}^{-1}$  functions are clearly different from each other.

From Fig. 5-9, it can be noticed that, to generate the same power from the loudspeaker, a larger voltage should be assigned from the waveform generator as the frequency decreases. This is reasonable and it may result from two aspects. On one hand, the impedance of the loudspeaker increases when the frequency approximates 110 Hz; and on the other, the efficiency of the loudspeaker significantly decreases at lower frequency because it is placed inside the cavity un baffled <sup>[207]</sup>. However, it is worth noting that the expression Eq. (5.10) is only effective within the frequency range under consideration. For higher frequencies, the relationship may change because the aforementioned two aspects are under different situations.

Then, based on Eq. (5.10), the transfer function  $H_{\text{LA}}^{-1}$  is obtained. Substitution of the  $H_{\text{LA}}^{-1}$  and utilization of the experimental results  $H_{\text{EMA}}$ , the  $H_{\text{cavity}}$  out of experiment are derived. These estimations based on the experimental results are shown in Fig. 5-10, compared with the simulation results  $\hat{H}_{\text{cavity}}$ . A good agreement is seen from the figure between the numerical and experimental results, even though there some unavoidably discrepancies between the simulation and the experiment. For example, the loudspeaker is not an ideal monopole source and its location cannot be exactly identified. Similarly, the microphone positions are approximate.



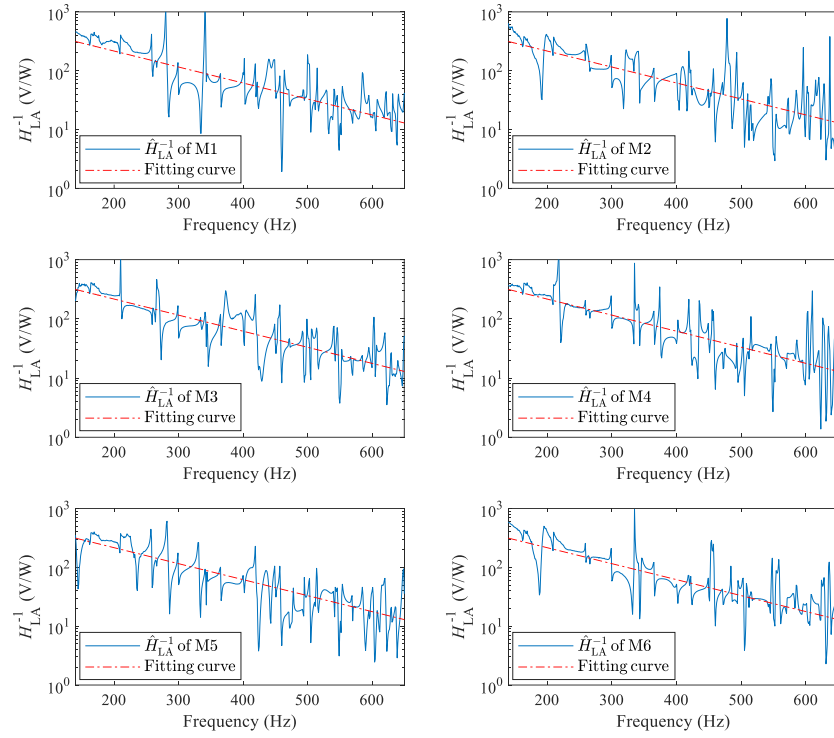


Fig. 5-9. Comparison between the best fitting  $H_{LA}^{-1}$  (see Eq. (16)) and the estimated  $\hat{H}_{LA}^{-1}$  of different microphones from M1 to M6 (i.e.,  $p_1$  to  $p_6$ ).

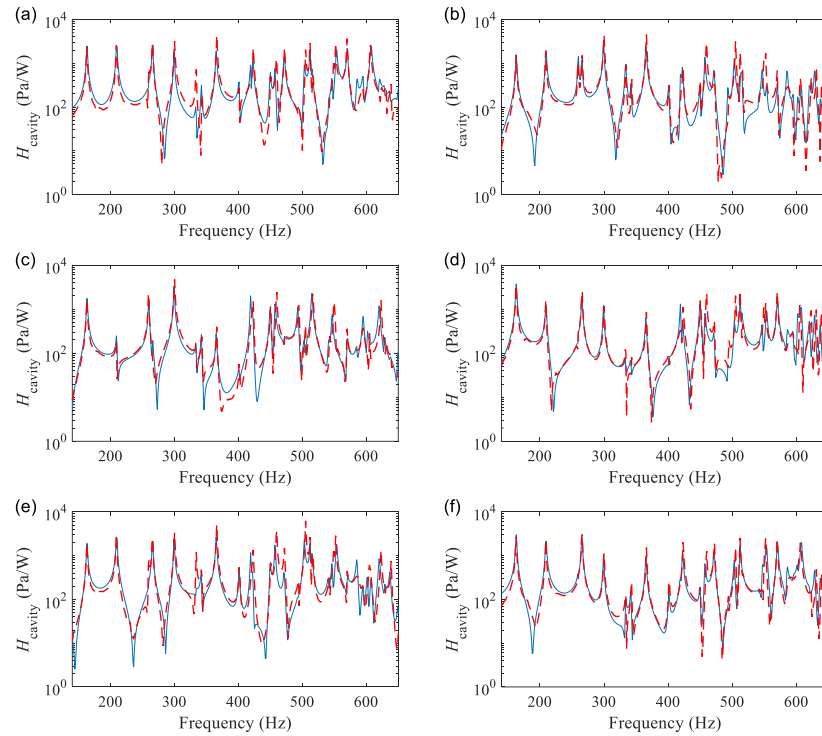


Fig. 5-10. FRFs (solid: COMSOL  $\hat{H}_{cavity}$ ; dashed: Experiment  $H_{cavity}$ ) of the Noise Box cavity within 141 to 650 Hz at 1 Hz intervals. Input power is from  $q$  (see Fig. 4-11) and output pressure is: (a)  $p_1$ ; (b)  $p_2$ ; (c)  $p_3$ ; (d)  $p_4$ ; (e)  $p_5$ ; (f)  $p_6$ .

## 5.2 Test panel characterization

The test panel to be mounted on the Noise-Box for structure-born and airborne noise investigations is a 4-mm thick aluminium plate, whose CAD drawing is shown in Appendix A.5 Clamped panel. This section is to characterize the mounted test panel on its own, without the coupling effect coming from the Noise-Box cavity. The targets are to obtain its modal parameters and meanwhile to identify its material properties and boundary conditions for model updating. The requiring modal parameters, including natural frequencies, mode shapes and modal damping ratios are obtained through EMA. Later, the parameters for model updating are identified with additional measurements and analyses. These parameters can be divided into two parts. One is the geometric and material parameters of the panel itself regardless of boundary conditions; the other is edge conditions of the test panel when it is mounted on the Noise-Box.

### 5.2.1 EMA of mounted test panel

#### 5.2.1.1 Experimental set-up

The practice of modal testing is about obtaining FRFs of the structure. Aimed at this, an experimental system was set up as shown in Fig. 5-11. Input excitation is the impact of hammer (PCB 086C03). Response of panel is the acceleration measured by accelerometer (PCB 333B30). Acquisition system (NI cDAQ) and sensor signal conditioner (PCB 483C) are the same instruments used in the cavity characterization. Test panel has been mounted on the Noise-Box test bench with the steel clamped frame and 80 screws (see Fig. 3-5(b)). The screws were fixed under controlled torque 17 N·m. Besides, the inner walls of the Noise-Box have been covered with absorbing materials to minimize the back effect from the acoustic cavity. The thermo-hygrometer (INKBIRO IBS-TH1 Mini) is kept inside, monitoring the temperature and humidity.

As shown by Fig. 5-12, a grid was labelled on the panel. It consists of 80 points arranged as  $10 \times 8$  in a quarter of the panel. They are the positions where the hammer should hit. In other words, roving hammer strategy was used to obtain the FRFs at different positions, for obtaining the mode shapes. The advantages are that mass loading of the accelerometers on the panel is minimized and that roving hammer is more convenient than roving accelerometers. Meanwhile, the grid was designed based on the mode shapes planned to identify. Considering the minimum as 5 points per wavelength, the current setting can reach to around the 48<sup>th</sup> mode. Moreover, six accelerometers were glued: 3 inside the first quarter and 3 inside the rest three quarters. As indicated from the figure, the accelerometers A2, A4, A5 and A6 are approximately symmetric about the central lines of the panel. In fact,

they were designed to be symmetric. Such an arrangement of hitting points and accelerometer locations is intended to take the advantage of the symmetry of the panel. Therefore, the grid is only on one quarter of the vibrating area of the plate, and A4-A6 are used to validate the symmetry and identify if the monitoring quarter is in phase or out of phase compared with A2. Then, the mode shape of the whole panel can be interpreted from the single quarter. This significantly reduces the number of hitting points.

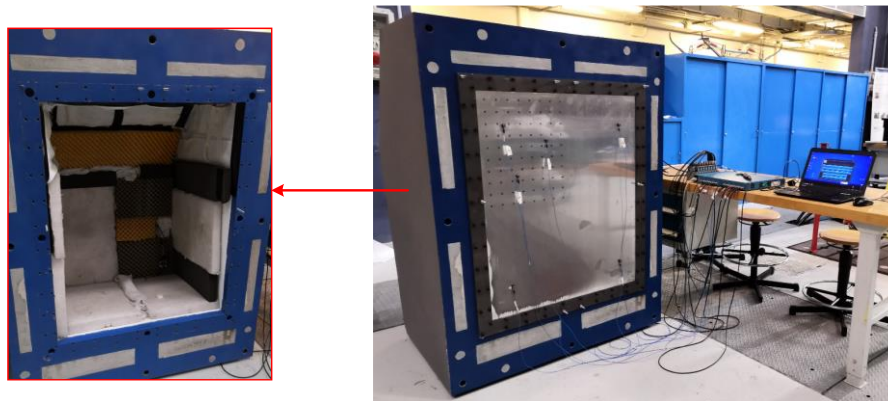


Fig. 5-11. Experimental set-up for mounted panel characterization

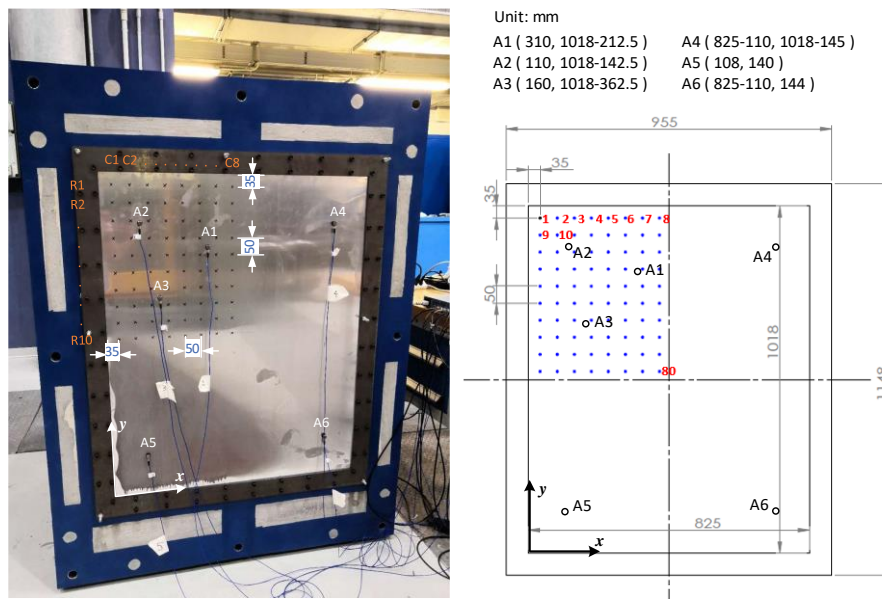


Fig. 5-12. Mounted test panel configuration: arrangement of accelerometers and hammering grid.

### 5.2.1.2 Hammer test procedures

At first, the frequency range of interest was determined. The frequency range to obtain all the modal parameters was proposed to reach the upper limit around 650 Hz, which is also the upper limit for the identified acoustic cavity modes in Section 5.1.3. However, the FRFs

can cover a wider frequency range, so that more natural frequencies can be identified from the resonance peaks. Then, the medium tip (in white) was selected and installed to the hammer. The resulting impulse can guarantee a sound spectrum till 1000-1500 Hz. Sampling frequency should be larger than 2 times of the maximum frequency of interest, and it was set as 5120 Hz in the experiment. The response duration was 15 sec, depending on the decay of the system.

Next, the grid points on the panel were hit by the hammer one by one. Each point was hit 10 times in succession, and the interval between two hits should larger than 15 sec. In the process, the time history of the signals generated from the hammer and accelerometers was acquired and stored.

Then, the signals were processed in MATLAB. Double hits were removed if any. FRF of every pair of output acceleration and input force was obtained using H1 estimator <sup>[208]</sup>, accompanied with the corresponding coherence function. Fig. 5-13 shows an example of the measured FRFs, whose output is acceleration at A1 and input is the force at Point 80 (refer to Fig. 5-12 for input-output locations).

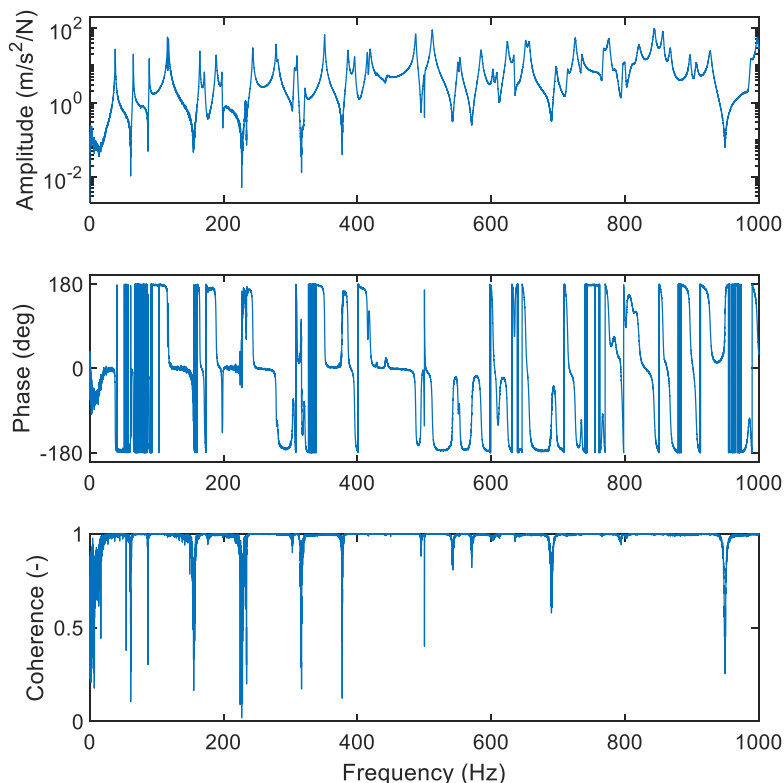


Fig. 5-13. Measured transfer function and coherence function of the uncoupled panel (see Fig. 5-12) between acceleration at A1 and force at Point 80.

### 5.2.1.3 Modal parameters identification

Modal parameters are identified based on the data acquired from modal testing. In our case, they were determined by the FRFs obtained from the hammer test, using the least-squares best fitting approach [87].

Theoretically, the FRF in terms of receptance between points  $j$  and  $k$  is given by (for  $N$  modes)

$$\alpha_{jk}(\omega) = \sum_{r=1}^N \frac{\phi_{j,r} \phi_{k,r}}{\omega_r^2 - \omega^2 + 2i\zeta_r \omega_r \omega} = \sum_{r=1}^N \frac{C_{jk,r}}{\omega_r^2 - \omega^2 + 2i\zeta_r \omega_r \omega}, \quad (5.11)$$

where,  $\omega_r$  are the natural frequencies,  $\zeta_r$  are the non-dimensional modal damping ratios, and  $C_{jk,r}$  are modal constants or modal residues. Meanwhile, the relationship  $C_{jk,r} = \phi_{j,r} \phi_{k,r}$  indicates the principle of reciprocity:  $\alpha_{kj} = \alpha_{jk}$ . For the receptance function in a frequency range that includes only  $n_1^{\text{th}}$  to  $n_2^{\text{th}}$  modes, Eq. (5.11) can be rewritten as [85,87]

$$\alpha_{jk}(\omega)_{\omega \in \omega_r} = \frac{1}{\omega^2 M_{jk}^R} + \sum_{r=n_1}^{r=n_2} \frac{C_{jk,r}}{\omega_r^2 - \omega^2 + 2i\zeta_r \omega_r \omega} + \frac{1}{K_{jk}^R}, \quad (5.12)$$

where,  $M_{jk}^R$  and  $K_{jk}^R$  are respectively the coefficients of the lower and upper residuals, which compensate for the out-of-band effects. According to the relationship between accelerance ( $\text{m}\cdot\text{s}^{-2}/\text{N}$ ) and receptance ( $\text{m}/\text{N}$ ), i.e.,  $A_{jk}(\omega) = -\omega^2 \alpha_{jk}(\omega)$ , the FRFs of the modal model are eventually given by

$$A_{jk}^{\text{mod}}(\omega)_{\omega \in \omega_r} = -\omega^2 \left( \frac{1}{\omega^2 M_{jk}^R} + \sum_{r=n_1}^{r=n_2} \frac{C_{jk,r}}{\omega_r^2 - \omega^2 + 2i\zeta_r \omega_r \omega} + \frac{1}{K_{jk}^R} \right). \quad (5.13)$$

Since FRFs are known from the hammer test, the unknown parameters  $\omega_r$ ,  $\zeta_r$ ,  $C_{jk,r}$ ,  $M_{jk}^R$  and  $K_{jk}^R$  can be determined through an optimization algorithm that makes the model FRFs  $A_{jk}^{\text{mod}}(\omega)$  best fit the experimental FRFs  $A_{jk}^{\text{exp}}(\omega)$ . In other words, it is to solve the problem:

$$\underbrace{\hat{\omega}_r, \hat{\zeta}_r, \hat{C}_{jk,r}}_{n_1 \leq r \leq n_2}, \hat{M}_{jk}^R, \hat{K}_{jk}^R = \arg \min \left\| A_{jk}^{\text{exp}}(\omega) - A_{jk}^{\text{mod}}(\omega) \right\|_{\omega \in \omega_r}^2. \quad (5.14)$$

Practically, the solution was obtained in MATLAB by implementing the function 'lsqnonlin', which is a nonlinear least-square solver. As shown by Eqs. (5.13)-(5.14), the number of modes in one solution is dependent, determined by the user. However, it is worth noting that the fitting frequency range should include only the identifying modes. Besides, the number of optimizing parameters will increase with the number of included modes. Consequently, the function is more complex and the first guess of those parameters becomes more essential for convergence or reaching the desire minimum. Furthermore, while Eq. (5.14) is expressed for a single FRF, it can also be expanded to multiple FRFs, where the functional for minimization is the square error of all the considered FRFs.

Since  $\hat{\omega}_r$  and  $\hat{\zeta}_r$  should respectively reach consistent values among different FRFs (provided that the system is linear and stable), the strategy implemented was to include the total 80 FRFs  $A_{1k}(\omega)$  and only one or several modes in one optimization. The first guess of natural frequency  $\omega_r$  was peak-picked from one of the experimental FRFs. Then, the best fitting results provided the modal parameters of the considered mode(s).  $\hat{\omega}_r$  and  $\hat{\zeta}_r$  are the natural frequency and the damping ratio, while  $\hat{C}_{1k,r}$  can be used to derive the mode shape. After the repetitions to other modes, all modal parameters within frequency range of interest were obtained (except that the 25<sup>th</sup> mode was identified from  $A_{2k}(\omega)$ ). The identified natural frequencies and damping ratios through this process are listed in Table 5-4, denoted as ‘global best fitting for 80 FRFs’. The FRF  $A_{180}^{\text{mod}}(\omega)$  reconstructed according to the modal model, using these globally identified natural frequencies and damping ratios is shown in Fig. 5-14. The reconstructed curve shows a good agreement with the experimental one.

On the other hand, it is practical to fit the whole curve (e.g.,  $A_{180}^{\text{exp}}(\omega)$ ) in one shot, identifying the 36 natural frequencies and damping ratios. However, this case requires the initial values of the optimizing parameters very close to the final results. In consequence, it was implemented for  $A_{180}^{\text{exp}}(\omega)$  using the primary fitting results as the initial values. Then, the further optimized results are shown in Table 5-4, denoted as ‘best fitting for  $A_{180}$ ’. As shown by Fig. 5-15, this optimization makes the model curve better match the experimental one, especially for in the low frequency region around the first four resonances.

If the results of the two fittings in Table 5-4 are compared, it can be noticed that the two sets of natural frequencies are very close for each mode but still slightly different. Though very small, the difference indicates the variation of natural frequencies among FRFs. Relatively, the low frequency region is more affected, and 1<sup>st</sup> mode is the most. To check the utmost variation, the 80 FRFs were analysed, by which, it was found that first natural frequency ranges between 37.6 Hz and 38.2 Hz. The main cause should be the long time span for the hammer test, where totally 80 points were respectively hit 10 times one by one. From morning to the afternoon, the environment was changed and the boundary conditions of the panel might be affected without notice. Due to the shift of natural frequencies, the damping ratios are overestimated in the global best fitting. Therefore, as for natural frequencies and damping ratios, the outcome of the single curve best fitting is preferred and adopted.

Table 5-4. Two sets of identified modal parameters for the uncoupled panel through EMA. The set on the right is the final decision for natural frequencies  $f_r$  and damping ratios  $\zeta_r$ .

Order	Global best fitting for 80 FRFs $A_{1k}$			Best fitting for $A_{180}$	
	Mode	$f_r$ (Hz)	$\zeta_r$	$f_r$ (Hz)	$\zeta_r$
1	(1,1)	37.86	0.00920	38.10	0.00462
2	(1,2)	65.03	0.00355	65.14	0.00176
3	(2,1)	88.69	0.00433	88.93	0.00157
4	(2,2)	116.14	0.00224	116.21	0.00141
5	(1,3)	117.62	0.00430	117.64	0.00278
6	(2,3)	164.51	0.00192	164.50	0.00137
7	(3,1)	171.04	0.00336	171.29	0.00282
8	(1,4)	188.85	0.00366	188.88	0.00297
9	(3,2)	197.42	0.00202	197.55	0.00149
10	(2,4)	233.08	0.00327	233.09	0.00242
11	(3,3)	243.65	0.00235	243.67	0.00200
12	(1,5)	278.71	0.00200	278.63	0.00173
13	(4,1)	280.42	0.00466	280.70	0.00446
14	(4,2)	305.63	0.00292	305.74	0.00274
15	(3,4)	309.70	0.00192	309.75	0.00140
16	(2,5)	321.69	0.00216	321.59	0.00204
17	(4,3)	351.00	0.00145	351.00	0.00123
18	(1,6)	385.73	0.00193	385.77	0.00164
19	(3,5)	395.80	0.00194	395.74	0.00178
20	(4,4)	414.83	0.00167	414.85	0.00142
21	(5,1)	418.69	0.00261	418.84	0.00233
22	(2,6)	428.68	0.00165	428.72	0.00104
23	(5,2)	442.66	0.00347	443.51	0.00360
24	(5,3)	487.02	0.00155	487.01	0.00142
25	(4,5)	<b>499.75</b>	<b>0.00144</b>	499.80	0.00097
26	(3,6)	500.52	0.00179	500.62	0.00182
27	(1,7)	511.93	0.00194	511.79	0.00181
28	(5,4)	550.32	0.00159	550.36	0.00139
29	(2,7)	553.20	0.00171	553.04	0.00155
30	(6,1)	584.63	0.00215	584.65	0.00195
31	(4,6)	602.43	0.00158	602.45	0.00149
32	(6,2)	608.40	0.00186	608.42	0.00181
33	(3,7)	624.10	0.00187	623.97	0.00176
34	(5,5)	633.87	0.00108	633.82	0.00101
35	(6,3)	651.32	0.00175	651.30	0.00160
36	(1,8)	656.78	0.00208	656.55	0.00197

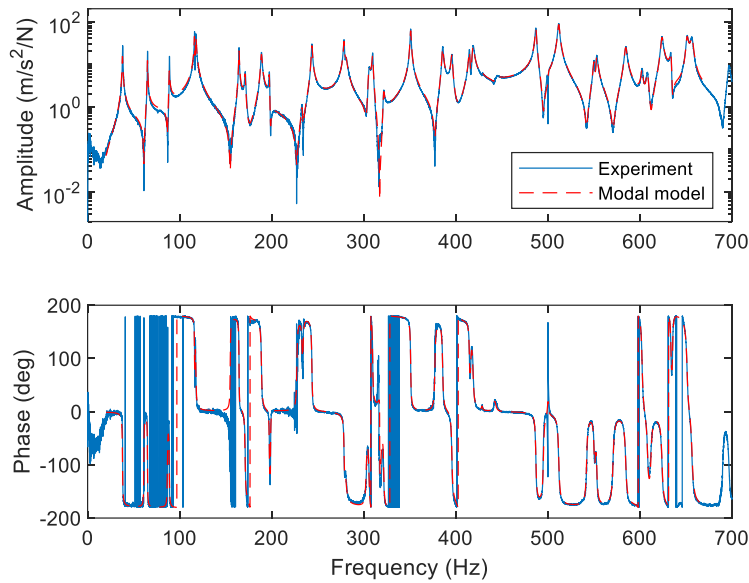


Fig. 5-14. Comparison of the uncoupled panel acceleration  $A_{180}(\omega)$  between experiment and the modal model with parameters from the global best fitting of 80 FRFs  $A_{1k}$  (see Table 5-4).

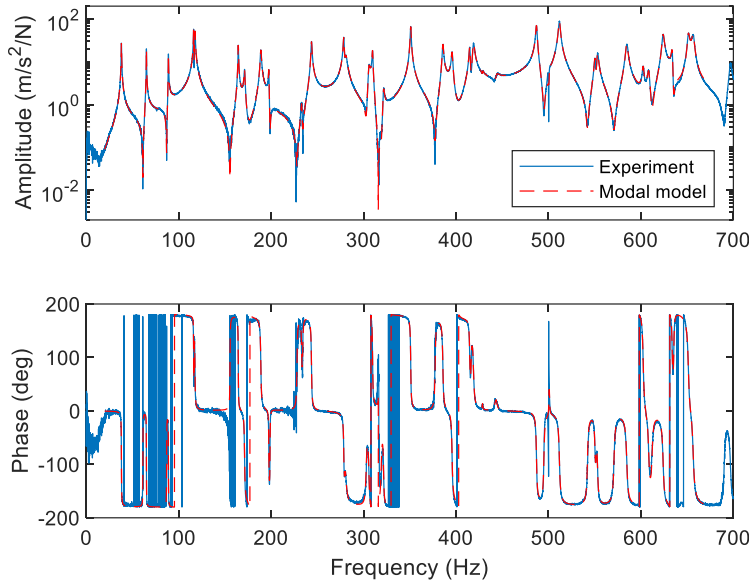


Fig. 5-15. Comparison of the uncoupled panel acceleration  $A_{180}(\omega)$  between experiment and the modal model with parameters from the single curve best fitting of the entire FRF  $A_{180}$  (see Table 5-4).

As indicated from the subscripts of  $A_{1k}(\omega)$  and  $\hat{C}_{1k,r}$ , this identification is based on the acceleration measured by A1 (see Fig. 5-12). According to the principle of reciprocity,  $A_{1k}(\omega) = A_{k1}(\omega)$  and  $\hat{C}_{1k,r} = \hat{C}_{k1,r}$ , the process is equivalent to hit the panel at A1 and measure the responses of the 80 grid points. Thus, the ratios of modal constants  $\hat{C}_{1k,r}, k = 1, \dots, 80$  approximate to the ratios of the plate displacements at those points for  $r^{\text{th}}$  mode. Fig. 5-16



shows an identified mode shape at 414.83 Hz (the 20<sup>th</sup> mode), normalized by the maximum amplitude, where Fig. 5-16(a) illustrates the non-dimensional displacement within the grid of 80 points at one quarter of the panel, and Fig. 5-16(b) depicts the mode shape of the whole panel. In Fig. 5-16(b), the rest three quarters were derived based on the first quarter by symmetricity or anti-symmetricity, according to the accelerations at A4, A5 and A6, respectively, compared with A2 (see Fig. 5-12 for A4, A5, A6 and A2). Concerning other mode shapes, the denotation  $(m,n)$  is used for listing them in Table 5-4, accompanied with other modal parameters.  $m$  and  $n$  are respectively the mode order (or the number of anti-nodes) in  $x$  and  $y$  directions. For example, the mode in Fig. 5-16 is represented by  $(4,4)$ .

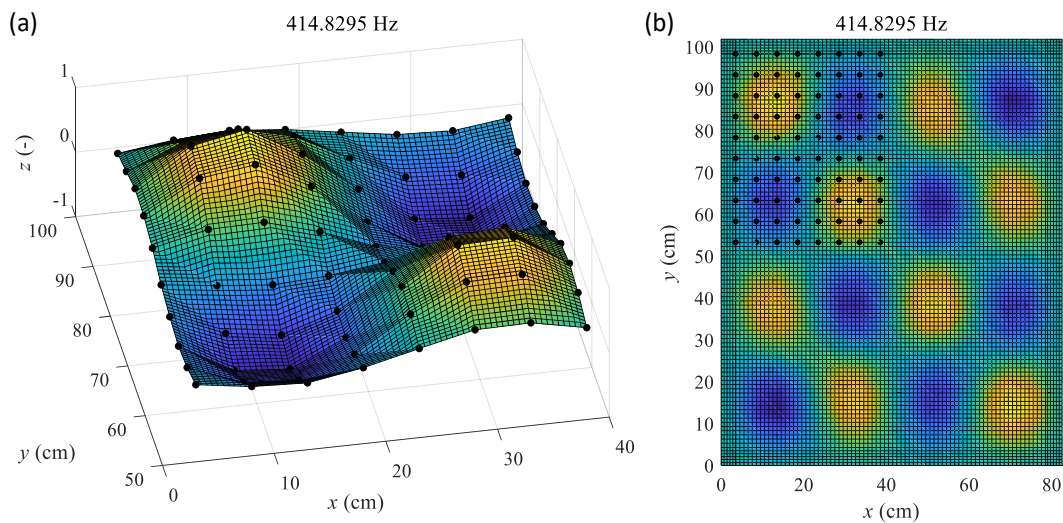


Fig. 5-16. Mode shape of the 20<sup>th</sup> mode of uncoupled panel represented by the non-dimensional displacement of: (a) the experimental grid in one quarter of the panel; (b) the whole panel.

#### 5.2.1.4 Discussion

In Section 5.2.1.3, it is mentioned that the panel's natural frequencies were changed over time. Indeed, this is a problem that had been noticed during the experiments and was tried to be addressed by controlling and monitoring the temperature. Before the test that has been introduced, there was another complete EMA, where the shift of natural frequencies is too serious to yield a correct mode shape because of the significant change of ambient temperature. Learned from that experience, the second EMA, as described from Section 5.2.1.1 to Section 5.2.1.3, has shortened the experimental time span and kept the environment stable (temperature:  $24.2 \pm 0.1^\circ\text{C}$ ). Nevertheless, it is interesting to figure out the real reasons why the panel's modal properties were changed. It is also very important to know how to stabilize or control the properties, so that we can make sure that the service panel is equivalent to the one we have characterized.

Table 5-5. Identified natural frequencies  $f_r$  and damping ratios  $\zeta_r$  from the besting fitting of experimental FRF  $A_{180}$ . Three measurements correspond to three different ambient temperatures  $T_A$  in the preliminary test. ( $T_0$  is an unknown original temperature.)

Order	Meas. 1 ( $T_A = T_0$ )		Meas. 2 ( $T_A > T_0$ )		Meas. 3 ( $T_A < T_0$ )	
	$f_r$ (Hz)	$\zeta_r$	$f_r$ (Hz)	$\zeta_r$	$f_r$ (Hz)	$\zeta_r$
1	39.08	0.00640	36.45	0.00572	43.09	0.00487
2	66.71	0.00254	62.90	0.00273	71.81	0.00287
3	89.41	0.00185	86.73	0.00191	94.19	0.00189
4	----	----	----	----	----	----
5	119.17	0.00292	115.10	0.00283	124.62	0.00301
6	166.07	0.00183	162.16	0.00177	171.44	0.00210
7	171.35	0.00275	168.74	0.00322	176.46	0.00341
8	190.58	0.00322	186.37	0.00341	196.10	0.00317
9	198.13	0.00194	194.81	0.00214	203.37	0.00162
10	234.85	0.00292	230.69	0.00283	240.59	0.00313
11	244.65	0.00213	240.98	0.00222	250.08	0.00188
12	280.19	0.00221	276.15	0.00284	285.77	0.00313
13	----	----	----	----	----	----
14	305.92	0.00315	302.62	0.00315	311.51	0.00311
15	311.01	0.00204	307.16	0.00202	316.62	0.00212
16	323.37	0.00220	319.10	0.00269	329.18	0.00213
17	351.61	0.00172	348.16	0.00173	357.17	0.00156
18	387.88	0.00190	383.53	0.00204	393.77	0.00171
19	396.85	0.00213	392.72	0.00208	402.64	0.00190
20	417.80	0.00310	411.84	0.00210	421.45	0.00168
21	430.99	0.00095	415.28	0.00278	423.59	0.00301
22	430.99	0.00095	426.64	0.00056	436.75	0.00112
23	443.41	0.00266	439.72	0.00285	449.30	----
24	487.07	0.00185	483.77	0.00193	492.84	0.00194
25	500.26	0.00139	496.33	0.00141	506.06	0.00122
26	501.81	0.00171	497.68	0.00165	507.78	0.00200
27	513.73	0.00208	509.35	0.00234	519.87	0.00203
28	549.99	0.00172	546.47	0.00180	555.83	0.00164
29	555.52	0.00197	551.15	0.00193	561.60	0.00178
30	583.03	0.00221	580.31	0.00218	589.06	0.00199
31	602.65	0.00161	598.71	0.00181	608.66	0.00178
32	607.82	0.00246	604.46	0.00331	613.90	0.00206
33	625.31	0.00203	621.06	0.00211	631.47	0.00200
34	633.62	0.00120	629.88	0.00132	639.52	0.00107
35	650.94	0.00172	647.65	0.00161	656.97	0.00177
36	658.45	0.00195	654.49	0.00238	664.59	0.00187
Time	2020/6/25 12:41		2020/6/29 17:46		2020/6/30 11:02	

Table 5-5 lists the natural frequencies and damping ratios identified from the experimental FRFs  $A_{180}^{\text{exp}}(\omega)$  of three measurements in the preliminary unrecorded test. The first measurement was performed immediately after the panel had been mounted. Then, the panel was kept mounted, and the second and third measurements were done respectively under higher and lower temperature. Unfortunately, the temperatures  $T_A$  were unmeasured

but they should be at least some degrees Celsius different from each other, since the experimenters remember the hot afternoon of Meas. 2 when the air conditioner was malfunctional and the cold morning of Meas. 3 when the air conditioner was just repaired and worked too hard. As shown by the table, the natural frequencies increase if the ambient temperature increases, and vice versa. The temperature may be influential in two ways: one is the thermal expansion and the other is the change of material properties. With reference to a paper on similar problem <sup>[147]</sup>, the former is considered dominant.

The thermal expansion is effective through several aspects. First and foremost, it leads to thermal stress in the panel, since the constrained edges avoid the panel expanding or contracting freely. If the plate is heated or cooled uniformly throughout the thickness, additional membrane forces are introduced. The heated case corresponds to in-plane compression that decreases the natural frequencies, while the cooled case corresponds to in-plane tension that functions inversely <sup>[147,157,161]</sup>. Moreover, due to its small thickness and wide span, the panel is rather sensitive to the membrane forces <sup>[157]</sup>. For validating such thermal effects, simulations were performed in COMSOL, comparing the natural frequencies of a clamped panel before and after the temperature is changed by 1°C. The original case ( $\pm 0^\circ\text{C}$ ) is the one analysed in Section 4.2.5.2. Table 5-6 lists simulation results. The decrease and increase of natural frequency are presented as expected, but the variations are larger than the experiments. This is reasonable, because in experiment, the temperature changed very slowly, during which the thermal stress was also releasing. Secondly, the thermal expansion could also affect the panel's edge conditions. For example, the deformation of screws might influence the clamping force.

Table 5-6. Numerical natural frequencies  $f_s$  of the ideally clamped panel without thermal expansion ( $\pm 0^\circ\text{C}$ ) and with thermal expansion caused by increase ( $+1^\circ\text{C}$ ) or decrease ( $-1^\circ\text{C}$ ) of temperature.

Mode order	$f_s$ (Hz)			Mode order	$f_s$ (Hz)			Mode order	$f_s$ (Hz)		
	$\pm 0^\circ\text{C}$	$+1^\circ\text{C}$	$-1^\circ\text{C}$		$\pm 0^\circ\text{C}$	$+1^\circ\text{C}$	$-1^\circ\text{C}$		$\pm 0^\circ\text{C}$	$+1^\circ\text{C}$	$-1^\circ\text{C}$
1	43.9	35.5	50.8	13	301.3	291.0	311.2	25	538.3	527.7	548.7
2	77.8	68.4	86.2	14	329.9	319.8	339.8	26	539.0	528.4	549.3
3	100.0	90.8	108.5	15	337.2	326.8	347.3	27	546.1	535.6	556.4
4	131.3	121.6	140.3	16	349.0	338.6	359.1	28	590.3	579.7	600.6
5	132.8	122.9	142.0	17	379.3	369.0	389.3	29	592.3	581.7	602.7
6	183.6	173.6	193.2	18	414.2	403.8	424.4	30	616.6	606.2	626.8
7	185.9	176.2	195.1	19	428.2	417.7	438.5	31	645.3	634.9	655.6
8	207.4	197.3	217.1	20	444.1	433.9	454.1	32	647.8	637.1	658.2
9	215.9	205.9	225.4	21	448.7	438.3	459.0	33	669.2	658.5	679.7
10	256.4	246.1	266.3	22	461.0	450.5	471.3	34	678.6	668.0	689.1
11	266.3	256.1	276.1	23	473.1	462.8	483.2	35	693.5	683.0	703.9
12	300.6	290.6	310.3	24	521.8	511.4	532.0	36	697.1	686.5	707.6

For demonstrating how the temperature affects the natural frequencies of different modes, the variations  $Er_f$  from the original values ( $f_r$  of Meas. 1 for experimental cases and  $f_s$  of  $\pm 0^\circ\text{C}$  for simulation cases) are computed and plotted in Fig. 5-17. Two main conclusions can be drawn from the figure. For one thing, from the experimental results (Fig. 5-17(a)), it can be noticed that the difference of natural frequencies between measurements is quite consistent among different modes. It seems slowly increase with the mode order, but the slope is very small, except the first several modes. For the other, a similar tendency is observed from the simulation results. Therefore, the frequency shift in experiment could mainly result from the thermal stress.

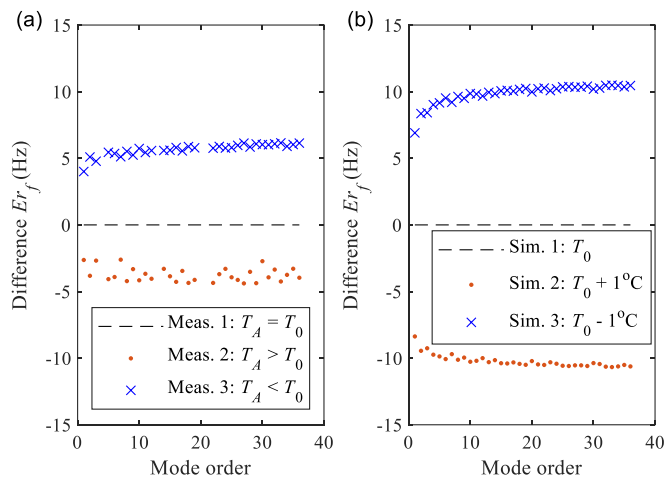


Fig. 5-17. Difference of natural frequencies between the temperature -increased or -decreased case and the original case: (a) three measurements in the preliminary test (Table 5-5); (b) three simulations for an assumed clamped panel (Table 5-6).

## 5.2.2 Free panel geometric and material properties

The geometric and material parameters are inherent properties of the panel itself, and thus unrelated to the boundary conditions or edge restraints. Hence, they can be identified either the panel is clamped or free. In this subsection, the panel is investigated under free-free boundary conditions to characterise these parameters.

Besides the modal parameters obtained in the previous subsection, the other pre-acknowledged information about the test panel is shown by its CAD drawing in Appendix A.5 Clamped panel. The material is known as aluminium, and all dimensions are specified. Particularly, thickness of the test panel is 4 mm. It is well-known to all that there are tolerances to the specified dimensions. Among them, the small deviation in thickness has the greatest impact on the test panel's vibroacoustic performance. Besides, though it is claimed to be made of aluminium, the material properties are not guaranteed as the pure

aluminium. When alloyed and treated differently, the aluminium product results in different properties. Therefore, the density, Young's modulus and Poisson's ratio are not going to be the same as what we assumed in Chapter 4. Since they are all decisive parameters for the plate model, all mentioned above, i.e., the thickness  $h$ , density  $\rho$ , Young's modulus  $E$  and Poisson's ratio  $\nu$  are determined at first. Later, the boundary conditions of the mounted plate will be characterized in the next subsection.

#### 5.2.2.1 Parameter value ranges

As a start point to updating the geometric and material parameters, their possible ranges are proposed based on *a priori* knowledge from simple measurements or literature review. The ranges of dimensions are provided based on repeated measurements using meter or calliper. Two 4-mm panels were manufactured and they were cut from one aluminium plate. One panel is the *test panel* with 80 holes, drawn in Appendix A.5 Clamped panel, and the other has 8 holes, shown by Appendix A.6 Free panel. They can be considered have the same material properties and the same tolerance of thickness. Since the latter is not used for the vibroacoustic investigation, it is called *substitute panel* to distinguish it from the test panel. Based on the measurement, it is confident that the errors of lateral dimensions are less than 1 mm and that the error of thickness is less than 0.1 mm. The ranges are, respectively, [954,955] mm, [1147,1148] mm and [3.9,4] mm. These are slightly enlarged ranges. The probability is higher that the real values are located close to the designed values. The ranges of material parameters are concluded from the ASM handbook <sup>[209]</sup>, focusing on the aluminium alloys that are commonly used for aluminium sheet or plate. The density can be [2590, 2730] kg/m<sup>3</sup>, but tends to be within [2630, 2700] kg/m<sup>3</sup>, as will be discussed later with the panel weight. Meanwhile, since the panel is observed soft and bright, we tend to believe that the aluminium has a relatively high purity. For another, the moduli of elasticity are also dependent mainly on the composition <sup>[209]</sup>. It is stated that the moduli in compression are approximately 2% higher than the tension situation. However, they are not distinguished here and both are claimed as Young's modulus. According to the handbook, the Young's modulus should within the range [68,79] GPa. Regarding the Poisson's ratio, a good agreement is seen among different aluminium alloys and it is approximately 0.33.

#### 5.2.2.2 Panel surface density

For identification of the aluminium density, the two panels are weighed by the balance Sartorius CP34001 S-OCE, as shown in Fig. 5-18. The test panel with 80 holes is 11.49671 kg, and the substitute panel with 8 holes is 11.52617 kg. According to their designed areas (1.09125 m<sup>2</sup> and 1.09607 m<sup>2</sup>) and the area error limit raised by lateral dimensions (-0.0021 m<sup>2</sup>), the surface densities should limit to [10.5354, 10.5557] kg/m<sup>2</sup> and [10.5159, 10.5361]

kg/m<sup>2</sup>, respectively. Then, corresponding to a given aluminium density within the possible range, the plate thickness is obtained as listed in Table 5-7. The final thickness is determined by a comprehensive consideration of both panels. As shown by the table, the test panel can be considered in its designed lateral dimensions, with the tolerances neglected. In this case, the surface density is  $\rho h$  known and equal to 10.5354 kg/m<sup>2</sup>. However, to determine respectively the material density  $\rho$  and the panel thickness  $h$  still needs more information, which can be obtained through experiments.

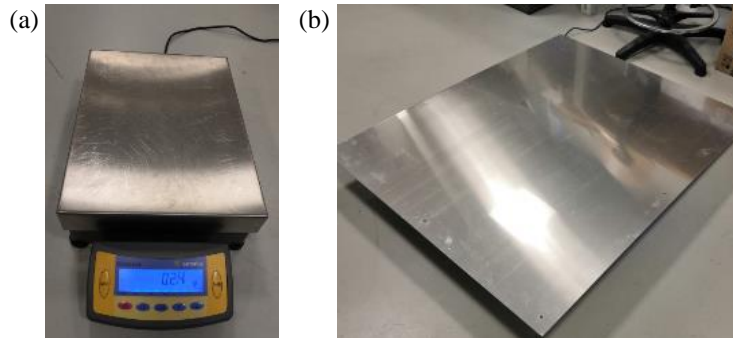


Fig. 5-18. Panel weighing: (a) Sartorius CP34001 S-0CE; (b) weighing process.

Table 5-7. Paring the aluminium density and the panel density based on the surface densities  $\rho h$ , which belong to [10.5354, 10.5557] kg/m<sup>2</sup> and [10.5159, 10.5361] kg/m<sup>2</sup>, respectively for the test and the substitute panels.

Density $\rho$ (kg/m <sup>3</sup> )	Thickness $h$ (mm)				Final
	Test panel		Substitute panel		
	min.	max.	min.	max.	
<b>2700</b>	3.902	3.910	3.895	3.902	<b>3.90</b>
<b>2680</b>	3.931	3.939	3.924	3.931	<b>3.93</b>
<b>2660</b>	3.961	3.968	3.953	3.961	<b>3.96</b>
<b>2632</b>	4.003	4.011	3.995	4.003	<b>4.00</b>

### 5.2.2.3 Natural frequencies of free-free plates

With the above discussions, we can say that the lateral dimensions, surface density and Poisson's ratio of the test panel are settled. The following is to determine the panel thickness, material density and Young's modulus according to its natural frequencies under a certain type of boundary conditions. Among the simply types of boundary conditions, the free-free one may be the easiest to approximate. The most popular strategy is to suspend the component with long strings or soft springs.

For free-free rectangular plates, there is also analytical formula to calculate the natural frequencies  $\omega_s$ . It is like Eq. (4.17), reformulated here referring to [201]:

$$\omega_s^2 = \frac{\pi^4 D}{a^4 \rho h} \left\{ G_x^4 + G_y^4 \left( \frac{a}{b} \right)^4 + 2 \left( \frac{a}{b} \right)^2 [H_x H_y + (1-\nu) J_x J_y] \right\}, \quad (5.15)$$

with  $G_x$ ,  $H_x$  and  $J_x$  are listed in Table 5-8, and  $G_y$ ,  $H_y$  and  $J_y$  are determined by substituting  $y$  for  $x$  and  $n$  for  $m$ . The indicators  $m$  and  $n$  are respectively the mode orders in  $x$  and  $y$  directions.

According to Eq. (5.15), when lateral dimensions  $a$ ,  $b$ , surface density  $\rho h$ , Poisson's ratio  $\nu$  and plate boundary conditions are fixed, the natural frequency is proportional to the flexural rigidity  $D$ , which is further in proportion to  $E$  and  $h^3$ . Therefore, if natural frequencies of the panel are known, the best fitting  $D$  is available. Then, based on the definition  $D = Eh^3/12(1-\nu^2)$ , the reasonable  $E$  and  $h$  within their possible ranges are determined.

Table 5-8. Frequency coefficients in Eq. (5.15) for free-free edges<sup>[201]</sup>.

$m$	$G_x$	$H_x$	$J_x$
1	0	0	0
2	0	0	$12/\pi^2$
3	1.506	1.248	5.017
4, 5, 6, ...	$m - \frac{3}{2}$	$\left(m - \frac{3}{2}\right)^2 \left[1 - \frac{2}{\left(m - \frac{3}{2}\right)\pi}\right]$	$\left(m - \frac{3}{2}\right)^2 \left[1 + \frac{6}{\left(m - \frac{3}{2}\right)\pi}\right]$

However, the challenge aspects are from two sides. For one thing, the panel is thin and large, making it difficult to reach the ideal free-free boundary conditions. Consequently, the experimental natural frequencies in the low frequency region may be significantly influenced by the suspension. For the other, the results determined from Eq. (5.15) will decrease in accuracy for higher order modes. Therefore, FEM is adopted to compute the natural frequencies. As proved in Section 4.2.5, the accuracy of COMSOL model is guaranteed for higher order modes. Thus, if the first several modes are significantly influenced by the boundary conditions, the higher order natural frequencies can be utilised.

#### 5.2.2.4 Experimental analysis of free-free panel

Aiming at the experimental natural frequencies of the panel under free-free boundary conditions, two tests were performed on the two panels, respectively, using two different suspension strategies. Since the three parameters (i.e.,  $\rho$ ,  $h$  and  $E$ ) to be obtained are identical for both panels, the substitute panel is also used, taking the advantage of fewer holes around the perimeter, which is closer to the plate model without inner holes.

As shown by Fig. 5-19, the first test uses the substitute panel with three accelerometers (PCB 333B30) glued. The panel is hanged up with thin nylon rope through the hole at one



of its corners. This suspension strategy is based on the fact that the free-free modes are less affected with fewer suspension points. However, the drawback is that the suspension point is far from the nodal lines of most modes as shown in Fig. 5-20. Under the same configuration, four measurements were done. Each measurement (with several hits at intervals of 45 sec) corresponds to one hitting position on the plate by the force hammer. Such a multi-input multi-output approach ensures that all the flexural modes can be identified from the FRFs processed by the output accelerations and the input forces. Then, the natural frequencies are recognized from the resonance peaks.

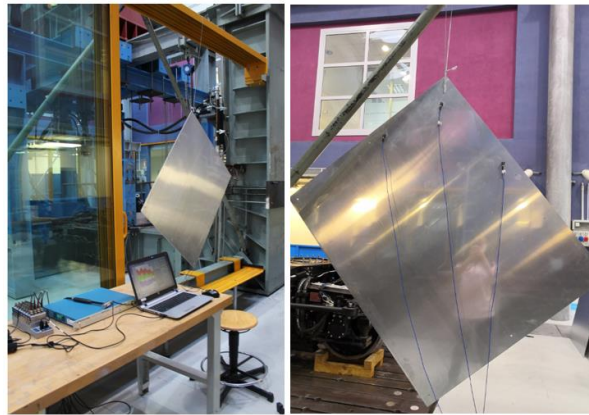


Fig. 5-19. Suspended panel test 1 configuration.

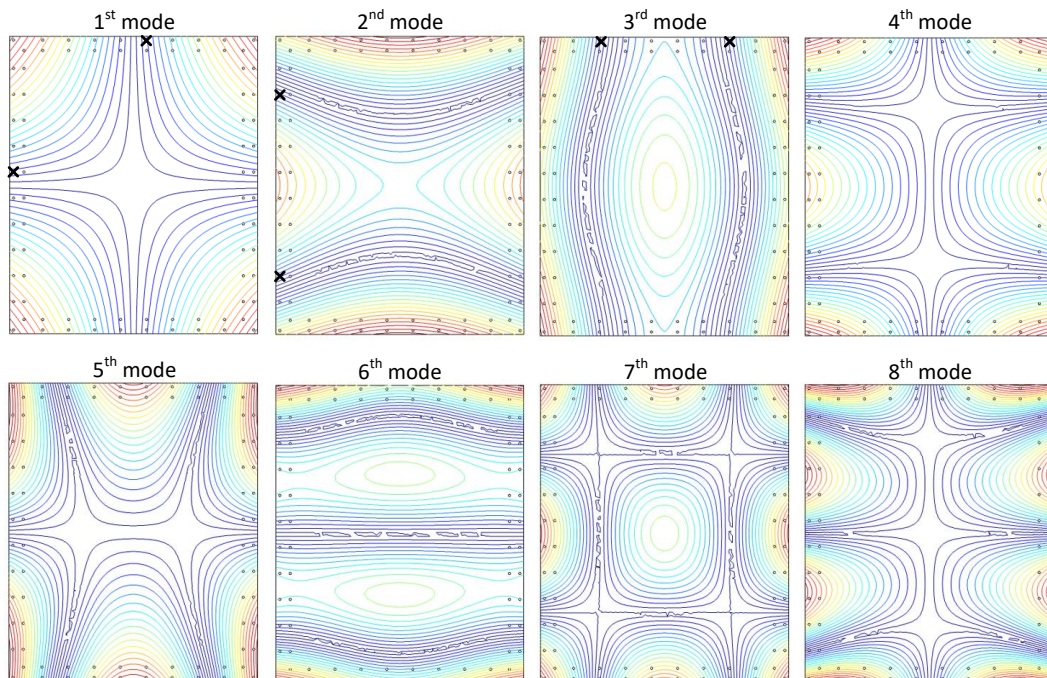


Fig. 5-20. The first 8 numerical mode shapes (except the six rigid body modes) of the test panel under free-free boundary conditions: contour colours *black* to *red* for normalized displacements from 0 to 1; **x** for suspension points in test 2.



As shown by Fig. 5-21, the second test uses the test panel itself. The test was performed after the mounted panel tests introduced in Section 5.2.1. Six accelerometers are on the test panel as they were used in the mounted panel tests. Hanged up by the steel wire rope, the test panel is constrained by two suspension points. Considering the nodal lines of the modes shown in Fig. 5-20, three configurations were implemented. The suspension points of Configuration 1 (see Fig. 5-21) are next to the nodal lines of 1<sup>st</sup> mode (see Fig. 5-20), and so on for Configurations 2 and 3. For each configuration, two measurements (several hits at intervals of 20 sec for each one) are made, corresponding to two hitting positions, respectively. Then, the natural frequencies are identified in the way similar to test 1.

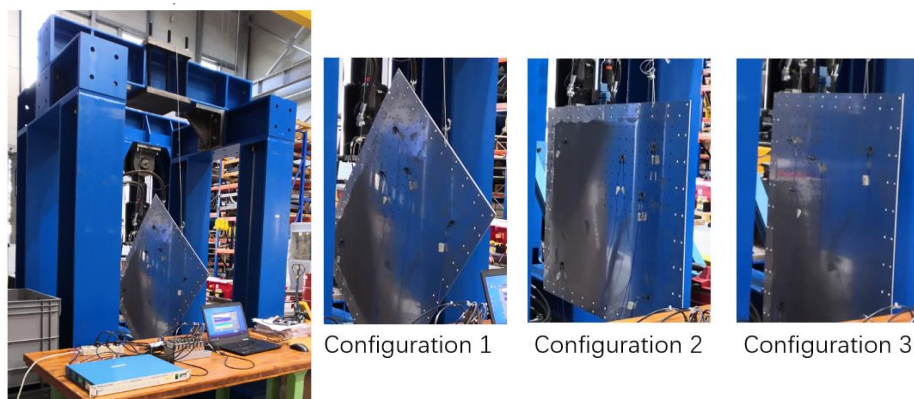


Fig. 5-21. Suspended panel test 2 configurations.

Under the same configuration, the natural frequencies are independent of the hitting positions but relevant to the excited modes. This is acknowledged and also observed in the test. Thus, as a summary, Table 5-9 lists the experimental natural frequencies of the two tests under different configurations. Indeed, the results of Test 2 have removed the natural frequencies that will not exist in the free-free panel and are for sure raised by the suspension. Then, for each flexural mode listed, the natural frequencies are compared among configurations or between tests, and they are shown in good agreement. In test 2, very small variations are seen among the three configurations, indicating that the three types of suspensions lead to similarly increases of the natural frequencies. By comparison, the first 10 modes may be affected the most, but still have the maximum absolute discrepancy  $\Delta f_{i2}$  less than 0.6 Hz. Concerning the differences between Test 2 and Test 1, they may result from the additional small holes in the test panel and the stiffening effect out of an additional suspension point. The former regarding details of the panel should be more effective at high frequencies, while the latter related to the boundary conditions should be more influential at low frequencies. As shown by Table 5-9, the outcome is that the natural frequencies obtained from Test 2 is larger than those from Test 1 for most modes.

Table 5-9. Natural frequencies of the suspended (free-free) panels. Experimental results: Tests 1 and 2. Numerical results: Cases L, U, A and B.

Mode order	Test 1 $f_{i1}$ (Hz)	Test 2 (Hz)					$f_{i2} - f_{i1}$ (Hz)	Case L $f_{Low}$ (Hz)	Case U $f_{Up}$ (Hz)	Case A $f_A$ (Hz)	Case B $f_B$ (Hz)	$f_B - f_A$ (Hz)
		Conf. 1	Conf. 2	Conf. 3	$\Delta f_{i2}$	Ave., $f_{i2}$						
1	<b>14.71</b>	15.2	15	15.05	0.2	<b>15.1</b>	<b>0.4</b>	11.44	12.82	11.66	14.58	2.92
2	<b>17.24</b>	17.9	18.05	17.6	0.45	<b>17.9</b>	<b>0.6</b>	15.10	16.92	15.39	18.98	3.59
3	<b>29.07</b>	30.05	30.2	30.25	0.2	<b>30.2</b>	<b>1.1</b>	23.49	26.31	23.93	25.90	1.97
4	<b>33.09</b>	34.55	34.3	34.55	0.25	<b>34.5</b>	<b>1.4</b>	27.98	31.34	28.51	31.15	2.64
5	<b>36.67</b>	36.85	37.25	37.35	0.5	<b>37.2</b>	<b>0.5</b>	31.99	35.83	32.59	40.47	7.88
6	<b>45.69</b>	46.85	46.9	47.15	0.3	<b>47</b>	<b>1.3</b>	44.35	49.68	45.19	49.53	4.34
7	<b>61.02</b>	62	61.9	62.15	0.25	<b>62</b>	<b>1</b>	54.95	61.54	55.98	56.06	0.08
8	<b>62.84</b>	66.65	66.3	66.3	0.35	<b>66.4</b>	<b>3.6</b>	55.08	61.69	56.11	62.45	6.33
9	<b>69.71</b>	69.8	70	69.65	0.35	<b>69.8</b>	<b>0.1</b>	63.48	71.10	64.68	68.45	3.78
10	<b>77.02</b>	78.1	78.65	78.1	0.55	<b>78.3</b>	<b>1.3</b>	72.96	81.72	74.33	81.18	6.85
11	<b>88.64</b>	89.7	89.5	89.7	0.2	<b>89.6</b>	<b>1</b>	86.20	96.55	87.82	88.06	0.23
12	<b>94.33</b>	96.8	96.5	96.6	0.3	<b>96.6</b>	<b>2.3</b>	86.90	97.34	88.54	94.75	6.21
13	<b>103.5</b>	104.3	104.4	104.5	0.2	<b>104.4</b>	<b>0.9</b>	93.90	105.17	95.67	95.73	0.06
14	<b>105.3</b>	108.2	108.1	108.2	0.1	<b>108.2</b>	<b>2.9</b>	100.76	112.85	102.65	115.11	12.46
15	<b>130.6</b>	130.7	130.7	130.6	0.1	<b>130.7</b>	<b>0.1</b>	124.13	139.04	126.47	126.71	0.24
16	<b>137.4</b>	139.2	139.3	139.1	0.2	<b>139.2</b>	<b>1.8</b>	131.22	146.97	133.69	134.01	0.32
17	<b>138.5</b>	140.8	140.8	140.8	0	<b>140.8</b>	<b>2.3</b>	131.71	147.52	134.19	134.69	0.50
18	<b>140.9</b>	142.7	142.7	142.7	0	<b>142.7</b>	<b>1.8</b>	132.58	148.49	135.08	141.30	6.22
19	<b>146.3</b>	146.8	146.6	146.9	0.3	<b>146.8</b>	<b>0.5</b>	143.97	161.25	146.68	149.86	3.18
20	<b>160.2</b>	160.9	160.9	161.1	0.2	<b>161</b>	<b>0.8</b>	153.64	172.09	156.54	158.56	2.02
21	<b>166.5</b>	168.9	168.8	168.8	0.1	<b>168.8</b>	<b>2.3</b>	157.96	176.92	160.94	168.25	7.31
22	<b>187.4</b>	189.6	189.6	189.8	0.2	<b>189.7</b>	<b>2.3</b>	179.56	201.11	182.94	185.09	2.15
23	<b>194.2</b>	196.8	196.6	196.7	0.2	<b>196.7</b>	<b>2.5</b>	186.17	208.51	189.67	190.89	1.22
24	<b>204.6</b>	206.1	206	206.2	0.2	<b>206.1</b>	<b>1.5</b>	196.87	220.50	200.58	204.34	3.76
25	<b>213.5</b>	213.9	214.1	214	0.2	<b>214</b>	<b>0.5</b>	206.39	231.17	210.28	211.01	0.73
26	<b>218.2</b>	218.6	218.6	218.8	0.2	<b>218.7</b>	<b>0.5</b>	213.80	239.47	217.83	217.87	0.04
27	<b>221.9</b>	221.7	221.8	221.7	0.1	<b>221.7</b>	<b>-0.2</b>	213.90	239.58	217.93	220.30	2.37
28	<b>231.6</b>	232.1	232	232.4	0.4	<b>232.2</b>	<b>0.6</b>	223.50	250.33	227.71	229.09	1.38
29	<b>246.2</b>	248.3	248.2	248.3	0.1	<b>248.3</b>	<b>2.1</b>	238.80	267.46	243.30	243.74	0.44
30	<b>248.5</b>	250.6	250.5	250.7	0.2	<b>250.6</b>	<b>2.1</b>	239.94	268.74	244.46	247.06	2.60
31	<b>254.1</b>	256.1	256.1	256.1	0	<b>256.1</b>	<b>2</b>	245.01	274.42	249.63	251.78	2.15
32	<b>265.4</b>	267.7	267.5	267.7	0.2	<b>267.6</b>	<b>2.2</b>	257.83	288.78	262.68	264.93	2.25
33	<b>287.1</b>	288.2	288.2	288.4	0.2	<b>288.3</b>	<b>1.2</b>	277.29	310.57	282.52	283.67	1.15
34	<b>304.2</b>	304.8	304.7	305	0.3	<b>304.8</b>	<b>0.6</b>	297.84	333.59	303.45	303.54	0.09
35	<b>315.3</b>	x	316.3	316.6	0.3	<b>316.5</b>	<b>1.2</b>	306.23	342.98	311.99	312.30	0.31
36	<b>317.5</b>	317.5	317.4	317.8	0.4	<b>317.6</b>	<b>0.1</b>	308.84	345.91	314.66	315.01	0.35
37	<b>318</b>	318.7	318.7	318.8	0.1	<b>318.7</b>	<b>0.7</b>	309.71	346.89	315.55	315.61	0.06
38	<b>318.5</b>	320	319.9	320.4	0.5	<b>320.1</b>	<b>1.6</b>	309.87	347.06	315.71	317.28	1.57
39	<b>325.9</b>	326	326	326.1	0.1	<b>326</b>	<b>0.1</b>	316.98	355.03	322.95	324.26	1.31
40	<b>338.4</b>	339.4	339.4	339.6	0.2	<b>339.5</b>	<b>1.1</b>	329.53	369.07	335.73	336.92	1.19
41	<b>350.8</b>	352.9	352.7	353	0.3	<b>352.9</b>	<b>2.1</b>	340.18	381.01	346.59	347.00	0.41
42	<b>351.7</b>	353.7	353.6	353.8	0.2	<b>353.7</b>	<b>2</b>	342.53	383.64	348.98	350.09	1.11
43	<b>390.4</b>	390.4	390.2	390.7	0.5	<b>390.4</b>	<b>0</b>	379.74	425.32	386.89	387.21	0.32
44	<b>390.4</b>	391.4	391.3	391.6	0.3	<b>391.4</b>	<b>1</b>	380.63	426.31	387.80	388.64	0.84
45	<b>401.7</b>	401.9	401.8	402	0.2	<b>401.9</b>	<b>0.2</b>	390.95	437.86	398.31	398.38	0.07
46	<b>404.2</b>	405.2	405.2	405.5	0.3	<b>405.3</b>	<b>1.1</b>	396.80	444.42	404.27	404.99	0.72
47	<b>405.4</b>	405.9	405.8	406.1	0.3	<b>405.9</b>	<b>0.5</b>	398.33	446.14	405.84	406.32	0.48
48	<b>417.3</b>	417.3	417.2	417.6	0.4	<b>417.4</b>	<b>0.1</b>	406.18	454.93	413.83	414.11	0.28
49	<b>441.8</b>	443.1	443.3	443.2	0.2	<b>443.2</b>	<b>1.4</b>	430.90	482.61	439.01	439.21	0.20

Table 5-9 (Continued). Natural frequencies of the suspended (free-free) panels. Experimental results: Tests 1 and 2. Numerical results: Cases L, U, A and B.

Mode order	Test 1 $f_{t1}$ (Hz)	Test 2 (Hz)					$f_{t2} - f_{t1}$ (Hz)	Case L $f_{Low}$ (Hz)	Case U $f_{Up}$ (Hz)	Case A $f_A$ (Hz)	Case B $f_B$ (Hz)	$f_B - f_A$ (Hz)
		Conf. 1	Conf. 2	Conf. 3	$\Delta f_{t2}$	Ave., $f_{t2}$						
50	<b>443.5</b>	444.2	444.3	444.3	0.1	<b>444.3</b>	<b>0.8</b>	433.01	484.98	441.17	441.36	0.19
51	<b>450.6</b>	450.5	450.7	450.6	0.2	<b>450.6</b>	<b>0</b>	438.83	491.49	447.09	447.41	0.32
52	<b>451.5</b>	452.5	452.4	452.7	0.3	<b>452.5</b>	<b>1</b>	442.00	495.04	450.32	450.97	0.65
53	<b>475.6</b>	476.8	476.8	477	0.2	<b>476.9</b>	<b>1.3</b>	461.81	517.23	470.50	470.55	0.05
54	<b>476.6</b>	477.8	477.7	478	0.3	<b>477.8</b>	<b>1.2</b>	467.02	523.05	475.81	476.06	0.25
55	<b>478</b>	479	479	479.2	0.2	<b>479.1</b>	<b>1.1</b>	469.40	525.72	478.24	478.80	0.56
56	<b>504.1</b>	505.1	505	505.4	0.4	<b>505.2</b>	<b>1.1</b>	495.08	554.48	504.40	504.70	0.30
57	<b>507.6</b>	507.3	507.1	507.4	0.3	<b>507.3</b>	<b>-0.3</b>	496.67	556.26	506.02	506.35	0.33
58	<b>514</b>	514.6	514.5	514.8	0.3	<b>514.6</b>	<b>0.6</b>	500.46	560.51	509.88	510.02	0.14
59	<b>520</b>	520.3	520.1	520.6	0.5	<b>520.3</b>	<b>0.3</b>	511.86	573.28	521.49	521.65	0.16
60	<b>532.2</b>	532.1	532	532.4	0.4	<b>532.2</b>	<b>0</b>	521.09	583.62	530.90	531.11	0.21
61	<b>564.2</b>	565.6	565.5	565.9	0.4	<b>565.7</b>	<b>1.5</b>	552.74	619.06	563.14	563.22	0.08
62	<b>566.3</b>	566.8	566.6	567	0.4	<b>566.8</b>	<b>0.5</b>	554.40	620.91	564.83	565.02	0.19
63	<b>566.9</b>	567.6	567.6	567.9	0.3	<b>567.7</b>	<b>0.8</b>	557.26	624.10	567.74	568.03	0.29
64	<b>576.7</b>	577.3	577.3	577.5	0.2	<b>577.4</b>	<b>0.7</b>	565.50	633.34	576.14	576.20	0.06
65	<b>585.1</b>	584.4	584.3	584.8	0.5	<b>584.5</b>	<b>-0.6</b>	573.30	642.08	584.09	584.14	0.05
66	<b>590.4</b>	590	590.1	590.1	0.1	<b>590.1</b>	<b>-0.3</b>	578.39	647.79	589.28	589.59	0.31
67	<b>597.8</b>	596.6	596.6	596.7	0.1	<b>596.6</b>	<b>-1.2</b>	582.53	652.43	593.49	593.64	0.15
68	<b>617.6</b>	619.1	619	619.4	0.4	<b>619.2</b>	<b>1.6</b>	605.44	678.08	616.83	616.92	0.09
69	<b>621.6</b>	623.2	623.1	623.3	0.2	<b>623.2</b>	<b>1.6</b>	606.60	679.38	618.02	618.09	0.07
70	<b>632.5</b>	632.3	632.2	632.4	0.2	<b>632.3</b>	<b>-0.2</b>	621.42	695.97	633.12	633.35	0.23
71	<b>649.7</b>	648.9	648.9	649.3	0.4	<b>649</b>	<b>-0.7</b>	639.66	716.41	651.70	651.75	0.05
72	<b>659.5</b>	659.1	659	659.5	0.5	<b>659.2</b>	<b>-0.3</b>	643.69	720.92	655.81	655.85	0.04
73	<b>661.1</b>	660.2	660.1	660.6	0.5	<b>660.3</b>	<b>-0.8</b>	646.58	724.15	658.75	658.77	0.02
74	<b>667.6</b>	667.8	667.9	668.3	0.5	<b>668</b>	<b>0.4</b>	658.43	737.41	670.82	670.97	0.15
75	<b>674.4</b>	674.9	674.8	675.3	0.5	<b>675</b>	<b>0.6</b>	664.65	744.37	677.16	677.29	0.13
76	<b>691.9</b>	692.3	692.2	692.9	0.7	<b>692.5</b>	<b>0.6</b>	680.05	761.63	692.85	692.87	0.02
77	<b>692.9</b>	694.3	694.1	695	0.9	<b>694.5</b>	<b>1.6</b>	681.60	763.36	694.43	694.59	0.16

### 5.2.2.5 Numerical analysis of free-free panel

FEM is used to compute the natural frequencies of the free-free panel. The modelling approach has been introduced in Section 4.2. Here, COMSOL is used and the maximum shell element size is 0.02 m. Rectangular elements are used because of higher accuracy. Since the small holes, even if their total number is 80, have little influence on the natural frequencies within the considered frequency region, such details are ignored in the FE models. In fact, it is also proved that adding the holes will decrease the mesh quality, reducing the predicting accuracy, which may exceed the influence of the holes themselves. Therefore, the geometry of the analysing panel is a rectangular plate of  $a \times b = 0.955\text{m} \times 1.148\text{m}$  without any holes. Thickness and material parameters are assumed based on  $\rho h = 10.5354 \text{ kg/m}^2$ ,  $\rho \in [2630, 2700] \text{ kg/m}^3$ ,  $h \in [3.9, 4] \text{ mm}$ ,  $E \in [68, 79] \text{ GPa}$  and  $\nu = 0.33$ . With an initial set of assumed parameters, a set of natural frequencies is obtained. These natural frequencies can compare with the experimental results. Then, according to

the errors between the numerical and experimental sets, the next set of assumed parameters can be proposed. The proposal can incorporate the analytical formula Eq. (5.15) or utilise an optimization algorithm. The experimental natural frequencies of Test 1 (see Table 5-7) are used as the target.

However, as previously mentioned in Section 5.2.2.3, the boundary conditions in the experiment are probably not ideally free. If the constraint raised by suspension affects the flexural modes of the panel, it is important and beneficial to figure out the cut-off mode order. Then, the parameter updating or optimizing process can refer to a certain frequency range higher than the cut-off mode order. To check if the suspension condition matters, two sets of parameters were implemented to draw the lower and upper limits of the numerical natural frequencies: *Case L* with  $\rho = 2700 \text{ kg/m}^3$ ,  $h = 3.9 \text{ mm}$ ,  $E = 68 \text{ GPa}$  for the lower limit and *Case U* with  $\rho = 2630 \text{ kg/m}^3$ ,  $h = 4 \text{ mm}$ ,  $E = 79 \text{ GPa}$  for the upper limit. As shown in Table 5-7, the experimental natural frequencies of the first 5 modes are larger than the upper limits of numerical ones. Hence, the boundary conditions of the FE model are probably not consistent with the experimental ones. For further confirmation, spring foundation was added at the suspension point in the FE model according to Test 1. The change rule of natural frequencies can somehow prove the hypothesis. In this investigation, the implemented parameters are  $\rho = 2680 \text{ kg/m}^3$ ,  $h = 3.93 \text{ mm}$ ,  $E = 69 \text{ GPa}$ . *Case A* is the original without spring foundation, and *Case B* includes the spring foundation at the suspension point with stiffness in the normal direction  $k_z = 10^5 \text{ N/m}$ .

Numerical natural frequencies of all above cases are listed in Table 5-7 alongside the experimental ones. As indicated from the table, the first five natural frequencies of the numerical model will always smaller than the experimental results, if the plate is completely free in the model. However, enforcing a soft restraint at the suspension point successively increases the natural frequencies to reach or surpass the experimental ones. Since this trial restraint is not conform to the real suspension, it is not able to correct the error between numerical and experimental results, but it highlights the modes that are significantly influenced by the suspension. As shown by  $f_B - f_A$ , the influence is decreasing as the frequency increases. Four regions are divided for the influence: 1<sup>st</sup> to 5<sup>th</sup> modes are generally affected; within 6<sup>th</sup> to 24<sup>th</sup> modes, the effect is still significant but dependent on the mode shape; higher than the 24<sup>th</sup> mode, the increase is less than 3 Hz; higher than the 42<sup>nd</sup> mode, the difference is less than 1 Hz. The values should rely on other parameters of the panel, but the change rule is instructive.

### 5.2.2.6 Determination of parameters

Based on the parameters updating approach introduced in Section 5.2.2.5, the final parameters are determined as  $\rho = 2680 \text{ kg/m}^3$ ,  $h = 3.93 \text{ mm}$ ,  $E = 69 \text{ GPa}$  and  $\nu = 0.33$ . These are the parameters of Case A, whose natural frequencies are listed in Table 5-7. Fig. 5-22 shows the difference between the predicting results  $f_A$  to the test results  $f_{t1}$ . Similarly, other cases are also depicted for comparison. As shown by the figure, the natural frequencies of Case A (i.e.,  $f_A$ ) are very close to the results of Test 1 (i.e.,  $f_{t1}$ ), especially when the mode order is higher than 42. Besides, it can be seen that there is a wider difference between the lower limit  $f_L$  and the upper limit  $f_U$  as the mode order increases. Using the same parameters as Case A, Case B (i.e.,  $f_B$ ) better matches the test results in the low frequency range due to a small modification to boundary conditions. Overall, the updated parameters should match well with the test panel.

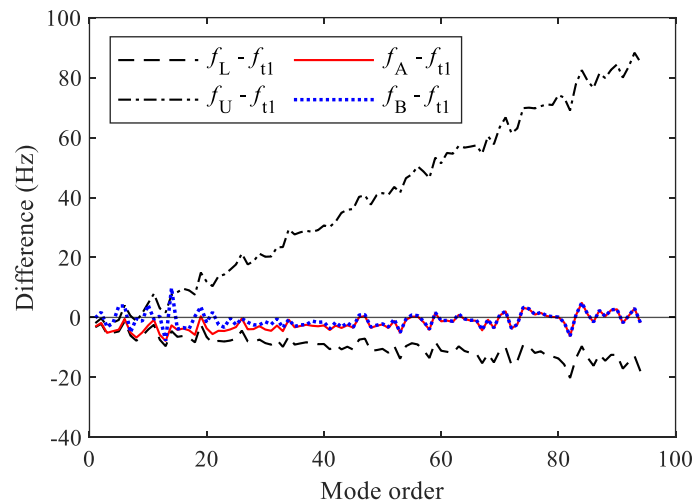


Fig. 5-22. Change of the difference between numerical (Cases L, U, A and B) and experimental (Test 1) natural frequencies over mode order, for the free-free test panel.

There are also other factors that may cause the numerical model different from the experimental settlement. For example, the membrane forces raised by gravity can increase the flexural natural frequencies. By simulation in COMSOL about this effect, the increase has been proved tiny and even smaller as the frequency increases. The mass of the accelerometers will slightly reduce the natural frequencies and be more influential in the high frequency range. This is also investigated in the FEA and proved not important in the considered frequency range. Similarly, air loading and small variation of lateral dimensions are also considered. The combination of all these effects is very small and makes no difference to the determination of parameters.

### 5.2.3 Mounted panel edge conditions

With all the geometric and material parameters determined, the only uncertainties are the edge conditions. In Section 5.2.1, the uncoupled dynamic properties of the mounted panel have been characterized, which should depend on the panel's edge conditions. Hence, they also provide important information to update the panel's model. Ideally, the panel should be clamped or simply supported. However, the simulations via FEM (COMSOL), where the updated panel thickness and material properties have been implemented, demonstrate that both conditions cannot model the test panel well. As shown by Table 5-10 and Fig. 5-23, the disagreement in natural frequencies points out the discrepancy. Note that, those highlighted in red in the table have exchanged the order to match the vibrating mode.

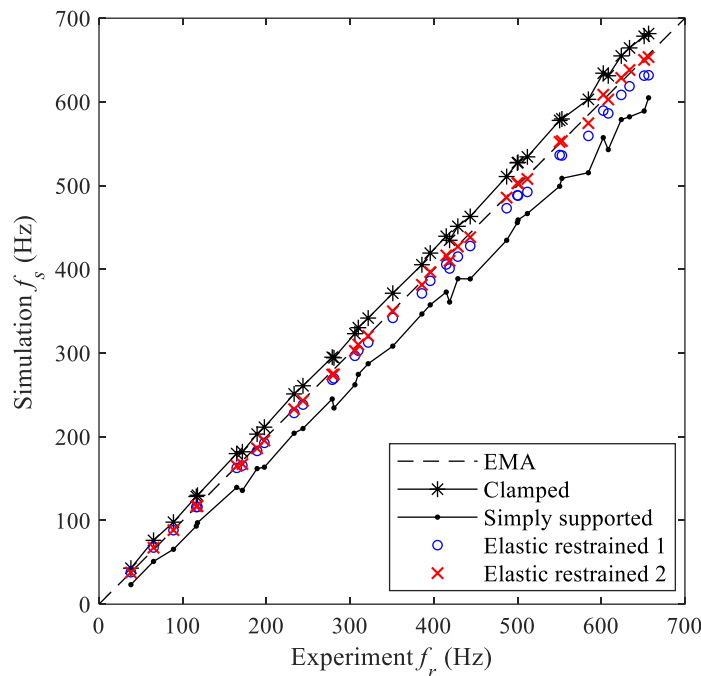


Fig. 5-23. Scatter plot for natural frequencies of the mounted plate from numerical simulation vs from experimental measurement. Corresponding data are listed in Table 5-10. ‘Elastic restrained 1’ is for  $k_{\theta_x} = 8 \text{ kN/rad}$ ,  $k_{\theta_y} = 14 \text{ kN/rad}$ ; ‘Elastic restrained 2’ is for  $k_{\theta_x} = 5 \text{ kN/rad}$ ,  $k_{\theta_y} = 9 \text{ kN/rad}$ ,  $E = 76 \text{ GPa}$ .

Aimed at yielding the natural frequencies and modes consistent with the experimental results, a more precise edge model is applied. As shown in Fig. 5-24, it is assumed that the edges are rigidly supported but elastically restrained against rotation. The two horizontal edges possess the same rotational stiffness  $k_{\theta_x}$ , and the two vertical ones are  $k_{\theta_y}$ . The assumption proposes a condition between the clamped ( $k_{\theta_x} = k_{\theta_y} = \infty$ ) and the simply supported ( $k_{\theta_x} = k_{\theta_y} = 0$ ) cases. The different stiffnesses between horizontal and vertical edges are based on the fact that they are constrained by different number of bolts and that the gravity of the test panel as well as the mounting frame may take effect. The test panel

for EMA, also as the mounted panel for modelling, is shown in Fig. 5-12 for its configuration in experiment.

Table 5-10. Natural frequencies and modes of the mounted test panel in experiment and simulations.

Order	Mode	EMA $f_r$ (Hz)	Simulation $f_s$ (Hz)			
			Clamped $E = 69$ GPa	Simply supported $E = 69$ GPa	$k_{\theta_x} = 8$ kN/rad $k_{\theta_y} = 14$ kN/rad $E = 69$ GPa	$k_{\theta_x} = 5$ kN/rad $k_{\theta_y} = 9$ kN/rad $E = 76$ GPa
1	(1,1)	<b>38.10</b>	43.01	23.33	38.15	37.73
2	(1,2)	<b>65.14</b>	76.24	51.06	67.64	67.52
3	(2,1)	<b>88.93</b>	98.00	65.56	88.31	88.49
4	(2,2)	<b>116.21</b>	128.61	93.29	116.01	116.91
5	(1,3)	<b>117.64</b>	130.08	97.28	116.23	117.18
6	(2,3)	<b>164.50</b>	179.88	139.50	162.80	165.10
7	(3,1)	<b>171.29</b>	182.05	135.92	165.58	167.38
8	(1,4)	<b>188.88</b>	203.16	161.97	183.11	186.13
9	(3,2)	<b>197.55</b>	211.44	163.64	192.67	195.48
10	(2,4)	<b>233.09</b>	251.16	204.16	228.43	233.01
11	(3,3)	<b>243.67</b>	260.86	209.83	238.41	242.97
12	(1,5)	<b>278.63</b>	295.05	245.10	268.12	274.25
13	(4,1)	<b>280.70</b>	294.35	234.38	269.74	274.51
14	(4,2)	<b>305.74</b>	323.12	262.08	296.67	302.62
15	(3,4)	<b>309.75</b>	330.31	274.47	302.97	310.09
16	(2,5)	<b>321.59</b>	341.78	287.27	312.61	320.43
17	(4,3)	<b>351.00</b>	371.48	308.24	341.96	349.90
18	(1,6)	<b>385.77</b>	405.47	346.65	371.22	381.52
19	(3,5)	<b>395.74</b>	419.40	357.54	386.25	396.81
20	(4,4)	<b>414.85</b>	439.50	372.84	405.85	416.61
21	(5,1)	<b>418.84</b>	434.73	360.89	400.96	410.18
22	(2,6)	<b>428.72</b>	451.39	388.80	415.17	427.22
23	(5,2)	<b>443.51</b>	463.16	388.57	427.86	438.38
24	(5,3)	<b>487.01</b>	510.83	434.69	472.99	485.65
25	(4,5)	<b>499.80</b>	527.19	455.86	488.42	502.84
26	(3,6)	<b>500.62</b>	527.74	459.02	488.08	503.04
27	(1,7)	<b>511.79</b>	534.35	466.60	492.46	507.95
28	(5,4)	<b>550.36</b>	577.93	499.24	536.54	552.19
29	(2,7)	<b>553.04</b>	579.61	508.71	536.00	553.3
30	(6,1)	<b>584.65</b>	603.07	515.39	559.37	574.59
31	(4,6)	<b>602.45</b>	634.29	557.29	589.61	608.58
32	(6,2)	<b>608.42</b>	631.24	543.05	586.30	602.88
33	(3,7)	<b>623.97</b>	654.98	578.88	608.36	628.66
34	(5,5)	<b>633.82</b>	664.49	582.20	618.64	638.14
35	(6,3)	<b>651.30</b>	678.52	589.13	631.38	650.20
36	(1,8)	<b>656.55</b>	681.61	604.90	631.85	653.55



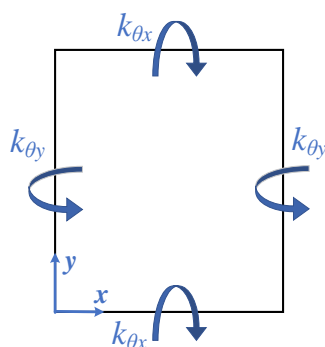


Fig. 5-24. Rotational stiffness along panel edges.

Based on the new model, the edge conditions can be updated via the two parameters  $k_{\theta_x}$  and  $k_{\theta_y}$ . However, the analysis on the influence of the two parameters finds that the accuracy can be further improved if Young's modulus  $E$  is included as an updating parameter. Though Young's modulus of the panel has been identified in Section 5.2.2, it is still considered as an updatable parameter here for obtaining a better model that matches the test case. This does not mean that the material property has changed. The necessity may be related to the installation of the panel, which can raise unknown in-plane tension or compression. Since the membrane forces are not introduced to the plate model, they may be compensated by Young's modulus, even resulting in anisotropic  $E_x$  and  $E_y$ . In <sup>[84]</sup>, a panel (aluminium plate) with similar installation has been implemented an advance approach to update the numerical model. In that case, the numerical model with  $E_x = 66$  GPa and  $E_y = 81$  GPa matches the test system very well. In the paper, it is not explained why the best model holds such an anisotropic behaviour, where  $E_y$  is 22.7% larger than  $E_x$  and even out of the range of common values for aluminium. Referring to this, we suggest that it may be associated with the membrane forces and will be less significant if the thickness-to-span ratio ( $h/l$ ) is higher. In fact, the panel in that paper is of 'A2' dimensions (international paper sizes 420mm  $\times$  594mm) with 3-mm thickness, i.e.,  $h/l \approx 1/200 < 1/100$ , which indicates that it is sensitive to the membrane forces <sup>[157]</sup>. Similarly, our mounted panel has  $h/l \approx 1/250 \sim 1/200 < 1/100$ . Moreover, the reference <sup>[84]</sup> indicates that the rotational stiffness is not uniformly distributed in every imperfectly clamped edge. However, such details are not discussed in this thesis.

Table 5-10 and Fig. 5-23 show the estimated results out of two updated numerical models with elastic edge restraints. The first model keeps the Young's modulus identified by Section 5.2.1,  $E = 69$  GPa. With the rotational edge stiffnesses  $k_{\theta_x} = 8$  kN/rad,  $k_{\theta_y} = 14$  kN/rad, the numerical results reach a good agreement with the experimental ones in the first several modes, but the discrepancy increases as the frequency increases. As can be observed from Fig. 5-23, if there is a fitting curve for the results of 'Elastic restrained 1', its slope is



smaller than the desire value. Raising the rotational edge stiffnesses can increase the slope, but it also increases the natural frequencies of the first several modes, breaking the previously reached agreement. By contrast, the second model has the Young's modulus updated, in addition to the rotational edge restraints. For simplicity, the mechanical behaviour is assumed to be isotropic, even though an orthotropic model should be better. This model has the updated parameters:  $k_{\theta_x} = 5$  kN/rad,  $k_{\theta_y} = 9$  kN/rad and  $E = 76$  GPa. Its natural frequencies are listed in the last column of Table 5-10 and plotted in Fig. 5-23 as 'Elastic restrained 2'. As the figure shows, the natural frequencies estimated by this model are in line with the results of EMA. This is the final updated model for the test panel in the uncoupled mounted situation.

However, the natural frequencies estimated from the final model still have small deviations from the experimental ones. As shown in Fig. 5-23, the estimation fluctuates around the expected line. The relationship between the deviation ( $f_s - f_r$ ) and the corresponding mode ( $m, n$ ) is analysed, which is also an important basis for updating the parameters. For a better understanding of the rules, three groups of the panel modes are distinguished from the others, as illustrated in Table 5-10 using the three shading colours:

- green. This group includes the 2<sup>nd</sup>, 5<sup>th</sup>, 8<sup>th</sup>, 12<sup>th</sup>, 18<sup>th</sup>, 27<sup>th</sup> and 36<sup>th</sup> modes, they can be regarded as the *axial modes* in  $y$  direction;
- blue. This group includes the 3<sup>rd</sup>, 7<sup>th</sup>, 13<sup>th</sup>, 21<sup>st</sup> and 30<sup>th</sup> modes, they can be regarded as the *axial modes* in  $x$  direction;
- grey. This group includes the 1<sup>st</sup>, 4<sup>th</sup>, 11<sup>th</sup>, 20<sup>th</sup> and 34<sup>th</sup> modes, they can be regarded as the *oblique modes*.

Then, focusing on the final model, we can notice some rules. At first, for the green group, from the 2<sup>nd</sup> to the 12<sup>th</sup> mode, the deviation between the estimated and the measured frequencies changes from positive (2.4 Hz) to negative (-4.2 Hz), after which, the deviation is about -4 Hz for the other modes. Since this is the group concerning the axial modes in  $y$  direction, it is highly related to  $k_{\theta_x}$  and  $E_y$ . The current combination of  $k_{\theta_x}$  and  $E$  demonstrates a not bad outcome. Secondly, in the blue group, the estimated natural frequencies are always smaller than the measured ones and the absolute deviation  $|f_s - f_r|$  increases with the frequency. At 3<sup>rd</sup> mode, it is 0.4 Hz, while at 30<sup>th</sup> mode, it is 10 Hz. Since this group of axial modes in  $x$  direction is more relevant to  $k_{\theta_y}$  and  $E_x$ , the current combination of  $k_{\theta_y}$  and  $E$  underestimates the increasing slope of natural frequency over mode order in  $x$  direction. Accordingly,  $E_x$  is expected higher than the assigned value  $E = 76$  GPa. Thirdly, attention is paid to the grey group. In the previous two groups, the estimated natural frequencies are smaller than the measured values since the 5<sup>th</sup> mode, but in the grey group (for the oblique modes), the estimated results are shown even larger than

the measured ones as the frequency increases. Hence, it is considered that there is a stiffening effect when the wavelengths in  $x$  and  $y$  directions are close to each other. This could be also related to the non-uniformity of rotational stiffness along a single edge, as mentioned previously, which is noticed from [84]. To sum up, the final updated parameters are determined with a comprehensive consideration over the above three points, reaching the best agreement in natural frequencies with a trade-off among different modes.

Finally, the updated model (implemented in COMSOL) is used to predict the frequency response of the mounted uncoupled test panel. For simulating the one of the measurements in the hammer test, a unit normal force is imposed at the location of Point 80 (see Fig. 5-12), and the acceleration at A1 position is evaluated. In addition, the numerical model is assigned with the damping loss factor  $\eta = 2\zeta_r \approx 0.003$  according to the damping ratios  $\zeta_r$  obtained from EMA listed in Table 5-4 for  $A_{180}$ . The simulation results and the measurement results of the acceleration  $A_{180}$  are shown and compared in Fig. 5-25. As expected, the FRFs between test and simulation match well if the natural frequencies nearby have a good agreement, e.g., around the first four resonances.

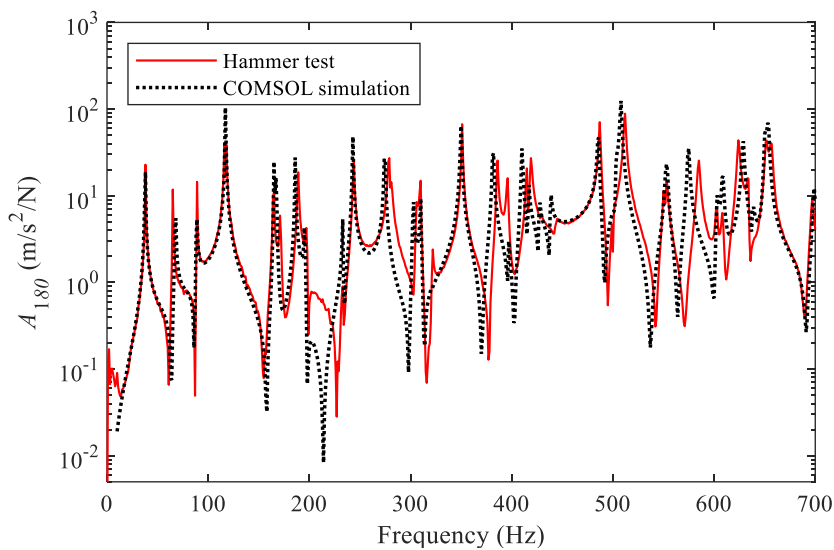


Fig. 5-25. Measured and simulated FRFs of the mounted panel, represented by the acceleration  $A_{180}$ , whose input location Point 80 and output location A1 are shown in Fig. 5-12.

### 5.3 Plate-cavity system characterization

When the previous two Sections 5.1 and 5.2 characterize the Noise-Box cavity and the mounted panel separately and try to avoid the coupling effect, this section considers them together, fully coupled with each other. Like the EMA of structures (introduced and utilized in Section 5.2.1), EMA is here applied to an interior vibroacoustic system, i.e., the plate-

cavity coupled Noise-Box, to obtain the modal parameters. Later, the results are compared between the coupled system and the uncoupled components, and between experiment and simulation. Due to the unknown change of plate mounting conditions between the coupled and uncoupled case, the plate-cavity system model is updated based on the identified coupled modes. Finally, the influence of the cavity on the plate is revealed from the updated FE model.

### 5.3.1 Improved EMA for plate-cavity system

EMA has been widely used for structural dynamics. As for interior acoustics, though EMA is applicable due to the existence of acoustic modes <sup>[210]</sup>, it is much less popular because of the difficulty in the characterization of the acoustical excitation sources. Concerning the EMA for vibroacoustic systems, it is even less discussed and only investigated in a very limited number of papers <sup>[93,94,211,212]</sup>. The tricky issue is that the coupled vibroacoustic problem is non-symmetric when formulated using the measurable variables: structural displacement  $w$  and the acoustic pressure  $p$ . A typical formulation, which can be derived from the FEM, is given by <sup>[188]</sup>

$$\left( \begin{bmatrix} [K] & -[C_{wp}] \\ [0] & [H] \end{bmatrix} - \omega^2 \begin{bmatrix} [M] & [0] \\ [C_{wp}]^T & [Q] \end{bmatrix} \right) \begin{Bmatrix} \{\hat{w}\} \\ \{\hat{p}\} \end{Bmatrix} = \begin{Bmatrix} \{\hat{F}\} \\ \{0\} \end{Bmatrix}, \quad (5.16)$$

where the first and second lines are respectively for the structural and acoustic fields.  $[K]$ ,  $[M]$ ,  $\{\hat{w}\}$  and  $\{\hat{F}\}$  are, respectively, the mass matrix, stiffness matrix, nodal unknown displacement vector and nodal force vector of the structure.  $[H]$ ,  $[Q]$  and  $\{\hat{w}\}$  are, respectively, the kinetic energy matrix, compressional energy matrix and nodal unknown sound pressure vector of the fluid.  $[C_{wp}]$  is the coupling matrix between two fields, derived from the fluid-structure interface.

From Eq. (5.16), it is clear that the system matrix is non-symmetric, so whether the model formulation expressed like Eq. (5.12) is still applicable to this case is not sure. The vibroacoustic system defined by Eq. (5.16) has two groups of FRFs, respectively for the two unknown variables  $w$  and  $p$  over a point force  $F$ . This subsection will prove in practice that the formula Eq. (5.12) derived from the modal model of a structure is still feasible to the FRFs between  $w$  and  $F$  in the coupled system, but for the FRFs between  $p$  and  $F$ , another expression should be used.

In fact, about the FRFs in the vibroacoustic system, Wyckaert <sup>[94]</sup> has proved the formulae theoretically using the right and left eigenvectors of the non-symmetric system. The right eigenvector  $\psi^{(r)}$  and left eigenvector  $\psi^{(l)}$  for the eigenvalue  $\lambda_r$  of the system are related by

$$\begin{Bmatrix} \psi_s^{(l)} \\ \psi_f^{(l)} \end{Bmatrix}_{\lambda_r} = \begin{Bmatrix} \psi_s^{(r)} \\ \frac{1}{\lambda_r^2} \psi_f^{(r)} \end{Bmatrix}_{\lambda_r}, \quad (5.17)$$

with subscripts  $s$  and  $f$  denoting the structure and the fluid, respectively. Suppose that the displacement of the plate at point  $j$  is  $w_j$ , that the sound pressure at point  $l$  inside the cavity is  $p_{cl}$ , and that the force at point  $k$  of the plate is denoted as  $F_k$ , the FRFs can be written as

$$A_{jk}(\omega) = \frac{w_j}{F_k} = \sum_{r=1}^N \left( \frac{P_r \psi_{srj} \psi_{srk}}{i\omega - \lambda_r} + \frac{(P_r \psi_{srj} \psi_{srk})^*}{i\omega - \lambda_r^*} \right) \quad (5.18)$$

and

$$H_{lk}(\omega) = \frac{p_{cl}}{F_k} = \sum_{r=1}^N \left( \frac{P_r \psi_{frl} \psi_{srk}}{i\omega - \lambda_r} + \frac{(P_r \psi_{frl} \psi_{srk})^*}{i\omega - \lambda_r^*} \right), \quad (5.19)$$

where,  $(\lambda_r, \lambda_r^*)$  are the pairs of eigenvalues of the corresponding characteristic problem, and  $\psi_{srj}$ ,  $\psi_{srk}$  and  $\psi_{frl}$  are elements in the corresponding right eigenvectors. Given the residuals  $C_{lk,r} = P_r \psi_{frl} \psi_{srk}$ , Eq. (5.19) can be expressed as

$$H_{lk}(\omega) = \sum_{r=1}^N \left( \frac{C_{lk,r}}{i\omega - \lambda_r} + \frac{C_{lk,r}^*}{i\omega - \lambda_r^*} \right). \quad (5.20)$$

However, this is not a complete expression for a fitting model when the lower and upper residuals outside the fitting band are significant. Besides, it is not specified about how to extract the modal parameters from the outcome.

Thus, in this subsection, to identify the modal parameters of the vibroacoustic system using the best fitting approach, like Section 5.2.1.3, an improved fitting curve model of  $H_{lk}$  is proposed:

$$H_{lk}^{\text{mod}}(\omega)_{\omega \in \omega_r} = \frac{1}{i\omega M_{lk}^R} + \sum_{r=n_1}^{r=n_2} \left( \frac{C_{lk,r}}{i\omega - (-\sigma_r + i\omega_r)} + \frac{C_{lk,r}^*}{i\omega - (-\sigma_r - i\omega_r)} \right) + \frac{1}{K_{lk}^R}, \quad (5.21)$$

with the lower and upper residuals added to Eq. (5.20), for the truncation of frequency range. Eigenvalues  $\lambda_r$  are replaced by  $-\sigma_r + i\omega_r$ , so that the damping ratios can be estimated through  $\zeta_r = \sigma_r/\omega_r$ . The mode shapes are considered relying on the imaginary parts of  $C_{lk,r}$ . Actually, if the terms in the middle of Eq. (5.21) are summed up for each mode, a formula similar to the middle term of Eq. (5.12) will come out. However, numerator of the formula is no longer a single real number but includes an additional term related to  $i\omega$ , which is due to the fact that the modal residuals  $C_{lk,r}$  in Eq. (5.21) are complex numbers with nonzero real parts. Besides, the lower and upper residuals for the out-of-band compensation are different between Eq. (5.21) and Eq. (5.12). There is no reference for these out-of-band residuals, but the practice shows that the two terms in Eq. (5.21) work instead of the counterparts in Eq. (5.12).

Then, the modal parameters of the system can be identified from two groups of FRFs. The measured FRFs between  $w$  and  $F$  are fitted using the model expressed by Eq. (5.12), while the measured FRFs between  $p$  and  $F$  are approached by Eq. (5.21). Even if only one group can reflect all the modes (with respect to the natural frequencies and damping ratios), it is recommended to use both groups. As is indicated from the simulation outcome (see Fig. 4-18), the response of the plate at the cavity-controlled modes could be not significant enough to distinguish the resonance, so it is hard to identify all modes from the first group. On the other hand, the second group will lack the information of the plate mode shapes. When both groups are applied, the information of the vibroacoustic system will be more complete, and the agreement between the two sets of results can improve the credibility.

Therefore, in the following EMA of the plate-cavity coupled Noise-Box, the two groups of FRFs are measured and then used to estimate the modal parameters.

### 5.3.1.1 Hammer testing

To obtain the FRFs, this test keeps using the hammer excitation. Consequently, the testing procedures are identical to the EMA of uncoupled panel in Section 5.2.1. Experimental set-up is also not much different. As shown by Fig. 5-26, the main difference (compared to Fig. 5-11) is the Noise-Box cavity, where the absorbing materials have been removed and six microphones (Brüel & Kjør Type 4188) are installed to detect the sound pressure inside. The locations of the microphones are specified in Fig. 5-27 with their coordinates under the depicted coordinate system. This coordinate system is used whenever the Noise-Box cavity is involved, in consistence with other chapters (e.g., see Fig. 3-3, Fig. 4-11 or Fig. 4-16). Besides, one more sensor signal conditioner (PCB 483C) is used for conditioning the microphone signals. The test panel configuration is the same as the uncoupled case, as shown by Fig. 5-12. Corresponding to the new coordinate systems, the accelerometers A1, A2 and A3 are respectively specified as  $w_1$ ,  $w_2$  and  $w_3$  with coordinates  $\mathbf{r}'_1$ ,  $\mathbf{r}'_2$  and  $\mathbf{r}'_3$  in Fig. 5-27, and Point 80 is associated with  $F_{80}$  and  $\mathbf{r}'_{F80}$ .

Next, for the hammer test procedures, we can refer to Section 5.2.1.2. In this case, determined by the module (NI 9239 instead of NI 9234) used in the acquisition (NI cDAQ), the sampling frequency is 5000 Hz. Totally 13 channels are active, acquiring the time history of signals from hammer, accelerometers and microphones. Using the input force  $F_{80}$  at  $\mathbf{r}'_{F80}$ , the output acceleration  $a_1$  at  $\mathbf{r}'_1$  and the output pressure  $p_{c1}$  at  $\mathbf{r}'_{c1}$  as examples (see Fig. 5-27 for the input-output locations), the measured FRFs  $a_1/F_{80}$  and  $p_{c1}/F_{80}$  are respectively presented in Fig. 5-28 and Fig. 5-29.

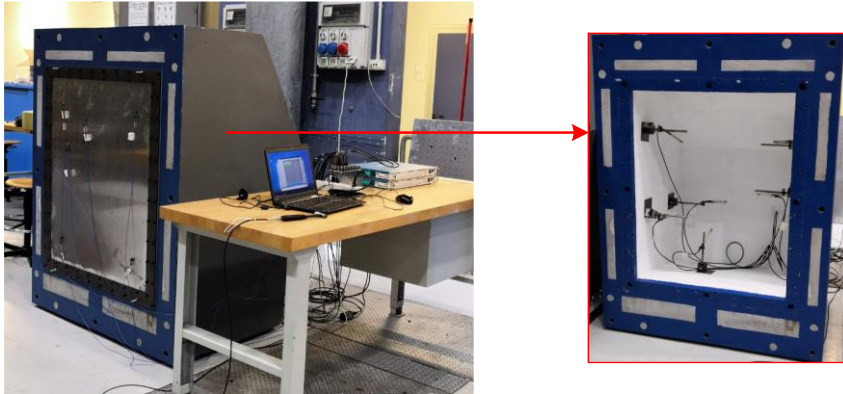


Fig. 5-26. Experimental set-up for plate-cavity system characterization

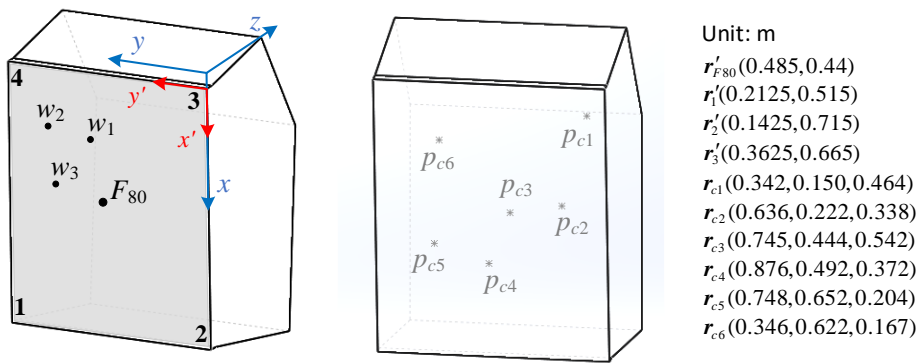


Fig. 5-27. Coordinates of input and output locations.

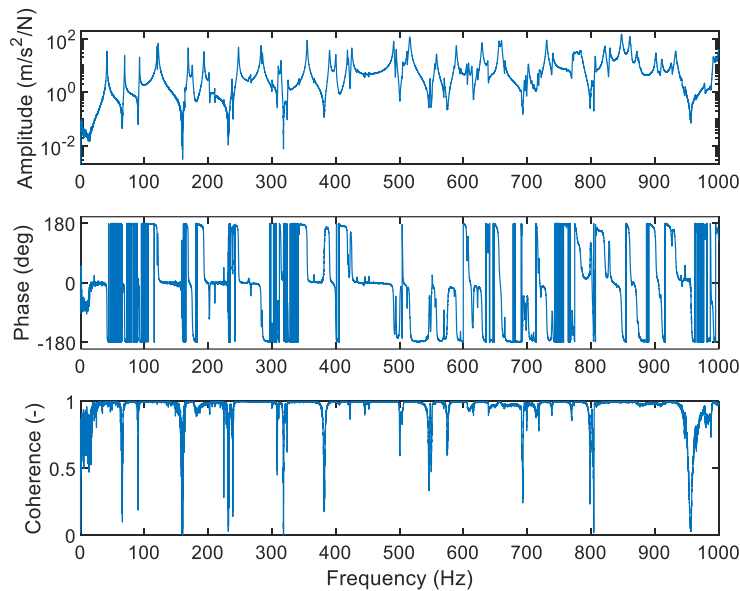


Fig. 5-28. Measured transfer function  $a_1/F_{80}$  and coherence function of the plate-cavity system (see Fig. 5-27) between acceleration at  $w_1$  and force at  $F_{80}$ .

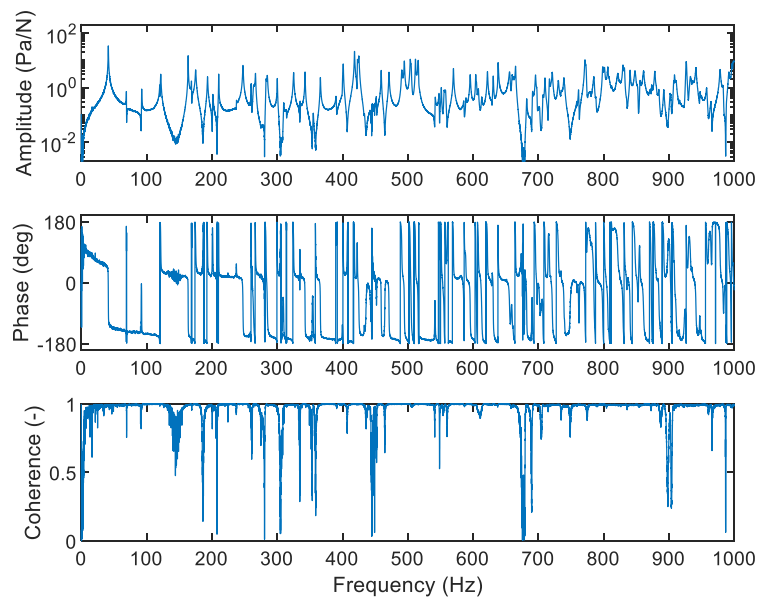


Fig. 5-29. Measured transfer function  $p_{c1}/F_{80}$  and coherence function of the plate-cavity system (see Fig. 5-27) between sound pressure at  $p_{c1}$  and force at  $F_{80}$ .

### 5.3.1.2 Modal parameters estimation

The modal parameters can be identified from the FRFs using the best curve fitting approach, similarly to Section 5.2.1.3. For the FRFs between panel acceleration (or displacement) and force, the formula Eq. (5.13) (or Eq. (5.12)) applied in the uncoupled case is continuously used in this case. For the FRFs between cavity pressure and force, the expression proposed in Eq. (5.21) is adopted. They will be seen performing well in the following results.

Two curve fitting strategies have been mentioned in Section 5.2.1.3, and they are used in this coupled case in the same way. Regarding the global best fitting approach that fits multiple FRFs simultaneously, the two groups of FRFs, i.e.,  $A_{jk} = a_j/F_k$  and  $H_{lk} = p_{c1}/F_k$ , are considered separately. As a result, two sets of modal parameters will be obtained based on the two groups of FRFs. Since the structural field and the acoustic field may be more sensitive to different modes, the natural frequencies and damping ratios can be chosen from the two sets dependently. As for mode shapes, the former set can only represent the panel, while the latter is for the cavity. Considering the different orders of amplitude, two fields are scaled independently. Fig. 5-30 shows an example of the identification results of mode shapes. The two modes are estimated together since they should interact with each other with so close the natural frequencies.

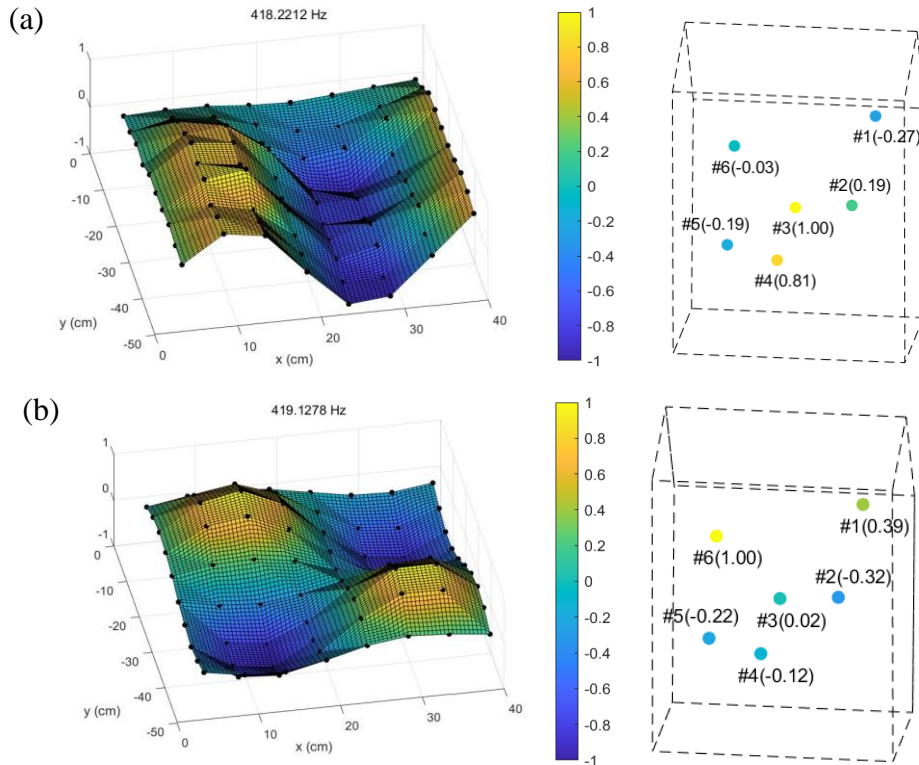


Fig. 5-30. Mode shapes of (a) 30<sup>th</sup> and (b) 31<sup>st</sup> modes of the plate-cavity system (see Table 5-11 for mode order and modal parameters). Plate is represented by the 1/4 panel grid (see Fig. 5-12), and cavity is by the 6 microphones (see Fig. 5-27).

After the global best fitting, which yields the modal parameters mode(s) by mode(s), the single curve best fitting for all modes is achievable by applying the previously estimated modal parameters as initial values. Table 5-11 lists the estimate results corresponding to the case when point force is acting on Point 80 (i.e., F<sub>80</sub> as shown in Fig. 5-27). Changing hitting position will see difference in modal residuals  $C_{jk,r}$  and  $C_{lk,r}$ , but marginal difference in natural frequencies and damping ratios. For validating the results, the estimate FRFs are reconstructed based on the listed modal parameters and compared with the measured ones, as illustrated in Fig. 5-31 and Fig. 5-32. As noticeable from the numerical investigation into the plate-cavity system (Section 4.4), the coupled modes can be categorized as plate controlled or cavity controlled. Both plate and cavity controlled modes have strong impact on the cavity's response, but the cavity controlled modes have much less influence on the plate. Sometimes, the cavity controlled modes are even too weak to observe or identify from the structural FRFs. Therefore, for the modal parameters in Table 5-11 that are identified from the panel accelerance  $A_{180} = a_1/F_{80}$ , some modes are missing. However, since they are cavity controlled, they can be estimated from the FRF related to the acoustic field, such as  $H_{180} = p_{c1}/F_{80}$ . Note that the input and output points are also important. For instance, at the 34<sup>th</sup> mode, when the exciting position is very close to a nodal line of plate,



both structural and acoustic fields are hardly excited. Since it is a plate controlled mode and the structural itself is barely vibrating, the acoustic field does even less resonance. Consequently, the parameters for this mode are hard to identified from  $H_{180}$ , and the natural frequency and damping ratio listed (*italic and red*) are estimated through  $H_{170}$  instead.

What's more, in Table 5-11, for the parameters that are available from both FRFs, most of them are in good agreement. This indicates that the two models, Eq. (5.13) for  $A_{jk}$  and Eq. (5.21) for  $H_{lk}$ , yield consistent natural frequencies and damping ratios, which are the expected outcomes if the models are accurate. It can also be found in Table 5-11 that the damping ratios of cavity controlled modes are usually smaller than 0.001 and the counterparts of the plate controlled ones tend to be larger. However, the discrepancy of the damping ratios between the two groups fades away as the frequency increases. It has been tried to distinguish the cavity controlled modes in Table 5-11 by shading grey and the basis of selection is the uncoupled acoustic modes (see Table 5-1). In particular, some rows are shading orange because there are two modes very close to one acoustic mode. They can be of two situations: (1) it is clear that one is cavity controlled and the other is plate controlled; (2) frequency splitting happens, while both are fully coupled by the plate and cavity. To determine the corresponding situation, it may be necessary to compare the coupled and uncoupled, plate and cavity responses. Such comparison is going to be discussed in the next subsection 5.3.2.

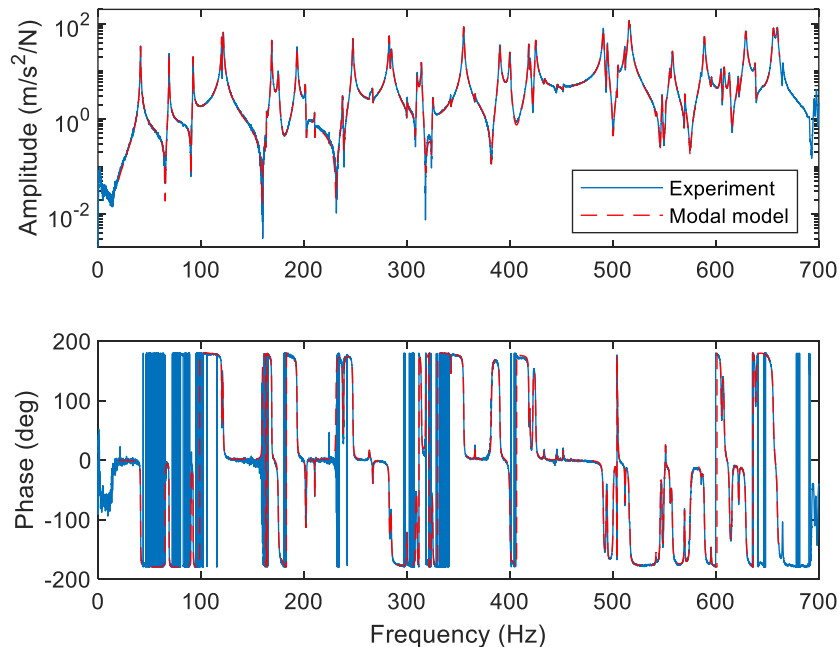


Fig. 5-31. Comparison of the coupled panel accelerance  $A_{180}(\omega)$  between experiment and the modal model estimation. The modal model uses the parameters listed in Table 5-11.

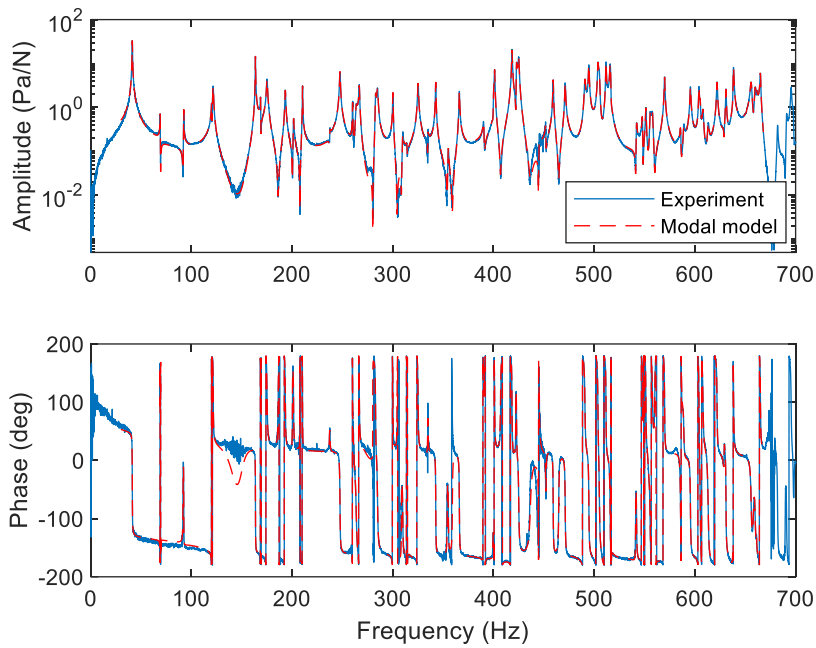


Fig. 5-32. Comparison of the transfer function  $H_{180} = p_{c1}/F_{80}$  between experiment and the modal model estimation. The modal model uses the parameters listed in Table 5-11.

Table 5-11. Two sets of identified modal parameters for the plate-cavity system. One set is estimated from the  $A_{180} = a_1/F_{80}$ , and the other is by  $H_{180} = p_{c1}/F_{80}$ .

Order	Best fitting for $A_{180}$			Best fitting for $H_{180}$				
	$f_r$ (Hz)	$\zeta_r$	$C_{180,r}$	$f_r$ (Hz)	$\sigma_r$	$\zeta_r$	$\text{Re}[C_{180,r}]$	$\text{Im}[C_{180,r}]$
1	41.4	0.0037	-0.254	41.4	-0.957	0.0037	24.446	-21.026
2	69.0	0.0015	-0.069	69.0	-0.763	0.0018	-0.329	0.406
3	92.5	0.0013	-0.054	92.5	-0.707	0.0012	0.285	-0.539
4	120.1	0.0012	0.111	120.2	-0.875	0.0012	-0.115	0.801
5	121.7	0.0027	0.352	121.6	-2.193	0.0029	-2.971	6.012
6	163.6	0.0007	-0.002	163.6	-0.668	0.0007	3.568	-9.372
7	168.7	0.0010	0.087	168.7	-1.098	0.0010	-0.539	1.537
8	175.1	0.0027	-0.052	175.2	-2.935	0.0027	-4.521	11.866
9	193.3	0.0016	0.107	193.3	-2.037	0.0017	-1.527	4.775
10	201.5	0.0014	-0.014	201.5	-1.868	0.0015	-0.400	0.937
11	210.4	0.0006	-0.001	210.4	-0.740	0.0006	-0.722	2.195
12	237.5	0.0011	0.006	237.5	-2.599	0.0017	-0.115	0.374
13	247.6	0.0013	0.126	247.6	-2.014	0.0013	3.883	-12.626
14	260.2	0.0007	-2E-5	260.1	-0.995	0.0006	-0.630	1.129
15	263.7	0.0038	0.005	263.7	-4.953	0.0030	2.327	-5.030
16	266.8	0.0013	-0.006	266.8	-2.155	0.0013	-2.309	6.508
17	282.9	0.0012	-0.127	282.9	-2.029	0.0011	-1.056	4.126
18	284.9	0.0018	-0.092	284.9	-3.220	0.0018	2.535	-8.491
19	300.1	0.0007	-0.003	300.1	-1.161	0.0006	-0.711	2.436
20	309.9	0.0012	-0.020	309.9	-2.547	0.0013	0.236	-0.555
21	314.1	0.0011	0.033	314.2	-3.617	0.0018	0.088	0.276
22	325.1	0.0011	-0.006	325.2	-2.176	0.0011	-1.896	7.470

Table 5-11 (continued). Two sets of identified modal parameters for the plate-cavity system. One set is estimated from the  $A_{180} = a_1/F_{80}$ , and the other is by  $H_{180} = p_{c1}/F_{80}$ .

Order	Best fitting for $A_{180}$			Best fitting for $H_{180}$				
	$f_r$ (Hz)	$\zeta_r$	$C_{180,r}$	$f_r$ (Hz)	$\sigma_r$	$\zeta_r$	$\text{Re}[C_{180,r}]$	$\text{Im}[C_{180,r}]$
23	334.9	0.0006	-2E-6	334.9	-1.880	0.0009	-0.171	0.300
24	342.7	0.0006	0.002	342.7	-1.182	0.0005	1.187	-4.350
25	355.2	0.0010	0.171	355.1	-1.977	0.0009	0.072	-0.207
26	366.1	0.0006	0.001	366.1	-1.592	0.0007	1.029	-3.550
27	390.2	0.0011	0.082	390.3	-2.839	0.0012	-0.217	1.042
28	400.0	0.0011	-0.054	400.0	-2.587	0.0010	1.296	-3.261
29	401.0	0.0015	0.005	401.1	-1.616	0.0006	-3.318	11.543
30	418.4	0.0007	0.047	418.4	-1.620	0.0006	-5.767	32.572
31	419.6	0.0010	0.031	419.6	-2.054	0.0008	0.397	-0.909
32				422.9	-1.659	0.0006	-3.348	15.703
33	425.1	0.0010	0.093	425.1	-2.822	0.0011	7.601	-39.105
34	433.4	0.0010	0.004	433.0	-3.023	0.0011		
35	445.7	0.0008	0.002	445.5	-3.757	0.0013	-0.584	0.518
36	451.9	0.0007	0.002	451.8	-2.240	0.0008	0.143	-0.605
37				459.3	-1.432	0.0005	1.589	-5.888
38				471.2	-2.034	0.0007	1.665	-7.173
39	490.7	0.0010	-0.159	490.8	-3.151	0.0010	-3.474	13.399
40	494.7	0.0006	-0.047	494.7	-1.981	0.0006	4.613	-18.280
41	503.7	0.0007	-0.007	503.8	-2.581	0.0008	-3.154	28.899
42	504.9	0.0009	0.021	505.1	-3.154	0.0010	1.275	-21.736
43	511.7	0.0005	-0.026	511.7	-1.548	0.0005	-2.070	16.642
44	515.8	0.0010	-0.194	515.9	-2.808	0.0009	1.549	-32.896
45	516.6	0.0009	-0.097	516.5	-3.136	0.0010	1.324	12.691
46	542.0	0.0007	-0.001	542.0	-1.984	0.0006	0.243	-0.780
47	547.8	0.0006	-0.003	547.8	-1.873	0.0005	-0.024	1.095
48	551.3	0.0007	0.001	551.4	-1.877	0.0005	-0.309	1.842
49	555.6	0.0009	-0.015	555.6	-3.108	0.0009	0.051	-2.339
50	557.8	0.0011	-0.054	557.8	-3.747	0.0011	-0.207	2.913
51	569.9	0.0005	-0.003	569.9	-1.744	0.0005	-1.567	8.447
52	585.8	0.0009	-0.007	585.7	-2.365	0.0006	-0.166	-0.910
53	588.9	0.0009	-0.097	589.0	-4.225	0.0011	0.440	1.179
54	595.6	0.0005	-0.003	595.6	-2.294	0.0006	1.203	-6.604
55				604.0	-1.753	0.0005	-1.059	5.474
56	605.2	0.0007	0.015	605.3	-2.718	0.0007	0.506	-4.566
57	608.0	0.0009	0.022	608.0	-3.557	0.0009	-0.240	3.225
58	613.3	0.0009	-0.016	613.2	-3.606	0.0009	0.412	-1.627
59	622.0	0.0006	-0.006	622.0	-2.222	0.0006	-1.122	8.325
60	629.1	0.0010	-0.142	629.0	-3.468	0.0009	-0.770	-0.267
61				630.9	-1.674	0.0004	1.727	-4.090
62				638.0	-2.558	0.0006	1.405	-15.738
63	638.3	0.0007	0.018	638.3	-2.581	0.0006	-3.960	29.025
64				651.4	-2.171	0.0005	-0.016	0.145
65	655.8	0.0011	0.176	655.8	-4.517	0.0011	3.047	-16.134
66	659.8	0.0012	-0.191	659.8	-4.723	0.0011	1.934	-12.414
67				661.2	-1.927	0.0005	1.058	-1.485
68				665.0	-2.113	0.0005	-2.490	12.710

### 5.3.2 Comparison between coupled and uncoupled situations

For understanding the modes of the plate-cavity system, it is worthwhile to compare them with the uncoupled plate and cavity. Combination of the three parts of EMA results that are respectively obtained in Section 5.1.3 (Table 5-1), Section 5.2.1.3 (Table 5-4) and Section 5.3.1.2 (Table 5-11) yields a summary shown in Table 5-12.

Table 5-12. Summary of experimental results on natural modes and frequencies of the uncoupled plate and cavity and the coupled plate-cavity system.

Uncoupled panel				Uncoupled cavity			Plate-cavity system		
Order	Mode	$f_{r,s}$ (Hz)	$\zeta_{r,s}$	Order	$(n_{2D}, n_y)$	$f_{r,a}$ (Hz)	Order	$f_{r,sa}$ (Hz)	$\zeta_{r,sa}$
				0	(0,0)	0			
1	(1,1)	38.1	0.0046				1	41.4	0.0037
2	(1,2)	65.1	0.0018				2	69.0	0.0018
3	(2,1)	88.9	0.0016				3	92.5	0.0012
4	(2,2)	116.2	0.0014				4	120.2	0.0012
5	(1,3)	117.6	0.0028				5	121.6	0.0029
				1	(1,0)	162.9	6	163.6	0.0007
6	(2,3)	164.5	0.0014				7	168.7	0.0010
7	(3,1)	171.3	0.0028				8	175.2	0.0027
8	(1,4)	188.9	0.0030				9	193.3	0.0017
9	(3,2)	197.6	0.0015				10	201.5	0.0015
				2	(0,1)	208.9	11	210.4	0.0006
10	(2,4)	233.1	0.0024				12	237.5	0.0017
11	(3,3)	243.7	0.0020				13	247.6	0.0013
				3	(2,0)	259.5	14	260.1	0.0006
				4	(1,1)	265.5	15	263.7	0.0030
12	(1,5)	278.6	0.0017				16	266.8	0.0013
13	(4,1)	280.7	0.0045				17	282.9	0.0011
				5	(3,0)	300.0	18	284.9	0.0018
14	(4,2)	305.7	0.0027				19	300.1	0.0006
15	(3,4)	309.8	0.0014				20	309.9	0.0013
16	(2,5)	321.6	0.0020				21	314.1	0.0011
				6	(2,1)	333.7	22	325.2	0.0011
				7	(4,0)	342.6	23	334.9	0.0009
17	(4,3)	351.0	0.0012				24	342.7	0.0005
				8	(3,1)	366.1	25	355.1	0.0009
18	(1,6)	385.8	0.0016				26	366.1	0.0007
19	(3,5)	395.7	0.0018				27	390.3	0.0012
				9	(4,1)	401.4	28	400.0	0.0010
				10	(0,2)	418.9	29	401.1	0.0006
20	(4,4)	414.8	0.0014				30	418.4	0.0006
				11	(5,0)	423.2	31	419.6	0.0010
21	(5,1)	418.8	0.0023				32	422.9	0.0006
22	(2,6)	428.7	0.0010				33	425.1	0.0011
23	(5,2)	443.5	0.0036				34	433.4	0.0010
				12	(1,2)	450.3	35	445.7	0.0008
				13	(6,0)	459.6	36	451.8	0.0008
							37	459.3	0.0005

Table 5-12 (continued). Summary of experimental results on natural modes and frequencies of the uncoupled plate and cavity and the coupled plate-cavity system.

Uncoupled panel				Uncoupled cavity			Plate-cavity system		
Order	Mode	$f_{r,s}$ (Hz)	$\zeta_{r,s}$	Order	$(n_{2D}, n_y)$	$f_{r,a}$ (Hz)	Order	$f_{r,sa}$ (Hz)	$\zeta_{r,sa}$
				14	(5,1)	471.9	38	471.2	0.0007
24	(5,3)	487.0	0.0014				39	490.8	0.0010
				15	(2,2)	494.5	40	494.7	0.0006
25	(4,5)	499.8	0.0010						
26	(3,6)	500.6	0.0018				41	503.8	0.0008
				16	(6,1)	505.1	42	505.1	0.0010
				17	(7,0)	512.1	43	511.7	0.0005
27	(1,7)	511.8	0.0018				44	515.9	0.0009
				18	(3,2)	516.4	45	516.5	0.0010
				19	(4,2)	542.7	46	542.0	0.0006
				20	(8,0)	549.4	47	547.8	0.0005
				21	(7,1)	551.9	48	551.4	0.0005
28	(5,4)	550.4	0.0014				49	555.6	0.0009
29	(2,7)	553.0	0.0016				50	557.8	0.0011
				22	(9,0)	570.1	51	569.9	0.0005
				23	(8,1)	586.9	52	585.7	0.0006
30	(6,1)	584.7	0.0020				53	589.0	0.0011
				24	(5,2)	594.7	54	595.6	0.0006
				25	(10,0)	604.9	55	604.0	0.0005
				26	(9,1)	606.3	56	605.3	0.0007
31	(4,6)	602.5	0.0015				57	608.0	0.0009
32	(6,2)	608.4	0.0018				58	613.2	0.0009
				27	(6,2)	623.0	59	622.0	0.0006
33	(3,7)	624.0	0.0018				60	629.0	0.0009
				28	(0,3)	630.9	61	630.9	0.0004
				29	(10,1)	638.8	62	638.0	0.0006
34	(5,5)	633.8	0.0010				63	638.3	0.0006
				30	(1,3)	651.6	64	651.4	0.0005
35	(6,3)	651.3	0.0016				65	655.8	0.0011
36	(1,8)	656.5	0.0020				66	659.8	0.0011
				31	(7,2)	661.4	67	661.2	0.0005
				32	(11,0)	664.9	68	665.0	0.0005

In Table 5-12, the coupled modes are listed in the same rows of its corresponding uncoupled controlling plate or cavity modes. As the table shows, the cavity controlled coupled modes have their natural frequencies approximated to the uncoupled situation, which indicates that vibration of the flexible plate has tiny influence on those modes. This is in consistence with what has been observed through the FE simulations (see Table 4-10 in Section 4.3.3). However, for the plate controlled coupled modes, the difference to the uncoupled panel is unlike the rule that was found from the simulations. In Section 4.3.3, the similar comparison was done on the simulation results out of the initial numerical models. The summary Table 4-10 indicates that the panel natural frequencies are slightly decreased by the backed cavity

except the first and the thirteenth modes. Therefore, the coupling between the panel and the cavity is not strong. Either the stiffening or mass effect from the cavity to the panel is limited. Even though the models that yield the simulation results have not yet been updated, the coupling mechanism should hold.

While looking back to the experiment on the uncoupled panel, it is found that the panel's natural frequencies are not stable and very sensitive to the mounting boundaries and temperature. Therefore, it can be expected that the boundary conditions of the panel in the coupled case are different from the identified uncoupled case. Limited to the plate controlled modes, their differences in natural frequencies to the uncoupled panel (the identified case listed in Table 5-12)  $\Delta f_{sa} = f_{r,sa} - f_{r,s}$ , are plotted in Fig. 5-33, versus the panel mode order. Meanwhile, the counterparts of simulations ( $\Delta f_{sa} = f_{sa} - f_s$ , based on Table 4-10) are plotted as reference. Then, it can be noticed that the difference in the experimental case too much exceeds the coupling effect that can be raised by the Noise-Box cavity. Instead, its relationship to the mode order is similar to the frequency shift observed in the discussion about different measurements of the uncoupled panel (see Section 5.2.1.4 and Fig. 5-17). Therefore, in the model updating of the plate-cavity system, the panel should be focused and the strategy could be similar to the uncoupled case in updating the mounting edge conditions (i.e., Section 5.2.3).

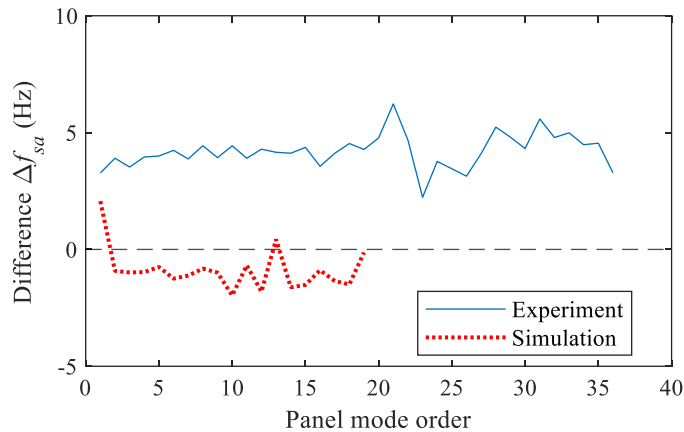


Fig. 5-33. Difference in natural frequencies of the mounted panel between the cavity backed case and *in vacuo* case. Experimental results correspond to Table 5-12:  $\Delta f_{sa} = f_{r,sa} - f_{r,s}$ ; simulation results correspond to Table 4-10:  $\Delta f_{sa} = f_{sa} - f_s$ .

Besides, Table 5-12 highlights two exceptions in red. One is the 15<sup>th</sup> coupled mode. It is not related to a plate or cavity mode in the table. Indeed, it was thought as a miss fitting but the double check found that this frequency is necessary for a perfect fitting. While checking its mode shape, it is noticed that the acoustic field is similar to the 16<sup>th</sup> mode but opposite in phase. Therefore, it may have a close relationship to the 4<sup>th</sup> cavity mode, but it is still not

rashly considered as controlled by that cavity mode, since the damping ratio is much larger than other cavity controlled modes. The reason for its presence is not yet figured out, but it is considered necessary to list as it is. The other is the 25<sup>th</sup> panel mode. The frequency of this mode is very close to the 26<sup>th</sup> panel mode. The 25<sup>th</sup> panel mode is hard to be identified. While it is slightly noticeable in the coupled case, it is even harder to find in the coupled case, since the next cavity mode better fits the 26<sup>th</sup> mode.

At last, one more important point is that, in the experiment, the uncoupled panel is not ideally *in vacuo*, but approximated by covering the cavity walls with sound absorbing materials. This may lead to some errors, especially for the first several modes. However, the influence can be investigated through numerical simulations. In this sense, the comparison between coupled and uncoupled cases is indeed between two coupled cases with the cavity in different boundary conditions, where one is enclosed by highly reflected walls and the other is surrounded with highly damped walls. If the modal damping ratios in Table 5-12 are compared between the two cases, it is observable that the coupled case has lower damping ratios in general. This is reasonable, because the absorbing materials do raise the damping of the whole system.

### 5.3.3 Plate-cavity system model updating

As mentioned above, the plate-cavity system model updating will focus on the structural part. Following Section 5.2.3 about panel model updating, the updating parameters are the edge rotational stiffnesses  $k_{\theta_x}$  and  $k_{\theta_y}$  (see Fig. 5-24) and the panel Young's modulus  $E$ . Air properties of the cavity are updated based on the experimental temperature:  $T_A = 23.8^\circ\text{C}$ . That is,  $\rho_0 = 1.1889 \text{ kg/m}^3$  and  $c = 345.42 \text{ m/s}$ . As for the panel, the fixed parameters are  $\rho = 2680 \text{ kg/m}^3$ ,  $h = 3.93 \text{ mm}$ ,  $\nu = 0.33$ , which are the updating results of the test panel under the uncoupled situation (outcome of Section 5.2). As a first attempt, the initial values of  $k_{\theta_x}$ ,  $k_{\theta_y}$  and  $E$  are set as  $k_{\theta_x} = 5 \text{ kN/rad}$ ,  $k_{\theta_y} = 9 \text{ kN/rad}$  and  $E = 76 \text{ GPa}$ , which are also the outcome of the uncoupled panel test. After the optimizing process for the least errors of natural modes and frequencies between numerical and experimental results, the updated parameters are determined as  $\hat{k}_{\theta_x} = 9 \text{ kN/rad}$ ,  $\hat{k}_{\theta_y} = 16 \text{ kN/rad}$  and  $\hat{E} = 77 \text{ GPa}$ . The results before and after this optimization are listed in Table 5-13, where the cavity controlled modes are shaded and numerical predicting errors  $Er_f$  are presented alongside. For a graphical comparison, the scatter plot of simulation frequency  $f_s$  vs experimental frequency  $f_r$  is shown in Fig. 5-34. Since the predictions of both models are close to the expected results, an alternative plot is also provided in the figure, illustrating the prediction errors.

Table 5-13. Natural frequencies and modes of the plate-cavity system in experiment (EMA) and simulations (Initial model:  $k_{\theta_x} = 5$  kN/rad,  $k_{\theta_y} = 9$  kN/rad and  $E = 76$  GPa; Updated model:  $k_{\theta_x} = 9$  kN/rad,  $k_{\theta_y} = 16$  kN/rad and  $E = 77$  GPa).

Order	EMA		Initial model		Updated model	
	$f_r$ (Hz)	Mode	$f_s$ (Hz)	$Er_f$ (Hz)	$f_s$ (Hz)	$Er_f$ (Hz)
1	<b>41.4</b>	(1,1)	40.7	-0.7	43.0	1.6
2	<b>69.0</b>	(1,2)	66.5	-2.5	70.5	1.4
3	<b>92.5</b>	(2,1)	87.3	-5.2	92.2	-0.3
4	<b>120.2</b>	(2,2)	115.6	-4.6	121.3	1.1
5	<b>121.6</b>	(1,3)	116.2	-5.5	121.7	0.1
6	<b>163.6</b>		162.8	-0.8	163.1	-0.6
7	<b>168.7</b>	(2,3)	163.3	-5.5	170.1	1.4
8	<b>175.2</b>	(3,1)	165.7	-9.5	173.2	-1.9
9	<b>193.3</b>	(1,4)	184.8	-8.5	192.0	-1.4
10	<b>201.5</b>	(3,2)	193.7	-7.8	201.7	0.3
11	<b>210.4</b>		210.0	-0.4	210.0	-0.4
12	<b>237.5</b>	(2,4)	230.3	-7.2	238.5	0.9
13	<b>247.6</b>	(3,3)	240.2	-7.4	249.0	1.4
14	<b>260.1</b>		260.4	0.3	260.8	0.7
15	263.7					
16	<b>266.8</b>		265.6	-1.1	265.8	-0.9
17	<b>282.9</b>	(1,5)	271.9	-11.0	280.4	-2.5
18	<b>284.9</b>	(4,1)	271.3	-13.6	281.6	-3.2
19	<b>300.1</b>		299.2	-0.9	299.7	-0.5
20	<b>309.9</b>	(4,2)	299.5	-10.3	309.9	0.0
21	<b>314.1</b>	(3,4)	306.7	-7.5	316.4	2.3
22	<b>325.2</b>	(2,5)	316.4	-8.7	325.7	0.6
23	<b>334.9</b>		334.8	-0.1	335.4	0.5
24	<b>342.7</b>		342.6	0.0	342.7	0.0
25	<b>355.1</b>	(4,3)	345.7	-9.4	356.7	1.6
26	<b>366.1</b>		365.6	-0.5	365.8	-0.3
27	<b>390.3</b>	(1,6)	377.2	-13.1	387.6	-2.7
28	<b>400.0</b>	(3,5)	391.7	-8.3	402.6	2.6
29	<b>401.1</b>		401.2	0.1	401.5	0.3
30	<b>418.4</b>		404.1	-14.3	415.3	-3.1
31	<b>419.6</b>	(4,4)	411.4	-8.2	423.3	3.7
32	<b>422.9</b>		423.0	0.1	423.2	0.4
33	<b>425.1</b>	(5,1)	419.8	-5.2	421.8	-3.3
34	<b>433.4</b>	(2,6)	422.2	-11.2	433.2	-0.2
35	<b>445.7</b>	(5,2)	432.0	-13.8	444.2	-1.5
36	<b>451.8</b>		450.1	-1.8	451.1	-0.7
37	<b>459.3</b>		457.3	-1.9	457.5	-1.8
38	<b>471.2</b>		471.8	0.6	471.9	0.7
39	<b>490.8</b>	(5,3)	478.6	-12.2	491.4	0.6
40	<b>494.7</b>		493.5	-1.3	494.7	0.0
		(4,5)	495.8		502.8	



Table 5-13 (continued). Natural frequencies and modes of the plate-cavity system in experiment (EMA) and simulations (Initial model:  $k_{\theta_x} = 5$  kN/rad,  $k_{\theta_y} = 9$  kN/rad and  $E = 76$  GPa; Updated model:  $k_{\theta_x} = 9$  kN/rad,  $k_{\theta_y} = 16$  kN/rad and  $E = 77$  GPa).

Order	EMA		Initial model		Updated model	
	$f_r$ (Hz)	Mode	$f_s$ (Hz)	$Er_f$ (Hz)	$f_s$ (Hz)	$Er_f$ (Hz)
41	<b>503.8</b>	(3,6)	496.0	-9.1	507.9	2.8
42	<b>505.1</b>		503.0	-2.2	508.8	3.7
43	<b>511.7</b>		513.0	1.3	512.0	0.2
44	<b>515.9</b>	(1,7)	501.1	-14.8	513.9	-2.0
45	<b>516.5</b>		515.1	-1.4	515.5	-1.0
46	<b>542.0</b>		540.6	-1.5	541.3	-0.8
47	<b>547.8</b>		548.4	0.6	546.5	-1.4
48	<b>551.4</b>		552.9	1.6	553.2	1.8
49	<b>555.6</b>	(5,4)	543.2	-12.4	558.9	3.3
50	<b>557.8</b>	(2,7)	545.3	-12.5	558.1	0.2
51	<b>569.9</b>		570.9	1.0	570.9	1.0
52	<b>585.7</b>		585.2	-0.5	585.6	-0.2
53	<b>589.0</b>	(6,1)	566.5	-22.5	581.8	-7.1
54	<b>595.6</b>		595.0	-0.6	595.1	-0.4
55	<b>604.0</b>		601.4	-2.6	601.5	-2.6
56	<b>605.3</b>		608.3	3.1	606.0	0.7
57	<b>608.0</b>	(4,6)	599.4	-8.7	613.2	5.2
58	<b>613.2</b>	(6,2)	592.9	-20.3	611.4	-1.8
59	<b>622.0</b>		620.7	-1.3	620.0	-2.0
60	<b>629.0</b>	(3,7)	618.5	-10.5	632.7	3.7
61	<b>630.9</b>		628.4	-2.5	628.5	-2.4
62	<b>638.0</b>		636.1	-2.0	636.7	-1.3
63	<b>638.3</b>	(5,5)	627.9	-10.4	642.9	4.6
64	<b>651.4</b>		649.3	-2.1	649.3	-2.0
65	<b>655.8</b>	(6,3)	640.2	-15.6	655.9	0.0
66	<b>659.8</b>	(1,8)	643.2	-16.7	656.5	-3.3
67	<b>661.2</b>		662.0	0.8	662.0	0.8
68	<b>665.0</b>		666.0	1.0	666.1	1.1

The natural frequencies of cavity controlled modes have a good agreement between the numerical and experimental results, no matter the numerical model is before or after model updating. This is easy to learn from Table 5-13, and the outcome has benefited from the accurate acoustic model. In comparison, the prediction for plate controlled modes has observable improvement in accuracy due to the mode updating. From Fig. 5-34, it can be seen that, for the initial model, the numerical results are smaller than the experimental ones and the errors will increase if the frequency goes higher. However, if the updated model is considered, the outcome is fluctuating around the reference line and the errors are reduced from all perspectives.

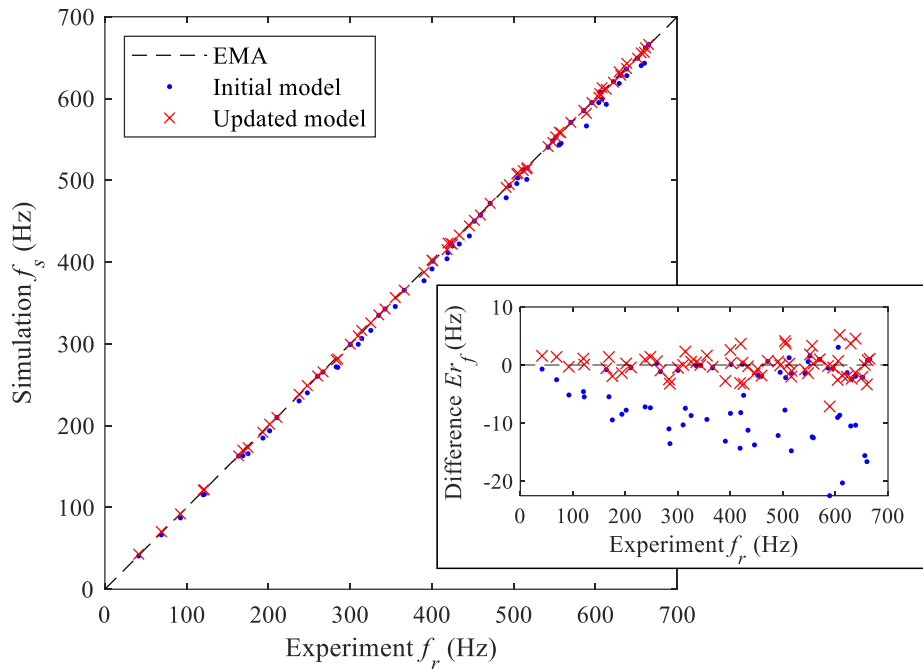


Fig. 5-34. Scatter plot for natural frequencies of the plate-cavity system or their difference between numerical simulation and experimental measurement. Corresponding data are listed in Table 5-13.

For further demonstrating the performance of the updated FE model of the plate-cavity system, the FRFs are also compared between numerical predictions and experimental outcomes. The FE model set-up in COMSOL has already been introduced in Section 4.4. The differences in this case are the updated parameters. Apart from the parameters introduced in the beginning of this subsections, which are necessary for the ‘eigenfrequency’ analysis, the parameters relevant to damping are also included in this ‘frequency domain’ analysis. For the cavity, wall impedances are applied, according to the sound absorption identified in the Noise-Box cavity characterization (Section 5.1.4) and using the relationship between wall impedance and sound absorption coefficient (Eq. (5.5)). Regarding the panel, approximating damping loss factor  $\eta = 2\zeta_r \approx 0.003$  is used (like predicting the FRFs of the uncoupled test panel in Section 5.2.3). Then, the harmonic analysis of the coupled system was conducted from 10 Hz to 700 Hz at intervals of 1Hz. The results obtained from COMSOL are compared with the experimental ones in Fig. 5-35 and Fig. 5-36, respectively for the acceleration at a point of the panel  $A_{180} = a_1/F_{80}$  and for the pressure at a location inside the cavity  $H_{280} = p_{c2}/F_{80}$ . It can be seen that the curves are not perfectly matched, but the errors are within an acceptable range. Besides, the good match of the FRFs  $H_{280}$  shown in Fig. 5-36 indicates that, even though the modal parameters used for model updating is principally identified from  $H_{180}$ , the updated model has an accurate prediction for any other FRFs.

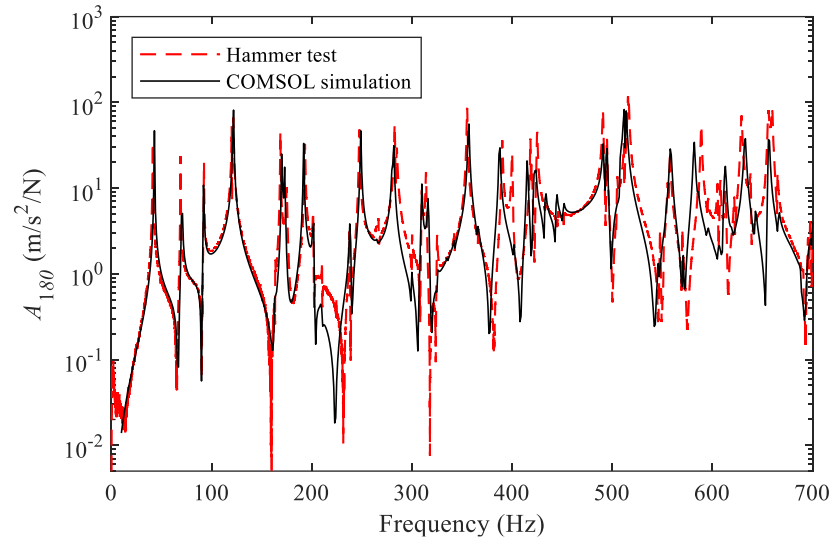


Fig. 5-35. Measured and simulated FRFs  $A_{180} = a_1/F_{80}$  of the plate-cavity system. The locations of the input force  $F_{80}$  and the output acceleration  $a_1$  (corresponding to displacement  $w_1$ ) are shown in Fig. 5-27.

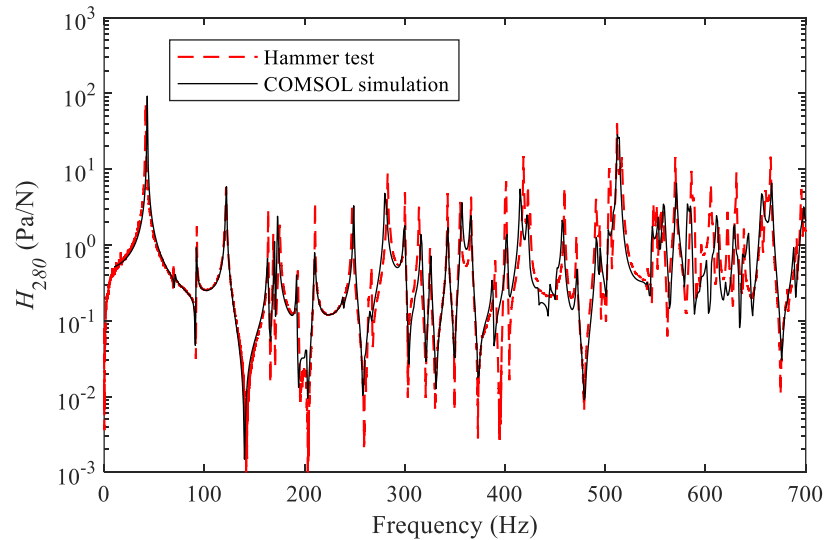


Fig. 5-36. Measured and simulated FRFs  $H_{280} = p_{c2}/F_{80}$  of the plate-cavity system. The locations of the input force  $F_{80}$  and the output acoustic pressure  $p_{c2}$  are shown in Fig. 5-27.

### 5.3.4 Influence of cavity on plate vibration

With the updated plate-cavity vibroacoustic model available, this subsection investigates the effects of the Noise-Box cavity on the test panel through both the experimental outcomes and the numerical simulations. While Section 5.3.2 compares the coupled and uncoupled modal parameters, this investigation directly compares the FRFs.

Fig. 5-37 shows the measured FRFs  $A_{180} = a_1/F_{80}$  of the hammer tests. One measurement (denoted as ‘without cavity’) is obtained in Section 5.2, where the inner walls of the cavity are covered with sound absorbing materials to avoid the feedback from cavity to the mounted panel. The other measurement (denoted as ‘with cavity’) is obtained in this section, where the cavity walls are highly reflected without covered by any other material. Three points can be learned from the discrepancy between the two FRFs. Firstly, lower peak amplitudes are observed in the ‘without cavity’ case, verifying the fact that the system damping is higher in the ‘without cavity’ situation. This is caused by the limitation of the experimental set-up, where the absorbing materials cannot realize a free field indeed. Secondly, cavity modes are only observable from the ‘with cavity’ curve. This is consistent with the simulation results in Section 4.4.3, pointing out one of major effects of the backed cavity. Thirdly, the two curves indicate a frequency shift that seems not raised by the coupling between plate and cavity but related to the boundary conditions of the test panel. However, it is hard to guarantee the same boundary conditions among different tests, especially when the mounting and dismounting processes are necessary between the two required measurements.

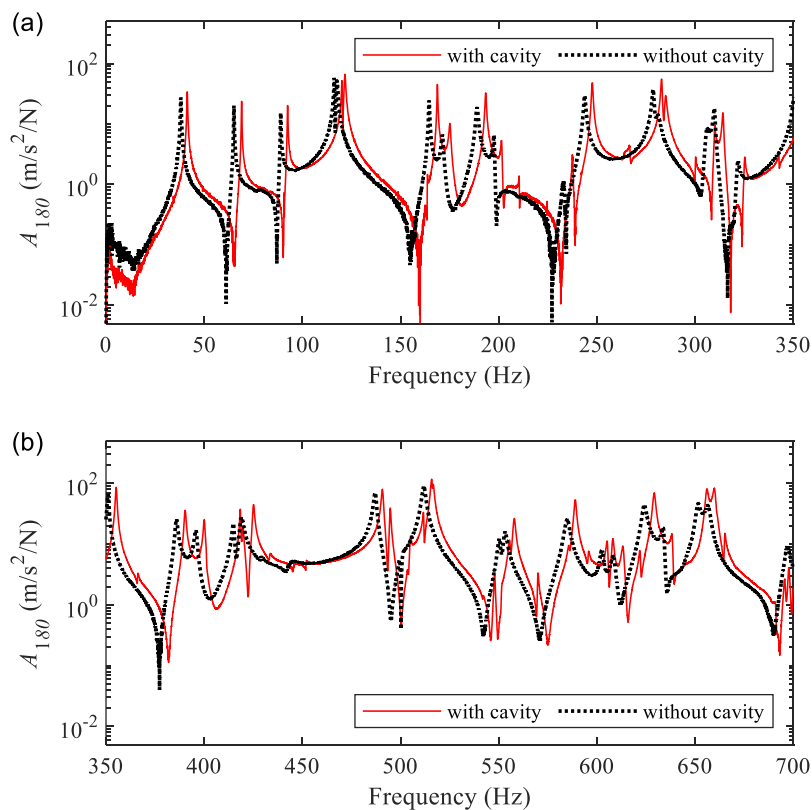


Fig. 5-37. The measured FRFs  $A_{180} = a_1/F_{80}$  of the mounted test panel with and without the backed Noise-Box cavity.

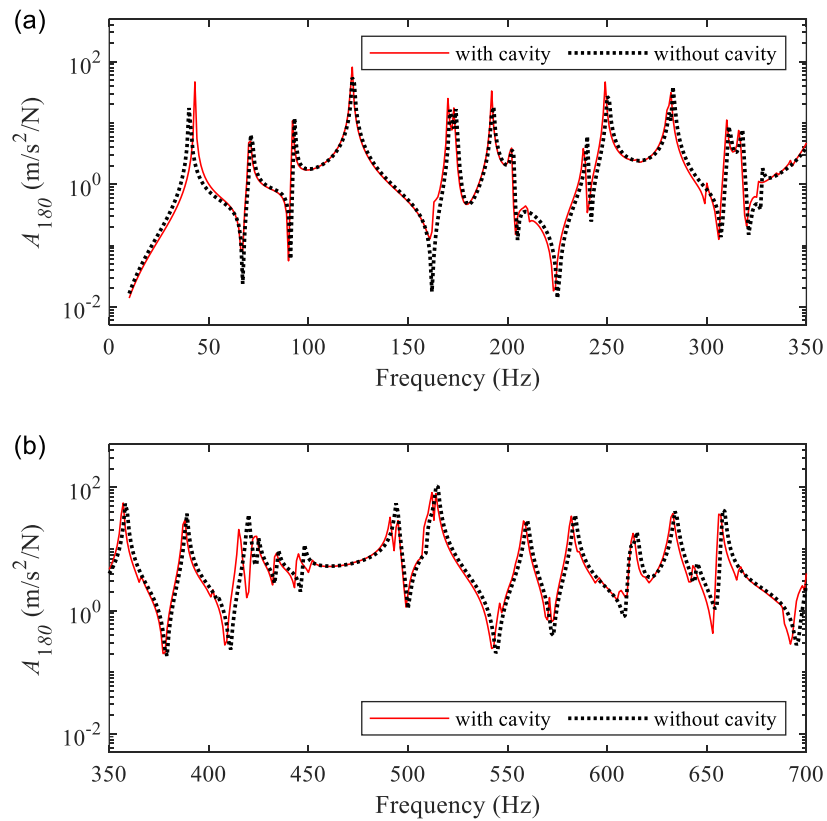


Fig. 5-38. The predicted FRFs  $A_{180} = a_1/F_{80}$  by COMSOL for the mounted test panel with and without the backed Noise-Box cavity.

By contrast, the numerical simulations have the advantage of controlling variables. In Section 5.3.3, the FE model of the plate-cavity coupled system has been updated and is available to predict the FRF  $A_{180} = a_1/F_{80}$  of the panel backed by the Noise-Box cavity. Starting from the same model, it is convenient to keep all the other setting and just remove the Noise-Box cavity. Then, the corresponding FRF  $A_{180}$  of the *in vacuo* mounted panel is available from analysis, where the boundary conditions and the material properties of the test panel are the same as the coupled situation. Fig. 5-38 shows the comparison of the simulation results. In the figure, ‘with cavity’ is predicted from the updated plate-cavity model, the same curve that is presented in Fig. 5-35 as ‘COMSOL simulation’; ‘without cavity’ is predicted from the same model but with the acoustic field and the Multiphysics coupling disabled. The simulation results demonstrate that the influence of the cavity on the panel is small and less significant than it is observed in experiment. To sum up, the cavity does influence the vibration of the panel, but the effect is quite limited.

## 5.4 Summary

Three experiments were performed for characterizing the Noise-Box cavity, the mounted test panel, and the coupled plate-cavity system, respectively. The characterization on one hand provides some important information of the component, and on the other hand identifies the necessary parameters to update the component's mathematical or numerical models.

In the experiment of Noise-Box cavity characterization, the opening of the cavity was covered by a 25-mm-thick plexiglass plate for an uncoupled acoustic field. Three measurements were done respectively for three characteristics:

- (1) For modal characteristics, the natural frequencies of the Noise-Box are identified from the measured FRFs of the cavity by peak-picking approach, while the mode shapes are known from the FEA results, since the numerical natural frequencies agree well with the experimental ones.
- (2) The average sound absorption coefficient is evaluated by the reverberation time measurement. The reverberation time of the Noise-Box cavity in 1/3 octave bands within 160~6300 Hz are within 0.7~3.71 sec. Corresponding the average sound absorption coefficient is between 0.006 and 0.032, which is small and meets the requirement of a reverberation room.
- (3) The sound field diffuseness is checked by several quantifiers. The mode count of 20 modes per third octave band accords with the cut-off frequency 650 Hz. Below this frequency, the acoustic field is dominated by the modal properties. The modal overlap factor no less than 1 and 3 respectively advocates the lower limit larger than 1250 Hz and 2500 Hz, where the latter agrees with the Schroeder frequency 2669 Hz, above which the sound field is ideally diffuse. Besides, the spatial standard deviation of the sound pressure levels indicates two other limits, i.e., 1000 Hz and 2500 Hz. By comparison, it can be concluded that there is a transition for the diffuse level from 650 Hz to 2500 Hz.

With respect to cavity model update, the air density and speed can be updated by temperature, and the wall impedance can be updated according to the sound absorption coefficient (Fig. 5-4).

The test panel characterization is for a 4-mm aluminium plate mounted on the Noise-Box. The panel is mounted as it would be in a formal test but the inner walls of the cavity are covered by sound absorbing material to avoid the cavity effect. Analyses were performed for three groups of parameters. The first group is obtained by EMA, where modal parameters of the first 36 modes were identified, using the best curving fitting approach. These parameters were later used as reference for plate model updating. However, the

mounted panel is found significantly influenced by the experimental environment, especially the change of temperature. This should be blamed on the thermal expansion and the large span-to-thickness ratio of the panel. The former causes thermal stress in plane because of the restrained plate edges, while the latter renders the panel sensitive to the membrane forces. Therefore, it would like to say that these modal parameters are for this specific mounting case. Secondly, it is a group of physical parameters: panel thickness  $h$ , material density  $\rho$ , Young's modulus  $E$  and Poisson's ratio  $\nu$ . Through the weight of the panel and its natural frequency measured in free-free boundary conditions, they are finally settled as  $\rho = 2680 \text{ kg/m}^3$ ,  $h = 3.93 \text{ mm}$ ,  $E = 69 \text{ GPa}$  and  $\nu = 0.33$ . Thirdly, they are the edge condition parameters, which rely on the model of the edge conditions. Since it is found by comparing the FEA and EMA results that the real boundary of the mounted panel is not ideally clamped or simply supported but a status in between, the model for condition 'rigidly supported but elastically restrained against rotation' is proposed. The rotational stiffnesses along width and length are considered different, denoted as  $k_{\theta_x}$  and  $k_{\theta_y}$ , respectively. Meanwhile, as a compensate for no consideration of membrane forces in the plate model,  $E$  is also considered as an updating parameter. Finally, the parameters best matching the test in EMA of the uncoupled mounted panel are  $k_{\theta_x} = 5 \text{ kN/rad}$ ,  $k_{\theta_y} = 9 \text{ kN/rad}$ ,  $E = 76 \text{ GPa}$ . In the model that includes structural damping, the damping loss factor of the plate can be approximated by  $\eta = 2\zeta_r \approx 0.003$ .

The characterization of the plate-cavity system is about the modified EMA for an interior vibroacoustic system. In the experiment, the absorbing material had been removed away from the walls, and six microphones were positioned inside the cavity. During the hammer test, acceleration at the panel and sound pressure in the cavity were acquired. Then, the modal parameters of the system were identified through the transfer functions  $H_{lk}$  (between sound pressure and force) and  $A_{jk}$  (between acceleration and force). Comparison between the coupled and uncoupled modes through experiments reveals that the boundary conditions and membrane forces in this case are different from the previous mounting case. Therefore, the conditioned parameters are updated again for this coupled plate-cavity case for better matching the experimental results. The updated parameters are  $k_{\theta_x} = 9 \text{ kN/rad}$ ,  $k_{\theta_y} = 16 \text{ kN/rad}$  and  $E = 77 \text{ GPa}$ . If damping is considered, the cavity walls can be assigned with frequency-dependant impedance according to the sound absorption coefficient (Fig. 5-4) or a given value averaged over the frequency range of interest; and the plate can adopt the approximating damping loss factor  $\eta = 2\zeta_r \approx 0.003$ .





## Chapter 6 Numerical investigation using wave based method

*This chapter develops and validates the wave based (WB) models that can be used to investigate the Noise-Box and its components. The problems that have already been investigated via FEM are solved here by WBM, with the parameters identified or updated in Chapter 5 applied. Corresponding results obtained from FEM will serve to validate the WB models, when the WBM will show more efficient than the FEM. Firstly, the general procedures of WBM for all problems is introduced. The next is the WBM for flexural vibration of thin plates, where a new weighted residual formulation is proposed for all types of restraints along the plate edges. Then, the WBM for interior acoustic problem is illustrated and applied to the Noise-Box cavity. Finally, the plate-cavity coupled Noise-Box is analysed by WBM, where the proposed formulation for elastically restrained plate is proved applicable to the plate-cavity problems.*

### 6.1 General procedures for WBM

Though the final wave based (WB) models depend on the problem types, the modelling procedures are identical. The following summarizes the general four steps <sup>[101]</sup> of WBM with respect to the generic steady-state dynamic problem given by Eq. (4.1):

- (1) Partitioning the problem domain into convex subdomains:

$$\Omega \simeq \tilde{\Omega} = \bigcup_{\alpha=1}^{n_{\alpha}} \Omega^{\alpha}. \quad (6.1)$$

The field variables are approximated by expansions inside each subdomain ( $\Omega^{\alpha}$ ), and convexity of the subdomain is a sufficient condition for their convergence <sup>[27]</sup>. Therefore, if the considered domain is nonconvex, it is necessary to partition it to convex subdomains. While it is an unbounded problem, there can be an additional unbounded subdomain enclosing all the others. Once the subdivision is performed, it is necessary to impose the continuity conditions between adjacent subdomains. The techniques about how to partition the domain and enforce the continuity conditions can be found in <sup>[136,151,152]</sup>. However, this step is not necessary, provided that the considered problem domain is originally convex.

- (2) Selecting a suitable set of wave functions for each subdomain and forming the field variable expansions:

$$u^{(\alpha)}(\mathbf{r}) \simeq \hat{u}^{(\alpha)}(\mathbf{r}) = \sum_{s=1}^{n_s} u_s^{(\alpha)} \psi_s^{(\alpha)}(\mathbf{r}) + \hat{u}_{F_v}^{(\alpha)}(\mathbf{r}) \quad \mathbf{r} \in \Omega^{\alpha}. \quad (6.2)$$

This step enforces the governing equation with the wave functions  $\psi_s^{(\alpha)}(\mathbf{r})$  coming from a complete set of functions that satisfies the homogeneous part of the equation and the function  $\hat{u}_{F_v}^{(\alpha)}(\mathbf{r})$  being a particular solution of the inhomogeneous part. The factors  $u_s^{(\alpha)}$  to the wave functions are called wave function contribution factors. They are independent unknowns that determine the final expression of  $\hat{u}^{(\alpha)}(\mathbf{r})$ . The number  $n_s$  denotes the total number of wave functions in the expansion. For convergence issues, there are truncation rules that relate the highest wavenumber of the wave functions to the physical wavenumber of the considered problem. The relationship is usually expressed with the aid of a user-defined truncation factor, which can be used for balancing the computational cost and the prediction accuracy.

- (3) Constructing the WB system of equations:

$$\mathbf{A}\mathbf{u} = \mathbf{f}, \quad (6.3)$$

where,  $\mathbf{A}$  is the  $n_s$  by  $n_s$  system matrix;  $\mathbf{u}$  is the vector of the  $n_s$  unknown wave function contribution factors; and  $\mathbf{f}$  is the vector related to the forcing terms. This step needs to impose the boundary conditions and the interface conditions. In case that the expanded field variable  $\hat{u}(\mathbf{r})$  may violate these conditions, the system is constructed using the weighted residual approach to minimize the errors. The weighted residual formulation can be derived based on a variational analysis and/or using the collocation, the least squares or the Galerkin method.

- (4) Solution and postprocessing. The wave function contribution factors are first obtained by solving the system of equations Eq. (6.3). Then, field variables are derived by back-substituting the contribution factors into the field variable expansions Eq. (6.2).

In this chapter, the WBM will be used to investigate the test panel, the Noise-Box cavity and the plate-cavity coupled Noise-Box. Since for all of them, the problem domains are convex, the first step can be skipped. Then, the steps (2) and (3) are predominant, determining the final WB model. Particularly, the field variable expansion in step (2) and the weighted residual formulation in step (3) are dependent on the considered problem. Thus, their expressions are introduced in the following sections respectively for the three problems corresponding to the three investigating targets. For every numerical case in the following problems, the WBM is implemented via MATLAB and their codes are provided in the database <sup>[213]</sup>.

## 6.2 WBM for flexural vibration of thin plate

In this section, a modified WBM for flexural vibration of thin plates is proposed and then used to analyse the mounted test panel and a 1D case. The new method extends the treatable

boundary conditions of the plate from the classical boundary conditions to any type of edge restraints. At first, the proposed WBM is detailly introduced following the WB modelling procedures, in considering the flexural vibration of a general convex thin plate, whose problem definition has been clarified in Section 2.2. Then, the method is utilized to analyse the uncoupled mounted test panel that has been identified in Section 5.2. In this part, the WBM results are compared with the corresponding results from FE simulation for validation. The reference FEM results have compared with the experimental ones in Fig. 5-25. At last, the proposed method is validated for 1D thin plates using a numerical case with FEM results.

### 6.2.1 Field variable expansion

Considering the flexural vibration problem defined in Section 2.2.1 of a 2D thin plate, the field variable, transverse displacement  $w(x,y)$  is first expanded using the wave functions  $\psi_s$ :

$$w(x, y) \approx \hat{w}(x, y) = \sum_{s=1}^{n_s} w_s \psi_s(x, y) + \hat{w}_F(x, y), \quad (6.4)$$

where,  $\psi_s$  satisfy the homogeneous part of Eq. (2.1),  $w_s$  are the contribution factors,  $n_s$  is the total number of wave functions, and  $\hat{w}_F$  is the particular solution of Eq. (2.1), which is given by <sup>[214]</sup>

$$\hat{w}_F(x, y) = -\frac{jF}{8k_b^2 D} [H_0^{(2)}(k_b |\mathbf{r} - \mathbf{r}_F|) - H_0^{(2)}(-jk_b |\mathbf{r} - \mathbf{r}_F|)], \quad (6.5)$$

where,  $|\mathbf{r} - \mathbf{r}_F| = \sqrt{(x - x_F)^2 + (y - y_F)^2}$  and  $H_0^{(2)}$  is the zero-order second kind Hankel function.

For the wave functions  $\psi_s$ , two different sets have been proposed <sup>[141,146,215]</sup>. The first set uses cosine functions and is given by

$$\begin{cases} \psi_{x_{s1},q}(x, y) = \cos(k_{x_{s1}} x) \exp(k_{y_{s1},q} y), & q = 1, 2, 3, 4, \quad s_1 = 0, 1, 2, \dots, n_1, \\ \psi_{y_{s2},q}(x, y) = \cos(k_{y_{s2}} y) \exp(k_{x_{s2},q} x), & q = 1, 2, 3, 4, \quad s_2 = 0, 1, 2, \dots, n_2. \end{cases} \quad (6.6)$$

The second set uses sine functions and is expressed as

$$\begin{cases} \psi_{x_{s1},q}(x, y) = \sin(k_{x_{s1}} x) \exp(k_{y_{s1},q} y), & q = 1, 2, 3, 4, \quad s_1 = 1, 2, \dots, n'_1, \\ \psi_{y_{s2},q}(x, y) = \sin(k_{y_{s2}} y) \exp(k_{x_{s2},q} x), & q = 1, 2, 3, 4, \quad s_2 = 1, 2, \dots, n'_2. \end{cases} \quad (6.7)$$

In both sets,  $k_{x_{s1}}$  and  $k_{y_{s2}}$  are determined by the  $L_x \times L_y$  rectangle that encloses the convex plate (see Fig. 2-1):  $k_{x_{s1}} = s_1 \pi / L_x$  and  $k_{y_{s2}} = s_2 \pi / L_y$ , while  $k_{y_{s1},q}$  and  $k_{x_{s2},q}$  are defined as

$$\begin{cases} k_{y_{s1},q} = -j^q \sqrt{k_b^2 + (j^q k_{x_{s1}})^2}, & q = 1, 2, 3, 4, \\ k_{x_{s2},q} = -j^q \sqrt{k_b^2 + (j^q k_{y_{s2}})^2}, & q = 1, 2, 3, 4. \end{cases} \quad (6.8)$$

The numbers  $n_1, n_2, n'_1, n'_2$  are recommended to follow the truncation rule <sup>[101]</sup>:

$$\frac{n_1}{L_x} \approx \frac{n_2}{L_y} \approx \frac{n'_1}{L_x} \approx \frac{n'_2}{L_y} \geq \frac{Tk_b}{\pi}, \quad (6.9)$$

where the truncation factor  $T$  is a user-defined value, which is usually between 1 to 6.

However, only the first wave function set Eq. (6.6) is used in this work. The reason is twofold. On one hand, the first set guarantees the convergence of the WBM <sup>[27]</sup>, while the second set is supplementary, which proved to be beneficial for non-convex plate problems but showed little improvement on the convex problem <sup>[141]</sup>. Since the considered plate is assumed to be convex, it is not advisable to include the additional second set. On the other hand, for rectangular plates and when the enclosing rectangular overlaps with the plate, using the second set will be problematic. Because the wave functions in the second set have the factors  $\sin(s_1\pi x/L_x)$  or  $\sin(s_2\pi y/L_y)$ , which are always zero along the plate edge ( $x = 0, L_x$  or  $y = 0, L_y$ ), they cannot provide sufficient information for constructing the weighted residual formulation of boundary conditions (discussed in Section 6.2.2). If the wave functions from second set are added, even if a few of them, it will find in practice that the system matrix tends to be singular. Therefore, the second set is not used, especially in the condition that rectangular plates are discussed in this work. Then, the total number of wave functions is given by

$$n_s = 4(n_1 + 1) + 4(n_2 + 1). \quad (6.10)$$

However, at some frequencies, the number  $n_s$  could be slightly smaller with the wave functions that are not linearly independent to the others, in order to avoid the model singularity. Besides, for relieving the ill condition of the WB model, the wave function scaling <sup>[27]</sup> is also implemented in this work:

$$\begin{cases} \psi_{xs1,q}(x, y) \leftarrow \psi_{xs1,q}(x, y) \exp(-k_{ys1,q} L_y), & \text{if } \text{Re}[k_{ys1,q}] > 0, \\ \psi_{ys2,q}(x, y) \leftarrow \psi_{ys2,q}(x, y) \exp(-k_{xs2,q} L_x), & \text{if } \text{Re}[k_{xs2,q}] > 0. \end{cases} \quad (6.11)$$

Additionally, limiting the scope to rectangular plates also avoid the convergence issue raised by the problem of corner stress singularities. It was found that, if there are stress singularities at the corners, the WBM will reduce its accuracy and convergence rate <sup>[215]</sup>. Introducing the special-purposed corner functions to the field variable expansion Eq. (6.4) can solve the problem <sup>[141]</sup>. However, the corner functions should be incorporated only when stress singularities appear, which means that identifying the corner stress singularities in advance is necessary. The stress singularity at a corner is determined by the angle of the corner and the boundary conditions of the intersecting edges. Vanmaele <sup>[137]</sup> summarized the characteristic equations and critical angles for different combinations of the classical boundary conditions (i.e., simply supported, clamped and free). Among those critical angles, the smallest one is  $90^\circ$ , which means if the angle is not larger than  $90^\circ$ , stress singularity will not appear regardless of the boundary conditions. Although the conclusion is for

classical boundary conditions, it can be extrapolated to the elastic restraints, since the classical ones are extreme cases for the elastic restraints. Thus, when the considered plate is rectangular, the special-purposed corner functions are not needed.

## 6.2.2 Weighted residual formulation for boundary conditions

The boundary conditions are satisfied in an approximate way using the weighted residual formulation, which can be constructed using variational principle<sup>[148,151]</sup>. The conventional formulation proposed by Desmet<sup>[27]</sup> can be applied for prescribed boundary conditions and was used widely for later researches<sup>[27,141,147,215,216]</sup>. Recently, Liu<sup>[148]</sup> modified the formulation for the general elastic restraints and proved its effectiveness. In this paper, an integrated formulation is proposed: when the restraints along edges belong to the first four types in Table 2-1 (i.e.,  $\mathbf{r} \in (\Gamma_{\bar{w}\bar{\theta}} \cup \Gamma_{\bar{m}\bar{Q}} \cup \Gamma_{\bar{w}\bar{m}} \cup \Gamma_{\bar{\theta}\bar{Q}})$  with the prescribed conditions), it turns out to be equivalent to the conventional formulation; when the edges are elastically restrained ( $\mathbf{r} \in \Gamma_{m^*Q^*}$ ), it can be reduced to the formulation proposed in<sup>[148]</sup>. Meanwhile, it is available for the partially elastic restraints ( $\mathbf{r} \in (\Gamma_{\bar{w}m^*} \cup \Gamma_{\bar{\theta}m^*} \cup \Gamma_{\bar{m}Q^*} \cup \Gamma_{\bar{\theta}Q^*})$ ), which are not considered in the two available formulations. The proposed weighted residual formulation of boundary conditions is given by

$$\begin{aligned} & \beta_w \int L_Q[\tilde{w}]R_w d\Gamma + \beta_\theta \int L_m[\tilde{w}]R_\theta d\Gamma - \beta_m \int L_\theta[\tilde{w}]R_m d\Gamma - \beta_Q \int \tilde{w}R_Q d\Gamma \\ & + \beta_c \left\{ \sum_{c=1}^{n_w} L_F[\tilde{w}(\mathbf{r}_c)]R_{cw}(\mathbf{r}_c) - \sum_{c=1}^{n_F} \tilde{w}(\mathbf{r}_c)R_{cF}(\mathbf{r}_c) \right\} = 0 \end{aligned} \quad (6.12)$$

where,  $R_w$ ,  $R_\theta$ ,  $R_m$ ,  $R_Q$ ,  $R_{cw}$  and  $R_{cF}$  are the residuals of the boundary conditions Eqs. (2.9)-(2.14), and their corresponding expressions are listed in Table 6-1.  $L_Q[\tilde{w}]$ ,  $L_m[\tilde{w}]$ ,  $L_\theta[\tilde{w}]$ ,  $\tilde{w}$  and  $L_F[\tilde{w}]$  are weighting functions, and  $\tilde{w}$  can have any functional form.  $\beta_w$ ,  $\beta_\theta$ ,  $\beta_m$ ,  $\beta_Q$  and  $\beta_c$  are new proposed activation coefficients, where  $\beta_w$ ,  $\beta_\theta$ ,  $\beta_m$  and  $\beta_Q$  are for the weighted residuals of the transverse displacement  $R_w$ , the rotational displacement  $R_\theta$ , the bending moment  $R_m$ , and the generalized shear force  $R_Q$ , respectively, and  $\beta_c$  is the activation coefficient for the corner residuals  $R_{cw}$  and  $R_{cF}$ . Each of the activation coefficients is equal to 1 or 0, determining whether the corresponding term exists or not. How to pre-set the values of the activation coefficients are determined by the type of edge restraints. For the restraint types mentioned in Table 2-1, the recommended values are listed in Table 6-2.

Unlike the other weighted residual formulations in WBM<sup>[27,148]</sup>, Eq. (6.12) introduces the activation coefficients  $\beta_w$ ,  $\beta_\theta$ ,  $\beta_m$ ,  $\beta_Q$  and  $\beta_c$ . For the plate with only the ideal restraint types ( $\mathbf{r} \in \Gamma_{\bar{w}\bar{\theta}} \cup \Gamma_{\bar{m}\bar{Q}} \cup \Gamma_{\bar{w}\bar{m}} \cup \Gamma_{\bar{\theta}\bar{Q}}$ ), the introduction is not necessary since a corresponding weighted residual term can only be used when it is available. Therefore, in the conventional WBM<sup>[27]</sup>,  $\beta_w = \beta_\theta = \beta_m = \beta_Q = \beta_c = 1$ , which is equivalent to the proposals of  $\beta_w$ ,  $\beta_\theta$ ,  $\beta_m$ ,  $\beta_Q$

and  $\beta_c$  in Table 6-2 for the first four types. Regarding the WBM for the general elastically restrained case proposed in <sup>[148]</sup>, its weighted residual formulation is proposed as

$$\int_{\Gamma} L_{\theta}[\tilde{w}]R_{m\theta}d\Gamma + \int_{\Gamma} \tilde{w}R_{Qw}d\Gamma = 0, \quad (6.13)$$

where,  $R_{m\theta}$  and  $R_{Qw}$  respectively have the same expressions as  $R_{m^*}(\mathbf{r})$  and  $R_{w^*}(\mathbf{r})$  in Table 6-1. By comparison, it corresponds to Eq. (6.12) with  $\beta_m = \beta_Q = 1$ ,  $\beta_w = \beta_{\theta} = \beta_c = 0$ . It considers the boundary conditions of elastic restraints Eqs. (2.13)-(2.14) as the mechanical type and doesn't include the corner residuals. The counterpart in Table 6-2 is the ninth restraint type, where the corner residuals are considered.

Table 6-1. Residuals for the boundary conditions (BCs) of a plate edge  $\mathbf{r} \in \Gamma$ .

Prescribed BCs		Elastically restrained BCs
$R_w$	$R_{\bar{w}}(\mathbf{r}) = \hat{w}(\mathbf{r}) - \bar{w}(\mathbf{r})$	$R_{w^*}(\mathbf{r}) = \hat{w}(\mathbf{r}) + \frac{L_Q[\hat{w}(\mathbf{r})]}{k_w + j\omega c_w}$
$R_{\theta}$	$R_{\bar{\theta}}(\mathbf{r}) = L_{\theta}[\hat{w}(\mathbf{r})] - \bar{\theta}(\mathbf{r})$	$R_{\theta^*}(\mathbf{r}) = L_{\theta}[\hat{w}(\mathbf{r})] + \frac{L_m[\hat{w}(\mathbf{r})]}{k_{\theta} + j\omega c_{\theta}}$
$R_m$	$R_{\bar{m}}(\mathbf{r}) = L_m[\hat{w}(\mathbf{r})] - \bar{m}(\mathbf{r})$	$R_{m^*}(\mathbf{r}) = L_m[\hat{w}(\mathbf{r})] + (k_{\theta} + j\omega c_{\theta})L_{\theta}[\hat{w}(\mathbf{r})]$
$R_Q$	$R_{\bar{Q}}(\mathbf{r}) = L_Q[\hat{w}(\mathbf{r})] - \bar{Q}(\mathbf{r})$	$R_{Q^*}(\mathbf{r}) = L_Q[\hat{w}(\mathbf{r})] + (k_w + j\omega c_w)\hat{w}(\mathbf{r})$
$R_{c_w}$	$R_{c_w}(\mathbf{r}_c) = \hat{w}(\mathbf{r}_c) - \bar{w}(\mathbf{r}_c)$	when $k_w = \infty$ , $R_{c_w^*}(\mathbf{r}_c) = \hat{w}(\mathbf{r}_c) - 0$
$R_{c_F}$	$R_{c_F}(\mathbf{r}_c) = L_{F_c}[\hat{w}(\mathbf{r}_c)] - (\bar{m}_{ns}(\mathbf{r}_c^+) - \bar{m}_{ns}(\mathbf{r}_c^-))$	when $k_w \neq \infty$ , $R_{c_F^*}(\mathbf{r}_c) = L_{F_c}[\hat{w}(\mathbf{r}_c)] - 0^a$

<sup>a</sup> Without a rigorous proof, it is considered that, for the corner intersecting by elastically restrained edges, the corner force vanishes, balanced by the springs.

Table 6-2. Restraints that can be considered by the proposed formulation Eq. (6.12), with their corresponding activation coefficients and case figure indicators.

No.	Restraint type	Prescribed values	$\beta_w$	$\beta_{\theta}$	$\beta_m$	$\beta_Q$	$\beta_c$
1	$\mathbf{r} \in \Gamma_{\bar{w}\bar{\theta}}$ (clamped)	$\bar{w} = \bar{\theta} = 0$ , $k_w = k_{\theta} = \infty$	1	1	0	0	1 ( $R_{c_w^*}$ )
2	$\mathbf{r} \in \Gamma_{\bar{m}\bar{Q}}$ (free)	$\bar{m} = \bar{Q} = 0$ , $k_w = k_{\theta} = c_w = c_{\theta} = 0$	0	0	1	1	1 ( $R_{c_F^*}$ )
3	$\mathbf{r} \in \Gamma_{\bar{w}\bar{m}}$ (pinned)	$\bar{w} = \bar{m} = 0$ , $k_w = \infty$ , $k_{\theta} = c_{\theta} = 0$	1	0	1	0	1 ( $R_{c_w^*}$ )
4	$\mathbf{r} \in \Gamma_{\bar{\theta}\bar{Q}}$ (symmetric)	$\bar{\theta} = \bar{Q} = 0$ , $k_{\theta} = \infty$ , $k_w = c_w = 0$	0	1	0	1	1 ( $R_{c_F^*}$ )
5	$\mathbf{r} \in \Gamma_{\bar{w}m^*}$	$\bar{w} = 0$ , $k_w$ or $c_w = \infty$ , $0 < k_{\theta} < \infty$	1	0	1	0	1 ( $R_{c_w^*}$ )
6	$\mathbf{r} \in \Gamma_{\bar{Q}m^*}$	$\bar{Q} = 0$ , $k_w = c_w = 0$ , $0 < k_{\theta} < \infty$	0	0	1	1	1 ( $R_{c_F^*}$ )
7	$\mathbf{r} \in \Gamma_{\bar{\theta}Q^*}$	$\bar{\theta} = 0$ , $k_{\theta}$ or $c_{\theta} = \infty$ , $0 < k_w < \infty$	0	1	0	1	1 ( $R_{c_F^*}$ )
8	$\mathbf{r} \in \Gamma_{\bar{m}Q^*}$	$\bar{m} = 0$ , $k_{\theta} = c_{\theta} = 0$ , $0 < k_w < \infty$	0	0	1	1	1 ( $R_{c_F^*}$ )
9	$\mathbf{r} \in \Gamma_{m^*Q^*}$	$0 < k_w < \infty$ , $0 < k_{\theta} < \infty$	0	0	1	1	1 ( $R_{c_F^*}$ )

However, Eqs. (2.13)-(2.14) can also be expressed in their kinematic forms. Since  $k_\theta$  and  $k_w$  are not equal to zero, Eqs. (2.13)-(2.14) are equivalent to ( $\mathbf{r} \in \Gamma$ )

$$L_\theta[w(\mathbf{r})] = -\frac{L_m[w(\mathbf{r})]}{k_\theta + j\omega c_\theta}, \quad (6.14)$$

$$w(\mathbf{r}) = -\frac{L_Q[w(\mathbf{r})]}{k_w + j\omega c_w}. \quad (6.15)$$

Therefore, the corresponding residuals can be  $R_{m^*}(\mathbf{r})$ ,  $R_{Q^*}(\mathbf{r})$  or  $R_{\theta^*}(\mathbf{r})$ ,  $R_{w^*}(\mathbf{r})$ , as expressed in Table 6-1. With this possibility, the formulations for partially elastic restraint types ( $\mathbf{r} \in \Gamma_{\bar{w}m^*}$ ,  $\mathbf{r} \in \Gamma_{\bar{Q}m^*}$ ,  $\mathbf{r} \in \Gamma_{\bar{\theta}Q^*}$  and  $\mathbf{r} \in \Gamma_{\bar{m}Q^*}$ ) are obtained intuitively, i.e., Eq. (6.12) with the activation coefficients in Table 6-2 for the fifth to eighth restraint types.

Besides, Table 6-1 reveals the relationships between the prescribed and elastically restrained boundary conditions. The prescribed  $\bar{w} = 0$  corresponds to  $k_w = \infty$ . Using either  $R_{\bar{w}}(\mathbf{r})$  or  $R_{w^*}(\mathbf{r})$  yields the same formulation, and  $R_{\bar{m}}(\mathbf{r})$  or  $R_{m^*}(\mathbf{r})$  should not be used. Corresponding relationship is similar for  $\bar{\theta} = 0$  versus  $k_\theta = \infty$ ,  $\bar{m} = 0$  versus  $k_\theta = c_\theta = 0$ , and  $\bar{Q} = 0$  versus  $k_w = c_w = 0$ . Hence, the residuals for elastically restrained boundary conditions actually include the residuals of the prescribed boundary conditions as long as the prescribed values are zero. Then, for a plate with any type of restraint listed in the examples of Table 2-1, it is possible to simply apply  $R_{w^*}(\mathbf{r})$ ,  $R_{\theta^*}(\mathbf{r})$ ,  $R_{Q^*}(\mathbf{r})$ ,  $R_{m^*}(\mathbf{r})$ ,  $R_{c_w^*}(\mathbf{r}_c)$ , and  $R_{c_F^*}(\mathbf{r}_c)$  for the residuals in Eq. (6.12).  $\beta_w$ ,  $\beta_\theta$ ,  $\beta_m$ ,  $\beta_Q$  and  $\beta_c$  are used to control and indicate which terms are used for the formulation.

Table 6-2 lists the recommended settings for the restraint types mentioned in Table 2-1. It suggests including corner residuals whenever it is possible.  $\beta_w$  and  $\beta_Q$  are not equal to 1 or 0 at the same time.  $\beta_w = 1$  only when  $k_w = \infty$ , otherwise  $\beta_Q = 1$ . In the case of  $0 < k_w < \infty$ , although  $R_{w^*}(\mathbf{r}) = 0$  is equivalent to  $R_{Q^*}(\mathbf{r}) = 0$ , the latter is used, i.e.,  $\beta_Q = 1$ . The reason is twofold. Firstly, in the formulation Eq. (6.12), the term activated by  $\beta_Q$  is more stable than the term activated by  $\beta_w$  provided that  $k_w$  is not extremely large. The difference in stability is related to the different weighting functions  $\tilde{w}$  and  $L_Q[\tilde{w}]$ . Secondly, the edge residual and the corner residual should be in conformity. In other words, it is necessary to use  $R_{Q^*}(\mathbf{r})$  instead of  $R_{w^*}(\mathbf{r})$  if  $R_{c_F^*}(\mathbf{r}_c)$  is effective. The values of  $\beta_\theta$  and  $\beta_m$  are determined in a similar way. However, since the corner residuals are not related to the edge rotation, when  $0 < k_\theta < \infty$ , the values of  $\beta_\theta$  and  $\beta_m$  can exchange on most occasions, while  $\beta_m = 1$  is slightly better than  $\beta_\theta = 1$ . With regard to the corner residuals, under the column of  $\beta_c$  indicates the corner residual that is available if the two edges are under the corresponding restraint type. However, it is possible that a corner is formed by two different edges that correspond to different corner residuals. When this happens,  $R_{c_w^*}$  is used, because the displacement of the corner is known by one of the two edges, which should have prescribed displacement.

Following the above discussions, especially Table 6-1 and Table 6-2, the activation coefficients  $\beta_w, \beta_\theta, \beta_m, \beta_Q, \beta_c$  and the residuals  $R_w, R_\theta, R_m, R_Q, R_{cw}, R_{cF}$  are determined. Then, the WB model is built according to the weighted residual formulation Eq. (6.12). Concerning the weighting functions  $L_Q[\tilde{w}], L_m[\tilde{w}], L_\theta[\tilde{w}], \tilde{w}$  and  $L_F[\tilde{w}]$ , an approach similar to the Galerkin method can be used. The weighting function  $\tilde{w}$  is expanded as  $\tilde{w} = \sum_{s=1}^{n_s} \tilde{w}_s \psi_s$ , where  $\tilde{w}_s$  are arbitrary. Then, after substituting the expansions of  $\hat{w}$  and  $\tilde{w}$  into Eq. (6.12), and considering the arbitrariness of  $\tilde{w}_s$ , the WB model is obtained. It is a square system of equations that can be expressed as

$$\mathbf{A}_{ss} \mathbf{w}_s = \mathbf{f}_s, \quad (6.16)$$

where,  $\mathbf{A}_{ss}$  is the  $n_s$  by  $n_s$  system matrix,  $\mathbf{w}_s$  is the vector of the  $n_s$  unknown contribution factors  $w_s$ , and  $\mathbf{f}_s$  is the vector related to the external force.

### 6.2.3 Model solution and postprocessing

Model solution is to solve the Eq. (6.16) and obtain the  $n_s$  unknown contribution factors  $w_s$ . The contribution factors need to be substituted back to Eq. (6.4) to obtain the approximated field variable, i.e., the transverse displacement  $\hat{w}(x, y)$ . This is the unavoidable postprocessing for WBM. For other field variables (e.g., the rotational displacement, the bending moment, etc.), they can all be easily derived, since the differential operators are applying to the wave functions. Similar to the element based methods, it is also necessary for WBM to check the convergence of the results by increasing degrees of freedom of the model. The strategy normally used for WBM is to increase the truncation factor  $T$  in Eq. (6.9). Then, according to the truncation rule, the number of wave functions (i.e., the degrees of freedom of the WB model) is increased.

### 6.2.4 Harmonic analysis on the mounted test panel

The new weighted residual formulation Eq. (6.12) enables the WBM to analyse a thin plate with any of the restraint types that are listed in Table 6-2. This has been validated with a series of numerical cases in our paper <sup>[217]</sup> that proposes the formulation, covering all the restraint types under uniform or non-uniform situations. The paper also discusses the method's accuracy, efficiency and convergence rate. The results show that the WBM is more efficient than FEM. In other words, with limited computation memory and time, the WBM enables the analysis to a higher frequency.

In this subsection, the proposed WBM is used to analyse the frequency response of the mounted test panel. As introduced and characterized in Section 5.2, this is a rectangular aluminium panel with



- dimensions:  $a \times b \times h = 0.825 \text{ m} \times 1.018 \text{ m} \times 3.93 \text{ mm}$ ;
- material properties:  $\rho = 2680 \text{ kg/m}^3$ ,  $E = 76 \text{ GPa}$ ,  $\nu = 0.33$  and  $\eta = 0.003$ ;
- edge conditions: rigidly supported ( $\bar{w} = 0$ ,  $k_w = \infty$ ) and elastically restrained against rotation ( $k_{\theta_x} = 5 \text{ kN/rad}$ ,  $k_{\theta_y} = 9 \text{ kN/rad}$ , as shown in Fig. 5-24), corresponding to the restraint type  $\mathbf{r} \in \Gamma_{\bar{w}m^*}$ .

In order to obtain the results that are directly comparable to the available results in Section 5.2.3, where a harmonic analysis on the update panel was performed via FEM, an identical simulation is conducted here with the harmonic force acting at Point 80. Note that the notations of the points and the coordinate system of the panel are unchanged and in consistence with those in Fig. 5-12. Therefore, the WBM is used to analyse the response of the above defined panel under a harmonic force excitation acting at the point  $\mathbf{r}_F$  (0.385m,0.533m). The analysing frequency range is from 10 Hz to 700 Hz at intervals of 1Hz.

Then, to do the targeted analysis, the WBM introduced from Section 6.2.1 to Section 6.2.3 are coded in MATLAB <sup>[213]</sup>. In default, the truncation factor that controls the number of wave function is set as  $T = 2$ . After the solution, the wave function contribution factors will be saved to the database. Then, in the later postprocessing, the users can derive the field variables they want with the contribution factors and the wave functions. Two postprocessing scripts are provided: one for the FRF  $A_{180}$  (output acceleration at A1, i.e.,  $\mathbf{r}_1$  (0.31m,0.8055m)) and the other for the field displacement at 415 Hz. With a few modifications, other outputs can be processed.

Fig. 6-1 shows the FRF in terms of the accelerance  $A_{180}$  predicted by the proposed WBM, compared with its counterpart obtained by FEM. The two curves agree well, indicating that the two approaches are alternative for the analysis. However, the computational efforts are different. The WBM is much more efficient <sup>[217]</sup>. In this case, when the two analyses are operating in the same computer, the FEA in COMSOL occupies 842 sec for the 691 frequencies, while the WB analysis costs only 23.4 sec. This is a rough comparison to demonstrate the efficiency of the WBM. For a more rigorous validation, the readers can refer to the paper <sup>[217]</sup>. In addition, Fig. 6-2 plots and compares the displacement fields (in their real parts) at 415 Hz, further verifying the agreement between the two methods. In a nutshell, the developed WBM and codes are validated. They can be used to analyse the forced vibration of the test panel, and the predicting results match the results from FEM.

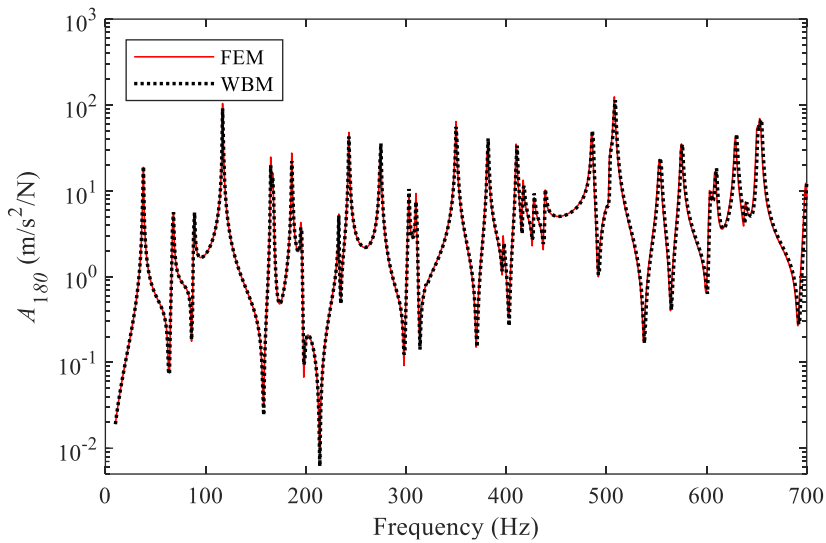


Fig. 6-1. FEM and WBM predictions on the FRF  $A_{180}$  of the mounted panel, whose input harmonic force and output acceleration are respectively located at Point 80 and Point A1 of Fig. 5-12.

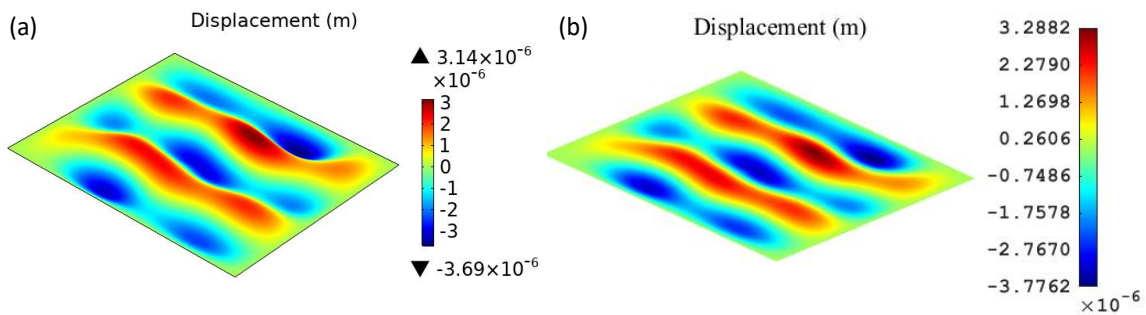


Fig. 6-2. Real parts of the displacement fields of the mounted panel at 415 Hz predicted by: (a) FEM; (b) WBM.

In view of the computational efficiency of WBM, the harmonic analysis is extended to 1500 Hz. Then, the FRFs are compared between the experiment and the WBM simulation in the frequency range 700-1500 Hz, as illustrated in Fig. 6-3. Due to the good matching between FEM and WBM simulations, comparison lower than 700 Hz should be identical to Fig. 5-25. Combining Fig. 5-25 and Fig. 6-3, we can find that the discrepancy between the measured and simulated curves becomes more apparent as the frequency increase. This outcome demonstrates the limitation of the updated model. If the model is extended to higher frequency range, the accuracy will decrease. However, the modal density and modal overlap also increase with the frequency. Hence, if the average response over space and frequency is considered, the predicting error will be more acceptable.

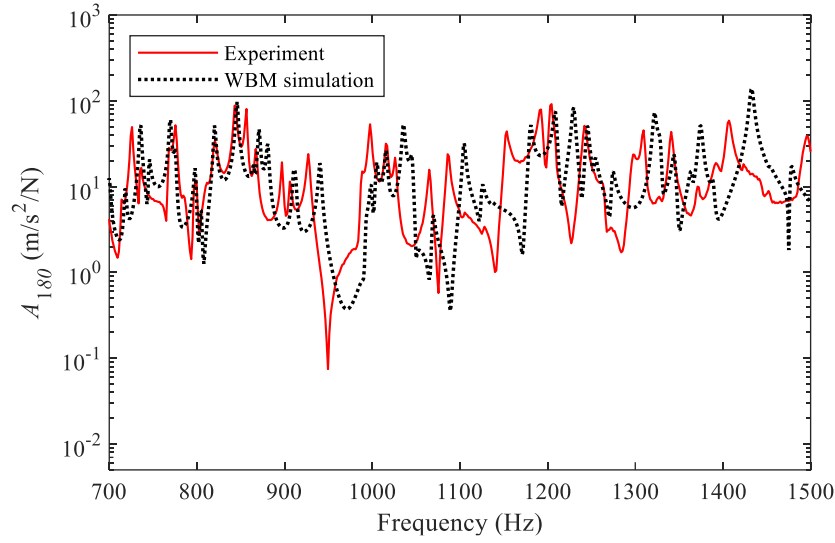


Fig. 6-3. Measured and WBM simulated FRFs  $A_{180}$  of the mounted panel, whose input harmonic force and output acceleration are respectively located at Point 80 and Point A1 of Fig. 5-12.

### 6.2.5 Validation for one-dimensional plates

For the 1D thin plate governed by Eq. (2.17), the transverse displacement  $w(x)$  can be expressed as

$$w(x) = \sum_{s=1}^4 w_s \psi_s(x) + \hat{w}_F(x), \quad (6.17)$$

where, the wave functions  $\psi_s(x)$  are given by

$$\psi_s(x) = e^{-j^s k_b x}, \quad s = 1, 2, 3, 4, \quad (6.18)$$

and the particular solution function  $\hat{w}_F(x)$  uses the expression for an infinite plate under the same line force excitation  $F$  [58]:

$$\hat{w}_F(x) = \frac{-jF}{4Dk_b^3} (e^{-jk_b|x-x_F|} - je^{-k_b|x-x_F|}). \quad (6.19)$$

In applying the WBM, the proposed weighted residual formulation Eq. (6.12) is continuously used, but the operators are instead defined by Eqs. (2.18)-(2.20) and the corner residuals never exist ( $\beta_c = 0$ ). Then, similarly, after introducing the weighted function  $\tilde{w} = \sum_{s=1}^4 \tilde{w}_s \psi_s$ , the 4 by 4 square system equation like Eq. (6.16) can be derived. Finally, the displacement  $w(x)$  is obtained after solution and postprocessing.

For validating the method, a 1D thin plate under harmonic line force excitation is now considered. The plate is the same as the one analysed in Section 4.2.6 for FE model validation. As shown by Fig. 2-2, the plate is in the  $x$ - $z$  plane with infinite length in  $y$  direction. The basic parameters are given by  $l = 1.018$  m,  $h = 4$  mm,  $\rho = 2680$  kg/m<sup>3</sup>,  $E =$

69 GPa,  $\nu = 0.33$ ,  $c_{w1} = c_{w2} = c_{\theta1} = c_{\theta2} = 0$ ,  $k_{w1} = k_{w2} = 10^6$  N/m,  $k_{\theta1} = k_{\theta2} = 10^4$  N/rad. The simulation case considers a line force  $F$  acting at  $x_F = 0.533$  m from 10 Hz to 700 Hz at intervals of 1 Hz. Then, the displacement at  $x_1 = 0.8055$  m is measured. The predicted FRF  $w_1/F$  is later compared with the results obtained from the validated FE model. As shown in Fig. 6-4, the two FRFs reach a good agreement. The WB model is proved. Interrelating the natural frequencies and mode shapes listed in Table 4-7, the FRFs show resonance peaks next to the natural frequencies, and the displacement fields are consistent with the mode shapes. The corresponding code for this case is also provided in [213].

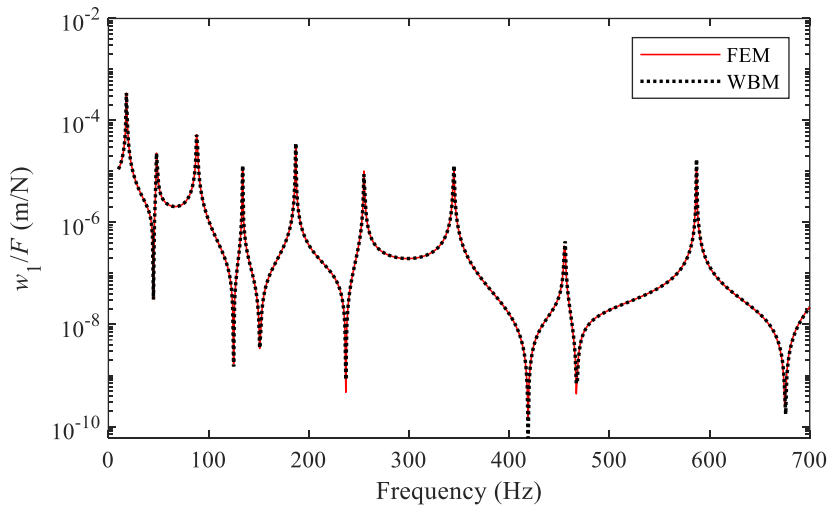


Fig. 6-4. FEM (in ANSYS, modelled by BEAM3 elements) and WBM predictions on the FRF  $w_1/F$  of the 1D thin plate with  $k_{w1} = k_{w2} = 10^6$  N/m,  $k_{\theta1} = k_{\theta2} = 10^4$  N/rad.

### 6.3 WBM for acoustic cavity

In this section, the traditional WBM [27] for uncoupled acoustic cavity is introduced and used to analyse the uncoupled Noise-Box cavity. It will concentrate on the 3D acoustic problem, with a simple validation for the 2D case. The WBM is implemented in MATLAB, and the self-developed codes are shared in [213].

#### 6.3.1 Field variable expansion

Considering the interior acoustic problem for a general convex cavity, which is defined in Section 2.3.1, the solution to the governing equation Eq. (2.22) can be expressed as

$$p(\mathbf{r}) \approx \hat{p}(\mathbf{r}) = \sum_{a=1}^{n_a} p_a \phi_a(\mathbf{r}) + \hat{p}_q(\mathbf{r}). \quad (6.20)$$

In this field pressure expansion Eq. (6.20),  $\phi_a$  and  $p_a$  are respectively the wave functions and their corresponding contribution factors.  $\hat{p}_q$  is a particular solution of the governing equation due to the inhomogeneous part.  $n_a$  is the total number of wave functions.

For 3D problems, where  $\mathbf{r}$  corresponds to  $(x,y,z)$  and  $q$  is a monopole source at  $\mathbf{r}_q$ , the particular solution  $\hat{p}_q$  can use the following expression:

$$\hat{p}_q(\mathbf{r}) = \frac{j\omega\rho_0q}{4\pi} \frac{e^{jk|\mathbf{r}-\mathbf{r}_q|}}{|\mathbf{r}-\mathbf{r}_q|}. \quad (6.21)$$

The acoustic wave functions  $\phi_a$ , as proposed in [27] are given by

$$\begin{cases} \phi_{xa1,ya2,\alpha}(x,y,z) = \cos(k_{xa1}x)\cos(k_{ya2}y)\exp(k_{za1a2,\alpha}z), \\ \phi_{xa3,za4,\alpha}(x,y,z) = \cos(k_{xa3}x)\cos(k_{za4}z)\exp(k_{ya3a4,\alpha}y), \\ \phi_{ya5,za6,\alpha}(x,y,z) = \cos(k_{ya5}y)\cos(k_{za6}z)\exp(k_{xa5a6,\alpha}x), \end{cases} \quad (6.22)$$

with

$$\begin{cases} k_{za1a2,\alpha} = (-1)^\alpha j\sqrt{k^2 - k_{xa1}^2 - k_{ya2}^2}, \quad \alpha = 1,2, \\ k_{ya3a4,\alpha} = (-1)^\alpha j\sqrt{k^2 - k_{xa3}^2 - k_{za4}^2}, \quad \alpha = 1,2, \\ k_{xa5a6,\alpha} = (-1)^\alpha j\sqrt{k^2 - k_{ya5}^2 - k_{za6}^2}, \quad \alpha = 1,2, \end{cases} \quad (6.23)$$

where,  $k_{xa1}$ ,  $k_{ya2}$ ,  $k_{xa3}$ ,  $k_{za4}$ ,  $k_{ya5}$ ,  $k_{za6}$  are determined by the  $L_x \times L_y \times L_z$  cuboid that encloses the convex cavity:  $k_{\beta ai} = a_i \pi / L_\beta$  ( $\beta = x, y$  or  $z$ ;  $i = 1, 2, 3, 4, 5$  or  $6$ ;  $a_i = 0, 1, 2, \dots, n_{ai}$ ); the numbers  $n_{ai}$  are recommended to follow the truncation rule [101]:

$$\frac{n_{a1}}{L_x} \approx \frac{n_{a2}}{L_y} \approx \frac{n_{a3}}{L_x} \approx \frac{n_{a4}}{L_z} \approx \frac{n_{a5}}{L_y} \approx \frac{n_{a6}}{L_z} \geq \frac{Tk}{\pi}. \quad (6.24)$$

In Eq. (6.24),  $T$  is the truncation factor that controls the least number of wave functions. It is usually set within 1 to 6 and set as 2 in this work. Then, the total number of wave functions is settled by  $n_a = 2[(n_{a1} + 1)(n_{a2} + 1) + (n_{a3} + 1)(n_{a4} + 1) + (n_{a5} + 1)(n_{a6} + 1)]$ . However, at some special frequencies, it is necessary to remove some wave functions to keep them linearly independent and avoid model singularity, leading to a total number  $n_a$  smaller than the above calculation result. Meanwhile, the wave function scaling is applied to the wave functions that comply with the given conditions, as follows

$$\begin{cases} \phi_{xa1,ya2,\alpha}(x,y,z) \leftarrow \phi_{xa1,ya2,\alpha}(x,y,z)\exp(-k_{za1a2,\alpha}L_z), \text{ if } \operatorname{Re}[k_{za1a2,\alpha}] > 0, \\ \phi_{xa3,za4,\alpha}(x,y,z) \leftarrow \phi_{xa3,za4,\alpha}(x,y,z)\exp(-k_{ya3a4,\alpha}L_y), \text{ if } \operatorname{Re}[k_{ya3a4,\alpha}] > 0, \\ \phi_{ya5,za6,\alpha}(x,y,z) \leftarrow \phi_{ya5,za6,\alpha}(x,y,z)\exp(-k_{xa5a6,\alpha}L_x), \text{ if } \operatorname{Re}[k_{xa5a6,\alpha}] > 0. \end{cases} \quad (6.25)$$

### 6.3.2 Weighted residual formulation for boundary conditions

The weighted residual formulation of this interior acoustic problem is given by [27]

$$\int_{\Omega_p} \frac{-j}{\rho_0\omega} \frac{\partial \tilde{p}}{\partial n} R_p d\Omega + \int_{\Omega_v} \tilde{p} R_v d\Omega + \int_{\Omega_z} \tilde{p} R_z d\Omega = 0, \quad (6.26)$$

where,  $R_p$ ,  $R_v$  and  $R_z$  are the residuals of the boundary conditions Eqs. (2.26)-(2.28). The weighting function  $\tilde{p}$  is expanded as  $\tilde{p} = \sum_{a=1}^{n_a} \tilde{p}_a \phi_a$ , where  $\tilde{p}_a$  are arbitrary. Then, after substituting the expansions of  $\hat{p}$  and  $\tilde{p}$  into Eq. (6.26), and considering the arbitrariness of  $\tilde{p}_a$ , the WB model is obtained. It is a square system of equations that can be expressed as

$$\mathbf{A}_{aa} \mathbf{p}_a = \mathbf{f}_a, \quad (6.27)$$

where,  $\mathbf{A}_{aa}$  is the  $n_a$  by  $n_a$  system matrix,  $\mathbf{p}_a$  is the vector of the  $n_a$  unknown contribution factors  $p_a$ , and  $\mathbf{f}_a$  is the vector related to the external monopole source.

Finally, solution of Eq. (6.27) yields the contribution factors  $p_a$ . By substituting  $p_a$  to the expansion Eq. (6.20), the acoustic pressure field is obtained.

### 6.3.3 Harmonic analysis on the Noise-Box cavity

The above described formulae and approach are implemented in MATLAB<sup>[213]</sup> and used to analyse the Noise-Box cavity. In this case, the simplified cavity geometry illustrated by Fig. 3-11 is used, whose cross section in  $x$ - $z$  plane is a pentagon. Inside the cavity, the monopole source and microphones are positioned at the same coordinates of the FEA simulation and the EMA experiment, as shown in Fig. 4-11. For a better demonstration of the WBM, the simplified cavity geometry, the source position  $\mathbf{r}_q$  and the microphone position  $\mathbf{r}_1$  are replicated in Fig. 6-5, enclosed by the rectangular box  $L_x \times L_y \times L_z$ .

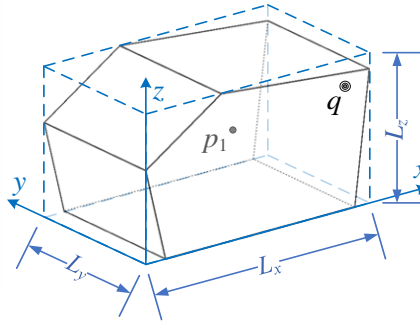


Fig. 6-5. Noise-Box cavity for WB analysis.

The simulation considers a harmonic monopole source at  $\mathbf{r}_q$  (1.15m, 0.065m, 0.595m) with the input amplitude  $q = 1 \text{ m}^3/\text{s}$  and the frequency changing from 100 to 700 Hz at intervals of 1 Hz step by step. Under the experimental temperature  $24.16^\circ\text{C}$ , the air properties are given by  $\rho_0 = 1.1875 \text{ kg/m}^3$  and  $c = 345.63 \text{ m/s}$ . According to the measured sound absorption  $\bar{\alpha}$ , as given in Table 5-2 and Fig. 5-4, a constant value  $\bar{\alpha} = 0.01$  is applied to the wall impedance, for the measured results are not much different among different frequency

ranges below 700 Hz. Then, based on Eq. (5.5), the wall impedance  $\bar{Z} = 163350 \text{ kg/m}^2/\text{s}$  is obtained and used for the boundary conditions of the cavity. For validating the WB model, the comparative simulation is also conducted in COMSOL, following the modelling approach introduced in Section 4.3.

After the solution and postprocessing, acoustic pressure fields are available for every simulated frequency. A comparison between the WBM and FEM results at 415 Hz is shown in Fig. 6-6, represented by their imaginary parts. The agreement between the two contour plots validates the effectiveness of the WBM and the correctness of the MATLAB codes. Besides, after the calculation of the sound pressure at  $r_1$  (0.424m, 0.151m, 0.321m) for all the analysed frequencies, the FRFs in terms of  $p_1/q$  is obtained. As Fig. 6-7 shows, the FRFs from WBM and FEM also match well as expected. Concerning the relative larger discrepancies around 590 Hz, they actually result from the simplification of the geometry. This can be observed from Fig. 6-6, where the cavity in FEM keeps the two slender vertical walls around the bottom surface. For validating this claim, the simplified geometry, as used in the WB model, is also analysed by FEM and compared with the WBM results in Fig. 6-8. As shown by the figure, the two curves match very well for all frequencies if the two cavities are identical. Therefore, in terms of accuracy, comparable results are obtained from the two methods. Whereas, for the efficiency and computational burden, the WBM is preferred in the frequency domain (harmonic) analysis. For example, in this considered case, the FE model has totally 79104 DOF and cost 2670 sec for the solutions of the 601 frequencies, while the WB model contains 442 wave functions for the highest frequency and utilized 178 sec in the same computer and operating conditions.

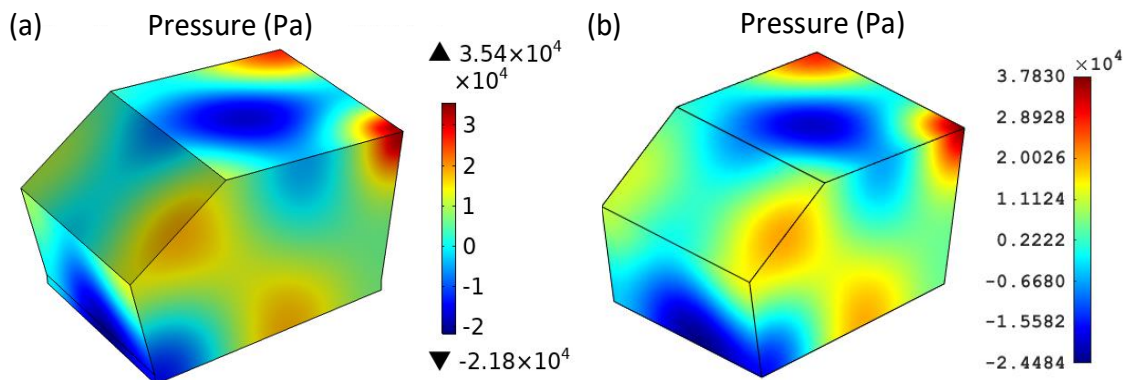


Fig. 6-6. Imaginary part of the acoustic pressure field over the surface of the Noise-Box cavity at 415 Hz predicted by: (a) FEM; (b) WBM. A monopole source is acting at  $r_q$  (1.15m, 0.065m, 0.595m) of Fig. 6-5 with amplitude  $q = 1 \text{ m}^3/\text{s}$ .

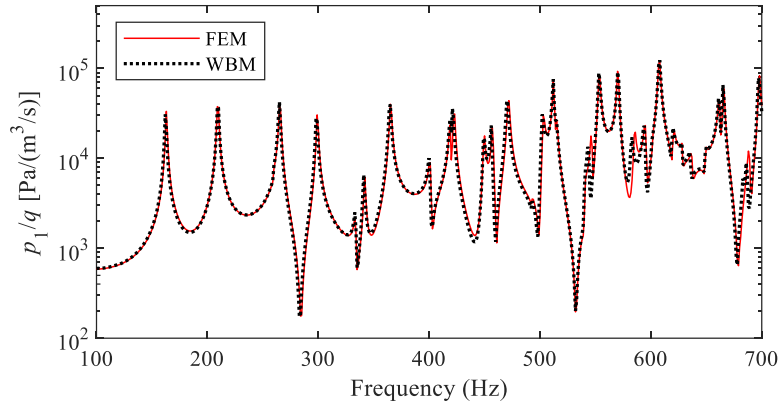


Fig. 6-7. FEM (detailed geometry) and WBM predictions on the FRF  $p_1/q$  of the Noise-Box cavity, whose input volume flow rate and output acoustic pressure are respectively located at  $\mathbf{r}_q$  (1.15m, 0.065m, 0.595m) and  $\mathbf{r}_1$  (0.424m, 0.151m, 0.321m) of Fig. 6-5.

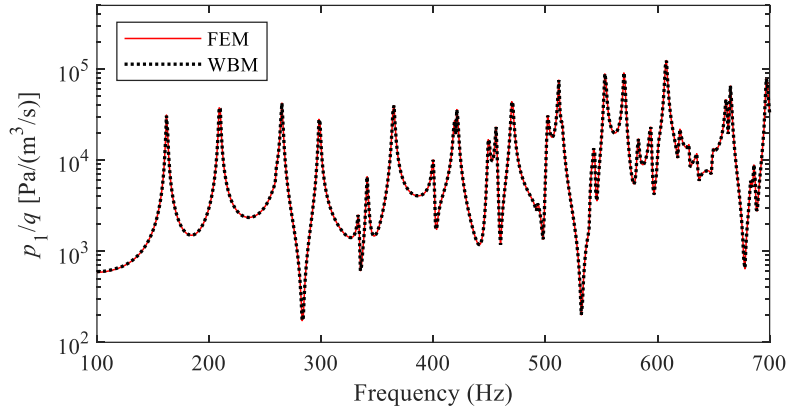


Fig. 6-8. FEM (simplified geometry) and WBM predictions on the FRF  $p_1/q$  of the Noise-Box cavity, whose input volume flow rate and output acoustic pressure are respectively located at  $\mathbf{r}_q$  (1.15m, 0.065m, 0.595m) and  $\mathbf{r}_1$  (0.424m, 0.151m, 0.321m) of Fig. 6-5.

### 6.3.4 Validation for two-dimensional cavities

For 2D cavities, where  $\mathbf{r}$  corresponds to  $(x, z)$  and  $q$  is a line source at  $\mathbf{r}_q$ , the wave functions of Eq. (6.20) are changed as

$$\begin{cases} \phi_{xa_1, \alpha}(x, z) = \cos(k_{xa_1} x) \exp(k_{za_1, \alpha} z), \\ \phi_{za_2, \alpha}(x, z) = \cos(k_{za_2} z) \exp(k_{xa_2, \alpha} x), \end{cases} \quad (6.28)$$

with

$$\begin{cases} k_{za_1, \alpha} = (-1)^\alpha j \sqrt{k^2 - k_{xa_1}^2}, \quad \alpha = 1, 2, \\ k_{xa_2, \alpha} = (-1)^\alpha j \sqrt{k^2 - k_{za_2}^2}, \quad \alpha = 1, 2, \end{cases} \quad (6.29)$$

and the particular solution can be expressed as

$$\hat{p}_q(\mathbf{r}) = \frac{\omega \rho_0 q}{4} H_0^{(2)}(k|\mathbf{r} - \mathbf{r}_q|). \quad (6.30)$$



The wavenumbers  $k_{xa1}$ ,  $k_{za2}$  are determined by the  $L_x \times L_z$  rectangular that encloses the convex cavity:  $k_{xa1} = a_1 \pi / L_x$  ( $a_1 = 0, 1, 2, \dots, n_{a1}$ ) and  $k_{za2} = a_2 \pi / L_z$  ( $a_2 = 0, 1, 2, \dots, n_{a2}$ ). Thus, the total number of wave functions is initially  $n_a = 2[(n_{a1} + 1) + (n_{a2} + 1)]$ , significantly less than the 3D situation. Then, after removing the dependent wave functions and applying the wave function scaling, the final set of wave functions are determined. Finally, as described in Section 6.3.2, the WB model is built based on the weighted residual formulation Eq. (6.26) with only the difference in eliminated the y coordinate.

Accordingly, the WBM for 2D acoustic problem as introduced above is coded and implemented in MATLAB. The scripts are provided in [213], and the validation is provided here in considering a 2D pentagonal cavity. The cavity is shown in Fig. 6-9, with all the coordinates of the critical points alongside. The numerical case considers a harmonic line source at  $\mathbf{r}_q$  (1.15m, 0.595m) with the input amplitude  $q = 1 \text{ m}^2/\text{s}$  and the frequency changing from 100 to 700 Hz at intervals of 1 Hz step by step. Under the temperature  $24.16^\circ\text{C}$ , the air properties are given by  $\rho_0 = 1.1875 \text{ kg/m}^3$  and  $c = 345.63 \text{ m/s}$ . The wall impedance is assumed the same as the 3D case, i.e.,  $\bar{Z} = 163350 \text{ kg/m}^2/\text{s}$ . For validating the WB model, the same geometry and set-up is built in COMSOL and analysed by FEM. Fig. 6-11 shows the FRFs  $p_1/q$  predicted by the two models, where a good agreement is observed, validating the MATLAB codes of WBM for 2D interior acoustic problems. Fig. 6-10 further illustrates their agreement in predicting the entire acoustic fields, using the imaginary parts at 415 Hz as an example.

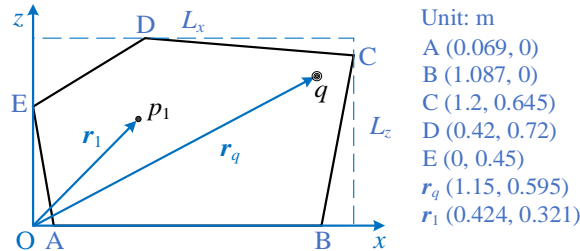


Fig. 6-9. 2D cavity for WB analysis.

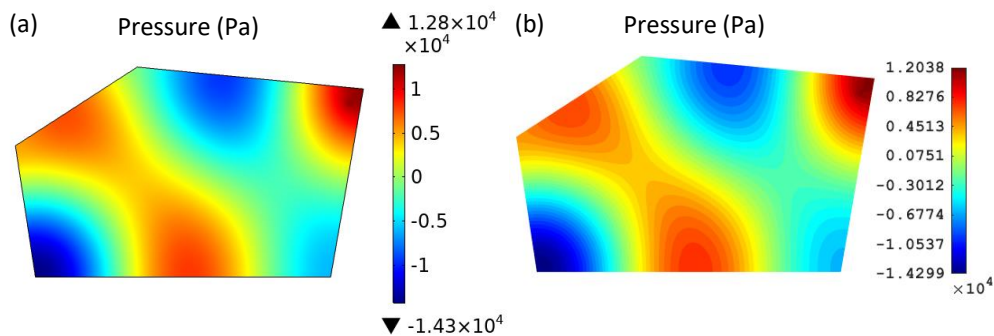


Fig. 6-10. Imaginary part of the acoustic field of 2D cavity at 415 Hz predicted by: (a) FEM; (b) WBM.

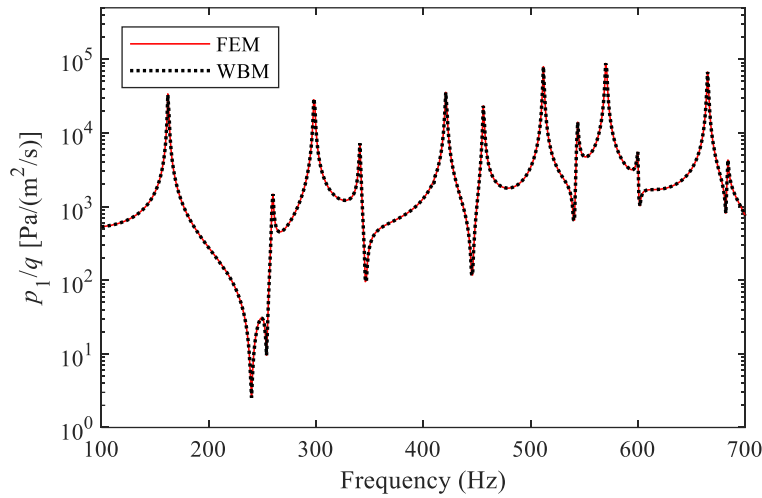


Fig. 6-11. FEM and WBM predictions on the FRF  $p_1/q$  of the 2D cavity shown in Fig. 6-9.

## 6.4 WBM for plate-cavity system

In this section, the traditional WBM is modified for the vibroacoustic analysis of a convex cavity bounded by a flexible panel with elastically restrained edges. The modification makes it possible to analyse the plate-cavity coupled Noise-Box with the updated restraint stiffnesses along panel edges. Firstly, the method is introduced by considering a general plate-cavity system, where the flexible structure is a general convex plate with any restraint types and the acoustic field is a general convex cavity with arbitrary boundary conditions. The comprehensive definition of the problem is described in Section 2.4. As it is mentioned in the definition that only one form of excitation is effective in one case, this section considers only the case when the plate is under point force excitation  $F$  (in other words,  $p_{\text{ext}} = q = 0$ ). Then, the method is applied to the Noise-Box test system for validation, compared with FEM. At last, the proposed WBM is also proved for its availability in 2D vibroacoustic problem.

### 6.4.1 Field variable expansion

Considering the vibroacoustic problem defined in Section 2.4 with only external force excitation  $F$ , the governing equation of the acoustic and the structural fields are respectively given by Eq. (2.22) with  $q = 0$  and Eq. (2.32) with  $p_{\text{ext}} = 0$ . Accordingly, the sound pressure field can be expanded as

$$p(\mathbf{r}) \approx \hat{p}(\mathbf{r}) = \sum_{a=1}^{n_a} p_a \phi_a(\mathbf{r}), \quad (6.31)$$

and the plate displacement field can be expressed by

$$w(\mathbf{r}') \approx \hat{w}(\mathbf{r}') = \sum_{s=1}^{n_s} w_s \psi_s(\mathbf{r}') - \sum_{a=1}^{n_a} p_a \hat{w}_a(\mathbf{r}') + \hat{w}_F(\mathbf{r}'). \quad (6.32)$$

The acoustic wave functions  $\phi_a$  and the structural wave functions  $\psi_s$  are respectively given by Eq. (6.22) and Eq. (6.6), as they are used in the uncoupled situations.  $w_s$  and  $p_a$  are the contribution factors of the wave functions, and thus  $(n_s + n_a)$  are the total number of wave functions. In this coupled situation, the truncation rule for the wave functions is given by

$$\frac{n_1}{L_{x'}} \approx \frac{n_2}{L_{y'}} \approx \frac{n_{a1}}{L_x} \approx \frac{n_{a2}}{L_y} \approx \frac{n_{a3}}{L_x} \approx \frac{n_{a4}}{L_z} \approx \frac{n_{a5}}{L_y} \approx \frac{n_{a6}}{L_z} \geq \frac{Tk_b}{\pi}. \quad (6.33)$$

The number of structural wave functions  $n_s = 4[(n_1 + 1) + (n_{a2} + 1)]$ , and the number of acoustic wave functions  $n_a = 2[(n_{a1} + 1)(n_{a2} + 1) + (n_{a3} + 1)(n_{a4} + 1) + (n_{a5} + 1)(n_{a6} + 1)]$ .

The particular solution  $\hat{w}_F$  is defined by Eq. (6.5) where  $\mathbf{r}'$  corresponds to  $(x', y')$ , the local coordinates of the plate. The term  $\sum_{a=1}^{n_a} p_a \hat{w}_a(\mathbf{r}')$  results from the term related to  $p(\mathbf{r}')$  in the inhomogeneous part of Eq. (2.32). Since  $p(\mathbf{r}')$  is also expanded by the acoustic wave functions  $\phi_a$ , each function  $\hat{w}_a(\mathbf{r}')$  is a particular solution in response to one of the wave functions  $\phi_a$ :

$$\hat{w}_a(x', y') = \frac{-j}{8Dk_b^2} \iint_{\Omega_s} \phi_a(u_x(\xi, \zeta), u_y(\xi, \zeta), u_z(\xi, \zeta)) [H_0^{(2)}(k_b \zeta) - H_0^{(2)}(-jk_b \zeta)] d\xi d\zeta \quad (6.34)$$

with  $\gamma = \sqrt{(x' - \xi)^2 + (y' - \zeta)^2}$  and the coordinate transformation functions  $u_x, u_y, u_z$  defined by Eq. (2.31).

Regarding Eq. (6.34), if the integral surface is flat, alternative expressions for  $\hat{w}_a(x', y')$  are available to avoid the surface integral evaluation. In <sup>[27]</sup>, a group of the alternative expressions have been proposed, based on the three different wave function expressions in Eq. (6.22). They are long expressions but helpful for efficient calculation. The readers can refer to <sup>[27]</sup> for more details. Though not explicitly listed here, these alternative expressions are actually adopted in our codes for the WBM.

#### 6.4.2 Weighted residual formulation for boundary conditions

The boundary conditions of the plate are the same as the previous uncoupled situation in Section 6.2, hence the weighted residual formulation is unchanged provided by Eq. (6.12). Regarding the acoustic field, the boundary condition Eq. (2.30) is introduced due to the plate's flexural vibration. Correspondingly, the weighted residual formulation for the coupled acoustic field is given by

$$\int_{\Omega_p} \frac{-j}{\rho_0 \omega} \frac{\partial \tilde{p}}{\partial n} R_p d\Omega + \int_{\Omega_v} \tilde{p} R_v d\Omega + \int_{\Omega_z} \tilde{p} R_z d\Omega + \int_{\Omega_s} \tilde{p} R_s d\Omega = 0, \quad (6.35)$$

with one more term added to the uncoupled situation (Eq. (6.26)) for the residual  $R_s$  of the boundary condition Eq. (2.30).

Then, by expressing the weighted residual formulations with the field variable expansions Eqs. (6.31)-(6.32) and the weight expansions  $\tilde{p} = \sum_{a=1}^{n_a} \tilde{p}_a \phi_a$  and  $\tilde{w} = \sum_{s=1}^{n_s} \tilde{w}_s \psi_s$ , the WB model of the vibroacoustic system can be obtained, represented by the following matrix form equation <sup>[27]</sup>:

$$\begin{bmatrix} \mathbf{A}_{ss} & \mathbf{C}_{sa} \\ \mathbf{C}_{as} & \mathbf{A}_{aa} + \mathbf{C}_{aa} \end{bmatrix} \begin{Bmatrix} \mathbf{w}_s \\ \mathbf{p}_a \end{Bmatrix} = \begin{Bmatrix} \mathbf{f}_s \\ \mathbf{f}_a \end{Bmatrix}. \quad (6.36)$$

The first line of Eq. (6.36) is expressed in view of the structural field.  $\mathbf{w}_s$  is the vector of the  $n_s$  unknown contribution factors  $w_s$ . The  $(n_s \times n_s)$  matrix  $\mathbf{A}_{ss}$  is completely structural determined, the same as it is in the uncoupled situation, involving the multiplication of two structural wave functions. The  $(n_s \times n_a)$  coupling matrix  $\mathbf{C}_{sa}$  is related to the functions  $\hat{w}_a(\mathbf{r}')$  in the structural field expansion. The  $(n_s \times 1)$  vector  $\mathbf{f}_s$  is related to the function  $\hat{w}_F(\mathbf{r}')$  raised by the external force. The second line is instead from the acoustic perspective.  $\mathbf{p}_a$  is the vector of the  $n_a$  unknown contribution factors  $p_a$ . The  $(n_a \times n_s)$  coupling matrix  $\mathbf{C}_{as}$  is caused by the boundary coupled with the flexible plate, involving the multiplication of the acoustic and structural wave functions. The  $(n_a \times n_a)$  matrix  $\mathbf{A}_{aa}$  is completely acoustic determined, the same as it is in the uncoupled situation, containing the multiplication of two acoustic wave functions. The  $(n_a \times n_a)$  matrix  $\mathbf{C}_{aa}$  is caused by the functions  $\hat{w}_a(\mathbf{r}')$  in the structural field expansion. The  $(n_a \times 1)$  vector  $\mathbf{f}_a$  involves from the function  $\hat{w}_F(\mathbf{r}')$  in the structural field expansion.

Finally, solution of Eq. (6.36) yields the contribution factors  $w_s$  and  $p_a$ . By substituting  $w_s$  and  $p_a$  to Eqs. (6.31)-(6.32), the acoustic pressure field and structural displacement field are obtained.

### 6.4.3 Harmonic analysis on the Noise-Box test system

As characterized by Chapter 5, the Noise-Box test system consists of an elastically restrained panel and a cavity with light sound absorption. According to the model updated in Section 5.3.3, the test panel is defined by

- geometry: thin rectangular plate,  $a \times b \times h = 0.825 \text{ m} \times 1.018 \text{ m} \times 3.93 \text{ mm}$ ;
- material properties: aluminium,  $\rho = 2680 \text{ kg/m}^3$ ,  $E = 77 \text{ GPa}$ ,  $\nu = 0.33$  and  $\eta = 0.003$ ;

- edge conditions: rigidly supported ( $\bar{w} = 0$ ,  $k_w = \infty$ ) and elastically restrained against rotation ( $k_{\theta_x} = 9$  kN/rad,  $k_{\theta_y} = 16$  kN/rad, as shown in Fig. 5-24), corresponding to the restraint type  $\mathbf{r} \in \Gamma_{\bar{w}m^*}$ .

The Noise-Box cavity is updated as

- geometry: cavity shown by Fig. 3-10;
- material properties: air at 23.8°C,  $\rho_0 = 1.1889$  kg/m<sup>3</sup> and  $c = 345.42$  m/s;
- boundary conditions: wall impedance caused by sound absorption, Eq. (5.5), Table 5-2 and Fig. 5-4.

The above vibroacoustic model has been analysed using FEM in Section 5.3.4, and the numerical results can be used for comparison in validating the WBM. However, the WB model built in this section slightly simplifies the Noise-Box cavity, like its WB modelling for the uncoupled case in Section 6.3.3. Precisely, the cavity geometry adopts the simplified one shown in Fig. 3-11, and the sound absorption coefficient is considered independent of the frequency and fixed as  $\bar{\alpha} = 0.01$ .

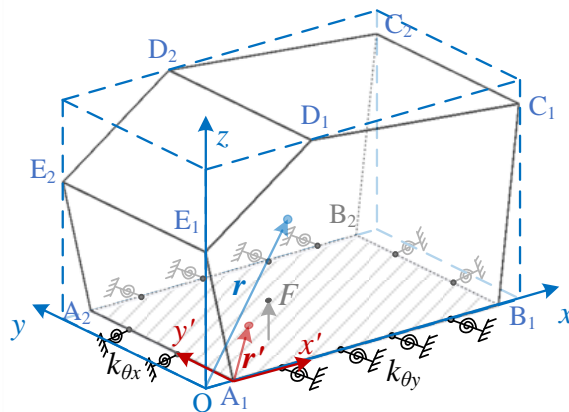


Fig. 6-12. The plate-cavity coupled Noise-Box for WB analysis.

As shown by Fig. 6-12, the WBM simulation considers a harmonic force acting at  $\mathbf{r}'_F$  (0.485m,0.44m), corresponding to the Point 80 of Fig. 5-12 and F80 of Fig. 5-27 in hammer tests. All procedures of the WBM are implemented in MATLAB with the codes provided in [213]. At first, a single frequency, 415 Hz, is considered. The cavity pressure field and the plate displacement field are plotted in Fig. 6-13(a). Corresponding results by the FEM COMSOL model updated in Section 5.3.4 are plotted in Fig. 6-13(b). This FE model is meshed under the rule introduced in Section 5.3.3: free mesh with the maximum element sizes of the plate and the cavity respectively set as 0.04 m and 0.056 m. Sound absorption coefficient of walls is defined according to Fig. 5-4. As the figure shows, the predictions from the two numerical models have similar field distributions but the contour values don't

match very well. This mismatch can be reasoned from the fact that 415 Hz is close to one of the natural frequencies of the coupled system. In Table 5-13, where lists the natural frequencies of the updated FE model, the 30<sup>th</sup> mode is 415.3 Hz. However, in the WB model, the natural frequency of this mode may be slightly father away from 415 Hz. This can be further checked by the next frequency response analysis that covers a range of frequencies.

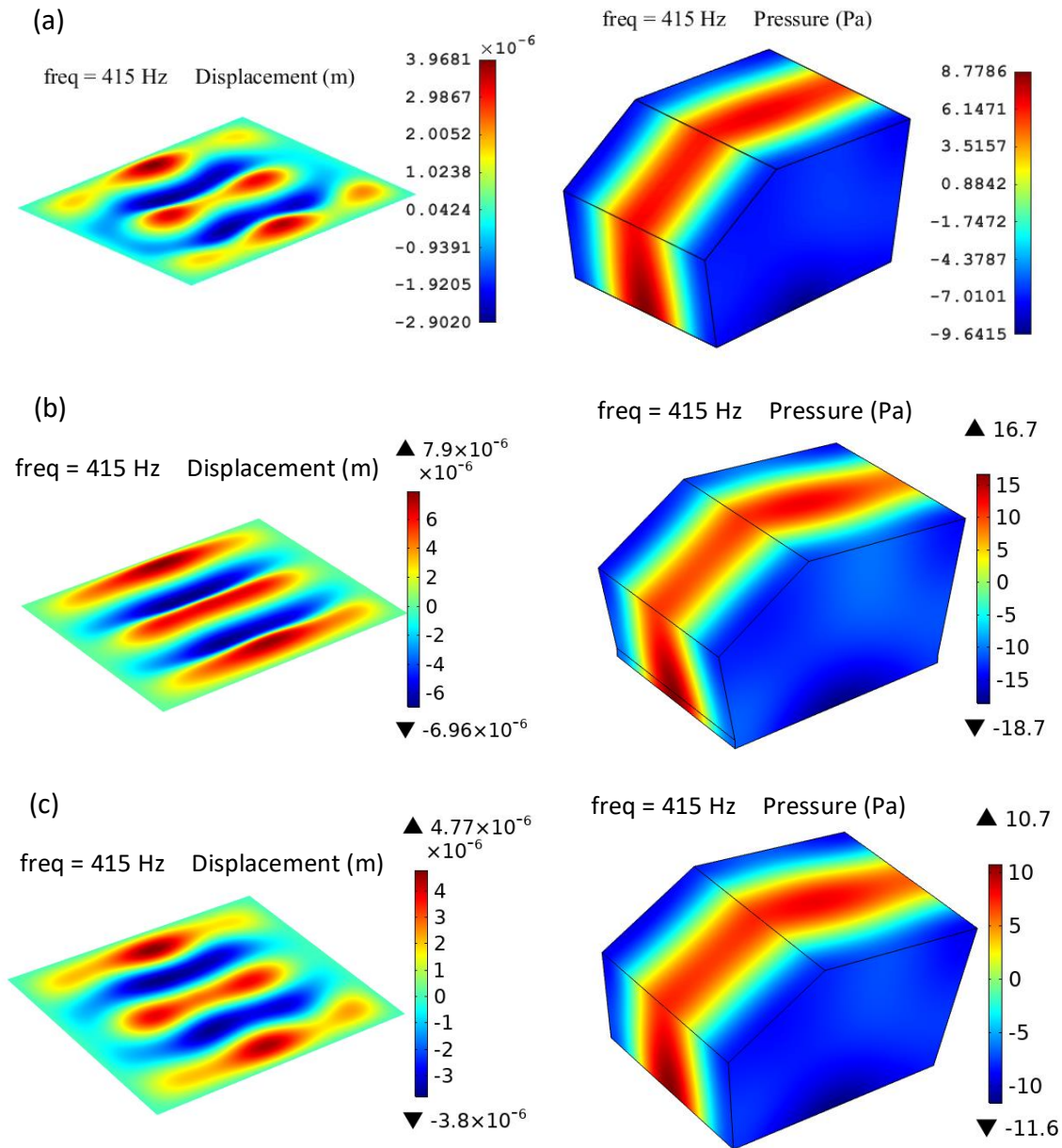


Fig. 6-13. Real parts of the field predictions at 415 Hz for Noise-Box under unit point force excitation at  $r'_F(0.485m,0.44m)$  of Fig. 6-12: (a) WBM (simplified model); (b) FEM 1 (detailed geometry, original mesh); (c) FEM 3 (simplified geometry, finer mesh).

Next, the exciting frequency changes from 10 Hz to 700 Hz at intervals of 1Hz to obtain the FRFs  $a_1/F$  and  $p_{c1}/F$ . They respectively correspond to  $A_{180} = a_1/F_{80}$  and  $H_{180} = p_{c1}/F_{80}$  of Section 5.3 (e.g., Fig. 5-27). The acceleration  $a_1$  is evaluated at  $\mathbf{r}'_1$  (0.2125m, 0.515m), and the pressure  $p_{c1}$  is probed at  $\mathbf{r}_{c1}$ (0.342m, 0.150m, 0.464m). The results predicted from the two numerical models described above are plotted and compared in Fig. 6-14. The FRFs match quite well at low frequencies but start to separate as the frequency increases, unlike the uncoupled cases (see Fig. 6-1 and Fig. 6-7), where a good agreement is observed in the whole frequency range. Further investigating the difference between two comparing FRFs (e.g., in Fig. 6-14(a)), we can find that the curves look alike in shape, but the WBM curve seems to be shifted towards rightwards from the FEM one, and the deviation increases with the frequency. Besides, in a detail view of the range approximating to 415 Hz, it can be seen that there is a resonance at 415 Hz in the FEM curve, while for WBM, the resonance is at 417 Hz. This is an explanation for the discrepancy in the contour values of the variable fields in Fig. 6-13. However, the primary cause that leads to the difference in natural frequencies should be investigated, and this should attribute to the numerical models. To know if it is related to the simplification of cavity geometry and wall impedance, a new FE model is built in COMSOL with the same simplification and analysed for the FRFs. While the new simulation results ('FEM 2') are compared with their counterparts from the previous FE model ('FEM 1'), as shown in Fig. 6-15, the differences are marginal. Hence, the simplification is not the main issue. Meanwhile, it is also proved that the simplification is feasible. Then, the attention is paid to the convergence of the two numerical approaches. For the WBM, the truncation factor  $T$  has tried to be raised from 2 to 3, and the results are little changed by the increasing the number of wave functions. Concerning the FEM, a finer mesh is applied to the simplified FE model ('FEM 2'), where the maximum plate element size is reduced from 0.04 m to 0.02 m. Since it is a conform mesh between plate and cavity, the finer mesh in the plate also forces a finer mesh in the cavity, the DOF of the FE model is significantly increased, as well as the computation time. This refined FE model can be referred to as 'FEM 3'. Thanks to the finer mesh, the FEM results are now closer to the WBM ones, as demonstrated by Fig. 6-16. In addition, Fig. 6-13(c) shows the plate displacement field and the cavity sound pressure field predicted by the refined FE model. As expected, the two fields better match the two predicted by WBM in Fig. 6-13(a). Thus, we can deduce that the predictions from FEM converge to the WBM results. Therefore, the WBM is validated, and the provided codes for the WBM are proved effective. Furthermore, the above investigation reveals that that the results from the WB model with  $T = 2$  are converged and accurate.

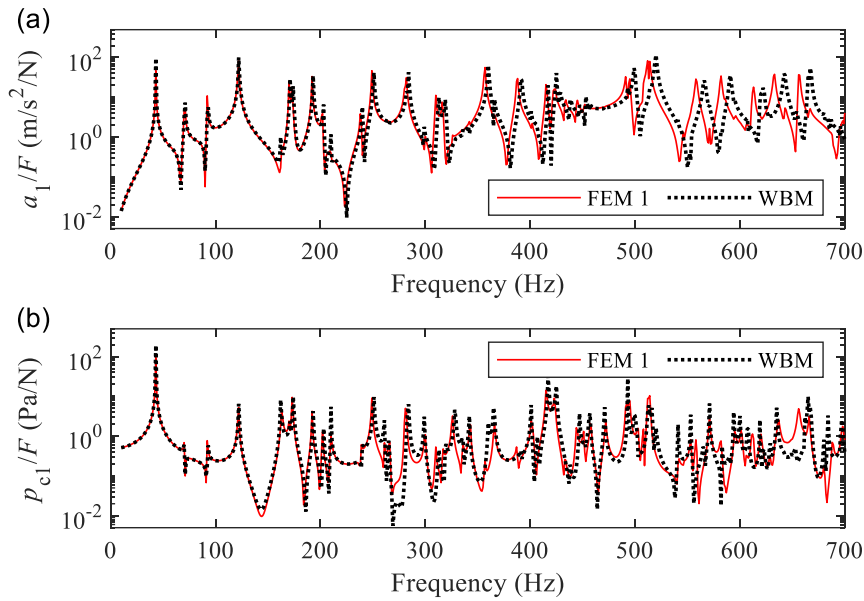


Fig. 6-14. FEM 1 (detailed geometry, original mesh) and WBM predictions on FRFs of the Noise-Box system. Input and outputs are located at  $\mathbf{r}'_F$  (0.485m, 0.44m),  $\mathbf{r}'_1$  (0.2125m, 0.515m) and  $\mathbf{r}_{c1}$  (0.342m, 0.150m, 0.464m) of Fig. 6-12.

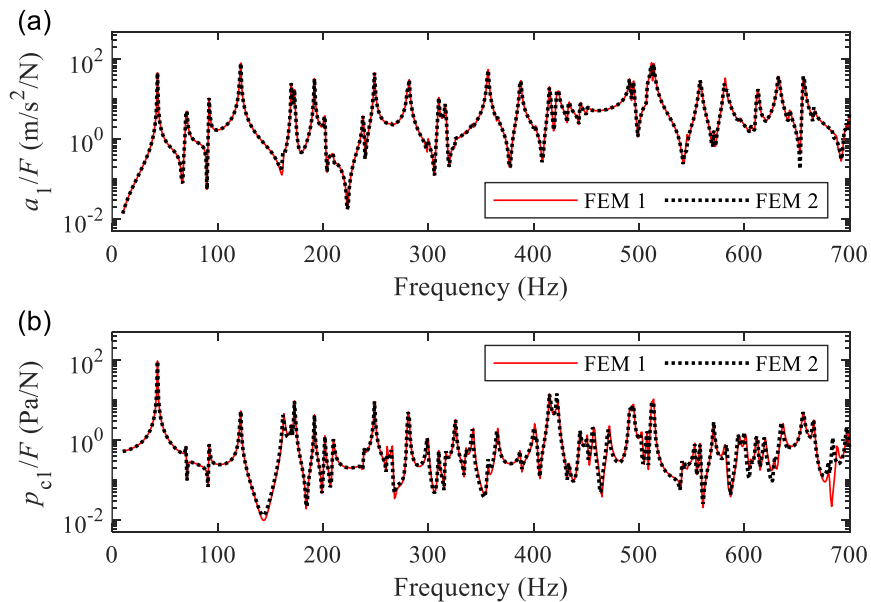


Fig. 6-15. FEM 1 (detailed geometry, original mesh) and FEM 2 (simplified geometry, original mesh) predictions on FRFs of the Noise-Box system. Input and outputs are located at  $\mathbf{r}'_F$  (0.485m, 0.44m),  $\mathbf{r}'_1$  (0.2125m, 0.515m) and  $\mathbf{r}_{c1}$  (0.342m, 0.150m, 0.464m) of Fig. 6-12.



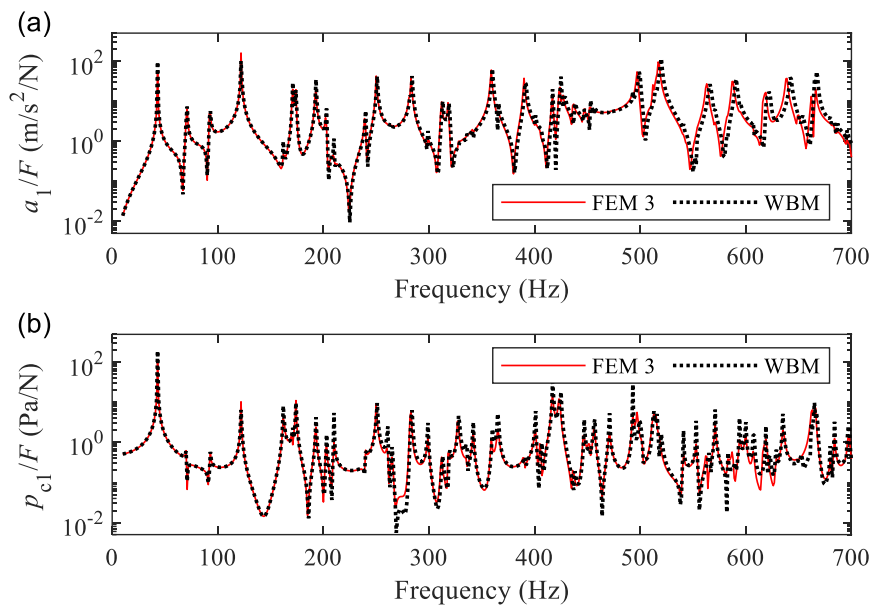


Fig. 6-16. FEM 3 (simplified geometry, finer mesh) and WBM predictions on FRFs of the Noise-Box system. Input and outputs are located at  $\mathbf{r}'_F$  (0.485m, 0.44m),  $\mathbf{r}'_1$  (0.2125m, 0.515m) and  $\mathbf{r}_{c1}$  (0.342m, 0.150m, 0.464m) of Fig. 6-12.

In addition to the accuracy, the WBM is advocated for its low demand for computation memory and time. In other words, it is much more efficient than the FEM. In this section, for analysing the Noise-Box system, three FE models were built. The first two were meshed under the same mesh setting, so their model sizes are roughly equal, which is about 105469 DOF. The computation times are also close, approximating to 1h 30min for the 691 frequencies from 10 Hz to 700 Hz. The third one with finer mesh has 253712 DOF and occupies totally 4h 45min for the same analysis. From the first FE model to the third FE model, the predictions are more accurate, but the model size and computation time surge. By contrast, the WBM with  $T = 2$  possesses no more than 1698 DOF (the number of wave functions), and the overall time of modelling and solution for the 691 frequencies is 30min 28sec.

Finally, as a by-product in this validation for WBM, the most precise FE model for the plate-cavity system in this thesis is proposed. In this model, there is no simplification in the cavity geometry and wall impedance, but the mesh density is increased. In other words, the decrease of plate element size from 0.04 m to 0.02 m is directly based on 'FEM 1'. Fig. 6-17 illustrates the geometry of mesh of this FE model. For the convenience to mention this specific model, it is denoted as 'FEM 4'. As a comparison between this model and the WB model, their predictions of the FRFs  $a_1/F$  and  $p_{c1}/F$  are plotted in Fig. 6-18. The agreement between FEM 4 and WBM is similar to its counterpart between FEM 3 and WBM, as shown

by Fig. 6-16. The difference caused by the simplification is marginal, in consistence with the comparison between ‘FEM 1’ and ‘FEM 2’, as shown by Fig. 6-15.

Therefore, through the analyses in this subsection, it is validated the WBM is accurate and efficient. Meanwhile, the proposed simplification in cavity geometry and wall impedance is reasonable and has marginal impact on the final results.

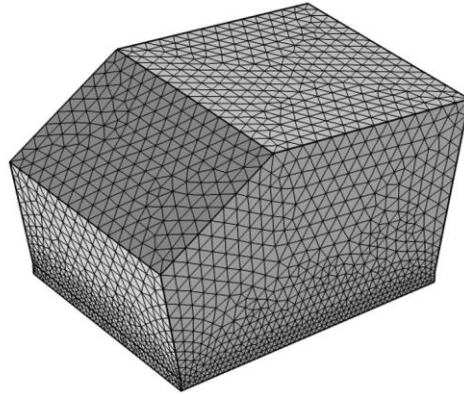


Fig. 6-17. FE model of the plate-cavity system with finer plate mesh, referred to as ‘FEM 4’.

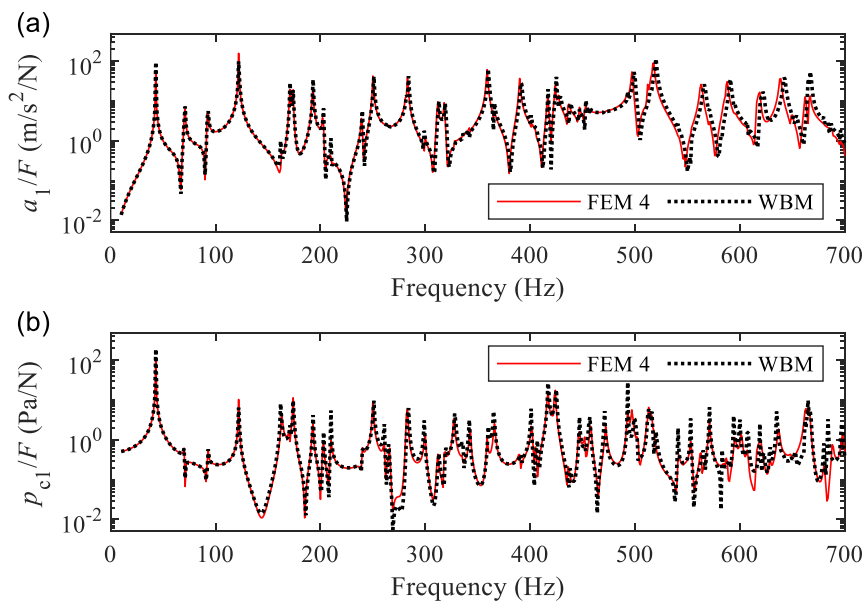


Fig. 6-18. FEM 4 (detailed geometry, finer mesh) and WBM predictions on FRFs of the Noise-Box system. Input and outputs are located at  $r'_F$  (0.485m, 0.44m),  $r'_1$  (0.2125m, 0.515m) and  $r_{c1}$  (0.342m, 0.150m, 0.464m) of Fig. 6-12.

#### 6.4.4 Validation for two-dimensional plate-cavity systems

In the 2D plate-cavity vibroacoustic problem, whose mathematical model is introduced in Section 2.4.2, the coordinates  $\mathbf{r}$  corresponds to  $(x, z)$  and  $\mathbf{r}'$  corresponds to  $x'$ . Accordingly, the field variable expansions can be represented by Eqs. (6.31)-(6.32), but the exact expressions of the imbedded functions are reduced by eliminating the  $y$  or  $y'$  coordinate. Three of them can be directly obtained from their correspondences in uncoupled situations: the acoustic wave functions  $\phi_a$  are defined as Eq. (6.28); the structural wave functions  $\psi_s$  are given by Eq. (6.18); and the particular solution function  $\hat{w}_F(x)$  due to the line force excitation  $F$  is expressed as Eq. (6.19). Then, the total number of wave functions is equal to  $(n_a + n_s) = 2[(n_{a1} + 1) + (n_{a2} + 1)] + 4$ , where  $n_{a1}$  and  $n_{a2}$  are determined by the truncation rule:

$$\frac{n_{a1}}{L_x} \approx \frac{n_{a2}}{L_z} \geq \frac{Tk_b}{\pi}. \quad (6.37)$$

Specially, the functions  $\hat{w}_a(\mathbf{r}')$  are additionally introduced in the coupled situation. Each function  $\hat{w}_a(\mathbf{r}')$  is a particular solution of the 1D plate governing equation in response to one of the wave functions  $\phi_a$ :

$$\hat{w}_a(x') = \frac{-j}{4Dk_b^3} \int_0^l \phi_a(x_0 + \xi \cos \alpha, z_0 + \xi \sin \alpha) (e^{-jk_b|x'-\xi|} - je^{-k_b|x'-\xi|}) d\xi, \quad (6.38)$$

where, one end of the plate, i.e.,  $\mathbf{r}'(0)$ , is at  $\mathbf{r}(x_0, z_0)$ ;  $\alpha_0$  is the angle between  $x'$ - and  $x$ -axes. Since the plate is flat, a less computational demanding expression can be used, which is given by

$$\hat{w}_a(x') = \frac{\exp[-jk_{xa}(x_0 + x' \cos \alpha_0) - jk_{za}(z_0 + x' \sin \alpha_0)]}{D[(k_{xa} \cos \alpha_0 + k_{za} \sin \alpha_0)^4 - k_b^4]}, \quad (6.39)$$

where  $k_{xa}$  and  $k_{za}$  are wavenumber components of the acoustic wave functions.

Later, implemented the weighted residual formulations following Section 6.4.2, the WB model in form of Eq. (6.36) is obtained for solution. Then, with the contribution factors  $w_s$  and  $p_a$ , the structural and acoustic variables can be derived.

To validate the WBM for a cavity coupled with an elastically restrained plate in the 2D situation, a vibroacoustic problem is raised, considering the interaction between the 1D plate discussed in Section 6.2.5 and the 2D cavity investigated in Section 6.3.4. To be specific, the 2D coupled vibroacoustic problem is depicted in Fig. 6-19.

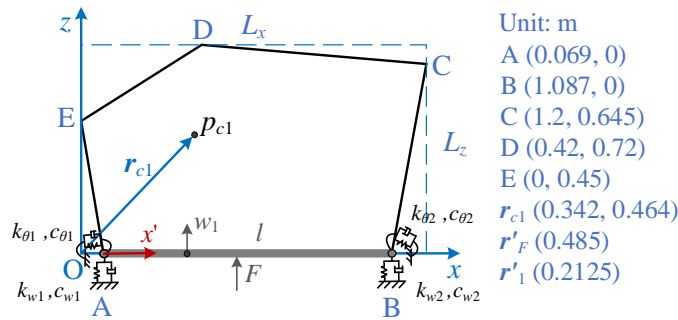


Fig. 6-19. Two-dimensional plate-cavity system for WB analysis

The plate is defined by  $l = 1.018$  m,  $h = 4$  mm,  $\rho = 2680$  kg/m<sup>3</sup>,  $E = 69$  GPa,  $\nu = 0.33$ ,  $c_{w1} = c_{w2} = c_{\theta1} = c_{\theta2} = 0$ ,  $k_{w1} = k_{w2} = 10^6$  N/m,  $k_{\theta1} = k_{\theta2} = 10^4$  N/rad. The cavity is a pentagon confined by its vertices A-B-C-D-E, and its interior air properties are given by  $\rho_0 = 1.1875$  kg/m<sup>3</sup> and  $c = 345.63$  m/s. This case considers the damping loss factor of the plate, i.e.,  $\eta = 0.003$ , but neglects the sound absorption of walls, i.e.,  $\bar{Z} = \infty$ . In the steady state analysis, a line force  $F$  is acting at  $x'_F = 0.485$  m harmonically with a given frequency within 10-700 Hz. From the analysis of a single frequency, the responses of the structural and acoustic fields are obtained. In terms of a wide frequency range, e.g., 10-700 Hz, the FRFs  $w_1/F$  and  $p_{c1}/F$  are evaluated. The displacement  $w_1$  is measured at  $x'_1 = 0.2125$  m, and the pressure  $p_{c1}$  is probed at  $(x'_1, z'_1) = (0.342\text{m}, 0.464\text{m})$ .

As a reference to validate the WBM, corresponding FE model is built in ANSYS, utilizing BEAM3 and FLUID29 elements. Note that the FE modelling approach has been validated in Section 4.4.4. Then, the WBM implemented in MATLAB (codes provided in [213]) and the FEM achieved by ANSYS are used to analyse the 2D vibroacoustic problem. The field responses at 415 Hz are compared in Fig. 6-20. The FRFs are compared in Fig. 6-21. They reveal that the predictions by the two numerical models meet a good agreement. As a result, the WBM for 2D plate-cavity vibroacoustic problems are proved accurate.

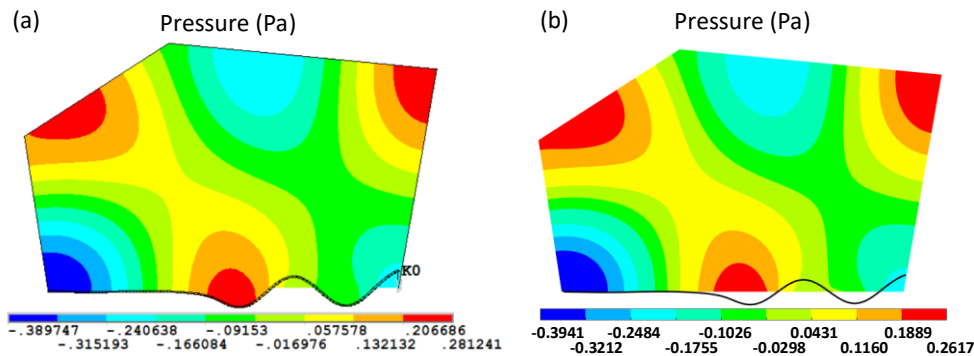


Fig. 6-20. Real parts of the field predictions at 415 Hz for the 2D plate-cavity system in Fig. 6-19: (a) FEM (ANSYS); (b) WBM.

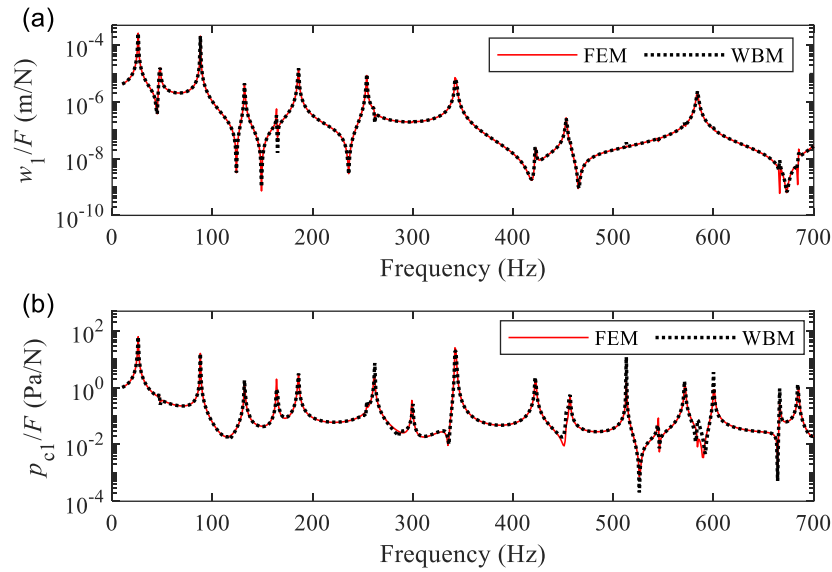


Fig. 6-21. FEM (ANSYS) and WBM predictions on FRFs of the 2D plate-cavity system in Fig. 6-19.

## 6.5 Summary

This chapter has successfully developed a group of WB models that can be used to analyse the Noise-Box and its components. All the MATLAB codes for these models as well as the solution and postprocessing are available in the database online <sup>[213]</sup>.

The WB model for flexural vibration of thin plate is able to investigate a plate with various types of edge conditions (all the 9 types shown in Table 2-1). Thanks to the new proposed weighted residual formulation, the WBM is available for the edge conditions that are partially or fully (visco)elastically restrained. When the WBM is used to analyse the mounted test panel, the obtained FRFs and variable field distributions are shown consistent with the FEM results, which validates the effectiveness of the model. Meanwhile, the WBM is proved more efficient, so that it can be used to analyse the problem to higher frequencies without significantly increasing its model size and computation time. For completeness, the WB model for a 1D thin plate is also provided. It is validated that the proposed formulation is applicable to the 1D plate problem.

The WB model for uncouple acoustic cavity is able to apply different wall impedance. In the chapter, it is used to analyse the Noise-Box in its simplified geometry. The WBM results agree well with the FEM predictions. However, a better agreement is obtained, when the FE model also uses the simplified geometry. Therefore, the WB model for the Noise-Box

cavity under monopole source excitation is validated. Similarly, the WB model for 2D cavity is built and validated.

The development of the WB model for a vibroacoustic plate-cavity system is in fact about how to combine the two uncoupled models and introduce the coupled terms. So, once the previous two uncoupled models are verified, the couple model doesn't need too much effort. Similarly, the WB model is validated by analysing the Noise-Box test system in frequency domain. The predicted FRFs and variable fields for either the plate or the cavity are compared with their corresponding results of the updated FE model ('FEM 1'). Within the frequency of interest, from 10 Hz to 700 Hz, it is found that the WBM and 'FEM 1' results may not reach a sufficient agreement within 500 to 700 Hz. But when the element size in the FE model, especially for the plate, is reduced (e.g., 'FEM 4', where plate element size is reduced from 0.04 m to 0.02 m), a better agreement is observed, which indicates that the previous discrepancy is raised by the not sufficiently fine elements in the FE model. This further reflects the efficiency of the WBM, for when 'FEM 4' occupies about 5 hours, the WBM uses about 30 min to complete the computation of 691 frequencies. In the end, the WB model for 2D plate-cavity system is also presented and validated by comparing the results with the FEA predictions.

## Chapter 7 Numerical investigation using statistical energy analysis

*This chapter develops SEA models for vibroacoustic analysis on the plate-cavity coupled Noise-Box. It starts with the general procedures for SEA, and then applies the SEA to the plate-cavity system, where two vibroacoustic problems are investigated. One problem has the system under a point force excitation, and the other considers the exterior acoustic excitation. For each problem, details about how to establish and validate the SEA models are illustrated; and as the investigation results, responses of the plate and cavity are presented, especially for the high frequency range.*

### 7.1 General procedures for SEA

The SEA is normally performed under the following procedures:

#### (1) Definition of subsystems

The overall system is divided into subsystems. Each subsystem is like a tank that can store energy. Since one subsystem is represented by the same group of dynamic parameters, it is important that the subsystem contains only ‘similar modes’. Characterized as ‘similar’, these modes are usually of the same type (flexure, extension, shear, acoustic, etc.) and in a separable component of the system (a beam, a plate, a cavity, etc.). The selection and definition of these subsystems should follow the criteria of similarity and significance <sup>[19]</sup>.

#### (2) Formulation of SEA equations based on energy or power flows

The connection among subsystems can be represented by energy or power flows. For example, as shown by Fig. 7-1, in a general SEA model of  $N$  subsystems, the energy flow equilibrium of subsystem  $i$  gives

$$\sum_{j=1, j \neq i}^N P_{ji} + P_i = \sum_{j=1, j \neq i}^N P_{ij} + P_{id}. \quad (7.1)$$

where,  $P_{ij}$  denotes the power transmitted from subsystem  $i$  to subsystem  $j$ ;  $P_i$  is the external power input to subsystem  $i$ ; and  $P_{id}$  is the power dissipated by subsystem  $i$ .

In the SEA, the dissipated and transmitted powers are considered proportional to the frequency and the dynamic energy, like they are in the modal resonators or reverberant fields. The dissipated power  $P_{id}$  is given by

$$P_{id} = \omega \eta_{id} E_i, \quad (7.2)$$

with  $\eta_{id}$  defined as damping loss factor and  $E_i$  as the dynamic energy of subsystem  $i$  at frequency  $\omega$ . The transmitted power  $P_{ij}$  is given by

$$P_{ij} = \omega \eta_{ij} E_i, \quad (7.3)$$

with  $\eta_{ij}$  defined as the coupling loss factor between subsystems  $i$  and  $j$ .

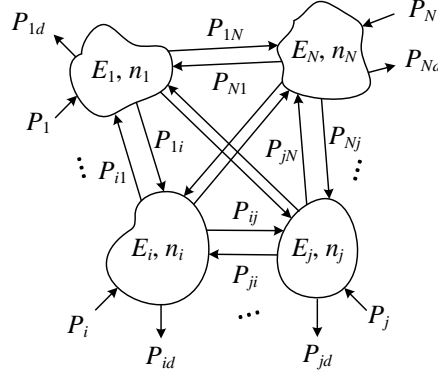


Fig. 7-1. SEA model of  $N$  subsystems

Then, rewriting Eq. (7.1) with Eqs. (7.2)-(7.3) for all the subsystems yields the system of equations:

$$\begin{Bmatrix} P_1 \\ P_2 \\ \vdots \\ P_N \end{Bmatrix} = \omega \begin{bmatrix} \eta_1 & -\eta_{12} & \cdots & -\eta_{1N} \\ -\eta_{21} & \eta_2 & \cdots & -\eta_{2N} \\ \vdots & \vdots & \ddots & \vdots \\ -\eta_{N1} & -\eta_{N2} & \cdots & \eta_N \end{bmatrix} \begin{Bmatrix} E_1 \\ E_2 \\ \vdots \\ E_N \end{Bmatrix}, \quad (7.4)$$

where  $\eta_i$  ( $i = 1, 2, \dots, N$ ) are given by

$$\eta_i = \eta_{id} + \sum_{j \neq i} \eta_{ij} \quad (i = 1, 2, \dots, N). \quad (7.5)$$

With  $n_i$  defined as the modal density of subsystem  $i$ , Eq. (7.4) can also be expressed as

$$\begin{Bmatrix} P_1 \\ P_2 \\ \vdots \\ P_N \end{Bmatrix} = \omega \begin{bmatrix} n_1 \eta_1 & -n_1 \eta_{12} & \cdots & -n_1 \eta_{1N} \\ -n_2 \eta_{21} & n_2 \eta_2 & \cdots & -n_2 \eta_{2N} \\ \vdots & \vdots & \ddots & \vdots \\ -n_N \eta_{N1} & -n_N \eta_{N2} & \cdots & n_N \eta_N \end{bmatrix} \begin{Bmatrix} E_1/n_1 \\ E_2/n_2 \\ \vdots \\ E_N/n_N \end{Bmatrix}. \quad (7.6)$$

This equation shows that the matrix is symmetric provided that the reciprocity relationship  $n_i \eta_{ij} = n_j \eta_{ji}$  is satisfied <sup>[16,19,218]</sup>. In this case, only the upper or lower triangular side of the matrix needs to be calculated.

### (3) Evaluation of SEA parameters

In the SEA model, represented by Eq. (7.5) or (7.6), most of the parameters are preliminarily unknown and need to be evaluated. Typically, the needed parameters for each subsystem include the modal density  $n_i$ , the damping loss factor  $\eta_{id}$ , the coupling loss factors  $\eta_{ij}$  ( $i \neq j$ ), and the input power from external sources  $P_i$ . There are no universal techniques to determine these parameters, and they rely on the properties of the subsystem and/or its



connections to the others. The modal density is dependent on the geometry and material properties and can be evaluated by theoretical, numerical or experimental method. The damping loss factor is usually obtained through measurement or predicted by empirical formulas. It is a synthetic parameter that incorporates various damping losses, e.g., the internal dissipation related to structure and material, the damping at connecting joints, the loss due to surface absorption or damping treatment, etc. The coupling loss factor can be evaluated by theoretical, empirical and/or numerical methods. The derivations are usually based on modal approach, wave approach, mobility approach or their combinations <sup>[19,219]</sup>. Experimental methods are also available but quite hard for accurate results. The external input power is sometimes measured but more often calculated based on the subsystem parameters and the source type and amplitude.

#### (4) Solution of energy and calculation of response

After the SEA parameters are evaluated, the unknowns left in Eq. (7.5) or (7.6) are the  $N$  subsystem energies. The SEA model turns out to a set of linear algebraic equations, whose DOF equals to the number of subsystems. The solution yields the primary variable, i.e., dynamic energy, of each subsystem. Then, according to the relationship between energy and other variables such as velocity, displacement, pressure, etc., the spatially averaged response on any subsystem is available.

This chapter develops the SEA models that can be used to investigate the vibroacoustic problems related to the plate-cavity coupled Noise-Box. Two scenarios are considered. The first scenario involves a force excitation, which may be informative for the structure-borne noise investigation. The second scenario focuses on acoustic excitation, so it is for the air-borne noise. In the SEA models of these scenarios, the SEA parameters are evaluated theoretically or partially from the experimental results. Then, all the formulae and equations are calculated and solved in MATLAB. The codes are available in the database <sup>[213]</sup>. For validating the analysing approach and programmed codes, an open source tool called ‘SEAlab’ <sup>[220]</sup> was found online and is used in this section to analyse the same cases for comparison.

## 7.2 SEA for plate-cavity system under force excitation

This scenario considers the Noise-Box under an external point forcing, as illustrated by Fig. 7-2. The system is divided into two subsystems:

- subsystem 1 for flexural wave of the test panel;
- subsystem 2 for acoustic wave in the Noise-Box cavity.

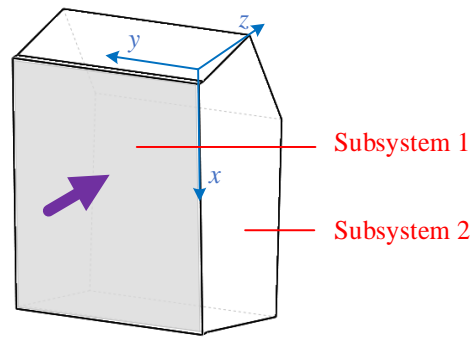


Fig. 7-2. Subsystems of the SEA model for the plate-cavity system with point force excitation.

The two subsystems are of the exact geometry (as Fig. 3-10), and the material parameters are set as the update ones (by Section 5.3.3). Specifically, the thin panel is defined by  $a \times b \times h = 0.825 \text{ m} \times 1.018 \text{ m} \times 3.93 \text{ mm}$ ,  $\rho = 2680 \text{ kg/m}^3$ ,  $E = 77 \text{ GPa}$ ,  $\nu = 0.33$  and  $\eta = 0.003$ ; the cavity is determined by volume  $V = 0.596 \text{ m}^3$ , total surface area  $S' = 4.26 \text{ m}^2$ , total length of all edges  $L' = 10.123 \text{ m}$ ,  $\rho_0 = 1.1889 \text{ kg/m}^3$  and  $c = 345.42 \text{ m/s}$ . A point force with unit root-mean-square (RMS) value is acting on the panel, i.e.,  $F_{\text{rms}} = 1 \text{ N}$ . The results to obtain are the energies of the two subsystems, the average velocity of the panel and the average acoustic pressure of the cavity. They should be solved for every 1/3 octave band from 100 Hz to 20 kHz.

## 7.2.1 Evaluation of SEA parameters

Modal density of the panel (subsystem 1) is given by

$$n_1(\omega) = \frac{k_b S}{2\pi c_g}, \quad (7.7)$$

where,  $S = ab$  is the area of the panel;  $k_b$  is the bending wavenumber determined by Eq. (2.3);  $c_g = 2\omega/k_b$  is group velocity of the flexural wave. Modal density of the cavity (subsystem 2) is evaluated by

$$n_2(\omega) = \frac{k^2}{2\pi^2 c} V + \frac{k}{8\pi c} S' + \frac{1}{16\pi c} L'. \quad (7.8)$$

Damping loss factor of the plate is defined as  $\eta_{1d} = \eta = 0.003$ . For the cavity, the damping loss factor is calculated by

$$\eta_{2d}(f) = \frac{c\bar{\alpha}S'}{8\pi fV}, \quad (7.9)$$

where  $\bar{\alpha}$  is the average absorption coefficient of the cavity. For simplicity, a constant damping loss factor  $\eta_{2d} = 0.002$  is used. This value is the calculated result for  $f = 1000 \text{ Hz}$

with  $\bar{\alpha} = 0.019$ , which corresponds to the measured average absorption coefficient listed in Table 5-2. However, it is expected that the damping loss factor of this cavity closed by flexible plate is different from the measurement result, because in that measurement, the opening of the cavity was covered by a thick plexiglass plate instead of the thin aluminium panel, which may reduce the sound absorption, and one corner of the cavity was added the loudspeaker and its support, which may increase the sound absorption. Nevertheless, this parameter can be updated in future investigations.

The coupling loss factor  $\eta_{12}$  denotes the coupling strength between a plate and a cavity. It can be evaluated based on its relationship to the plate's radiation efficiency  $\sigma$ , which is given by<sup>[16,58]</sup>

$$\eta_{12}(\omega) = \frac{\rho_0 c \sigma}{\omega \rho}. \quad (7.10)$$

Then, the other coupling loss factor  $\eta_{21}$  is available according to reciprocity relationship  $n_1 \eta_{12} = n_2 \eta_{21}$ . For calculating the radiation efficiency in Eq. (7.10), a number of approximate expressions have been proposed. The formulation proposed by the international standard BS EN ISO 12354-1 is presented in the Appendix B.3 from Eq. (B.14) to Eq. (B.16), which is claimed based on<sup>[131]</sup>. In addition, the asymptotes formulated by Leppington<sup>[221]</sup> are also adopted in parallel for comparison:

$$\sigma \sim \begin{cases} \frac{1}{\sqrt{1-\mu^2}} & \mu < 1, ka(1-\mu) \text{ large} \\ \frac{(a+b)}{\pi \mu k a b \sqrt{\mu^2-1}} \left\{ \ln\left(\frac{\mu+1}{\mu-1}\right) + \frac{2\mu}{\mu^2-1} \right\} & \mu > 1, ka(\mu-1) \text{ large} \end{cases}, \quad (7.11)$$

where  $\mu = k_b/k$  is the ratio between plate bending wavenumber and acoustic wavenumber;  $a$  and  $b$  are respectively the smaller and greater dimensions of the panel. As mentioned in<sup>[221]</sup>, when  $\mu \approx 1$ , the results are complicated, but the expression is not specified. Hence, in this work, provided that  $0.2 < a/b < 1.0$ ,  $\sigma$  is evaluated for a range of frequencies and  $\mu \approx 1$  is satisfied in the only frequency range that includes the coincidence frequency ( $\mu = 1$ ), the radiation efficiency  $\sigma$  for the only band that satisfies  $\mu \approx 1$  is approximated by

$$\sigma = 0.4\sqrt{ka} \quad \mu \approx 1. \quad (7.12)$$

Input power to the panel is evaluated by

$$P_1(\omega) = \frac{|F|^2 \operatorname{Re}[Y(\omega)]}{2} = F_{\text{rms}}^2 \cdot \operatorname{Re}[Y(\omega)], \quad (7.13)$$

where  $Y(\omega)$  is the point mobility of an infinite plate, which is given by

$$Y(\omega) = \frac{1}{8\sqrt{D\rho h}}. \quad (7.14)$$

## 7.2.2 Matrix form equation and solution

As a two-subsystem SEA model with only input to the subsystem 1, i.e.,  $N = 2$  and  $P_2 = 0$ , the matrix form equation like Eq. (7.6) is given by

$$\begin{Bmatrix} P_1 \\ 0 \end{Bmatrix} = \omega \begin{bmatrix} n_1(\eta_{1d} + \eta_{12}) & -n_1\eta_{12} \\ -n_2\eta_{21} & n_2(\eta_{2d} + \eta_{21}) \end{bmatrix} \begin{Bmatrix} E_1/n_1 \\ E_2/n_2 \end{Bmatrix}. \quad (7.15)$$

With all the evaluated SEA parameters substituted to Eq. (7.15), the energies  $E_1$  and  $E_2$  are then solved for every 1/3-octave band, where  $\omega$  corresponds to the central frequency. Afterwards, the root-mean-square velocity  $v_{\text{rms}}$  averaged over the panel surface area  $S$  and root-mean-square sound pressure  $p_{\text{rms}}$  averaged over the cavity volume  $V$  can be estimated respectively based on the following relationships

$$E_1 = \rho h S v_{\text{rms}}^2 \quad (7.16)$$

and

$$E_2 = \frac{p_{\text{rms}}^2 V}{\rho_0 c^2}. \quad (7.17)$$

## 7.2.3 Results and discussion

According to the method and procedures introduced above, two SEA models are developed in MATLAB. The difference between the two models is the evaluation of panel radiation efficiency  $\sigma$ . Model 1 is calculated from the equations in BS EN ISO 12354-1 (Eqs. (B.14)-(B.16)), while Model 2 adopts Leppington's formulation (Eqs. (7.11)-(7.12)). The primary variables, i.e., the subsystem energies  $E_1$  and  $E_2$  for 1/3-octave bands, of the two models are plotted in Fig. 7-3(a) and Fig. 7-3(b). Comparable results predicted via SEALab are shown in Fig. 7-3(c). The three plots show consistent results, except for the frequencies lower than 200 Hz and at 3150 Hz. The two reasons for the discrepancies are known. One reason has been mentioned previously, i.e., the different formulations for the panel radiation efficiency  $\sigma$  that are applied to Model 1 and Model 2, respectively. The formulation in the SEALab tool <sup>[219]</sup> is the same as Model 1, i.e., the Eqs. (B.14)-(B.16) from BS EN ISO 12354-1. Consequently, as shown by Fig. 7-3(d), the radiation efficiencies agree well between Model 1 and the SEALab model in the whole frequency range. Whereas, Model 2 adopts Leppington's formulation, and Fig. 7-3(d) indicates that this formulation yields different radiation efficiencies from the others at the frequencies lower than 630 Hz and at 3150 Hz. Since Model 1 and Model 2 are only different in the radiation efficiency  $\sigma$ , the outcome of this reason is observable from Fig. 7-3(a) and Fig. 7-3(b), where they show very small variations for the subsystem energy levels. The other reason is related to the difference between Model 1 (Fig. 7-3(a)) and SEALab model (Fig. 7-3(c)) at the frequencies lower than 200 Hz. It actually results from the fact that in SEALab, the cavity is treated as

2D cavity when the acoustic wavelength in  $z$  direction is larger than the cavity's dimension in  $z$  direction (i.e.,  $\lambda_z > L_z$ ). This will lead to the different modal densities of the cavity, and thus different results are obtained. However, this is not necessary for the considered plate-cavity system, because the situation ( $\lambda_z > L_z$ ) corresponds to a frequency range too low to apply the SEA method. Therefore, it can be deduced that both Model 1 and Model 2 are correct and applicable. In comparison, Model 2 that uses Leppington's formulation provides the upper limit of  $\sigma$  near the critical frequency when  $\sigma > 1$  [222].

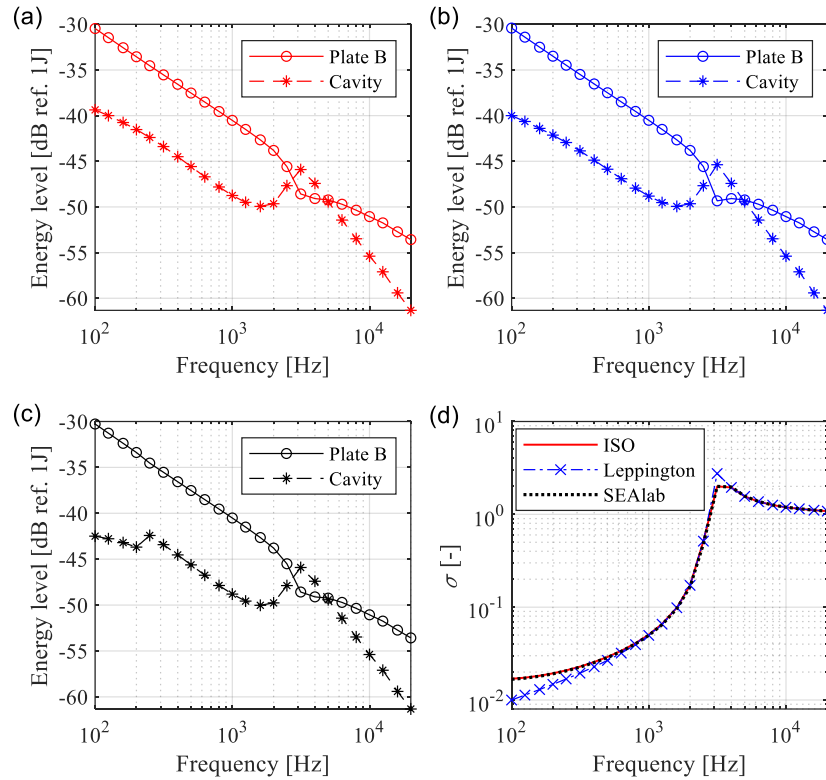


Fig. 7-3. Subsystem energy levels predicted by the SEA models of the plate-cavity system under the point force excitation  $F_{\text{rms}} = 1$  N: (a) Model 1 –  $\sigma$  from BS EN ISO 12354-1; (b) Model 2 –  $\sigma$  from Leppington's formulation; (c) SEA Lab model; (d) comparison of the radiation efficiencies  $\sigma$  among the SEA models.

Apart from validating the SEA models, Model 1 and Model 2, Fig. 7-3 also indicates that the coincidence between bending and acoustic waves happens at around 3150 Hz. In the coincidence region, it is possible that the vibration energy of the plate is smaller than the sound energy in the cavity, even though the external power is input directly to the plate.

Next, the plate and cavity energies obtained from Model 2 are used to derive the average velocity of the plate and the average SPL of the cavity. Calculated based on Eq. (7.16) and Eq. (7.17), the results are shown in Fig. 7-4. The corresponding results provided by SEA Lab are plotted alongside for comparison. Since in each subsystem, the relationship between

response and energy is fixed, the agreement in energy predictions is propagated to the response variable predictions.

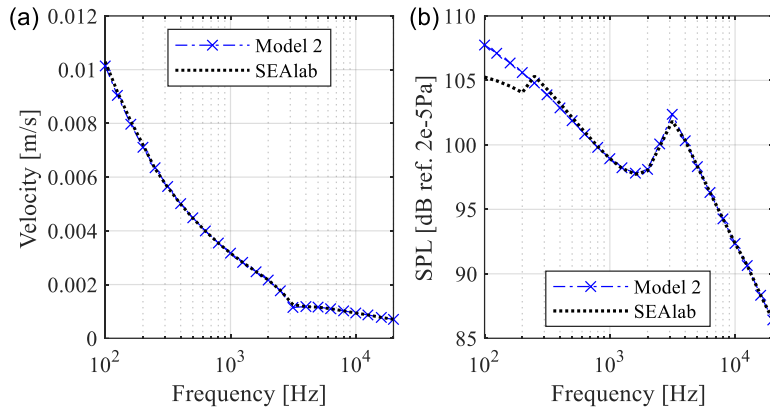


Fig. 7-4. Responses of the plate-cavity system under the point force excitation  $F_{\text{rms}} = 1$  N: (a) average velocity of the plate; (b) average SPL of the cavity.

Though the above results are obtained for a very wide frequency range from 100 Hz to 20 kHz, the reliability or accuracy of them is still a question. It depends on whether the assumptions used in SEA are valid. It is well-known that the SEA is particularly well suited for complex systems at high frequencies, where the subsystems will have large modal overlap and large numbers of modes in band that make the results more reliable. Thus, the modal overlap or number of modes in band is often used as an indicator for the lower frequency limit of SEA. However, the lower frequency limit is not a line saying whether the SEA model is correct. The fact is that the error will increase with the frequency decreasing. Therefore, for the knowledge about how much the SEA is suitable to the plate-cavity system, the modal overlap and the number of modes in each 1/3-octave band of the two subsystems are presented in Fig. 7-5.

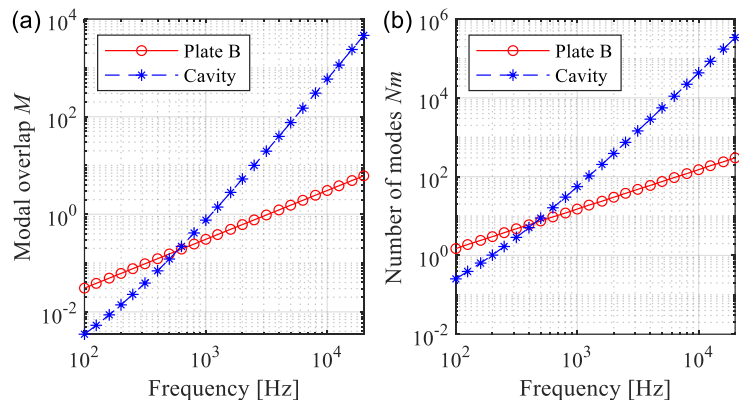


Fig. 7-5. Modal overlap and number of modes in 1/3-octave bands for the plate and cavity subsystems in their SEA models.

The modal overlap is calculated based on its definition as the ratio of the half-power bandwidth to the local natural frequency spacing, which is expressed as  $M = \eta\omega n(\omega)$ . The number of modes in the bandwidth  $\Delta\omega$  is given by  $N_m = \Delta\omega n(\omega)$ . According to Fig. 7-5, the lower limit frequency can be considered by referring to different criteria <sup>[22,23,218]</sup>. For example, the requirement  $M > 1$  yields  $f > 1000$  Hz for the cavity and  $f > 3150$  Hz for the plate;  $N_m > 20$  requires  $f > 630$  Hz and  $f > 1250$  Hz for the cavity and the plate, respectively; and  $N_m > 10$  corresponds to  $f > 500$  Hz.

### 7.3 SEA for plate-cavity system under acoustic excitation

This scenario considers the Noise-Box under the external acoustic excitation. It corresponds to the design shown in Fig. 3-6, where one side of the panel is facing the diffuse sound field produced by a reverberation chamber. For simulating the excitation, the reverberation chamber is considered as an additional subsystem. Then, the SEA model turns out to be composed of three subsystems, as shown in Fig. 7-6:

- subsystem 1 for acoustic wave in the reverberation chamber;
- subsystem 2 for flexural wave of the test panel;
- subsystem 3 for acoustic wave in the Noise-Box cavity.

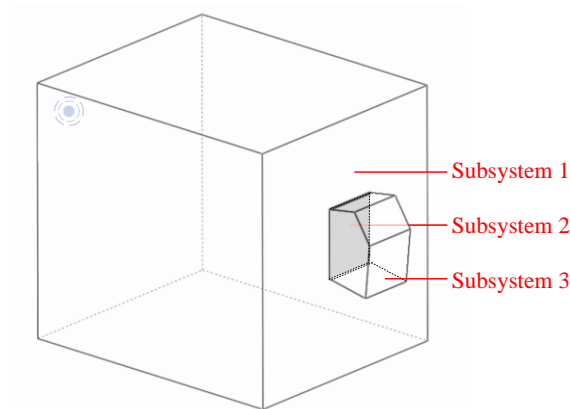


Fig. 7-6. Subsystems of the SEA model for the plate-cavity system under the acoustic excitation generated by a reverberation room.

The Noise-Box cavity and the test panel are the same as they are defined in Section 7.2. The additional subsystem 1 in this case is a rectangular cavity with the three dimensions given by  $3.7 \text{ m} \times 4.05 \text{ m} \times 3.35 \text{ m}$ . Air properties and damping loss factor are considered identical to the Noise-Box cavity. The excitation is a monopole source at a corner of the reverberation room with unit power input, i.e.,  $P_1 = 1 \text{ W}$ . Then, according to the equations provided in Section 7.2.1, the SEA parameters  $n_1(\omega)$ ,  $n_2(\omega)$ ,  $n_3(\omega)$ ,  $\eta_{1d}$ ,  $\eta_{2d}$ ,  $\eta_{3d}$ ,  $\eta_{12}$ ,  $\eta_{21}$ ,  $\eta_{23}$  and  $\eta_{32}$  are available. Regarding the estimation of the panel's radiation efficiency  $\sigma$ , the

Leppington's formulation is used. With respect to  $\eta_{13}$  and  $\eta_{31}$ , they are the coupling loss factors between two cavities and can be related to the transmission coefficients  $\tau_{13}$  and  $\tau_{31}$ . For instance, the relationship between  $\eta_{13}$  and  $\tau_{13}$  is given by

$$\eta_{13} = \frac{cS_p\tau_{13}}{4\omega V_1}. \quad (7.18)$$

In Eq. (7.18), the transmission coefficient  $\tau_{13}$  denotes the acoustic transmission through the non-resonant transmission path, which can be evaluated by the *mass law* [16]:

$$\tau_{13} = \left( \frac{2\rho_0 c}{2\pi f \rho h} \right)^2. \quad (7.19)$$

Once  $\eta_{13}$  is obtained,  $\eta_{31}$  is available according to the reciprocity relationship  $n_1\eta_{13} = n_3\eta_{31}$ .

Finally, the SEA model of this cavity-plate-cavity system is ready for solution:

$$\begin{Bmatrix} P_1 \\ 0 \\ 0 \end{Bmatrix} = \omega \begin{bmatrix} n_1\eta_1 & -n_1\eta_{12} & -n_1\eta_{13} \\ -n_2\eta_{21} & n_2\eta_2 & -n_2\eta_{23} \\ -n_3\eta_{31} & -n_3\eta_{32} & n_3\eta_3 \end{bmatrix} \begin{Bmatrix} E_1/n_1 \\ E_2/n_2 \\ E_3/n_3 \end{Bmatrix}, \quad (7.20)$$

with  $\eta_i = \eta_{id} + \eta_{ij} + \eta_{ik}$  ( $i, j, k = 1, 2, 3$  and  $i \neq j \neq k$ ).

Implemented in MATLAB, the above evaluations and solution yields the energies  $E_1$ ,  $E_2$  and  $E_3$  of the three subsystems. Fig. 7-7 shows their values, compared with the corresponding results obtained in SEALab. Some disagreement is seen between the two sets of results, especially for cavity 2 in  $f \leq f_c$ . Therefore, which one should be more accurate is checked. In Section 7.2.3, two differences have already been mentioned between the SEA model in this work (using Leppington's formulation) and the model in SEALab. But those two points alone will not cause the discrepancy in the frequency range between 630 Hz and 2500 Hz, so there should be other reasons. Then, it is found that the main cause is the evaluation of the transmission coefficient  $\tau_{13}$ . In SEALab,  $\tau_{13}$  is estimated according to EN 12354-1(2000) for  $f < f_c$ , as given by Eq. (B.11) in the footnote, and  $\tau_{13} = 0$  is applied for  $f \geq f_c$ . However,  $\tau_{13}$  is calculated by Eq. (7.19) in this work. Finally, it is concluded that using Eq. (7.19) is more accurate. In Eq. (B.11), the expression for  $f < f_c$  includes two terms: the first for the forced waves and the second for the free waves. In fact, the one for free waves has actually incorporated in the couplings between plate and cavity, i.e.,  $\eta_{12}$ ,  $\eta_{21}$ ,  $\eta_{23}$  and  $\eta_{32}$ . So, if it is considered again in  $\tau_{13}$ , which determines  $\eta_{13}$  and  $\eta_{31}$ , the power transmitted to subsystem 3 will be overestimated. Thus, as observed in Fig. 7-7, the SEALab model yields higher energy in the subsystem Cavity 2 for  $f < f_c$ . Regarding  $f \geq f_c$ , calculating  $\tau_{13}$  by Eq. (7.19) or simply setting  $\tau_{13} = 0$  makes little difference, for the results out of Eq. (7.19) are very small. This is the reason why the two models reach good matching results in the range  $f > f_c$ . All in all, the SEA model developed in this subsection for a cavity-plate-cavity system should be correct.



Next, based on the validated energies in Fig. 7-7, the subsystem response variables are determined. The average sound pressure of the two cavities and the average velocity of the vibrating plate are presented by Fig. 7-8. At last, the transmission loss  $TL$  of the panel is evaluated using Eq. (2.41), where  $L_S$  and  $L_R$  are respectively the average SPLs of Cavity 1 and Cavity 2 in this case,  $S$  is the area of the test panel,  $A_R = \bar{\alpha} S'$  is the sound absorption of Cavity 2. The outcome is plotted in Fig. 7-9. The TL curve evaluated by the SEA model is shown in accord with the typical TL curve shown in Fig. 2-7. In this case, the first structural resonance of the panel is lower than 100 Hz and the coincidence region is around 3150 Hz.

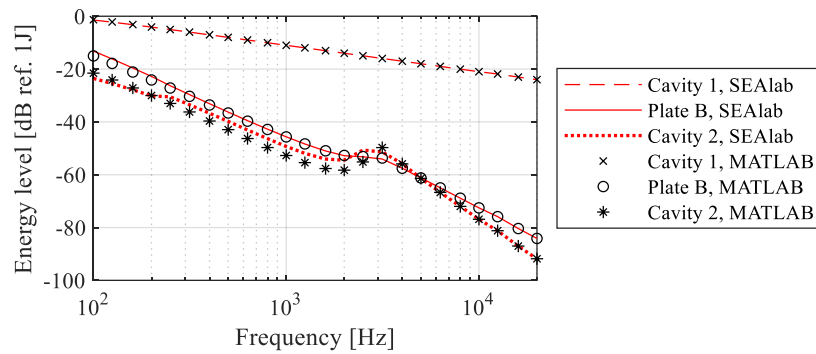


Fig. 7-7. Subsystem energies of the SEA models for the Noise-Box under acoustic excitation.

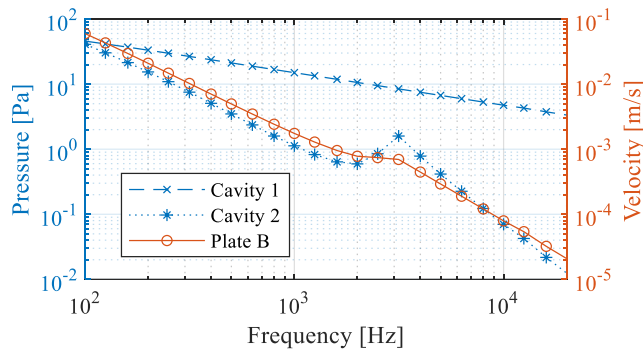


Fig. 7-8. Average response variables of the subsystems in the SEA model built in MATLAB for the Noise-Box under acoustic excitation.

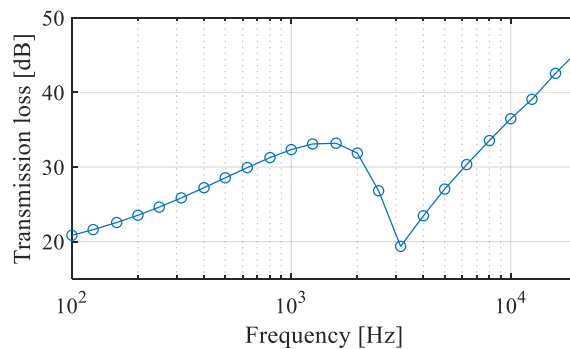


Fig. 7-9. Sound transmission loss of the test panel predicted from the SEA model built in MATLAB for the Noise-Box under acoustic excitation.

## 7.4 Summary

This chapter uses the SEA method to investigate the structure-borne and airborne noise of the plate-cavity coupled Noise-Box. The structure-borne noise problem considers an external point force acting on the plate; and the airborne noise problem analyses the sound transmission loss of the plate when the plate is excited by an exterior acoustic field. With the self-programmed codes implemented in MATLAB, SEA solutions of the two problems are respectively obtained. For validating the applied approach and codes, an open source software called ‘SEAlab’ is used to analyse the same problems for comparing the results. Finally, the response variables of the plate-cavity system are evaluated from the validated solutions. Results are provided for a wide frequency ranges from 100 Hz to 20 kHz at 1/3 octave bands, but the effective frequency range may be better limited to the frequencies higher than 1000 Hz or 1250 Hz, as a proposal after checking the modal overlap and number of modes in band. Note that the MATLAB codes for the SEA models introduced in this chapter are available in the database <sup>[213]</sup>.

The SEA tools for the two problems are developed following the general procedures: (1) defining subsystems; (2) formulating SEA equations; (3) evaluating SEA parameters; (4) solving for subsystem energies and then evaluating the response variables. In the first scenario, two subsystems are defined, respectively for the mounted panel and the Noise-Box cavity. When evaluating SEA parameters, it is found that the radiation efficiency  $\sigma$  of the panel is decisive for the coupling loss factors. As there are two popularly-used formulations in literatures for  $\sigma$ , two models are built. Model 1 uses the formulation from ISO12354-1, while Model 2 employs the formulation from Leppington. It is thought both models are applicable, when Model 1 better matches with the software ‘SEAlab’ for using the same  $\sigma$ . In the second scenario, three subsystems are defined, where the additional subsystem is a large cavity to simulate a reverberation room for the diffuse sound field excitation. Apart from  $\sigma$ , which determines the coupling loss factors panel and cavity, the transmission between two cavities should be considered. The developed SEA tool takes it as acoustic transmission through the non-resonant transmission path and evaluates it by mass law, which is different from the software ‘SEAlab’ but is found more accurate.

## Chapter 8 Structure-borne and airborne interior noise investigation

*This chapter investigates the structure-borne and airborne interior noise of the plate-cavity coupled Noise-Box through experiments and numerical simulations. The structure-borne interior noise is analysed for the case when a point force is acting on the plate, and the required results are the average SPLs of the Noise-Box cavity in 1/3 octave bands. The experimental results and the numerical outcomes from FEM, WBM and SEA are processed to the required ones for comparison. The airborne noise investigation focuses on the sound TL of the mounted plate. Different methods to obtain the TL are introduced and employed, including a non-standardized TL measurement, four analytical predictions through different approximate formulas and two numerical simulations respectively via FEM and SEA. Finally, the TL curves from different methods are compared and discussed.*

### 8.1 Structure-borne noise investigation

This section investigates the noise inside the Noise-Box cavity, originated from the structural vibration. The investigation involves experimental and numerical parts. In the experiment, the plate vibration is excited by a point force (or more exactly, an impulse), and the sound pressure inside the cavity is measured at six different positions. The numerical part uses the three numerical methods, i.e., FEM, WBM and SEA, to study the same cases that are performed through experiments. Corresponding to the different properties of these methods, the results may be presented in different ways. Both the experimental and numerical analyses are in the frequency domain and mainly focus on the frequency range below 1000 Hz. Only when the SEA model is discussed, the largest analysing frequency is raised to 1780 Hz, which is approximately the highest frequency for the reliable experimental results and the upper bound of the 1/3 octave band centred at 1600 Hz.

#### 8.1.1 Experimental set-up and results

The experimental set-up is identical to the characterization experiment of the coupled plate-cavity system, as introduced in Section 5.3.1.1. The microphone positions are the same as shown in Fig. 5-27, while the hitting location is not just limited to  $\mathbf{r}'_{F80}(0.485\text{m}, 0.44\text{m})$ , but changeable to another point for investigating the influence of input force location. The additional input point selected is  $\mathbf{r}'_{F18}(0.135\text{m}, 0.74\text{m})$ , where the notation 18 indicates that

it is Point 18 in the grid demonstrated by Fig. 5-12. It can be seen that this input point is next to the accelerometer A2.

After performing the hammer tests, two groups of FRFs were estimated based on the experimental data. Each group corresponds to one of the input points,  $r'_{F80}$  or  $r'_{F18}$ , and contains 6 FRFs for the 6 microphones, respectively. Using the denotation  $H_{lk} = p_{cl}/F_k$ , the obtained FRFs are  $H_{lk}$ ,  $l = 1, 2, \dots, 6$  and  $k = 80, 18$ . The FRFs illustrates the harmonic responses at a specific point of the cavity when the panel is under unit point force excitation. Since the acquisition time for each impulse is 15 sec, the frequency resolution of the spectrum is 1/15 Hz. Fig. 8-1 and Fig. 8-2 show some of the measured FRFs in the frequency range of interest (0~1000 Hz).

Fig. 8-1 compares the responses at two different microphone positions for the same input point, i.e.,  $H_{280}$  and  $H_{480}$ . The figure demonstrates that the responses inside the cavity are quite uniform around and lower than the first resonance. Then, the two curves separate as the frequency increases. Though only two FRFs are used in this comparison, the conclusions should be similarly obtained from the other FRFs in the same group. The uniformity of the acoustic fields in the frequency range around the first resonance can be further observed from the system mode shape shown in Fig. 4-17. However, in checking all the other FRFs by similar comparison, it is found that the microphone at  $r_{c1}$  behaves abnormally in the low frequency range. Since it is finally concluded as a problem raised by the instrument, the experimental data measured by this microphone is later not used as a benchmark or used for calculating the average SPL inside the cavity.

On the other hand, Fig. 8-2 compares the responses at the same microphone position but with two different input points. From the figure, it is observable that the FRF  $H_{218}$  is noisy in the low frequency range. This is highly related to the location of the input impulse. Point 18 is close to the edges of the mounted test panel, and thus very hard to excite the first several plate modes. Consequently, the response in the cavity is small. Meanwhile, it is the fact that inside the Noise-Box, the background noise is higher in the low frequency range.

The FRFs clearly inform us of the sound pressure amplitude at a specific position provided that the panel is excited by a harmonic point force. However, it is often the case that the excitation is not of a single frequency or the sound pressure is to be evaluated for a given bandwidth. In such a case, we can still use the FRFs to derive the required responses with the input informed.

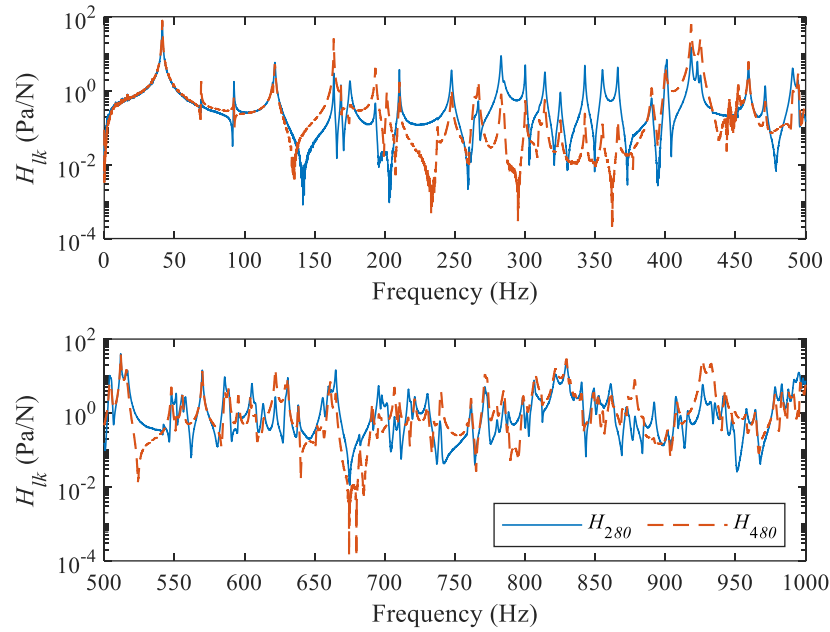


Fig. 8-1. Comparison of experimental FRFs in the plate-cavity system (for different microphone positions):  $H_{280} = p_{c2}/F_{80}$  and  $H_{480} = p_{c4}/F_{80}$ . Input and output locations are shown in Fig. 5-27.

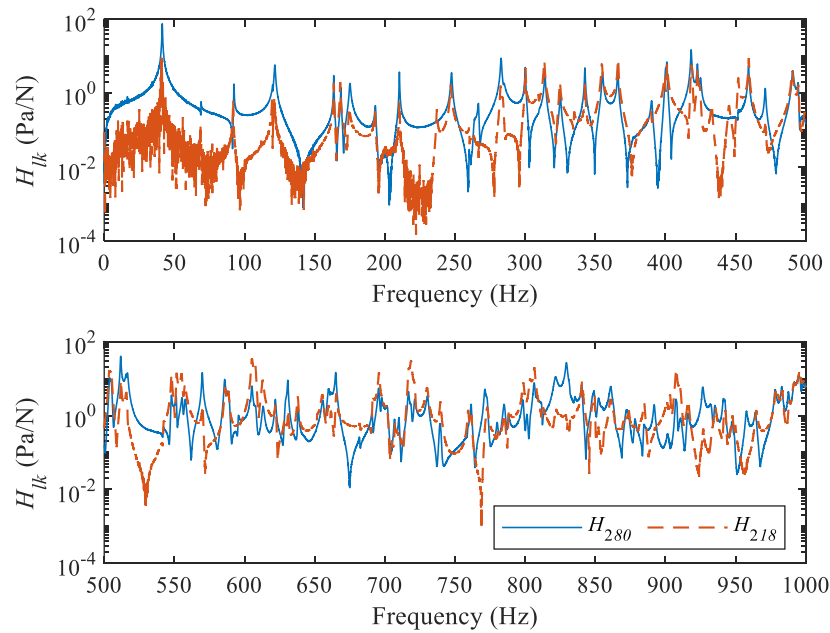


Fig. 8-2. Comparison of experimental FRFs in the plate-cavity system (for different force excitation positions):  $H_{280} = p_{c2}/F_{80}$  and  $H_{218} = p_{c2}/F_{18}$ . Output positions are shown in Fig. 5-27, and input location is  $\mathbf{r}'_{F18}(0.135\text{m}, 0.74\text{m})$ .

Now, consider the case in Section 7.2 that is used for SEA, a point force with uniform distribution in a 1/3 octave band is exciting the panel. The RMS value of the force is given by  $F_{\text{rms}} = 1$  N. Then, it is able to derive the measured SPLs in this case based on the FRFs, by calculating the power sum over the 1/3 octave band. For each discrete frequency  $f_i$  within

the 1/3 octave band of the central frequency  $f_m$  ( $f_{\text{low}} \leq f_i < f_{\text{up}}$ ,  $i = N$ , with  $f_{\text{low}}$ ,  $f_{\text{up}}$  and  $N$  respectively the lower bound, upper bound and the number of discrete frequencies), the response is given by

$$p_{\text{rms}}(f_i) = |H_{lk}(f_i)| \frac{F_{\text{rms}}}{\sqrt{N}}. \quad (8.1)$$

Then, the SPL at  $r_{cl}$  in the 1/3 octave band of  $f_m$  is calculated by

$$L_{p,l}(f_m) = 10 \lg \left( \frac{1}{p_{\text{ref}}^2} \sum_{i=1}^N [p_{\text{rms}}(f_i)]^2 \right) = 10 \lg \left( \frac{1}{N p_{\text{ref}}^2} \sum_{i=1}^N |H_{lk}(f_i)|^2 F_{\text{rms}}^2 \right), \quad (8.2)$$

where  $p_{\text{ref}} = 2 \times 10^{-5}$  Pa is the reference sound pressure. The average SPL over different microphone positions can be further calculated by

$$L_p(f_m) = 10 \lg \left[ \frac{1}{5} \sum_{l=2}^6 10^{L_{p,l}(f_m)/10} \right]. \quad (8.3)$$

Correspondingly, the standard deviation is

$$\sigma_M(f_m) = \sqrt{\sum_{l=2}^6 \frac{L_{p,l}(f_m) - L_p(f_m)}{5 - 1}}. \quad (8.4)$$

Based on the measured FRFs and Eqs. (8.1)-(8.2), the SPLs in the 1/3 octave bands at  $r_{c2}$  to  $r_{c6}$  were calculated. The results are shown in Fig. 8-3 and Fig. 8-4, respectively for point force excitation at  $r'_{F80}$  and  $r'_{F18}$ . Meanwhile, the average values and standard deviations of the SPLs over different microphone positions, which are calculated according to Eq. (8.3) and Eq. (8.4), are shown in Fig. 8-5 and Fig. 8-6.

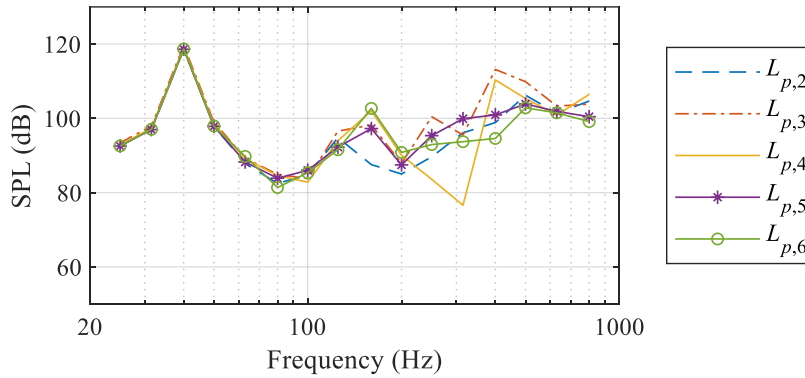


Fig. 8-3. SPLs in 1/3 octave bands at different positions inside the cavity of the plate-cavity system, when the plate is excited by force  $F_{\text{rms}} = 1$  N at  $r'_{F80}$  (see Fig. 5-27). The SPLs  $L_{p,2}$  to  $L_{p,6}$  correspond to microphones at  $r_{c2}$  to  $r_{c6}$ .

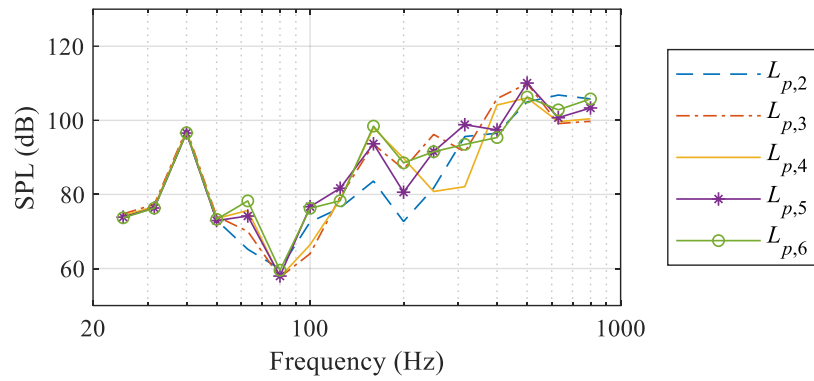


Fig. 8-4. SPLs in 1/3 octave bands at different positions inside the cavity of the plate-cavity system, when the plate is excited by force  $F_{\text{rms}} = 1$  N at  $\mathbf{r}'_{F18}(0.135\text{m}, 0.74\text{m})$  (see Fig. 5-27). The SPLs  $L_{p,2}$  to  $L_{p,6}$  correspond to microphones at  $\mathbf{r}_{c2}$  to  $\mathbf{r}_{c6}$ .

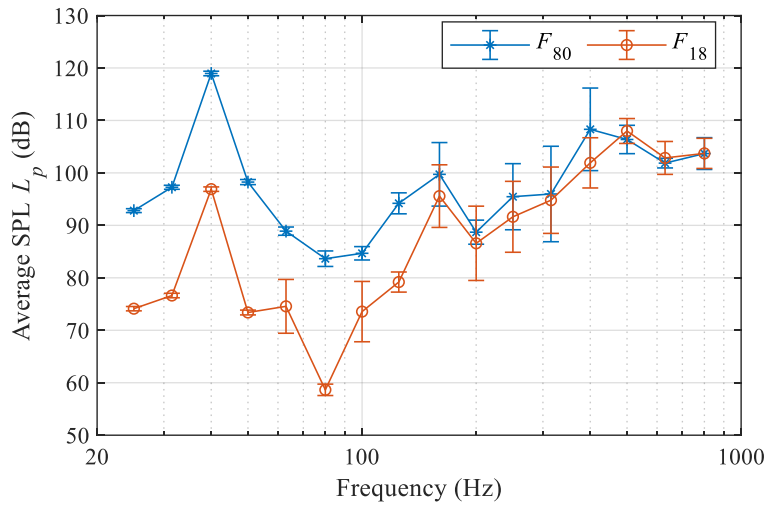


Fig. 8-5. Average SPLs of the five measuring points  $\mathbf{r}_{c2}$  to  $\mathbf{r}_{c6}$  inside the cavity (see Fig. 5-27), when the plate is excited by force  $F_{\text{rms}} = 1$  N at  $\mathbf{r}'_{F80}$  or  $\mathbf{r}'_{F18}(0.135\text{m}, 0.74\text{m})$ , with error bars representing the standard deviation  $\sigma_M$ .

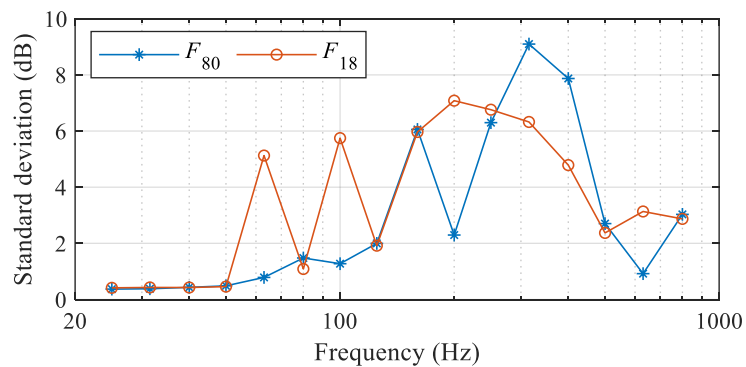


Fig. 8-6. Standard deviation of the SPLs over the five measuring points  $\mathbf{r}_{c2}$  to  $\mathbf{r}_{c6}$  inside the cavity (see Fig. 5-27), when the plate is excited by force  $F_{\text{rms}} = 1$  N at  $\mathbf{r}'_{F80}$  or  $\mathbf{r}'_{F18}(0.135\text{m}, 0.74\text{m})$ .

From Fig. 8-3 to Fig. 8-6, in addition to the variables of interest, we can also raise several viewpoints of the sound pressure field in the plate-cavity system. Firstly, it can be noticed that the acoustic field is quite uniform in the first four 1/3 octave bands (i.e.,  $f_m = 25, 31.5, 40, 50$  Hz), which are the frequency bands below the second natural frequency (see Table 5-12) of the system. Regarding the bands of 63 Hz and 100 Hz, the uniformity is highly related how well the 2<sup>nd</sup> and 3<sup>rd</sup> modes are excited. Point 80 is close to the nodal lines of these modes, thus the acoustic field is more uniform than the case of forcing Point 18. Secondly, Fig. 8-5 indicates that excitation position is decisive for the average SPL in the low frequency range, but its importance is decreasing as the frequency increases. Based on these available results, when frequency larger than 500 Hz, the difference in average SPL is less than 2 dB. As we know that the exact exciting position in a subsystem is not considered for SEA, similar analyses may be used to check the SEA assumptions. At last, considering the standard deviations with respect to the microphone positions, as shown by Fig. 8-6, they are lower than 3.2 dB when the frequency is larger than 500 Hz. As the standard deviation can indicate whether the average SPL can fully represent the response of the cavity, 3.2 dB might not low enough. Therefore, increasing the frequency or the number of microphones may be necessary.

### 8.1.2 Numerical results of FEM and WBM

The analyses in Section 8.1.1 are repeatable with the numerical models. Particularly, the FE and the WB models are available for the FRFs between two points, which are comparable with the measured FRFs of the experiment. Then, if it is necessary to obtain the response in a 1/3 octave band or for a spatial average, it is optional to apply the derivations introduced in Section 8.1.1, based on the predicted FRFs. On the other hand, the SEA model directly provides the results in 1/3 octave bands, but it is not available for a single-frequency response or the response at a specific point.

At first, the plate-cavity system is considered under harmonic point force excitation, and the structure-borne noise at a single position inside the cavity is predicted by FEM and WBM. With the same input and output positions that are fixed in the experiment, the predicted FRFs should agree with the measured FRFs. Therefore, the FRFs  $H_{lk}$ ,  $l = 2, 3, 4, 5, 6$  and  $k = 80, 18$  are evaluated using FEM and WBM, respectively, and then compared with the experimental results that are obtained in Section 8.1.1. The FE model uses the most accurate one that is mentioned in Section 6.4.3 denoted as ‘FEM 4’, which is the updated COMSOL model with a finer mesh. The WB model is the one developed in Section 6.4.3. The analyses are from 10 Hz to 1000 Hz at intervals of 1 Hz. As an example, the predicted and measured  $H_{218} = p_{c2}/F_{18}$  are shown and compared in Fig. 8-7. Note that there is already a comparison for  $H_{280}$  in Fig. 5-36. A good agreement is seen at low frequencies. The



agreement is meaningful, indicating that the numerical models can be used to predict the response at any other point inside the cavity, without repeating the experiment. Considering the example shown by Fig. 8-7, it demonstrates the possibility to reproduce the FRFs at low frequencies when the signals are polluted by noise. However, the numerical and experimental curves don't match very well in the higher frequency part. Nevertheless, Fig. 8-7 also shows that when the frequency goes higher, the modal density increases and curves are smoother, so it is possible that the bandwidth or spatial average responses may have a good agreement between prediction and measurement. This is analysed in the next case.

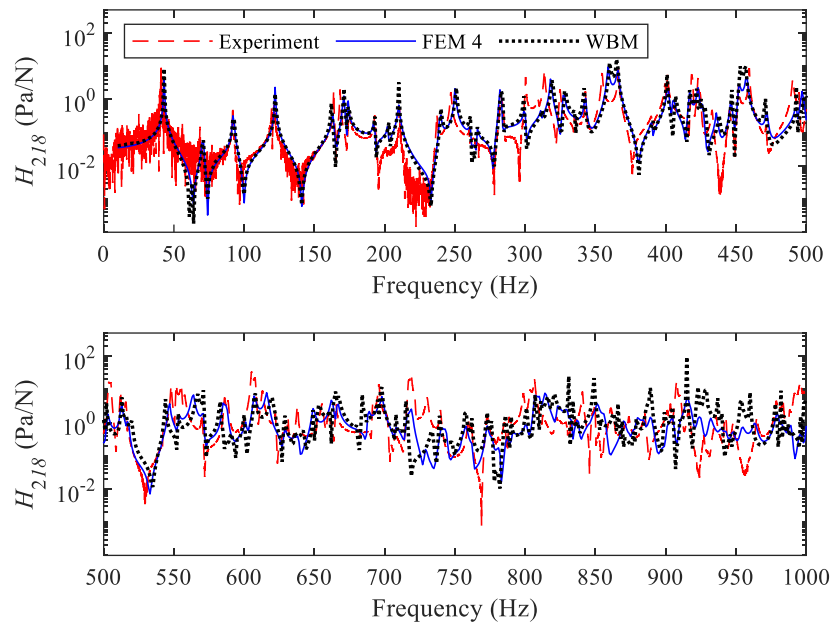


Fig. 8-7. Measured and predicted FRFs of the plate-cavity system under force excitation at Point 18:  $H_{218} = p_{c2}/F_{18}$ . The input and output are located at  $\mathbf{r}'_{F18}(0.135\text{m}, 0.74\text{m})$  and  $\mathbf{r}_{c2}(0.636\text{m}, 0.222\text{m}, 0.338\text{m})$  of Fig. 5-27. The models of FEM 4 and WBM are defined in Section 6.4.3.

Next, consider the case when a point force of  $F_{\text{rms}} = 1$  N with uniform distribution in a 1/3 octave band is exciting the panel. As numerical results, the local and average SPLs in the 1/3 octave band are estimated here based on the predicted FRFs from FEM and WBM. The calculations are expressed by Eqs. (8.1)-(8.4).

For the circumstance when the force is at  $\mathbf{r}'_{F80}(0.485\text{m}, 0.44\text{m})$ , the estimated SPLs at the measuring positions are shown in Fig. 8-8 for the FEM results and in Fig. 8-9 for the WBM results. They are comparable to the experimental results in Fig. 8-3. The average SPLs over the five positions are demonstrated in Fig. 8-10(a). Except at 40 Hz, where is next to the first resonance of the system, the WBM predictions are generally closer to the experimental results, especially for higher frequencies. The agreement shown in the band-limited SPLs (shown as Fig. 8-10) can be considered as another interpretation of the agreement in the

original FRFs (as exemplified by Fig. 8-7). However, in the high frequency range, thanks to the wider bandwidth and larger modal density and overlap, the discrepancy between numerical and experimental results is not bound to increase even though the FRF curves are not matched very well. Additionally, Fig. 8-10(b) compares the standard deviations, which indicate the spatial variations of the sound fields. The numerical model works well if both the average SPLs and their standard deviations are consistent with experimental results. In fact, deriving the band-limited spatially averaged SPLs from the numerical FRFs has its pros and cons. For example, in this case, the frequency resolution of numerical FRFs is 1 Hz, which is much less than the value 1/15 Hz in the experimental FRFs. Then, in the low-frequency bands, the derived values from numerical FRFs may not accurate enough due to the limited number of data points within range. However, it is feasible to include plenty of measurements points in the numerical model to estimate the spatial average, while in the experiment, it is hard to manage.

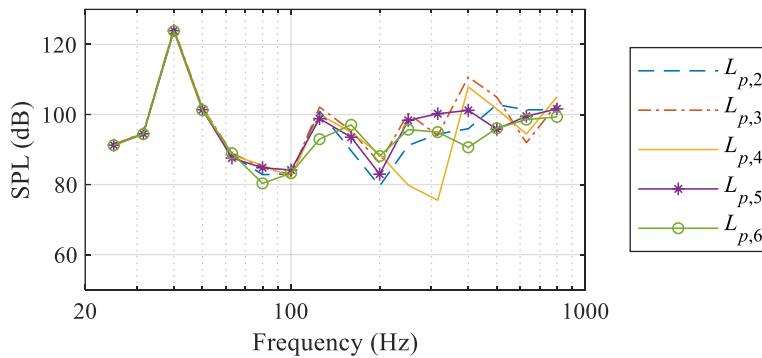


Fig. 8-8. SPLs predicted by FEM for different positions inside the cavity of the plate-cavity system, when the plate is excited by force  $F_{\text{rms}} = 1 \text{ N}$  at  $\mathbf{r}'_{F80}$  (see Fig. 5-27). The SPLs  $L_{p,2}$  to  $L_{p,6}$  correspond to microphones at  $\mathbf{r}_{c2}$  to  $\mathbf{r}_{c6}$ .

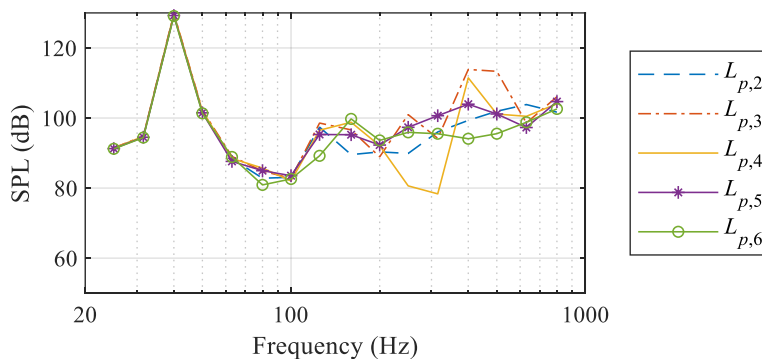


Fig. 8-9. SPLs predicted by WBM for different positions inside the cavity of the plate-cavity system, when the plate is excited by force  $F_{\text{rms}} = 1 \text{ N}$  at  $\mathbf{r}'_{F80}$  (see Fig. 5-27). The SPLs  $L_{p,2}$  to  $L_{p,6}$  correspond to microphones at  $\mathbf{r}_{c2}$  to  $\mathbf{r}_{c6}$ .

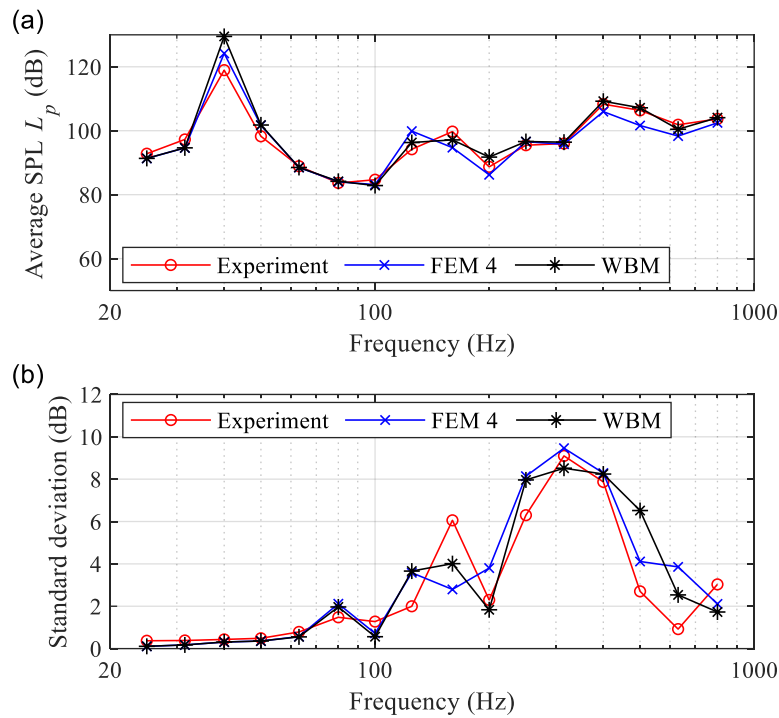


Fig. 8-10. Experimental, FEM and WBM results on (a) spatial average and (b) standard deviation of the SPLs at points  $r_{c2}$  to  $r_{c6}$  inside the cavity (see Fig. 5-27), when the plate is excited by force  $F_{rms} = 1$  N at  $r'_{F80}$ .

For the other circumstance when the force is acting at  $r'_{F18}(0.135\text{m}, 0.74\text{m})$ , the spatially averaged SPLs in every 1/3 octave band and their standard deviations are shown in Fig. 8-11. As expected, the results are different from the previous ones due to the change of exciting position. The numerical SPLs more or less follow the change caused by input force position as they are shown in the experiment (see Fig. 8-5), but the agreement between numerical and experimental results shown in Fig. 8-11 is not so good as their counterparts shown in Fig. 8-10 for the previous circumstance. The most significant differences are in four bands. For the first two bands centred at 25 Hz and 31.5 Hz, the experimental SPLs have larger values are due to the noise in the FRFs. Regarding 63 Hz and 80 Hz, the main issue is that the bound between the two bands is very close to one of the natural frequencies of the plate-cavity system. As can be indicated by Table 5-13, the resonance peak in the numerical model is 71 Hz, belonging to the band of 80 Hz, while in the experimental FRFs, it is 69 Hz, one of the frequencies in the band of 63 Hz. Consequently, at 63 Hz, the experimental SPL is larger, but at 80 Hz, the numerical SPLs are larger. Such a discrepancy is not demonstrated by Fig. 8-10, because when  $r'_{F18}$  is forced, the mode around 70 Hz is hardly excited. Therefore, for the numerical results, it is important to have an accurate prediction on the resonance frequencies in the low frequency range, and in the calculation

of band-limited SPLs, special attention should be paid to the resonances around the boundary of each band.

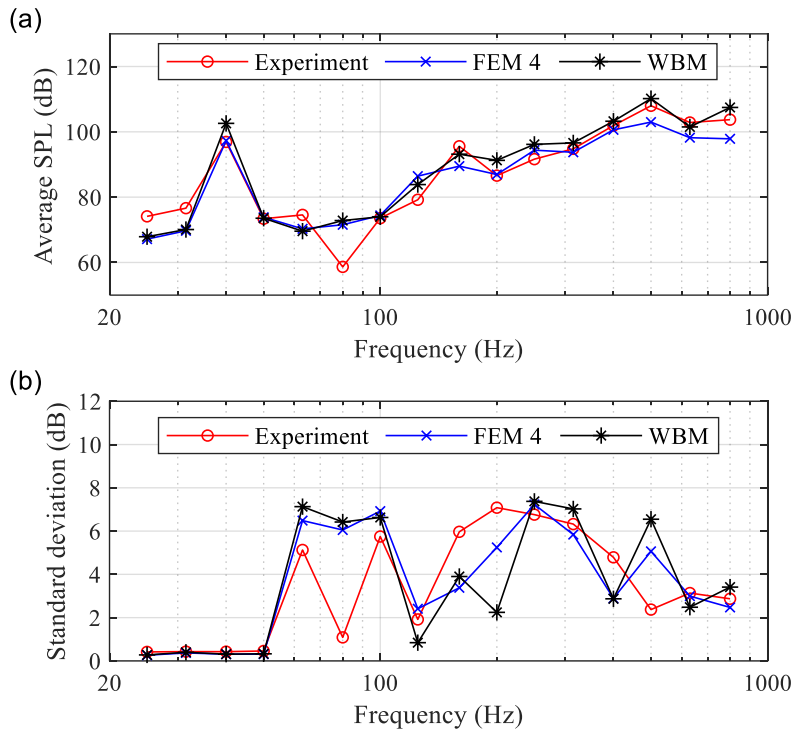


Fig. 8-11. Experimental, FEM and WBM results on (a) spatial average and (b) standard deviation of the SPLs at points  $r_{c2}$  to  $r_{c6}$  inside the cavity (see Fig. 5-27), when the plate is excited by force  $F_{\text{rms}} = 1$  N at  $r'_{F18}(0.135\text{m}, 0.74\text{m})$ .

Finally, considering the above two circumstances synthetically and laying focus on Fig. 8-10 and Fig. 8-11, we can conclude that it is applicable to use the proposed method to estimate the SPLs in a given bandwidth based on the previously updated FE and WB models. In comparison, the WBM yields the estimations that better match the experimental results than FEM in the higher frequency part of the considered region.

In addition, since it is convenient to add measuring points to the numerical model, a comparison is made based on the WB model to analysing the difference in the calculated results of the 1/3-octave-band SPLs in terms of spatial average and standard deviation, between 6 and 5 microphones. Thus, the previously omitted response at  $r_{c1}$  is evaluated. Fig. 8-12 shows the new calculated results with 6 microphones and their comparison to experimental and WBM outcomes of 5 microphones. It can be seen from the figure that adding one more microphone makes little difference on the average SPLs, but slightly reduces the standard deviations.

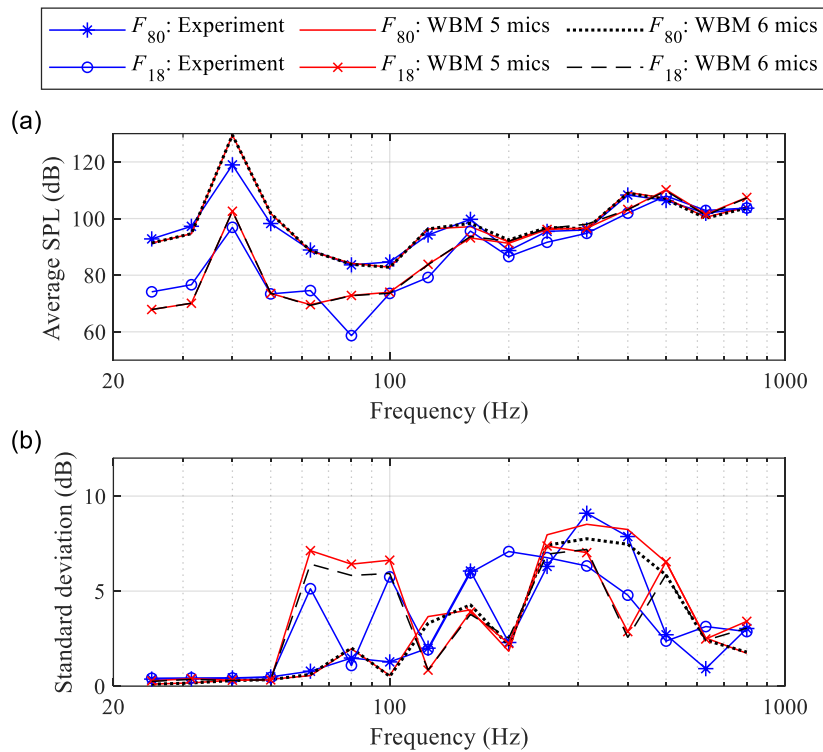


Fig. 8-12. WBM results on (a) spatial average and (b) standard deviation of the SPLs at 6 microphone positions ( $r_{c1}$  to  $r_{c6}$ , see Fig. 5-27), compared with original experimental and WBM results of 5 microphone positions ( $r_{c2}$  to  $r_{c6}$ ).

### 8.1.3 Numerical results of SEA

In this subsection, the results obtained by SEA for the same case are incorporated for comparison. The SEA model is introduced in Section 7.2 and the results of the average SPLs inside the cavity is shown in Fig. 7-8(b). The curve of ‘Leppington’ in Fig. 7-8(b) is replicated here to compare with the experimental results and the simulation results of numerical methods. Considering the uncertainty of cavity damping as mentioned in Section 7.2.1, an additional simulation is performed with the only modification of the damping loss factor from  $\eta_{2d} = 0.002$  to  $\eta_{2d} = 0.001$ . In fact, the latter is corresponding to the average absorption coefficient  $\bar{\alpha} = 0.01$  at  $f = 1000$  Hz, which is consistent with the WB model. Concerning the experimental results, the calculation in Section 8.1.1 is extended to the higher frequencies until the largest frequency can reach the upper bound of the 1600 Hz 1/3 octave band. For the numerical results mentioned in Section 8.1.2, the results out of WBM are used for comparison. Then, all these results are plotted in Fig. 8-13. As shown by the figure, the SEA results start to be consistent with experimental ones at around 630 Hz. At the frequency bands lower than 400 Hz, the SEA model significantly over-estimates the

SPLs. The figure also indicates that the damping loss factor of the cavity is better approximated by  $\eta_{2d} = 0.001$ .

Besides, through the additional experimental results at 1000 Hz, 1250 Hz and 1600 Hz 1/3 octave bands, it can be seen that they tend to be independent of the force exciting position. When comparing the standard deviations of the five SPLs  $L_{p,2}$  to  $L_{p,6}$  again, as shown in Fig. 8-14, we can find that the standard deviations further decrease as the frequency increases. At 1600 Hz, the standard deviations are about 1 dB, smaller than the 1.5 dB limit. Therefore, the sound field has a good uniformity at this 1/3 octave band.

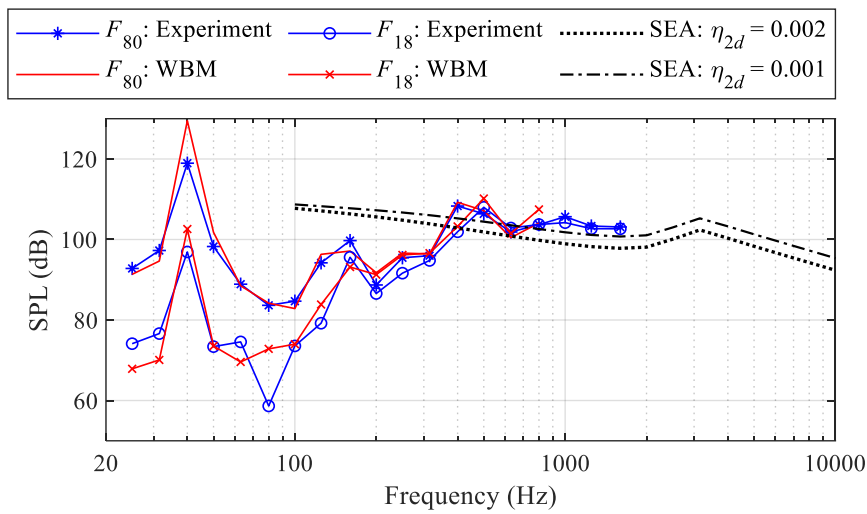


Fig. 8-13. Experimental, WBM and SEA results on the average SPLs inside the cavity of the plate-cavity system, when the plate is excited by force  $F_{\text{rms}} = 1$  N at  $\mathbf{r}'_{F80}$  or  $\mathbf{r}'_{F18}$  (0.135m, 0.74m) of Fig. 5-27.

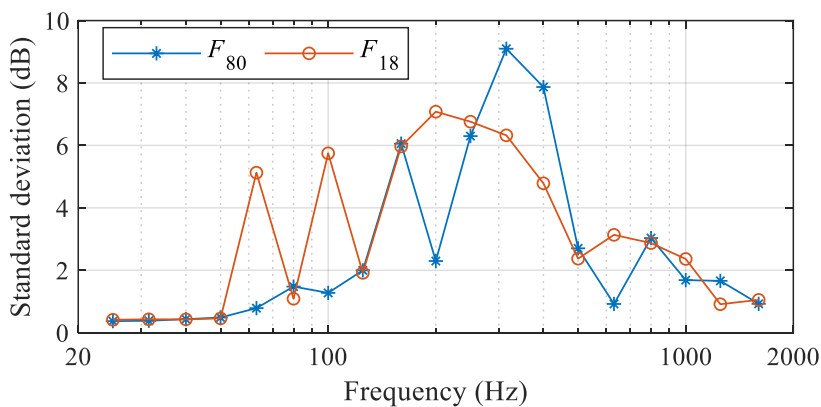


Fig. 8-14. Standard deviation of the experimental SPLs over the five microphones  $\mathbf{r}_{c2}$  to  $\mathbf{r}_{c6}$  inside the cavity (see Fig. 5-27), when the plate is excited by force  $F_{\text{rms}} = 1$  N at  $\mathbf{r}'_{F80}$  or  $\mathbf{r}'_{F18}$  (0.135m, 0.74m).

## 8.2 Airborne noise investigation

This section focuses on the airborne noise, i.e., the portion of noise inside a cabin that is originated from an exterior acoustic field. In this case, how much sound can be insulated by the partition in between is important. Therefore, in this section, using the Noise-Box, the sound transmission loss of the mounted test panel is investigated. The investigation is experiment-based and supplemented by analytical predictions and numerical simulations.

### 8.2.1 Experimental set-up

As mentioned in Section 2.5, the measurement of sound transmission loss in laboratory can be conducted using two standardized methods. The two methods are illustrated in Fig. 2-8, where the diagrams indicate that one or two reverberation rooms are necessary. Since the Noise-Box cavity can be regarded as a reverberation room, it is possible to apply the sound intensity measurement method shown by Fig. 2-8(b) without transporting the facilities and the test element to another reverberation room. Regarding this one-reverberation-room method, it is an important issue about how to accurately estimate the transmitted power  $\Pi_{tr}$ , since it is hard to avoid the reflection from the environment in the receiving side. Therefore, the best condition is an anechoic chamber, but some other space is still optional, provided that the requirements for background noise, field indicators and associated field criteria are satisfied <sup>[174]</sup>.

There are standardized procedures to measure the airborne transmission loss using sound intensity <sup>[172,174,176]</sup>. However, this section proposes an approach that is practicable in an ordinary laboratory and uses only the microphones instead of the sound intensity probes. Nevertheless, it is similar to the sound intensity measurement method. Concerning the calculation of TL based on Eq. (2.36), the input power  $\Pi_{in}$  is still informed by the SPL in the source room  $L_S$ , but the transmitted power  $\Pi_{tr}$  is evaluated according to ISO 3744 (2010) <sup>[223]</sup> instead of measuring the sound intensity nearby. Fig. 8-15 shows the overall experimental set-up. It can be considered as a detailing of Fig. 2-8(b) for a specific measurement. Noise-Box cavity serves as the reverberant source room, inside which is a loudspeaker (FaitalPRO 3FE22), 6 microphones (Brüel & Kjær Type 4188) and the thermo-hygrometer (INKBIRO IBS-TH1 Mini). The loudspeaker is placed next to a corner, used for exciting the sound field in the source room. The 6 microphones are located at the positions that depicted in Fig. 5-27, aimed at measuring the SPL in the source room. The thermo-hygrometer is recording the temperature and humidity inside the cavity during experiment. The test panel is mounted on the Noise-Box normally, by the steel clamping frame and 80 screws. The 6 accelerometers (PCB 333B30) on the test panel are at the positions shown by Fig. 5-12, which are unchanged throughout all the experiments related

to the mounted panel. In this experiment, the response of the panel is not required for the sound transmission loss, but the accelerations are still measured, in case that they will be helpful for future data processing or analysis.

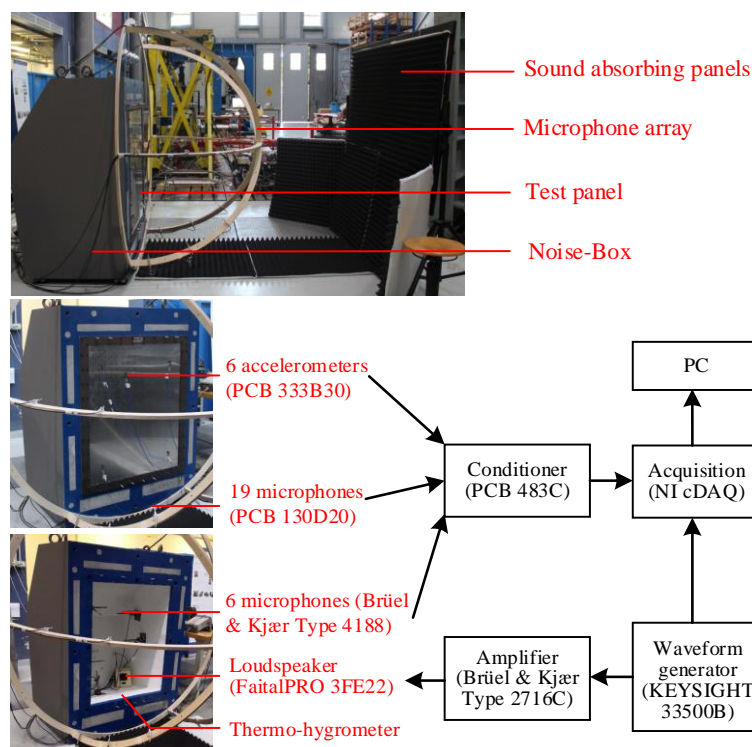


Fig. 8-15. Photograph and schematic of experimental set-up for sound transmission loss of test panel

Regarding the measurement of the sound power transmitted through the panel, a hemispherical microphone array with 19 microphones is used, as shown in Fig. 8-15, fixed by a wooden frame. Fig. 8-16 defines the positions of the microphones in the array, which is proposed in the international standard ISO 3744 (2010) <sup>[223]</sup> for determining the sound power level of a broadband noise source. Specifically, the radius of the measurement surface  $r = 1$  m, and only one microphone is placed at the coincident positions 10 and 20 (but its output will be used twice for representing different microphone). The standard allows the test environment to be a laboratory room or a flat open field, but it is important to make sure that the space is adequately isolated from the background noise and provides an acoustic free field <sup>[223]</sup>. As shown by Fig. 8-15, the experiment is performed in a large laboratory room, which may not satisfy the requirement, but sound absorbing panels are employed to minimize the reflections from surrounding objects. The pyramidal sound-absorbing panels are efficient sound absorbers made of open cell polyurethane foam, with the sound absorption coefficient  $\alpha \geq 0.4$  for 250-8000 Hz ( $\alpha \geq 1.0$  at 500 Hz). Though may be affected by the reverberant field inside, the room has an advantage of the stable meteorological conditions.



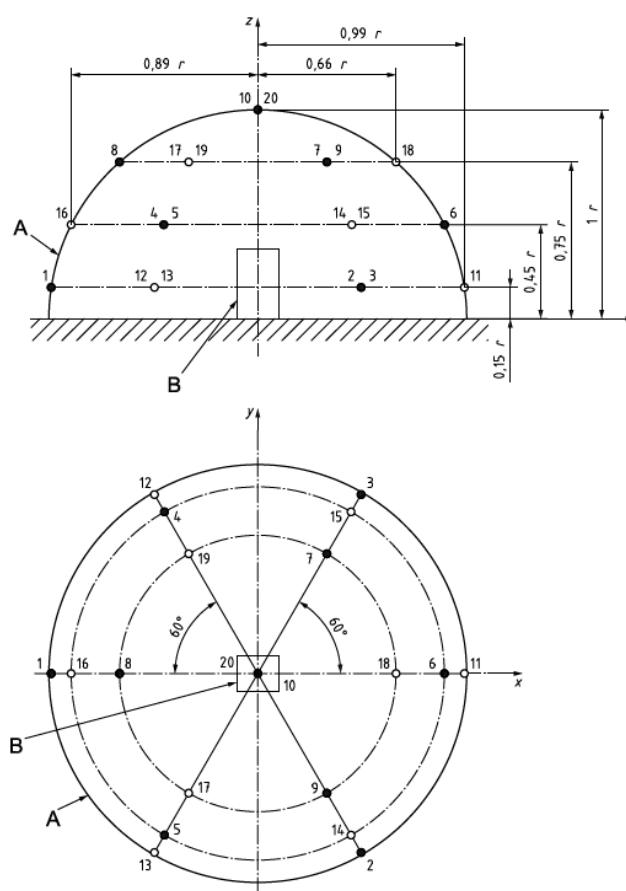


Fig. 8-16. Microphone positions on the hemispherical measurement surface<sup>[223]</sup>.

## 8.2.2 Experiment and results

During the measurement, all the instruments are connected as illustrated in Fig. 8-15. A waveform generator (KEYSIGHT 33500B) and a power amplifier (Brüel & Kjær Type 2716C) are used to provide a desired input to drive the loudspeaker. The signal generated by the waveform generator is a white noise up to 13 kHz. The data acquisition is supported by signal conditioners (PCB 483C) and acquisition modules NI 9239 in a CompactDAQ platform. Totally 32 channels are used: 6 for accelerometers, 19 for outer microphones, 6 for inner microphones and 1 for input signal generated by the waveform generator. The sampling frequency is 25 kHz. While the loudspeaker is continuously radiating noise, 20 measurements are done, and each of them lasts for 30 seconds. Afterwards, for evaluating the background noise, measurements are repeated with the loudspeaker turned off. The temperature and humidity recorded by the thermo-hygrometer are respectively 23°C and 58%RH.

Then, the experimental data are processed and the results are presented for discretized frequencies or 1/3 octave bands within 100-10000 Hz. Because one of the microphones

inside the Noise-Box cavity (which measures  $p_{c1}$  in Fig. 5-27) didn't function well in the test, the SPL in the source room  $L_S$  is calculated by the power average of the sound pressures measured by the other 5 microphones. Fig. 8-17 shows all the results related to the sound field inside the Noise-Box cavity (i.e., the source room). In the sound power spectrum (Power Spectrum Density, PSD) shown by Fig. 8-17(a), the resonances at cavity modes are clearly observed in the low frequency range. Fig. 8-17(b) shows that the SPL is larger than 90 dB in the 1/3 octave bands larger than 125 Hz. Fig. 8-17(c) indicates the standard deviation  $\sigma_M$  of the SPLs over the 5 microphone positions is less than 2 dB when the central frequency  $f_m \geq 500$  Hz and less than 1.5 dB when  $f_m \geq 1250$  Hz. This parameter is used to check the uniformity of the sound field inside the cavity. Though slightly different from the results shown in Fig. 5-7 for the uncoupled cavity, Fig. 8-17(c) agrees with Fig. 5-7 that the sound field in the source room reaches an acceptable diffuseness since 1250 Hz.

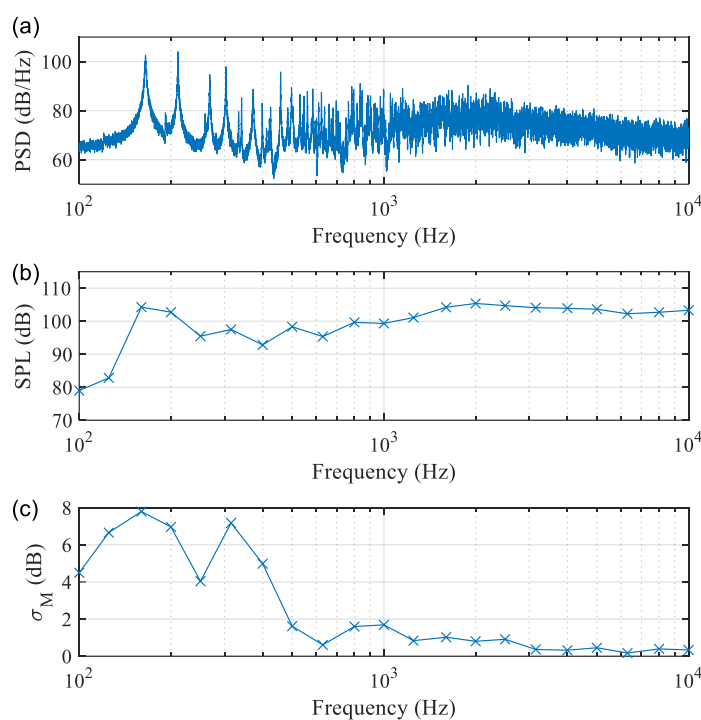


Fig. 8-17. Sound field inside the Noise-Box measured by 5 microphones: (a) averaged sound power spectrum density,  $p_{\text{ref}} = 2 \times 10^{-5}$  Pa; (b) averaged sound pressure level in 1/3 octave band; (c) standard deviation of the five SPLs in 1/3 octave band.

For the receiving side, the surface average SPLs are calculated for every frequency or each 1/3 octave band. The results are plotted in Fig. 8-18. Note that the average is over 20 microphones, as indicated by Fig. 8-16. The distribution of the SPLs over the measurement surface is also estimated, based on the signals acquired by the microphone array. The results are obtained for every 1/3 octave band, and Fig. 8-19 shows the distribution at 1000 Hz 1/3 octave band as an example.

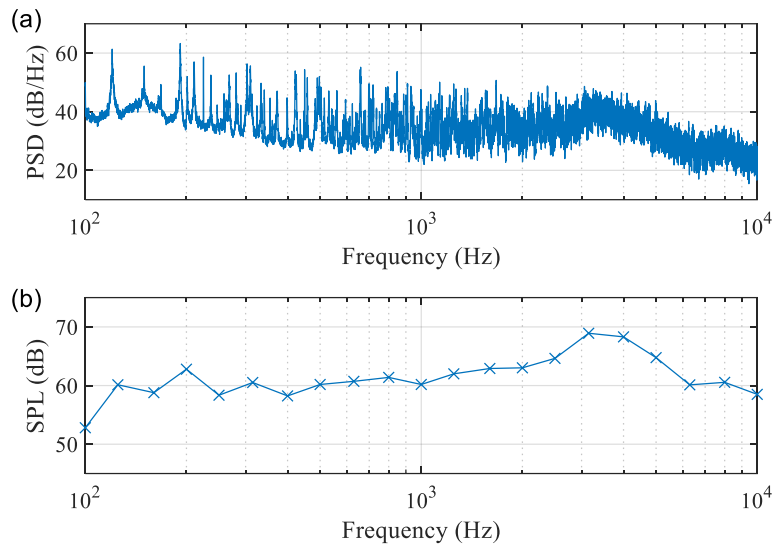


Fig. 8-18. Average SPL measured by the hemispherical microphone array ( $L'_{sm}$ ) presented in: (a) power spectrum density; (b) 1/3 octave bands.

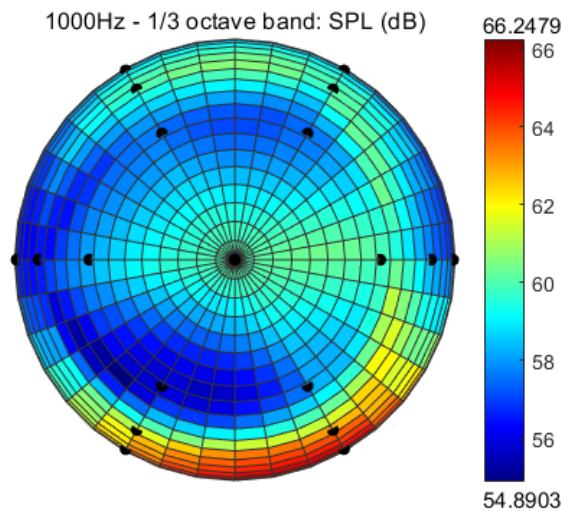


Fig. 8-19. Measured SPL distribution on the hemispherical measurement surface for the 1000 Hz 1/3 octave band.

The distribution in Fig. 8-19 indicates that the sound radiated from the plate-cavity system is directional. At 1000 Hz 1/3 octave band, the surface average shown by Fig. 8-18(b) is 60.2 dB, and Fig. 8-19 shows a distribution between 54.9 dB and 66.2 dB. The distribution can help to analyse some errors that are introduced due to the limitations of the applied approach. For example, the higher SPLs measured by the microphones close to the floor, is partially influenced by the reflection from the floor and the front surface of the Noise-Box (see Fig. 8-15), where the former is unwanted and the latter, serving as the reflecting plane, is required. In <sup>[223]</sup>, it is required that the reflecting plane shall be at least 0.5 m larger than the flat bottom of the hemisphere, but this is not the case in the experiment. Fortunately,

with the panel imbedded in the reflecting plane, the sound is mostly propagating forward. Furthermore, in checking the criteria for background noise, the surface average SPLs are compared between the conditions of noise source ‘on’ and noise source ‘off’, as shown in Fig. 8-20. A relative criterion is defined by the difference between the measured surface average SPL when the noise source is on (denoted as  $L'_{sm}$ ) and the background noise SPL when the noise source is off (denoted as  $L_{sm,B}$ ). Fig. 8-20 shows that this criterion is better satisfied as the frequency increases. The requirement of 6 dB difference starts to be satisfied at 200 Hz. Starting from 500 Hz, the difference is larger than 10 dB, and at 1250 Hz, it's already larger than 15 dB. Depending on the difference  $\Delta L_{sm} = L'_{sm} - L_{sm,B}$ , corrections for the background noise are applied<sup>[223]</sup> by  $L_{sm} = L'_{sm} - K_1$ , where the correction  $K_1 = 0$  if  $\Delta L_{sm} > 15$  dB;  $K_1 = -10\lg(1-10^{-0.1\Delta L_{sm}})$  if  $6 \text{ dB} \leq \Delta L_{sm} \leq 15$  dB; and  $K_1 = 1.3$  dB if  $\Delta L_{sm} < 6$  dB. For comparison, the corrected surface average SPL  $L_{sm}$  is also plotted in Fig. 8-20. Then, the later data processing is based on the  $L_{sm}$ , incorporated the correction for background noise.

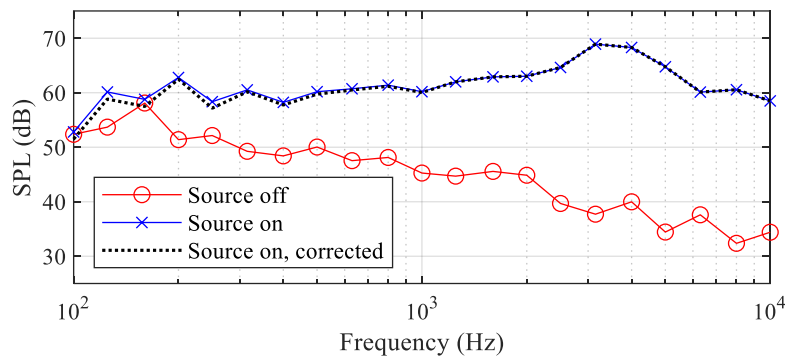


Fig. 8-20. Comparison of the surface average SPL in experiment  $L'_{sm}$  (Source on), the background noise  $L_{sm,B}$  (Source off) and the surface average SPL corrected for background noise  $L_{sm}$  (Source on, corrected). All of them are measured by the hemispherical microphone array.

Finally, the sound transmission loss is calculated based on Eq. (2.36). Supposed that the Noise-Box cavity is diffused, the incident sound power is given by

$$\Pi_{in} = \frac{1}{4} \frac{|p_c|^2}{2\rho_0 c} S, \quad (8.5)$$

where  $p_c$  is the sound pressure inside the Noise-Box cavity, and  $S$  is the area of the test element. Meanwhile, measured by the hemispherical microphone array, the transmitted sound power is expressed as

$$\Pi_{tr} = \frac{|p_m|^2}{2\rho_0 c} S_m, \quad (8.6)$$

where  $p_m$  is the sound pressure corresponding to the surface average SPL of the measurement surface (with the correction for background noise), and  $S_m$  is the area of the

measurement surface. Then, the sound transmission loss of the test element can be calculated by

$$TL = 10 \lg \frac{|p_c|^2}{|p_m|^2} - 10 \lg 4 + 10 \lg \frac{S}{S_m}. \quad (8.7)$$

This equation is very close to the expression for the intensity transmission loss, which is given in Eq. (2.42). In this case, the test panel area is  $S = ab = 0.825 \text{ m} \times 1.018 \text{ m}$ ; the hemispherical surface area is  $S_m = 2\pi r^2 = 2\pi \text{ m}^2$ ; and the first term in Eq. (8.7) can be equivalently obtained by the subtraction of the SPL in the source room  $L_S$  and the corrected surface average SPL  $L_{sm}$ . The results computed from the experimental data are plotted in Fig. 8-21. The two TL curves are respectively computed from the sound pressures in narrow bands and in 1/3 octave bands. For the frequencies lower than 500 Hz, the 1/3-octave-band TLs are not provided, since the Noise-Box cavity is highly controlled by modes and the standard deviations  $\sigma_M$  (as shown by Fig. 8-17(c)) are far over the 1.5 dB limit. Fig. 8-21 shows that the TL of the test panel is between 20-30 dB within 500 Hz and 10 kHz. However, as aforementioned, considering the sound diffuseness inside the Noise-Box cavity, the results at  $f_m \geq 1250$  Hz are more credible. Besides, it can be concluded that the coincidence region is around 3150 Hz.

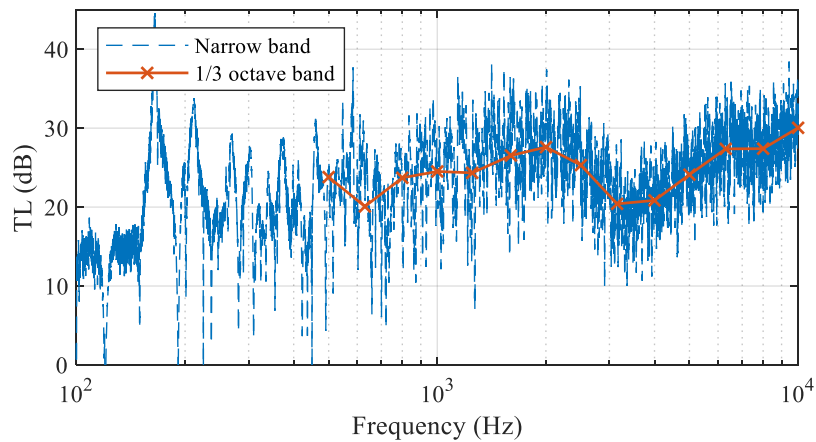


Fig. 8-21. Experimental TL curves in narrow bands and 1/3 octave bands.

### 8.2.3 Analytical predictions

Section 2.5 has mentioned about three schemes for estimating the TL analytically. Now, these schemes are applied to the test panel, and their results are compared among themselves as well as the experimental ones. Their equations for estimating TL are specified in Appendix B. Note that in the analytical models, the parameters are given by  $l_1 = 1.018$  m,  $l_2 = 0.825$  m,  $h = 3.93$  mm,  $\rho = 2680$  kg/m<sup>3</sup>,  $E = 69$  GPa,  $\nu = 0.33$ ,  $\eta = 0.003$ ,  $\rho_0 = 1.1921$  kg/m<sup>3</sup>,  $c = 344.96$  m/s and  $f_1 = 40.6$  Hz, where the Young's modulus is the one

updated in free-free conditions, the air properties correspond to the experimental temperature 23°C, and the first resonance of the panel is provided according to the panel acceleration measured in the experiment. Fig. 8-22 shows the analytical estimations, compared with the experimental results obtained in Section 8.2.2 (shown by Fig. 8-21).

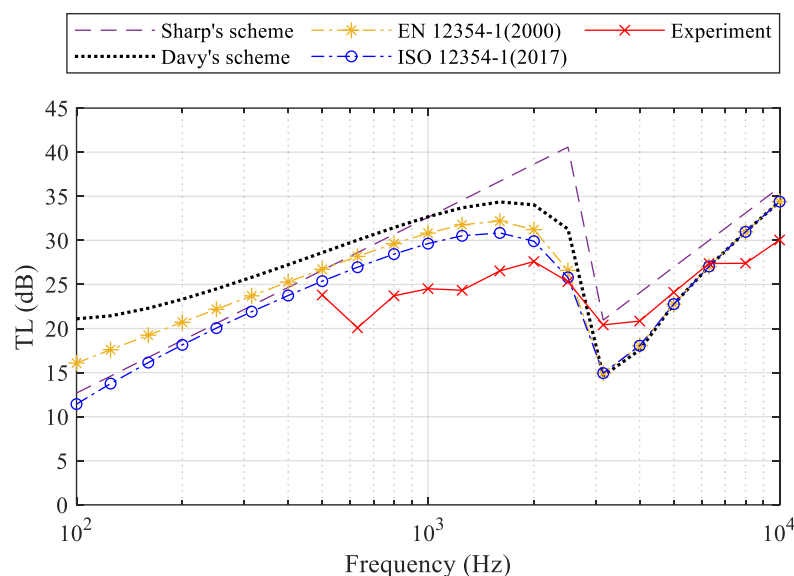


Fig. 8-22. Comparison of the analytical solutions and experimental results on sound transmission loss of the test panel.

As shown in Fig. 8-22, the experimental results are provided in 1/3 octave bands. While compared with formular predictions, the experimental results show the agreement on two points: the critical frequency  $f_c \approx 3150$  Hz and the slope from 630 Hz to 1600 Hz. As discussed in Section 5.1.5, 630 Hz is about the cut-off frequency for the modal region of the cavity. The frequency 1600 Hz is approximate to  $f_c/2$ .

However, the disagreement is also obvious. In  $500 \text{ Hz} \leq f < f_c$ , all the estimations are larger than the experimental ones. After analysing the results showed in Section 8.2.2, it is assured that the experimental results underestimate the TL of the test panel in this region. The underestimation is related to the measurement approach and set-up. As illustrated by Fig. 8-19, the transmitted sound power is over-estimated due to the sound reflected from the floor to the measurement surface. Besides, owing to the shape and size of the panel, the hemisphere with  $r = 1$  m may not sufficiently ensure most sound energy passing though the measurement surface with normal incidence. Possible leakage and flanking noise exist. All these factors lead to a higher sound power level measured by the measurement surface. Meanwhile, when the incident sound field to the panel is not guaranteed completely diffused, this factor influences both the incident sound measurement and the sound transmission. In this regard, it seems the former is more affected. Since the sound field in

the source room is considered diffused, the sound power incident to the panel is divided by 4 in Eq. (8.5) for the equability of all directions. However, as shown in Fig. 8-15, the loudspeaker is not so far away facing the test panel, so it is probable that most sound is propagating towards the panel and thus we underestimate the incident power.

On the other hand, regarding the frequency range higher than the critical frequency, i.e.,  $f > f_c \approx 3150$  Hz, the incidence can be confidently considered as a diffuse sound field (according to the conclusion of Section 5.1.5). The measurement is also less affected by the reflection from floor, since the majority of sound energy is not anymore concentrated to the area next to the floor, as exemplified by Fig. 8-23, indicating the reflected sound power is only a small portion of the overall. For the frequency range from 3150 Hz to 6300 Hz, the experimental results are between Sharp's predictions and the others. Meanwhile the slope is in accord with the Sharp's curve. The errors in this range are considered mainly from two sides. For one thing, as aforementioned, the measurement surface leads to the over-estimation of transmitted sound power in the receiving side, which will reduce the TL; for the other, two factors may make the limit angle of the field incidence  $\theta_L$  smaller, even less than  $78^\circ$ , and this will result in larger  $f_c$  larger TL at  $f = f_c$  but smaller TL in  $f > f_c$ . One factor is the small size of the source room, because of which, the loudspeaker is not far from the test panel (see Fig. 8-15). The second factor considers that the edges of the test panel are directly on the surrounding walls of the source room. Lastly, an abnormal thing is the reduction of TL at 8000 Hz. While checking all the experimental details for the reason, it was noticed that the specification of the sound absorbing materials, which are used to avoid sound reflections, indicates that the sound absorption is guaranteed only for 250-8000 Hz with  $\alpha \geq 0.4$ . Therefore, if the sound absorbing panels don't function well above 8000 Hz, it can explain why the measured TL is reduced.

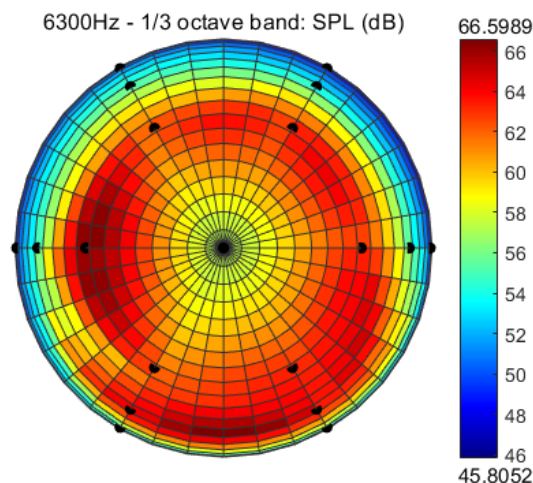


Fig. 8-23. Measured SPL distribution on the hemispherical measurement surface for the 6300 Hz 1/3 octave band.

Fig. 8-22 also compares the estimations from different prediction schemes. The Sharp's scheme was proposed earliest. In this case, its prediction of three straight lines within 100-10000 Hz. The slopes of the curve in the mass-law and damping-controlled regions are consistent with the theoretical curve shown in Fig. 2-7. In comparison, the slopes of the other three prediction, Davy's scheme, EN 12354-1(2000) and ISO 12354-1(2017), are smaller in  $f < f_c/2$ , but larger in  $f > f_c$ . For the region  $100 \text{ Hz} < f < f_c/2$ , their slopes are around 4.5 dB/octave, and the discrepancy in TLs between any two of them increases as the frequency decreases. Davy's prediction is larger than EN 12354-1(2000) and ISO 12354-1(2017). It is larger than EN 12354-1(2000) by 2~5 dB, and the latter is larger than ISO 12354-1(2017) by 1~5 dB. In the region  $f_c/2 < f < f_c$ , they have smoother transition than Sharp's. When keeping the relative relationship from  $f_c/2$  to  $f_c$ , the three curves coincide for  $f > f_c$ . The Sharp's prediction is larger than the others from  $f_c/2$  to 10000 Hz. It is claimed in <sup>[169]</sup> that the Sharp's method provides better prediction around  $f_c$ . Fig. 8-22 also shows that the result of Sharp's scheme is closest to the experimental result at 3150 Hz, which is about the critical frequency. Even so, it should be known that the results around  $f_c$  are highly related to the panel loss factor  $\eta$  or  $\eta_{\text{tot}}$ , but this parameter is often difficult to have an accurate determination.

## 8.2.4 Numerical simulations and results

The TL of the test panel is also analysed using the numerical approaches FEM and SEA, respectively. The FE model for sound transmission loss is built in COMSOL using the same techniques introduced in <sup>[224]</sup>. As shown by Fig. 8-24, for FEM, a TL measurement using sound intensity method is simulated in COMSOL. The diffuse sound field provided by reverberation room is simulated by a large number of uncorrelated plane waves in random direction, and the perfectly matched layers are to fulfil the free field condition in the receiving side. After the frequency domain analysis, the sound powers incident to the front face of the panel and transmitted out from the back face of the panel are computed. Then, the two sound powers are used to calculate the TL according to on Eq. (2.36). Material properties are the same as they are set for the analytical solutions. The analysed frequencies are from 100 Hz to 1280 Hz in 1/24 octave bands and the results are shown in Fig. 8-25. There are also the SEA results in 1/3 octave bands. The SEA model is obtained by modifying the model built via MATLAB in Section 7.3. Three subsystems are used, but the source room is switched from the large cavity to the small Noise-Box cavity to be consistent with the experiment. Since the receiving side is a large reverberation room, the SEA simulates the TL measurement by the two-room method. Besides, the material properties of the panel and cavities are also modified accordingly. Afterwards, without any other



change, the analysis can be performed and the results are plotted in Fig. 8-25 to compare with the experimental ones.

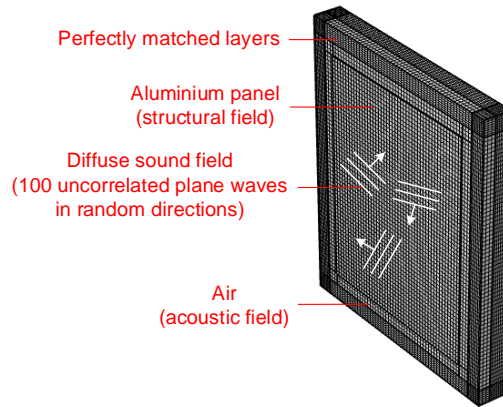


Fig. 8-24. FE model for the analysis of sound transmission loss of the test panel.

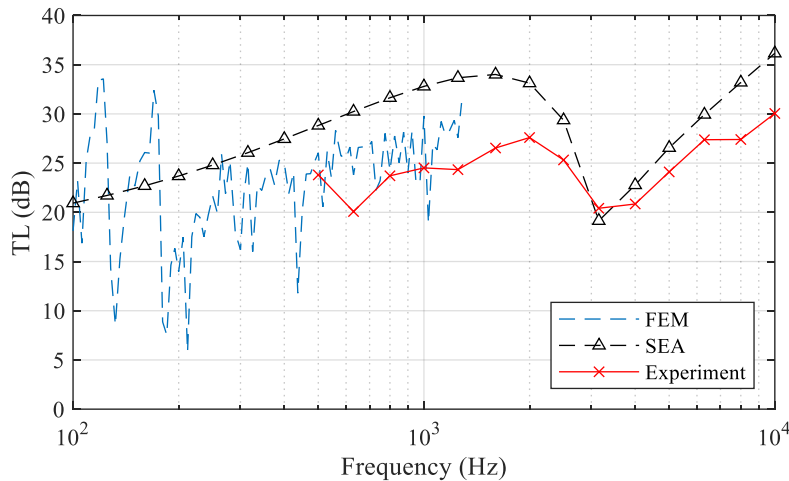


Fig. 8-25. Comparison of the numerical solutions and experimental results on sound transmission loss of the test panel.

The FEM and SEA results are shown together in Fig. 8-25, compared with experimental curves. Their relative relationship to the analytical results can be estimated by incorporating Fig. 8-22 for comparison. Firstly, the FEM results are discussed. The FEM curve is fluctuating when the frequency changes. This is a normal thing, since in FEA, the result at each frequency is obtained with a single frequency excitation. When the frequency is close to a panel resonance, the TL will be smaller than the general trend; and conversely, when it is about an anti-resonance, the TL will be larger than the nearby frequencies. The limited number of random waves and directions should be partially responsible. One way to smooth the curve is to average the results for wider bands. Nevertheless, the fluctuating range will decrease as the frequency increases, for the response is less influenced by the panel size

and boundary conditions. Within 100-200 Hz, the TL varies a lot with the frequency. In fact, this range is within the first ten modes of the panel (see Table 5-10), where the TL may be still in the resonance region or not completely enter the mass controlled region. From 500 Hz to 1250 Hz, a fitting curve to the FEM results can be expected between the SEA curve and the 'Experiment' curve. Next, concerning the SEA results, it would be better to compare them with the analytical results in Fig. 8-22. For  $f < f_c$ , the SEA results agree well with Davy's estimations, while in  $f \geq f_c$ , they better agree with the Sharp's. However, the correlations rely on the methods that have been used to determine the SEA parameters.

### 8.3 Summary

This chapter uses experimental and numerical approaches to investigate the structure-borne and airborne interior noise of the plate-cavity coupled Noise-Box. The structure-borne path considers the excitation originated from a normal force with uniform spectrum acting at a given point of the plate, and the airborne path focuses on the sound TL of test panel.

The structure-borne noise investigation covers an experiment and three numerical simulations, respectively by FEM, WBM and SEA. In the experiment, the plate was excited by hammer impulse, while the sound pressure inside the cavity was measuring with 5 microphones. The output points were fixed, and the input point changed for different groups of FRFs. The average SPLs of the cavity in 1/3 octave bands are calculated from the FRFs. Different input point yields different outcome, indicating the influence of the input location. The results show that it is less significant as the frequency increases. The spatial variation inside the cavity was also checked by the standard deviations of the local SPLs. The results indicate a better uniformity when the frequency is larger than 500 Hz. In the numerical simulations, FE and WB analyses were performed respectively for the FRFs, while SEA was conducted directly for the average SPLs. The process from numerical FRFs to average SPLs is the same as the experimental ones, thus the final results should match well with the experimental ones if it is the case for every FRF. All the experimental and numerical results are finally compared in a single figure. While the experiment, FEM and WBM results are not available for high frequencies and SEA results are not accurate at low frequencies, they reach an agreement in the range between 500 Hz and 1600 Hz.

The sound TL of the mount test panel is measured, analytically estimated and numerically computed in the airborne noise investigation. For measuring the TL, an experimental set-up was designed with reference to the guidelines for one-reverberation-room measurement. In the set-up, the Noise-Box cavity serves as the source reverberation room, and the transmitted sound power is measured by a hemispherical microphone array. The

experimental TL was obtained for the 1/3 octave bands from 500 Hz to 10 kHz, based on the SPL inside the cavity and the radiated sound power measured by the microphone array. Then, for the approximate estimation by analytical formulae, three prediction schemes were employed. They are respectively the formulations from Sharp, Davy and EN 12354-1(2000) or ISO 12354-1(2017). Unsurprisingly, the prediction results are not well agreed for all frequencies. Discrepancies at  $f < f_c$  can reach several decibels. Through the comparison between the experimental results and the analytical predictions, accompanied by the experimental error analysis, it is considered that the experimental results have underestimated the TL from 500 Hz to 2000 Hz. The main reason is attributed to the overestimated sound power in the receiving side, caused by the sound reflections. Meanwhile, the cavity resonances are shown influential at frequencies lower than 630 Hz and 1250 Hz, respectively for two levels of cavity diffuseness. In the end, the TL is analysed via FEM and SEA, respectively. At low frequencies (less than 200 Hz), the FEM results are highly fluctuating due to the resonance of the panel. For the range from 500 Hz to 1280 Hz, the TLs of FEM are concentrated in a strip about 1 to 5 dB over the experimental curves. On the other hand, the SEA results are larger than the FEM results and experimental results for most frequencies. They are close to Davy's formulation for  $f < f_c$ , and Sharp's formulation for  $f \geq f_c$ . Throughout all the results, the consistency is seen for the variation trend of TL over frequency: from 500 Hz to 1600 Hz, the TL increases by about 4.5 dB/octave; from 4 kHz to 10 kHz, the TL increases by about 9 dB/octave; and a dip presents at 3150 Hz, where should be a region of coincidence.



## Chapter 9 Conclusions and future perspectives

### 9.1 Conclusions

Nowadays, the public are paying more attention to the transport comfort and the risk of noise to their health and safety. Interior noise has becoming one of the most important issues for vehicle industry. In fact, engineers and researchers are facing a big challenge in further mitigating the interior noise of traditional vehicles and handling the different noise features in new vehicles. To overcome the difficulties, it is essential to have more investigations on the problem, where we need the test equipment and reliable CAE tools. Therefore, this dissertation designs, constructs and validates a benchmarking and testing tool *Noise-Box* for interior vibroacoustic problems. Experimental and numerical techniques (e.g., EMA, FEM, WBM and SEA) with necessary adaptations or modifications are used to characterize and investigate the plate-cavity coupled Noise-Box. Consequently, a benchmarking and testing tool for vehicle interior noise is developed and ready for application, with the following identified characteristics and validated analysis tools at hand:

- characteristics of the Noise-Box cavity, including natural frequencies and modes, reverberation time and sound absorption in different 1/3 octave bands, sound field diffuseness represented by mode count, modal density or modal overlap in different 1/3 octave bands;
- EMA for a test panel mounted on the Noise-Box. The associated techniques include the developed codes for modal parameters estimation using the single-DOF/multi-DOF local and global curve fittings, which ensure a good matching between the experimental and modal-model FRFs;
- EMA for the plate-cavity vibroacoustic system. The associated techniques involve the new codes different from the curve fittings employed in the uncoupled situation, for the modal-model polynomials of transfer functions are different;
- FEM for analysing the plate-cavity system or its components via ANSYS or COMSOL, with the knowledge about how to select the element types, determine the mesh style, model different boundary conditions, etc.;
- WBM for predicting the steady-state response of the plate-cavity system or its components in low to mid frequency ranges efficiently. This technique is implemented in MATLAB by the self-developed codes, whose accuracy and efficiency are validated;
- SEA for studying the plate-cavity system under force or acoustic excitation. This technique is implemented in MATLAB by validated self-developed codes;

- techniques for measuring sound TL of panels using the Noise-Box, and for predicting the sound TL using analytical approximations, FEM or SEA.

Throughout the design, the characterization and the investigations of the Noise-Box system in this work, we can draw the conclusions from the following four aspects:

(1) Characteristics of the Noise-Box test bench

- The Noise-Box test bench is finally built up as an approximately pentagonal prism with six rigid concrete walls and one opening. With two sidewalls parallel, it is able to use a 2D model to analyse the cavity, which has been proved in the modal analyses of the Noise-Box cavity. Except for them, all the other walls are unparallel, for the utmost diffuseness inside. Besides, the only opening side is ready for the mounting of a test panel by elastic or rigid supports, forming a panel-cavity coupled system for investigations. Such a simple system was designed for benchmark purpose and for its potential to be used to develop a variety of noise mitigation measures.
- The concrete walls of the Noise-Box are no less than 200 mm in thickness, enclosing a small of 0.596 m<sup>3</sup>. The entire facility occupies around 2 m<sup>3</sup> and weighs about 2.5 tons. It can be moved with eyebolts and mounted to the window of a standard reverberation chamber.
- The natural frequencies and modes of the Noise-Box cavity has been characterized through experiment and FEA, where the two sets of results match very well. The first five non-zero natural frequencies are 163 Hz, 209 Hz, 259 Hz, 266 Hz and 300 Hz at the room temperature 24°C.
- The 1/3-octave-band reverberation times in 160 - 6300 Hz (obtained by T20 measurement) are within 0.7 - 3.71 sec. Correspondingly, the average sound absorption coefficients are between 0.006 and 0.032, which are small and meet the requirement of a reverberation room.
- The quantifiers of sound field diffuseness indicate that the low-frequency modal region should be cut off at about 650 Hz, while the fully diffuse sound field is available at higher than 2500 Hz. In the middle is a transition for the diffuse level, where a division can also add at around 1000~1250 Hz.
- When a flexible panel is mounted onto the Noise-Box, the vibroacoustic coupling effects can be investigated. In the presented case when mounted on it the thin aluminium panel with the first resonance at around 40 Hz, the cavity is seen not so strongly influencing the vibration of the panel except that the cavity is resonant. The cavity has a stiffening effect on the panel's first resonance, but has a small mass effect on the others. Besides, the coupled natural frequencies are very close to either

the structural ones or the acoustic ones. Therefore, it is a weak coupling between the panel and the cavity.

(2) Mathematical models of the plate-cavity system

- The thin aluminium panel considered in this work can be modelled as a Kirchhoff plate or a Mindlin plate with little difference in final results, due to its small thickness-to-span ratio  $h/a < 1/200 \ll 1/20$ .
- The material parameters and thickness of the plate are easier to determine based on the dynamic test of the plate under free-free conditions. The parameters best matching the experimental and numerical natural frequencies yields  $\rho = 2680 \text{ kg/m}^3$ ,  $h = 3.93 \text{ mm}$ ,  $E = 69 \text{ GPa}$  and  $\nu = 0.33$ .
- The mounted test panel is harder to have an accurate model for two reasons. Both are related to the size of the panel, which has been identified as  $0.825 \text{ m} \times 1.018 \text{ m} \times 3.93 \text{ mm}$ . This size indicates an extremely small thickness-to-span ratio  $h/a < 1/200 < 1/100$ . In this case, the membrane forces may not be negligible, for their effects on the plate bending vibration. Theoretically, the membrane forces are zero if no tensions are normal to the plate edges, but in the experiment, it is hard to know the initial tensions raised by installation and they will also be dependent on the temperature due to thermal expansion. This is one of the findings during the characterization of the mounted test panel, and the first hard point in modelling the test panel. Secondly, it is difficult to achieve perfectly clamped boundary conditions. This is on one hand related to the rigidity of the supports and on the other hand associated with the bending stiffness of the panel. The smaller thickness-to-span ratio may indicate harder to resist rotation along the plate edges, provided that the supports are rigid enough to fix the displacement. Consequently, the boundary conditions can be at a stage between the clamped and the simply supported.
- Despite the two modelling difficulties of the plate, the thesis finds out that introducing rotational stiffnesses on the plate edges and performing model updating for these stiffnesses and the Young's modulus can yield a plate model that matches well with the test panel. For the uncoupled case, the updated model has  $k_{\theta_x} = 5 \text{ kN/rad}$ ,  $k_{\theta_y} = 9 \text{ kN/rad}$ ,  $E = 76 \text{ GPa}$ ; and for the coupled cases,  $k_{\theta_x} = 9 \text{ kN/rad}$ ,  $k_{\theta_y} = 16 \text{ kN/rad}$  and  $E = 77 \text{ GPa}$ . In both cases, the rotation stiffness  $k_{\theta_x}$  of the shorter edges is smaller than  $k_{\theta_y}$  of the longer ones. The damping loss factor is not updated, approximated by the identified modal damping ratios in EMA, i.e.,  $\eta = 2\zeta_r \approx 0.003$ .
- The model of the cavity is only updated for the air properties and the wall impedance, respectively relying on the temperature and the average sound absorption coefficient.

### (3) Numerical methods for the plate-cavity system

- In the FEM implemented in ANSYS or COMSOL, the thumb of rule for mesh should follow the instruction, i.e., at least either 10 linear or 5 quadratic elements per wavelength.
- For elastically restrained edge conditions, they can be modelled by nodal-based spring-damper elements in ANSYS, and by edge loads in COMSOL.
- The COMSOL models and ANSYS models yield consistent results for the same problem. COMSOL is more convenient for using the default element type can yield the results with good accuracy, while ANSYS is more flexible in selecting different element types and imposing some special boundary conditions. Thus, this thesis finally uses COMSOL for the 3D problems and ANSYS for the 2D problems.
- The new weighted residual formulation proposed in the WBM for flexural vibration of plates with arbitrary edge conditions is proved effective. And this formulation still works well when the plate is coupled with an acoustic field.
- The MATLAB codes of WBM are validated. The WBM is shown more efficient than the FEM for analysing the harmonic steady-state problems. It can be used to extend the FRFs to the frequencies higher than those analysed in FEM without a huge increase of model size and computation time.
- The MATLAB codes for SEA are verified by comparing with the open source software ‘SEAlab’. The comparison reveals that the analytical formulae for the panel’s sound radiation efficiency and the non-resonant transmission coefficients in SEAlab are different from our codes. When different formulae are used, the results will be slightly different. The SEA models can be used for a wide-frequency-range prediction, but the effective frequency range should be checked with the SEA assumptions.

### (4) Experimental techniques for the plate-cavity system

- Modal parameters of the coupled system and the uncoupled components are obtained through EMA. For different analysis objects, the techniques to extract the modal parameters are different. For the uncoupled cavity, due to the lack of information in the signal transfer path, peak picking technique is used to identify the natural frequencies. For the uncoupled panel and the coupled plate-cavity system, the modal parameters are similarly estimated by least-squares besting curve fitting approach, but the fitting polynomials are different. While the typical modal model of a multi-DOF dynamic system can be applied to the FRFs between acceleration and input force, the FRFs between sound pressure and the input force need to be modelled by more general polynomial. The curve fitting approach works well, for the reconstructed FRFs have a good agreement with the measured FRFs.



- In the experimental investigation of structure-borne interior noise, the panel is excited by hammer impulse with a flat spectrum up to 1780 Hz. The data processing demonstrates how to convert the raw data to the FRFs comparable with the FEM or BEM results, and to band-limited average responses comparable with the SEA ones.
- In the experimental investigation of airborne interior noise, a measurement method implemented on the Noise-Box for sound TL of the test panel is proposed. The Noise-Box cavity serves as the source reverberation room, when the transmitted power to the receiving side is measured by a hemispherical microphone array. The experimental arrangement has some drawbacks for the reflectors in the receiving side and the inadequately diffuse field at low frequencies in the source side. Nevertheless, the variation trend of TL over frequency is in accordance with the theoretical results, and the coincidence at about 3150 Hz is accurately predicted. The results have been compared with the counterparts estimated by different approximate formulations and numerical simulations. It is deduced that the measurement underestimates the TL from 500 Hz to 2000 Hz and that the Noise-Box has the potential for being the source room for frequencies higher than 630 Hz.

Though the dissertation is sort of applying the existing methods to develop a vibroacoustic investigation system that are equipped with matched test equipment and numerical models, several innovative points can be highlighted:

- The Noise-Box for benchmarks and investigations of interior noise problems is a new tool. It will be useful and helpful for developing experimental and numerical techniques in acoustics or vibro-acoustics, and can be used for developing interior noise mitigation measures.
- An improved EMA for plate-cavity vibroacoustic systems is presented, so that the modal parameters of both plate- and cavity-controlled modes are identified with good accuracy. While the modal parameters are estimated by best curve fitting approach, the FRFs  $A_{jk} = a_j/F_k$  and the FRFs  $H_{lk} = p_{cl}/F_k$  are modelled by different polynomials. Two groups of modal parameters are obtained, respectively based on  $A_{jk}$  and  $H_{lk}$ . The final modal parameters can be determined through a comparison between the two groups, where it should be noticed that most of them are agreed.
- A modified weighted residual formulation in the WBM for plate bending problems is proposed. The formulation can be used to build the WB model of a plate under any type of edge restraints, including the prescribed restraints (i.e., clamped, simply supported, free and symmetric), the general (visco)elastic restraints with translational and rotational stiffnesses (and damping coefficients), and the partially (visco)elastic restraints with either translational or rotational stiffness (and damping), which is an extension of the classical WBM that considers only the prescribed restraints.

## 9.2 Future perspectives

This dissertation is only a start point for the Noise-Box, and there will be much future work on the device. The following raises some proposals from three perspectives.

The first perspective concerns some unsettled problems that are noticed during this research.

Problem 1: effect of in-plane forces or thermal load on the vibration behaviour of the mounted thin plate. To solve this problem needs to establish another mathematical model for the plate, included the membrane forces and thermal expansion of the material. The FEM and the WBM can be used to solve this problem, and a new corresponding experiment should be designed and performed.

Problem 2: a well-developed technique to use the Noise-Box for sound TL measurement. This requires not a little improvement on the currently used method, and there are several improving directions. For the receiving side, two options are considered. One uses the microphone array and the other utilises sound intensity probes. Under the first option, we need to avoid the unexpected reflections and improve the microphone array arrangement. The second option can follow the standard requirements defined in ASTM E2249-19 or ISO 15186. For the source side, regarding the lack of sound field diffuseness in low frequency range, we can develop some corrections through some numerical and experimental investigations. In this process, it is necessary to obtain the benchmarks from a standard TL measurement.

The second perspective regards the further investigations on several points that have been started in this work.

Point 1: extending the experimental structure-borne noise investigation to higher frequencies. In this case, the panel can be excited by a shaker. If the response of the panel is also considered, it would be a better choice to use the laser doppler velocimeter.

Point 2: changing the cavity wall impedance to see its influence and validate the related modelling in the numerical models. This can be achieved by gluing the sound absorbing panels to the concrete walls.

Point 3: changing for another test panel. There is a thinner aluminium panel prepared. The tests on this panel can reveal the effects of panel thickness on many characteristics, such as modal properties, edge conditions, damping loss factor, sound TL, sensitivity to membrane forces and thermal load, etc.

Point 4: changing the boundary conditions of the panel. This can be done in two ways. One is to remove some screws. The more screws are removed, the edges will be less firmly clamped. The other way recalls the design of the Noise-Box, where it points out that the

Noise-Box is also available for the elastic mounting. In both ways, the influence of boundary conditions can be studied.

Point 5: experimental investigation on the response of the plate-cavity system under exterior acoustic excitation. This thesis has presented this case in the SEA. It can be a validation of the numerical models, and a test for the difference between force and acoustic excitation, or between the noise reduction and the sound transmission loss.

Point 6: being benchmarks or setting benchmark cases for other numerical techniques. The discussed cases may be already able to serve as benchmarks. Other numerical methods can be used to analyse the same cases for comparison. Similarly, experimental and numerical results can be prepared for other benchmark cases.

The third perspective considers the applications of the Noise-Box.

Application 1: measuring the sound absorption of small elements. With the opening closed by a rigid and highly reflected wall, the Noise-Box can be used as a small reverberation room for the sound absorption measurement. If necessary, diffusers can be added inside.

Application 2: vibroacoustic characterization of different panel structures. The Panel structure can be optimized based on the experimental results, and the optimized structure can be tested again on the Noise-Box.

Application 3: testing active noise control logics. The active noise control reduces the interior noise by introducing secondary sound sources into the system, which is functioning with a certain logic. To know whether a new developed logic will work, it may need repeatedly test and debug, the Noise-Box can provide a platform for the test and final validation. Meanwhile, the simple and well-known features of the test bench may help to speed up the process.

Application 4: testing an active structural-acoustic control. This control technique reduces the radiated sound by applying mechanical inputs to the structure. The flexible panel mounted on the noise box can be the controlling object for testing this control technique.



## Bibliography

- [1] FAHY F. *Advanced Applications in Acoustics, Noise and Vibration*[M]. FAHY F, WALKER J, eds.. London: Spon Press, 2004. DOI:10.1201/9781315273396.
- [2] GENUIT K. *Vehicle Interior Noise - Combination of Sound, Vibration and Interactivity*[J]. *Sound and Vibration*, 2009, 43(12): 8–13.
- [3] HAMMER M S, SWINBURN T K, NEITZEL R L. *Environmental Noise Pollution in the United States: Developing an Effective Public Health Response*[J]. *Environmental Health Perspectives*, 2014, 122(2): 115–119. DOI:10.1289/ehp.1307272.
- [4] MÜNZEL T, SCHMIDT F P, STEVEN S, et al. *Environmental Noise and the Cardiovascular System*[J]. *Journal of the American College of Cardiology*, 2018, 71(6): 688–697. DOI:10.1016/j.jacc.2017.12.015.
- [5] BASNER M, BABISCH W, DAVIS A, et al. *Auditory and Non-Auditory Effects of Noise on Health*[J]. *The Lancet*, 2014, 383(9925): 1325–1332. DOI:10.1016/S0140-6736(13)61613-X.
- [6] ZEVITAS C D, SPENGLER J D, JONES B, et al. *Assessment of Noise in the Airplane Cabin Environment*[J]. *Journal of Exposure Science and Environmental Epidemiology*, 2018, 28(6): 568–578. DOI:10.1038/s41370-018-0027-z.
- [7] SOETA Y, SHIMOKURA R. *Survey of Interior Noise Characteristics in Various Types of Trains*[J]. *Applied Acoustics*, 2013, 74(10): 1160–1166. DOI:10.1016/j.apacoust.2013.04.002.
- [8] WILBY J F. *Aircraft Interior Noise*[J]. *Journal of Sound and Vibration*, 1996, 190(3): 545–564. DOI:10.1006/jsvi.1996.0078.
- [9] QATU M S. *Recent Research on Vehicle Noise and Vibration*[J]. *International Journal of Vehicle Noise and Vibration*, 2012, 8(4): 289–301. DOI:10.1504/IJNVN.2012.051536.
- [10] DOBRZYNSKI W. *Almost 40 Years of Airframe Noise Research: What Did We Achieve?*[J]. *Journal of Aircraft*, 2010, 47(2): 353–367. DOI:10.2514/1.44457.
- [11] ZHENG X, DAI W, QIU Y, et al. *Prediction and Energy Contribution Analysis of Interior Noise in a High-Speed Train Based on Modified Energy Finite Element Analysis*[J]. *Mechanical Systems and Signal Processing*, 2019, 126: 439–457. DOI:10.1016/j.ymsp.2019.02.042.
- [12] SHORTER P. *Recent Advances in Automotive Interior Noise Prediction*[C]//SAE Technical Papers. SAE International, 2008. DOI:10.4271/2008-36-0592.
- [13] BEIN T, ELLIOTT S, FERRALLI L, et al. *Integrated Solutions for Noise & Vibration Control in Vehicles*[J]. *Procedia - Social and Behavioral Sciences*, 2012, 48: 919–931. DOI:10.1016/j.sbspro.2012.06.1069.
- [14] FISCHER J, BEHRENDT M, LIESKE D, et al. *Measurement and Analysis of the Interior Noise and the Transfer Path of Acoustic Phenomena into the Driver Cabin of a Battery Electric Vehicle*[C]//INTERNOISE 2014 - 43rd International Congress on Noise Control Engineering: Improving the World Through Noise Control. .
- [15] POZAR M, COOK H E. *On Determining the Relationship between Vehicle Value and Interior Noise*[C]//SAE Technical Papers. SAE International, 1998. DOI:10.4271/980621.
- [16] HAMBRIC S A, SUNG S H, NEFSKE D J. *Engineering Vibroacoustic Analysis: Methods and Applications*[M]. HAMBRIC S A, SUNG S H, NEFSKE D J, eds.//*Engineering Vibroacoustic Analysis: Methods and Applications*. Chichester (UK): John Wiley & Sons,

- Ltd, 2016. DOI:10.1002/9781118693988.
- [17] PETYT M. Introduction to Finite Element Vibration Analysis[M]. 2 edition. Cambridge: Cambridge University Press, 2010.
- [18] KATSIKADELIS J T. The Boundary Element Method for Engineers and Scientists: Theory and Applications[M]. 2 edition. Amsterdam: Academic Press, 2016.
- [19] LYON R H, DEJONG R G. Theory and Application of Statistical Energy Analysis, Second Edition[M]. Boston: Butterworth-Heinemann, 1995.
- [20] IHLENBURG F, BABUŠKA I. Finite Element Solution of the Helmholtz Equation with High Wave Number Part I: The h-Version of the FEM[J]. Computers and Mathematics with Applications, 1995, 30(9): 9–37. DOI:10.1016/0898-1221(95)00144-N.
- [21] IHLENBURG F, BABUŠKA I. Finite Element Solution of the Helmholtz Equation with High Wave Number Part II: The h-p Version of the Fem[J]. SIAM Journal on Numerical Analysis, 1997, 34(1): 315–358. DOI:10.1137/S0036142994272337.
- [22] LE BOT A, COTONI V. Validity Diagrams of Statistical Energy Analysis[J]. Journal of Sound and Vibration, 2010, 329(2): 221–235. DOI:10.1016/j.jsv.2009.09.008.
- [23] LAFONT T, TOTARO N, BOT A Le. Review of Statistical Energy Analysis Hypotheses in Vibroacoustics[Z]. Royal Society, 2014(2014–02–08). DOI:10.1098/rspa.2013.0515.
- [24] DESMET W, PLUYMERS B, ATAK O. “MID-FREQUENCY” CAE Methodologies for Mid-Frequency Analysis in Vibration and Acoustics[M]. KU Leuven, 2012.
- [25] SHORTER P J, LANGLEY R S. Vibro-Acoustic Analysis of Complex Systems[J]. Journal of Sound and Vibration, 2005, 288(3): 669–699. DOI:10.1016/J.JSV.2005.07.010.
- [26] BERNHARD R J, HUFF J E. Structural-Acoustic Design at High Frequency Using the Energy Finite Element Method[J]. Journal of Vibration and Acoustics, 1999, 121(3): 295. DOI:10.1115/1.2893979.
- [27] DESMET W. A Wave Based Prediction Technique for Coupled Vibro-Acoustic Analysis[D]. KULeuven, division PMA, Ph.D. Thesis 98D12, 1998.
- [28] MOLARES A R, SOBREIRA-SEOANE M A. Benchmarking for Acoustic Simulation Software[C]//Proceedings - European Conference on Noise Control. . DOI:10.1121/1.2934429.
- [29] NÉJADE A. C-Valor — a Vibro-Acoustic Software Validation Tool[J]. Sound and Vibration, 2010, 44(2): 5–7.
- [30] HORNIKX M, KALTENBACHER M, MARBURG S. A Platform for Benchmark Cases in Computational Acoustics[J]. Acta Acustica United with Acustica, 2015, 101(4): 811–820. DOI:10.3813/AAA.918875.
- [31] Fourth Computational Aeroacoustics (CAA) Workshop on Benchmark Problems[EB/OL][2021–04–15]. <https://www.math.fsu.edu/CAA4/problems.html>.
- [32] Benchmark Platform on Computatinal Methods for Archtectura/Environmental Acoustics[EB/OL][2021–04–15]. <http://news-sv.aij.or.jp/kankyo/s26/AIJ-BPCA/index.html>.
- [33] European Acoustics Association: Benchmark Cases for Computational Acoustics[EB/OL][2021–04–15]. <https://eaa-bench.mec.tuwien.ac.at/main/>.
- [34] MILO D. DAHL. Fourth Computational Aeroacoustics (CAA) Workshop on Benchmark Problems[C]//Proceedings of a Conference Held at Ohio Aerospace Institute and Cosponsored by the Ohio Aerospace Institute. .
- [35] FINE1. D7.1 - Review of State of the Art for Industrial Interior Noise Predictions[R]. .
- [36] HUANG H B, HUANG X R, YANG M L, et al. Identification of Vehicle Interior Noise Sources Based on Wavelet Transform and Partial Coherence Analysis[J]. Mechanical

- Systems and Signal Processing, 2018, 109: 247–267. DOI:10.1016/j.ymsp.2018.02.045.
- [37] THOMPSON D. Vehicle Interior Noise[M]//Railway Noise and Vibration. Elsevier, 2009: 465–483. DOI:10.1016/b978-0-08-045147-3.00014-1.
- [38] HARRISON M. Interior Noise: Assessment and Control[M]//Vehicle Refinement. Elsevier, 2004: 145–233. DOI:10.1016/b978-075066129-4/50006-7.
- [39] MAO Q, PIETRZKO S. Control of Noise and Structural Vibration[M]. London: Springer, 2013. DOI:10.1007/978-1-4471-5091-6.
- [40] CHEER J. Active Control of the Acoustic Environment in an Automobile Cabin[D]. University of Southampton, 2012.
- [41] LIU Z S, LEE H P, LU C. Passive and Active Interior Noise Control of Box Structures Using the Structural Intensity Method[J]. Applied Acoustics, 2006, 67(2): 112–134. DOI:10.1016/j.apacoust.2005.04.010.
- [42] DAMMAK K, KOUBAA S, EL HAMI A, et al. Numerical Modelling of Vibro-Acoustic Problem in Presence of Uncertainty: Application to a Vehicle Cabin[J]. Applied Acoustics, 2019, 144: 113–123. DOI:10.1016/j.apacoust.2017.06.001.
- [43] GEORGIEV V B. Simplified Reduced-Scale Modelling of Vehicle Interior Noise[D]. Loughborough University, Ph.D. Thesis, 2006.
- [44] MARBURG S, BEER H J, GIER J, et al. Experimental Verification of Structural-Acoustic Modelling and Design Optimization[J]. Journal of Sound and Vibration, 2002, 252(4): 591–615. DOI:10.1006/jsvi.2001.4037.
- [45] DOWELL E H, VOSS H M. The Effect of a Cavity on Panel Vibration[J]. AIAA Journal, 1963, 1(2): 476–477. DOI:10.2514/3.1568.
- [46] LYON R H. Noise Reduction of Rectangular Enclosures with One Flexible Wall[J]. The Journal of the Acoustical Society of America, 1963, 35(11): 1791–1797. DOI:10.1121/1.1918822.
- [47] DOWELL E H, GORMAN G F, SMITH D A. Acoustoelasticity: General Theory, Acoustic Natural Modes and Forced Response to Sinusoidal Excitation, Including Comparisons with Experiment[J]. Journal of Sound and Vibration, 1977, 52(4): 519–542. DOI:10.1016/0022-460X(77)90368-6.
- [48] AL-BASSYIOUNI M, BALACHANDRAN B. Sound Transmission through a Flexible Panel into an Enclosure: Structural–Acoustics Model[J]. Journal of Sound and Vibration, 2005, 284(1–2): 467–486. DOI:10.1016/j.jsv.2004.06.040.
- [49] ZHANG H, SHI D, ZHA S, et al. Parameterization Study on the Moderately Thick Laminated Rectangular Plate-Cavity Coupling System with Uniform or Non-Uniform Boundary Conditions[J]. Composite Structures, 2018, 194: 537–554. DOI:10.1016/j.compstruct.2018.04.034.
- [50] ZHANG H, SHI D, ZHA S, et al. Vibro-Acoustic Analysis of the Thin Laminated Rectangular Plate-Cavity Coupling System[J]. Composite Structures, 2018, 189: 570–585. DOI:10.1016/j.compstruct.2018.01.099.
- [51] XIE X, ZHENG H, QU Y. A Variational Formulation for Vibro-Acoustic Analysis of a Panel Backed by an Irregularly-Bounded Cavity[J]. Journal of Sound and Vibration, 2016, 373: 147–163. DOI:10.1016/j.jsv.2016.03.003.
- [52] MI Y, ZHENG H. An Interpolation Method for Coupling Non-Conforming Patches in Isogeometric Analysis of Vibro-Acoustic Systems[J]. Computer Methods in Applied Mechanics and Engineering, 2018, 341: 551–570. DOI:10.1016/j.cma.2018.07.002.
- [53] SHI S X, JIN G Y, LIU Z G. Vibro-Acoustic Behaviors of an Elastically Restrained Double-Panel Structure with an Acoustic Cavity of Arbitrary Boundary Impedance[J]. Applied

- Acoustics, 2014, 76: 431–444. DOI:10.1016/j.apacoust.2013.09.008.
- [54] CHEN Y, JIN G, SHI S, et al. A General Analytical Method for Vibroacoustic Analysis of an Arbitrarily Restrained Rectangular Plate Backed by a Cavity With General Wall Impedance[J]. *Journal of Vibration and Acoustics*, 2014, 136(3). DOI:10.1115/1.4027136.
- [55] XIE X, YANG H, ZHENG H. A Weak Formulation for Interior Acoustic Analysis of Enclosures with Inclined Walls and Impedance Boundary[J]. *Wave Motion*, 2016. DOI:10.1016/j.wavemoti.2016.04.012.
- [56] LIU Z, FARD M, DAVY J L. Acoustic Properties of the Porous Material in a Car Cabin Model[C]//*Proceedings of the 23rd International Congress on Sound and Vibration, ICSV 2016*. .
- [57] GORMAN R, KRYLOV V. Investigation of Acoustic Properties of Vehicle Compartments Using Reduced-Scale Simplified Models[J]. *Proceedings of the Institute of Acoustics*, 2004, 26(2): 37–48.
- [58] FAHY F, GARDONIO P. *Sound and Structural Vibration: Radiation, Transmission and Response*[M]. Amsterdam: Elsevier, 2007. DOI:10.1016/B978-0-12-373633-8.X5000-5.
- [59] PRETLOVE A J. Free Vibrations of a Rectangular Panel Backed by a Closed Rectangular Cavity[J]. *Journal of Sound and Vibration*, 1965, 2(3): 197–209. DOI:10.1016/0022-460X(65)90108-2.
- [60] PRETLOVE A J. Forced Vibrations of a Rectangular Panel Backed by a Closed Rectangular Cavity[J]. *Journal of Sound and Vibration*, 1966, 3(3): 252–261. DOI:10.1016/0022-460X(66)90094-0.
- [61] GUY R W. The Steady State Transmission of Sound at Normal and Oblique Incidence through a Thin Panel Backed by a Rectangular Room—a Multi-Modal Analysis[J]. *Acta Acustica United with Acustica*, 1979, 43(5): 295–304.
- [62] PAN J, BIES D A. The Effect of Fluid–Structural Coupling on Sound Waves in an Enclosure—Theoretical Part[J]. *The Journal of the Acoustical Society of America*, 1990, 87(2): 691–707. DOI:10.1121/1.398939.
- [63] ZHANG H, SHI D, ZHA S, et al. Sound-Vibration Behaviors of the Thin Orthotropic Rectangular Fluid–Structure Coupled System Resting on Varying Elastic Winkler and Pasternak Foundations[J]. *Results in Physics*, 2018, 11: 188–200. DOI:10.1016/j.rinp.2018.09.002.
- [64] SADRI M, YOUNESIAN D. Nonlinear Free Vibration Analysis of a Plate-Cavity System[J]. *Thin-Walled Structures*, 2014, 74: 191–200. DOI:10.1016/j.tws.2013.09.023.
- [65] DU J T, LI W L, XU H A, et al. Vibro-Acoustic Analysis of a Rectangular Cavity Bounded by a Flexible Panel with Elastically Restrained Edges[J]. *The Journal of the Acoustical Society of America*, 2012, 131(4): 2799–2810. DOI:10.1121/1.3693652.
- [66] CHEN Y, JIN G, FENG Z, et al. Modeling and Vibro-Acoustic Analysis of Elastically Restrained Panel Backed by Irregular Sound Space[J]. *Journal of Sound and Vibration*, 2017, 409: 201–216. DOI:10.1016/j.jsv.2017.07.053.
- [67] NEHETE D V, MODAK S V, GUPTA K. Experimental Studies in Finite Element Model Updating of Vibro-Acoustic Cavities Using Coupled Modal Data and FRFs[J]. *Applied Acoustics*, 2019, 150: 113–123. DOI:10.1016/J.APACOUST.2019.01.029.
- [68] SEHGAL S, KUMAR H. Structural Dynamic Model Updating Techniques: A State of the Art Review[J]. *Archives of Computational Methods in Engineering*, 2016, 23(3): 515–533. DOI:10.1007/s11831-015-9150-3.
- [69] IMREGUN M, VISSER W J, EWINS D J. Finite Element Model Updating Using Frequency Response Function Data - I. Theory and Initial Investigation[J]. *Mechanical Systems and Signal Processing*, 1995, 9(2): 187–202. DOI:10.1006/mssp.1995.0015.



- [70] IMREGUN M, SANLITURK K Y, EWINS D J. Finite Element Model Updating Using Frequency Response Function Data - II. Case Study on a Medium-Size Finite Element Model[J]. *Mechanical Systems and Signal Processing*, 1995, 9(2): 203–213. DOI:10.1006/mssp.1995.0016.
- [71] LIN R M, ZHU J. Model Updating of Damped Structures Using FRF Data[J]. *Mechanical Systems and Signal Processing*, 2006, 20(8): 2200–2218. DOI:10.1016/j.ymsp.2006.05.008.
- [72] NEHETE D V., MODAK S V., GUPTA K. A Method for Vibro-Acoustic FE Model Updating of Cavities Using Frequency Response[M]//*Mechanisms and Machine Science*. Kluwer Academic Publishers, 2015: 1033–1041. DOI:10.1007/978-3-319-09918-7\_91.
- [73] NEHETE D V, MODAK S V, GUPTA K. Structural FE Model Updating of Cavity Systems Incorporating Vibro–Acoustic Coupling[J]. *Mechanical Systems and Signal Processing*, 2015, 50–51: 362–379. DOI:10.1016/j.ymsp.2014.05.028.
- [74] LIN R M, LIM M K, DU H. Improved Inverse Eigensensitivity Method for Structural Analytical Model Updating[J]. *Journal of Vibration and Acoustics, Transactions of the ASME*, 1995, 117(2): 192–198. DOI:10.1115/1.2873889.
- [75] COLLINS J D, HART G C, HASSELMAN T K, et al. Statistical Identification of Structures[J]. *AIAA Journal*, 1974, 12(2): 185–190. DOI:10.2514/3.49190.
- [76] NEHETE D V, MODAK S V, GUPTA K. Coupled Vibro-Acoustic Model Updating Using Frequency Response Functions[J]. *Mechanical Systems and Signal Processing*, 2016, 70–71: 308–319. DOI:10.1016/j.ymsp.2015.09.002.
- [77] MODAK S V. Direct Matrix Updating of Vibroacoustic Finite Element Models Using Modal Test Data[J]. *AIAA Journal*, 2014, 52(7): 1386–1392. DOI:10.2514/1.J052558.
- [78] PIRNAT M, ČEPON G, BOLTEŽAR M. Structural-Acoustic Model of a Rectangular Plate-Cavity System with an Attached Distributed Mass and Internal Sound Source: Theory and Experiment[J]. *Journal of Sound and Vibration*, 2014, 333(7): 2003–2018. DOI:10.1016/j.jsv.2013.11.044.
- [79] TANAKA N, TAKARA Y, IWAMOTO H. Eigenpairs of a Coupled Rectangular Cavity and Its Fundamental Properties[J]. *The Journal of the Acoustical Society of America*, 2012, 131(3): 1910–1921. DOI:10.1121/1.3682046.
- [80] LI W L. Vibration Analysis of Rectangular Plates with General Elastic Boundary Supports[J]. *Journal of Sound and Vibration*, 2004, 273(3): 619–635. DOI:10.1016/S0022-460X(03)00562-5.
- [81] LAURA P A A, GROSSI R O. Transverse Vibrations of Rectangular Plates with Edges Elastically Restrained against Translation and Rotation[J]. *Journal of Sound and Vibration*, 1981, 75(1): 101–107. DOI:10.1016/0022-460X(81)90237-6.
- [82] LI W L, ZHANG X, DU J, et al. An Exact Series Solution for the Transverse Vibration of Rectangular Plates with General Elastic Boundary Supports[J]. *Journal of Sound and Vibration*, 2009, 321(1–2): 254–269. DOI:10.1016/j.jsv.2008.09.035.
- [83] EFTEKHARI S A, JAFARI A A. Accurate Variational Approach for Free Vibration of Variable Thickness Thin and Thick Plates with Edges Elastically Restrained against Translation and Rotation[J]. *International Journal of Mechanical Sciences*, 2013, 68: 35–46. DOI:10.1016/j.ijmecsci.2012.12.012.
- [84] VAN OPHEM S, VAN DE WALLE A, DECKERS E, et al. Efficient Vibro-Acoustic Identification of Boundary Conditions by Low-Rank Parametric Model Order Reduction[J]. *Mechanical Systems and Signal Processing*, 2018, 111: 23–35. DOI:10.1016/j.ymsp.2018.03.057.
- [85] AVITABILE P. *Modal Testing: A Practitioner’s Guide*[M]. Chichester (UK): John Wiley

- & Sons, Ltd, 2018.
- [86] SCHWARZ B J, RICHARDSON M H. Experimental Modal Analysis[J]. *CSI Reliability Week*, 1999, 35(1).
- [87] EWINS D J. Modal Analysis and Modal Testing[M]. M.J. CROCKER, ed.//*Handbook of Noise and Vibration Control*. Hoboken: John Wiley & Sons, Inc., 2007: 565–574. DOI:10.1002/9780470209707.ch47.
- [88] VIVOLO M. Vibro-Acoustic Characterization of Lightweight Panels by Using a Small Cabin[D]. KU Leuven, Ph.D. Thesis, 2013.
- [89] ARRUDA J R F, HUALLPA B. Acoustic and Structural Experimental Modal Analysis : Similarities and Differences[R]. . DOI:10.13140/RG.2.1.2165.4162.
- [90] ACCARDO G, EL-KAFIFY M, PEETERS B, et al. Experimental Acoustic Modal Analysis of an Automotive Cabin[C]//*Conference Proceedings of the Society for Experimental Mechanics Series*. Springer New York LLC, 2015: 33–58. DOI:10.1007/978-3-319-15236-3\_4.
- [91] ACCARDO G, CHIARIOTTI P, CORNELIS B, et al. Experimental Acoustic Modal Analysis of an Automotive Cabin: Challenges and Solutions[C]//*Journal of Physics: Conference Series*. IOP Publishing, 2018: 12026. DOI:10.1088/1742-6596/1075/1/012026.
- [92] OUISSE M, FOLTÊTE E. On the Properness Condition for Modal Analysis of Non-Symmetric Second-Order Systems[J]. *Mechanical Systems and Signal Processing*, 2011, 25(2): 601–620. DOI:10.1016/j.ymssp.2010.08.017.
- [93] YAMAGUCHI T, YOSHIMURA T. Experimental Modal Analysis of Vibro-Acoustic System : Production of Proto-Acoustic Exciter and Mode Identification of Coupling System[C]//*The Proceedings of the Dynamics & Design Conference*. . DOI:10.1299/jsmedmc.2010.\_106-1\_.
- [94] WYCKAERT K, AUGUSZTINOVICZ F, SAS P. Vibro-acoustical Modal Analysis: Reciprocity, Model Symmetry, and Model Validity[J]. *The Journal of the Acoustical Society of America*, 1996, 100(5): 3172–3181. DOI:10.1121/1.417127.
- [95] MELENK J M, BABUŠKA I. The Partition of Unity Finite Element Method: Basic Theory and Applications[J]. *Computer Methods in Applied Mechanics and Engineering*, 1996, 139(1–4): 289–314. DOI:10.1016/S0045-7825(96)01087-0.
- [96] PERREY-DEBAIN E, TREVELYAN J, BETTESS P. Wave Boundary Elements: A Theoretical Overview Presenting Applications in Scattering of Short Waves[J]. *Engineering Analysis with Boundary Elements*, 2004, 28(2): 131–141. DOI:10.1016/S0955-7997(03)00127-9.
- [97] FARHAT C, HARARI I, FRANCA L P. The Discontinuous Enrichment Method[J]. *Computer Methods in Applied Mechanics and Engineering*, 2001, 190(48): 6455–6479. DOI:10.1016/S0045-7825(01)00232-8.
- [98] KITA E, KAMIYA N. Trefftz Method: An Overview[J]. *Advances in Engineering Software*, 1995, 24(1–3): 3–12. DOI:10.1016/0965-9978(95)00067-4.
- [99] CESSNAT O, DESPRES B. Application of an Ultra Weak Variational Formulation of Elliptic Pdes to the Two-Dimensional Helmholtz Problem[J]. *SIAM Journal on Numerical Analysis*, 1998, 35(1): 255–299. DOI:10.1137/S0036142995285873.
- [100] ROUCH P, LADEVÈZE P. The Variational Theory of Complex Rays: A Predictive Tool for Medium-Frequency Vibrations[J]. *Computer Methods in Applied Mechanics and Engineering*, 2003, 192(28–30): 3301–3315. DOI:10.1016/S0045-7825(03)00352-9.
- [101] DECKERS E, ATAK O, COOX L, et al. The Wave Based Method: An Overview of 15 Years of Research[J]. *Wave Motion*, 2014, 51(4): 550–565. DOI:10.1016/j.wavemoti.2013.12.003.

- [102] MAXIT L, GUYADER J L. Extension of SEA Model to Subsystems with Non-Uniform Modal Energy Distribution[J]. *Journal of Sound and Vibration*, 2003, 265(2): 337–358. DOI:10.1016/S0022-460X(02)01459-1.
- [103] MAXIT L, GUYADER J L, EGE K, et al. SmEdA Vibro-Acoustic Modeling of a Trimmed Truck Cab in the Mid-Frequency Range[C]//SAE Technical Papers. . DOI:10.4271/2018-01-1506.
- [104] GAO R, ZHANG Y, KENNEDY D. A Hybrid Boundary Element-Statistical Energy Analysis for the Mid-Frequency Vibration of Vibro-Acoustic Systems[J]. *Computers & Structures*, 2018, 203: 34–42. DOI:10.1016/j.compstruc.2018.05.007.
- [105] VERGOTE K, VAN GENECHTEN B, VANDEPITTE D, et al. On the Analysis of Vibro-Acoustic Systems in the Mid-Frequency Range Using a Hybrid Deterministic-Statistical Approach[J]. *Computers & Structures*, 2011, 89(11–12): 868–877. DOI:10.1016/j.compstruc.2011.03.002.
- [106] ZHU D, CHEN H, KONG X, et al. A Hybrid Finite Element-Energy Finite Element Method for Mid-Frequency Vibrations of Built-up Structures under Multi-Distributed Loadings[J]. *Journal of Sound and Vibration*, 2014, 333(22): 5723–5745. DOI:10.1016/j.jsv.2014.06.024.
- [107] BABUŠKA I, MELENK J M. The Partition of Unity Method[J]. *International Journal for Numerical Methods in Engineering*, 1997, 40(4): 727–758. DOI:10.1002/(SICI)1097-0207(19970228)40:4<727::AID-NME86>3.0.CO;2-N.
- [108] LUOSTARI T, HUTTUNEN T, MONK P. Improvements for the Ultra Weak Variational Formulation[J]. *International Journal for Numerical Methods in Engineering*, 2013, 94(6): 598–624. DOI:10.1002/nme.4469.
- [109] HUTTUNEN T, MONK P, COLLINO F, et al. The Ultra-Weak Variational Formulation for Elastic Wave Problems[J]. *SIAM Journal on Scientific Computing*, 2004, 25(5): 1717–1742. DOI:10.1137/S1064827503422233.
- [110] LADEVÈZE P. A New Computational Approach for Structure Vibrations in the Medium Frequency Range[J]. *Comptes Rendus de L Academie Des Sciences Serie II Fascicule B-Mecanique Physique Chimie Astronomie*, 1996, 332(12): 849–856.
- [111] LADEVÈZE P, ARNAUD L, ROUCH P, et al. The Variational Theory of Complex Rays for the Calculation of Medium-Frequency Vibrations[J]. *Engineering Computations (Swansea, Wales)*, 2001, 18(1–2): 193–214. DOI:10.1108/02644400110365879.
- [112] RIOU H, LADEVÈZE P, ROUCH P. Extension of the Variational Theory of Complex Rays to Shells for Medium-Frequency Vibrations[J]. *Journal of Sound and Vibration*, 2004, 272(1–2): 341–360. DOI:10.1016/S0022-460X(03)00775-2.
- [113] LADEVÈZE P, BLANC L, ROUCH P, et al. A Multiscale Computational Method for Medium-Frequency Vibrations of Assemblies of Heterogeneous Plates[J]. *Computers and Structures*, 2003, 81(12): 1267–1276. DOI:10.1016/S0045-7949(03)00041-5.
- [114] LI H, LADEVEZE P, RIOU H. Extended Variational Theory of Complex Rays in Heterogeneous Helmholtz Problem[J]. *Computational Mechanics*, 2017, 59(6): 909–918. DOI:10.1007/s00466-017-1385-4.
- [115] RIOU H, LADEVEZE P, SOURCIS B. The Multiscale VTCR Approach Applied to Acoustics Problems[J]. *Journal of Computational Acoustics*, 2008, 16(4): 487–505. DOI:10.1142/S0218396X08003750.
- [116] KOVALEVSKY L, RIOU H, LADEVÈZE P. On the Use of the Variational Theory of Complex Rays for the Analysis of 2-D Exterior Helmholtz Problem in an Unbounded Domain[J]. *Wave Motion*, 2013, 50(3): 428–436. DOI:10.1016/j.wavemoti.2012.10.005.
- [117] MARBURG S, NOLTE B. *Computational Acoustics of Noise Propagation in Fluids -Finite and Boundary Element Methods[M]*. Berlin: Springer-Verlag, 2008. DOI:10.1007/978-3-

- 540-77448-8.
- [118] VLAHOPOULOS N, GARZA-RIOS L O, MOLLO C. Numerical Implementation, Validation, and Marine Applications of an Energy Finite Element Formulation[J]. *Journal of Ship Research*, 1999, 43(3): 143–156. DOI:10.5957/jsr.1999.43.3.143.
- [119] WANG A, VLAHOPOULOS N, BUEHRLE R D, et al. Energy Finite Element Analysis of the NASA Aluminum Testbed Cylinder[C]//SAE Technical Papers. . DOI:10.4271/2005-01-2372.
- [120] CHEN S, WANG D, LI W, et al. Automobile Interior Noise Prediction Based on Energy Finite Element Method[C]//SAE Technical Papers. . DOI:10.4271/2011-01-0507.
- [121] ZHANG W, RAVEENDRA R. Calibration of International Space Station (ISS) Node 1 Vibro-Acoustic Model-Report 2[R/OL]. [2021–04–14]. <http://www.sti.nasa.gov>.
- [122] YAO D, ZHANG J, WANG R qian, et al. Lightweight Design and Sound Insulation Characteristic Optimisation of Railway Floating Floor Structures[J]. *Applied Acoustics*, 2019, 156: 66–77. DOI:10.1016/j.apacoust.2019.07.005.
- [123] CHEN S M, WANG D F, ZAN J M. Interior Noise Prediction of the Automobile Based on Hybrid FE-SEA Method[J]. *Mathematical Problems in Engineering*, 2011, 2011. DOI:10.1155/2011/327170.
- [124] MATTSON S G, LABYAK D, PRUETZ J, et al. Prediction of Muffler Insertion Loss by a Hybrid FE Acoustic-SEA Model[J]. *SAE International Journal of Passenger Cars - Mechanical Systems*, 2009, 2(1): 1323–1329. DOI:10.4271/2009-01-2042.
- [125] LARKO J M, COTONI V. Vibroacoustic Response of the NASA Acts Spacecraft Antenna to Launch Acoustic Excitation[C]//14th International Congress on Sound and Vibration 2007, ICSV 2007. .
- [126] CORDIOLI J A, CALÇADA M, ROCHA T, et al. Application of the Hybrid FE-SEA Method to Predict Sound Transmission Through Complex Sealing Systems[J]. *SAE International Journal of Passenger Cars - Mechanical Systems*, 2011, 4(2): 1320–1329. DOI:10.4271/2011-01-1708.
- [127] LYON R H, MAIDANIK G. Power Flow between Linearly Coupled Oscillators[J]. *Journal of the Acoustical Society of America*, 1962, 34(5): 623–639. DOI:10.1121/1.1918177.
- [128] LYON R H, EICHLER E. Random Vibration of Connected Structures[J]. *The Journal of the Acoustical Society of America*, 1964, 36(7): 1344–1354. DOI:10.1121/1.1919207.
- [129] LYON R H, SCHARTON T D. Vibrational-Energy Transmission in a Three-Element Structure[J]. *The Journal of the Acoustical Society of America*, 1965, 38(2): 253–261. DOI:10.1121/1.1909649.
- [130] FAHY F. Statistical Energy Analysis: A Critical Overview[J]. *Philosophical Transactions of the Royal Society of London. Series A: Physical and Engineering Sciences*, 1994, 346(1681): 431–447. DOI:10.1098/rsta.1994.0027.
- [131] MAIDANIK G. Response of Ribbed Panels to Reverberant Acoustic Fields[J]. *The Journal of the Acoustical Society of America*, 1962, 34(6): 809–826. DOI:10.1121/1.1918200.
- [132] PETRONE G, MELILLO G, LAUDIERO A, et al. A Statistical Energy Analysis (SEA) Model of a Fuselage Section for the Prediction of the Internal Sound Pressure Level (SPL) at Cruise Flight Conditions[J]. *Aerospace Science and Technology*, 2019, 88: 340–349. DOI:10.1016/j.ast.2019.03.032.
- [133] MARZBANRAD J, HAFEZIAN M, MOZAFFARIKHAH M. Automotive Interior Cabin Noise Analysis and Optimization Using Statistical Energy Analysis and Response Surface Methodology[J]. *International Journal of Automotive Research*, 2019, 9(1): 2887–2894. DOI:10.22068/ijae.9.1.2887.

- [134] FORSSÉN J, TOBER S, CORAKCI A C, et al. Modelling the Interior Sound Field of a Railway Vehicle Using Statistical Energy Analysis[J]. *Applied Acoustics*, 2012, 73(4): 307–311. DOI:10.1016/j.apacoust.2011.09.012.
- [135] ZHANG J, XIAO X, SHENG X, et al. SEA and Contribution Analysis for Interior Noise of a High Speed Train[J]. *Applied Acoustics*, 2016, 112: 158–170. DOI:10.1016/j.apacoust.2016.05.019.
- [136] BERGEN B. Wave Based Modelling Techniques for Unbounded Acoustic Problems[D]. KULeuven, division PMA, Ph.D. Thesis 2011D07, 2011.
- [137] VANMAELE C. Development of a Wave Based Prediction Technique for the Efficient Analysis of Low- and Mid-Frequency Structural Vibrations[D]. KULeuven, division PMA, Ph.D. Thesis 2007D11, 2007.
- [138] DECKERS E, VANDEPITTE D, DESMET W. A Wave Based Method for the Axisymmetric Dynamic Analysis of Acoustic and Poroelastic Problems[J]. *Computer Methods in Applied Mechanics and Engineering*, 2013, 257: 1–16. DOI:10.1016/J.CMA.2013.01.001.
- [139] VAN HAL B, DESMET W, VANDEPITTE D. Hybrid Finite Element - Wave-Based Method for Steady-State Interior Structural-Acoustic Problems[J]. *Computers and Structures*, 2005, 83(2–3): 167–180. DOI:10.1016/j.compstruc.2004.04.019.
- [140] VAN GENECHTEN B, VERGOTE K, VANDEPITTE D, et al. A Multi-Level Wave Based Numerical Modelling Framework for the Steady-State Dynamic Analysis of Bounded Helmholtz Problems with Multiple Inclusions[J]. *Computer Methods in Applied Mechanics and Engineering*, 2010, 199(29–32): 1881–1905. DOI:10.1016/J.CMA.2010.01.013.
- [141] VANMAELE C, VANDEPITTE D, DESMET W. An Efficient Wave Based Prediction Technique for Dynamic Plate Bending Problems with Corner Stress Singularities[J]. *Computer Methods in Applied Mechanics and Engineering*, 2009, 198(30–32): 2227–2245. DOI:10.1016/J.CMA.2009.01.015.
- [142] VERGOTE K. Dynamic Analysis of Structural Components in the Mid Frequency Range Using the Wave Based Method: Non-Determinism and Inhomogeneities[D]. KULeuven, division PMA, Ph.D. Thesis 2012D03, 2012.
- [143] DEVRIENDT H, VANDEPITTE D, DESMET W. Vibro-Acoustic Simulation of Damped Orthotropic Plates with the Wave Based Method[C]//*Proceedings of the 26th Conference on Noise and Vibration Engineering, ISMA 2014*. .
- [144] XIA X, XU Z, ZHANG Z, et al. Bending Vibration Prediction of Orthotropic Plate with Wave-Based Method[J]. *Journal of Vibroengineering*, 2017, 19(3): 1546–1556. DOI:10.21595/jve.2016.17326.
- [145] JONCKHEERE S, VANDEPITTE D, DESMET W. A Wave Based Approach for the Dynamic Bending Analysis of Kirchhoff Plates under Distributed Deterministic and Random Excitation[J]. *Computers and Structures*, 2015, 156: 42–57. DOI:10.1016/j.compstruc.2015.04.007.
- [146] KLANNER M, ELLERMANN K. Wave Based Method for the Steady-State Vibrations of Thick Plates[J]. *Journal of Sound and Vibration*, 2015, 345: 146–161. DOI:10.1016/j.jsv.2015.02.004.
- [147] CHEN Q, FEI Q, DEVRIENDT H, et al. The Dynamic Bending Analysis of Plates under Thermal Load Using an Efficient Wave-Based Method[J]. *Thin-Walled Structures*, 2019: 106421. DOI:10.1016/j.tws.2019.106421.
- [148] LIU L, CORRADI R, RIPAMONTI F, et al. Wave Based Method for Flexural Vibration of Thin Plate with General Elastically Restrained Edges[J]. *Journal of Sound and Vibration*, 2020, 483: 115468. DOI:10.1016/j.jsv.2020.115468.

- [149] WARBURTON G B, EDNEY S L. Vibrations of Rectangular Plates with Elastically Restrained Edges[J]. *Journal of Sound and Vibration*, 1984, 95(4): 537–552. DOI:10.1016/0022-460X(84)90236-0.
- [150] XIANG Y, LIEW K M, KITIPORNCHAI S. Vibration Analysis of Rectangular Mindlin Plates Resting on Elastic Edge Supports[J]. *Journal of Sound and Vibration*, 1997, 204(1): 1–16. DOI:10.1006/jsvi.1996.0922.
- [151] VAN HAL B. Automation and Performance Optimization of the Wave Based Method for Interior Structural-Acoustic Problems[D]. KULeuven, division PMA, Ph.D. Thesis 2004D10, 2004.
- [152] PLUYMERS B. Wave Based Modelling Methods for Steady-State Vibro-Acoustics[D]. KULeuven, division PMA, Ph.D. Thesis 2006D04, 2006.
- [153] DECKERS E, BERGEN B, VAN GENECHTEN B, et al. An Efficient Wave Based Method for 2D Acoustic Problems Containing Corner Singularities[J]. *Computer Methods in Applied Mechanics and Engineering*, 2012, 241–244: 286–301. DOI:10.1016/j.cma.2012.06.009.
- [154] GENECHTEN B Van, BERGEN B, VANDEPITTE D, et al. A Trefftz-Based Numerical Modelling Framework for Helmholtz Problems with Complex Multiple-Scatterer Configurations[J]. *Journal of Computational Physics*, 2010, 229(18): 6623–6643. DOI:10.1016/j.jcp.2010.05.016.
- [155] PLUYMERS B, DESMET W, VANDEPITTE D, et al. Application of an Efficient Wave-Based Prediction Technique for the Analysis of Vibro-Acoustic Radiation Problems[J]. *Journal of Computational and Applied Mathematics*, 2004, 168(1–2): 353–364. DOI:10.1016/j.cam.2003.05.020.
- [156] PLUYMERS B, DESMET W, VANDEPITTE D, et al. On the Use of a Wave Based Prediction Technique for Steady-State Structural-Acoustic Radiation Analysis[J]. *CMES - Computer Modeling in Engineering and Sciences*, 2005, 7(2): 173–183. DOI:10.3970/cmes.2005.007.173.
- [157] VENTSEL E, KRAUTHAMMER T. *Thin Plates and Shells: Theory, Analysis, and Applications*[M]. New York: Marcel Dekker, Inc., 2001.
- [158] BHASKAR K, VARADAN T K. *Plates: Theories and Applications*[M]. John Wiley & Sons, Ltd, 2014.
- [159] KLANNER M. Wave Based Method for Structural Vibrations of Thick Plates[D]. University of Technology Graz, Ph.D. Thesis, 2018.
- [160] CHANDRASHEKHARA K. *Theory of Plates*[M]. Hyderabad: Universities Press, 2001.
- [161] RAO S S. *Vibration of Continuous Systems*[M]//*Vibration of Continuous Systems*. 2 edition. Hoboken: John Wiley & Sons, Inc., 2019. DOI:10.1002/9781119424284.
- [162] SZILARD R. *Theories and Applications of Plate Analysis*[M]//*Theories and Applications of Plate Analysis*. Hoboken, NJ, USA: John Wiley & Sons, Inc., 2004. DOI:10.1002/9780470172872.
- [163] CREMER L, HECKL M, PETERSSON B A T. *Structure-Borne Sound: Structural Vibrations and Sound Radiation at Audio Frequencies*[M]. 3 edition. Berlin: Springer, 2005. DOI:10.1007/b137728.
- [164] MINDLIN R D. *Introduction To The Mathematical Theory Of Vibrations Of Elastic Plates*[M]. YANG J, ed.. Singapore, SINGAPORE: World Scientific Publishing Company, 2006.
- [165] ZHENG X, YAO Z. Some Applications of the Trefftz Method in Linear Elliptic Boundary-Value Problems[J]. *Advances in Engineering Software*, 1995, 24(1–3): 133–145. DOI:10.1016/0965-9978(95)00065-8.

- [166] KINSLER L, FREY A, COPPENS A, et al. *Fundamentals of Acoustics*[M]. 4 edition. New York: John Wiley & Sons, Inc., 1999.
- [167] CROCKER M J, KESSLER F M. *Noise and Noise Control: Volume 2*[M]. Boca Raton: Crc Press, 2018.
- [168] LONG M. *Architectural Acoustics*[M]. 2nd edition. Amsterdam: Academic Press, 2014.
- [169] BIES D A, HANSEN C H, HOWARD C Q. *Engineering Noise Control*[M]. 5th edition. Boca Raton: CRC Press, 2017.
- [170] NORTON M P, KARCZUB D G. *Fundamentals of Noise and Vibration Analysis for Engineers*[M]. 2nd edition. Cambridge: Cambridge University Press, 2007.
- [171] ISO 12354-1. *Building Acoustics — Estimation of Acoustic Performance of Buildings from the Performance of Elements — Part 1: Airborne Sound Insulation between Rooms*[Z/OL]. Geneva: International Organization for Standardization, 2017(2017). <https://www.iso.org/standard/70242.html>.
- [172] ISO 15186-1. *Acoustics — Measurement of Sound Insulation in Buildings and of Building Elements Using Sound Intensity — Part 1: Laboratory Measurements*[Z/OL]. Geneva: International Organization for Standardization, 2003(2003). <https://www.iso.org/standard/26097.html>.
- [173] ASTM E90-09. *Standard Test Method for Laboratory Measurement of Airborne Sound Transmission Loss of Building Partitions and Elements*[Z]. West Conshohocken, PA: ASTM International, 2016(2016). DOI:10.1520/E0090-09R16.
- [174] ASTM E2249-19. *Standard Test Method for Laboratory Measurement of Airborne Sound Transmission Loss of Building Partitions and Elements Using Sound Intensity*[Z]. West Conshohocken, PA: ASTM International, 2019(2019). DOI:10.1520/E2249-19.
- [175] ISO 10140-1. *Acoustics — Laboratory Measurement of Sound Insulation of Building Elements — Part 1: Application Rules for Specific Products*. [Z/OL]. Geneva: International Organization for Standardization, 2016(2016). <https://www.iso.org/standard/67232.html>.
- [176] ISO 15186-2. *Acoustics — Measurement of Sound Insulation in Buildings and of Building Elements Using Sound Intensity — Part 2: Field Measurements*[Z/OL]. Geneva: International Organization for Standardization, 2010(2010). <https://www.iso.org/standard/30105.html>.
- [177] ISO 16283-1. *Acoustics — Field Measurement of Sound Insulation in Buildings and of Building Elements — Part 1: Airborne Sound Insulation*[Z/OL]. Geneva: International Organization for Standardization, 2014(2014). <https://www.iso.org/standard/55997.html>.
- [178] PIOLLET E, LAROCHE S, BIANKI M A, et al. *A Mobile Reverberation Cabin for Acoustic Measurements in an Existing Anechoic Room*[C]//Proceedings of the INTER-NOISE 2016 - 45th International Congress and Exposition on Noise Control Engineering: Towards a Quieter Future. .
- [179] Autoneum[EB/OL][2021-04-11]. <https://www.autoneum.com/innovation/research-and-development/>.
- [180] DUVAL A, RONDEAU J-F, DEJAEGER L, et al. *Diffuse Field Absorption Coefficient Simulation of Porous Materials in Small Reverberant Rooms: Finite Size and Diffusivity Issues*[C]//10eme Congrès Français d’Acoustique. .
- [181] The RIETER AUTOMOTIVE ISOKELL System[EB/OL][2021-04-12]. <https://www.yumpu.com/en/document/read/4968465/the-rieter-automotive-isokell-system>.
- [182] BŁASZAK M A. *Acoustic Design of Small Rectangular Rooms: Normal Frequency Statistics*[J]. *Applied Acoustics*, 2008, 69(12): 1356–1360. DOI:10.1016/j.apacoust.2007.10.005.

- [183] HERNANDEZ D, LIU E J, HUANG J H, et al. Design and Construction of a Small Reverberation Chamber Applied to Absorption and Scattering Acoustic Measurements[J]. *Advanced Materials Research*, 2014, 1077: 197–202. DOI:10.4028/www.scientific.net/AMR.1077.197.
- [184] ISO 3741. Acoustics — Determination of Sound Power Levels and Sound Energy Levels of Noise Sources Using Sound Pressure — Precision Methods for Reverberation Test Rooms.[Z/OL]. Geneva: International Organization for Standardization, 2010(2010). <https://www.iso.org/standard/52053.html>.
- [185] BOLT R H. Note on Normal Frequency Statistics for Rectangular Rooms[J]. *Journal of the Acoustical Society of America*, 1946, 18(1): 130–133. DOI:10.1121/1.1916349.
- [186] SCHROEDER M R, KUTTRUFF K H. On Frequency Response Curves in Rooms. Comparison of Experimental, Theoretical, and Monte Carlo Results for the Average Frequency Spacing between Maxima[J]. *The Journal of the Acoustical Society of America*, 1962. DOI:10.1121/1.1909022.
- [187] HASAN M, HODGSON M. Effectiveness of Reverberation Room Design: Room Size and Shape and Effect on Measurement Accuracy[C]//*Proceedings of the 22nd International Congress on Acoustics*. .
- [188] ATALLA N, SGARD F, SGARD F. *Finite Element and Boundary Methods in Structural Acoustics and Vibration*[M]. Boca Raton: CRC Press, 2015.
- [189] ELLIS R W, SMITH C W. A Thin-Plate Analysis and Experimental Evaluation of Couple-Stress Effects[J]. *Experimental Mechanics*, 1967, 7(9): 372–380.
- [190] HESSE C, PAPANTONI V, ALGERMISSEN S, et al. Frequency-Independent Radiation Modes of Interior Sound Radiation: Experimental Study and Global Active Control[J]. *Journal of Sound and Vibration*, 2017, 401: 204–213. DOI:10.1016/j.jsv.2017.04.038.
- [191] WRONA S, PAWELCZYK M. Shaping Frequency Response of a Vibrating Plate for Passive and Active Control Applications by Simultaneous Optimization of Arrangement of Additional Masses and Ribs. Part II: Optimization[J]. *Mechanical Systems and Signal Processing*, 2016, 70–71: 699–713. DOI:10.1016/j.ymsp.2015.08.017.
- [192] MAHRAN M, ELSABBAGH A, NEGM H. A Comparison between Different Finite Elements for Elastic and Aero-Elastic Analyses[J]. *Journal of Advanced Research*, 2017, 8(6): 635–648. DOI:10.1016/j.jare.2017.06.009.
- [193] OLIAZADEH P, FARSHIDIANFAR A, CROCKER M J. Study of Sound Transmission through Single- and Double-Walled Plates with Absorbing Material: Experimental and Analytical Investigation[J]. *Applied Acoustics*, 2019, 145: 7–24. DOI:10.1016/j.apacoust.2018.09.014.
- [194] WYRWAL J, PAWELCZYK M, LIU L, et al. Double-Panel Active Noise Reducing Casing with Noise Source Enclosed inside – Modelling and Simulation Study[J]. *Mechanical Systems and Signal Processing*, 2021, 152: 107371. DOI:10.1016/j.ymsp.2020.107371.
- [195] EGAB L, WANG X. Objective Evaluation of Interior Trim Effects on Sound Quality and Noise Reduction of a Coupled Plate Cavity System[J]. *Mechanical Systems and Signal Processing*, 2016, 70–71: 919–931. DOI:10.1016/j.ymsp.2015.09.035.
- [196] XIN F X, LU T J. Analytical and Experimental Investigation on Transmission Loss of Clamped Double Panels: Implication of Boundary Effects[J]. *The Journal of the Acoustical Society of America*, 2009, 125(3): 1506–1517. DOI:10.1121/1.3075766.
- [197] BHATTACHARYA M C, GUY R W, CROCKER M J. Coincidence Effect with Sound Waves in a Finite Plate[J]. *Journal of Sound and Vibration*, 1971, 18(2): 157–169. DOI:10.1016/0022-460X(71)90342-7.
- [198] OCHS J B, SNOWDON J C. Transmissibility across Simply Supported Thin Plates. I.

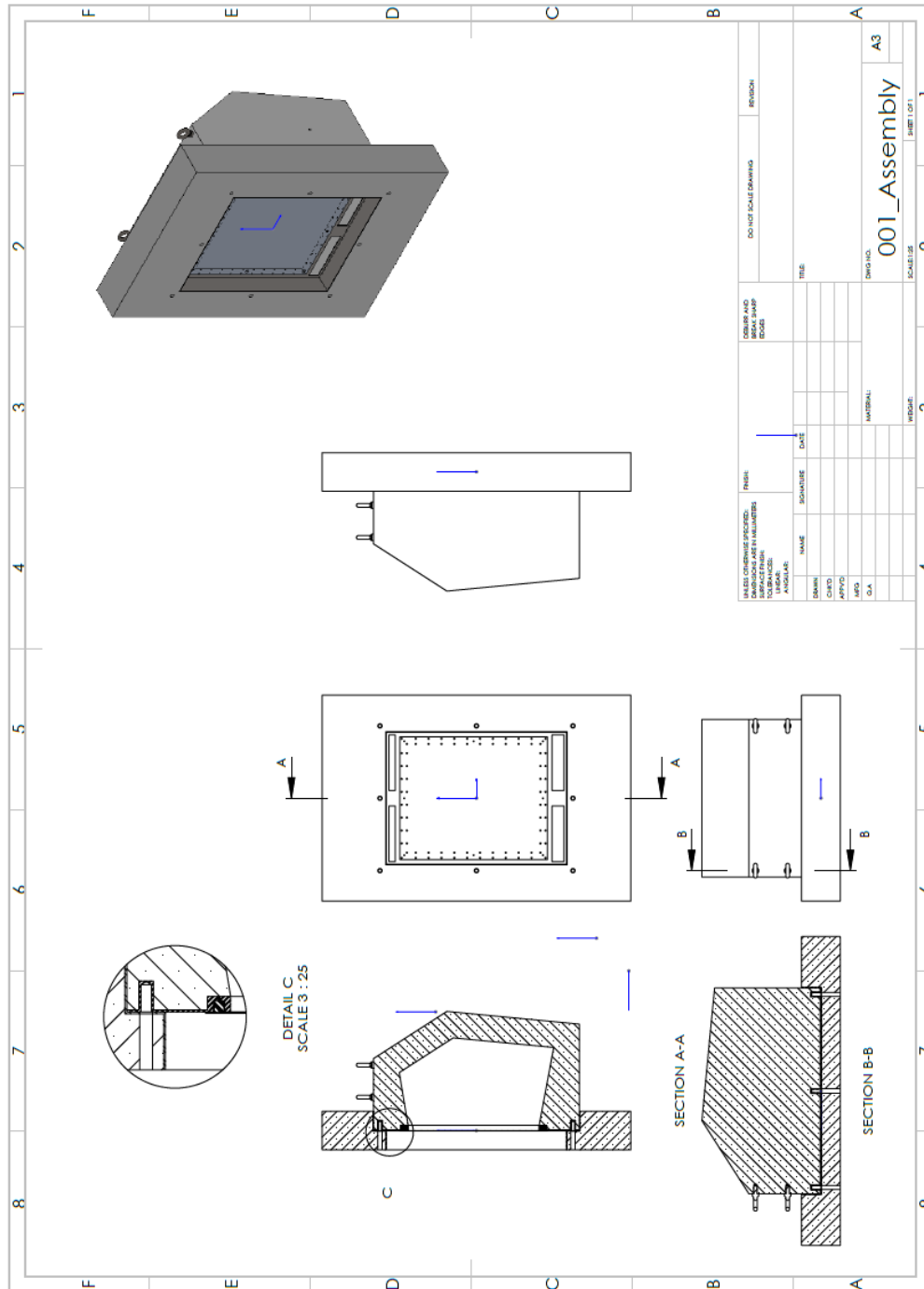


- Rectangular and Square Plates with and without Damping Layers[J]. *The Journal of the Acoustical Society of America*, 1975, 58(4): 832–840. DOI:10.1121/1.380730.
- [199] DUMOND P, MONETTE D, ALLADKANI F, et al. Simplified Setup for the Vibration Study of Plates with Simply-Supported Boundary Conditions[J]. *MethodsX*, 2019, 6: 2106–2117. DOI:10.1016/j.mex.2019.09.023.
- [200] CHAPELLE D, BATHE K J. *The Finite Element Analysis of Shells-Fundamentals*[M]. 2nd edition. Berlin Heidelberg: Springer-Verlag, 2011. DOI:10.1007/978-3-642-16408-8.
- [201] LEISSA A W. Vibration of Plates (NASA-SP-160)[R/OL]. [2020–02–17]. <https://ntrs.nasa.gov/search.jsp?R=19700009156>.
- [202] WARBURTON G B. The Vibration of Rectangular Plates[J]. *Proceedings of the Institution of Mechanical Engineers*, 1954, 168(1): 371–384. DOI:10.1243/pime\_proc\_1954\_168\_040\_02.
- [203] *Acoustic Module User’s Guide*[M]. COMSOL 5.4, 2018.
- [204] ISO 3382-2. Acoustics — Measurement of Room Acoustic Parameters — Part 2: Reverberation Time in Ordinary Rooms.[Z/OL]. Geneva: International Organization for Standardization, 2008(2008). <https://www.iso.org/standard/36201.html>.
- [205] ASTM C423-17. Standard Test Method for Sound Absorption and Sound Absorption Coefficients by the Reverberation Room Method[Z]. West Conshohocken, PA: ASM International, 2017(2017). DOI:10.1520/C0423-17.
- [206] NÉLISSE H, NICOLAS J. Characterization of a Diffuse Field in a Reverberant Room[J]. *The Journal of the Acoustical Society of America*, 1997, 101(6): 3517–3524. DOI:10.1121/1.418313.
- [207] BERANEK L L, MELLOW T J. *Loudspeaker Systems*[M]//Acoustics: Sound Fields and Transducers. Elsevier, 2012: 289–389. DOI:10.1016/b978-0-12-391421-7.00007-5.
- [208] BRANDT A. *Noise and Vibration Analysis: Signal Analysis and Experimental Procedures*[M]. Hoboken: John Wiley & Sons, Inc., 2011.
- [209] ANDERSON K, WERITZ J, KAUFMAN J G. Properties and Selection of Aluminum Alloys[M]. ASM International, 2019. DOI:10.31399/asm.hb.v02b.9781627082105.
- [210] SAS P, AUGUSZTINOVICZ F. Acoustic Modal Analysis[M]. SILVA J M M, MAIA N M M, eds.//*Modal Analysis and Testing*. Dordrecht: Springer Netherlands, 1999: 487–506. DOI:10.1007/978-94-011-4503-9\_23.
- [211] MORI E, YOSHIMURA T. Experimental Modal Analysis of Vibro-Acoustic Coupling Structure[C]//*The Proceedings of the Dynamics & Design Conference*. . DOI:10.1299/jsmedmc.2007.\_624-1\_.
- [212] OUISSE M, FOLTÊTE E. Model Correlation and Identification of Experimental Reduced Models in Vibroacoustical Modal Analysis[J]. *Journal of Sound and Vibration*, 2015, 342: 200–217. DOI:10.1016/j.jsv.2014.12.042.
- [213] LIU L. MATLAB Codes for WBM and SEA of the Noise-Box Plate-Cavity System[J]. *Mendeley Data*, V1, 2021. DOI:10.17632/4k6ffxmmwr.1.
- [214] JUNGER M C, FEIT D. *Sound, Structures, and Their Interaction*[M]. 2 edition. Cambridge: MIT press, 1986.
- [215] VANMAELE C, VANDEPITTE D, DESMET W. An Efficient Wave Based Prediction Technique for Plate Bending Vibrations[J]. *Computer Methods in Applied Mechanics and Engineering*, 2007, 196(33–34): 3178–3189. DOI:10.1016/j.cma.2007.03.002.
- [216] VERGOTE K, VANMAELE C, VANDEPITTE D, et al. An Efficient Wave Based Approach for the Time-Harmonic Vibration Analysis of 3D Plate Assemblies[J]. *Journal of Sound and Vibration*, 2013, 332(8): 1930–1946. DOI:10.1016/j.jsv.2012.11.018.

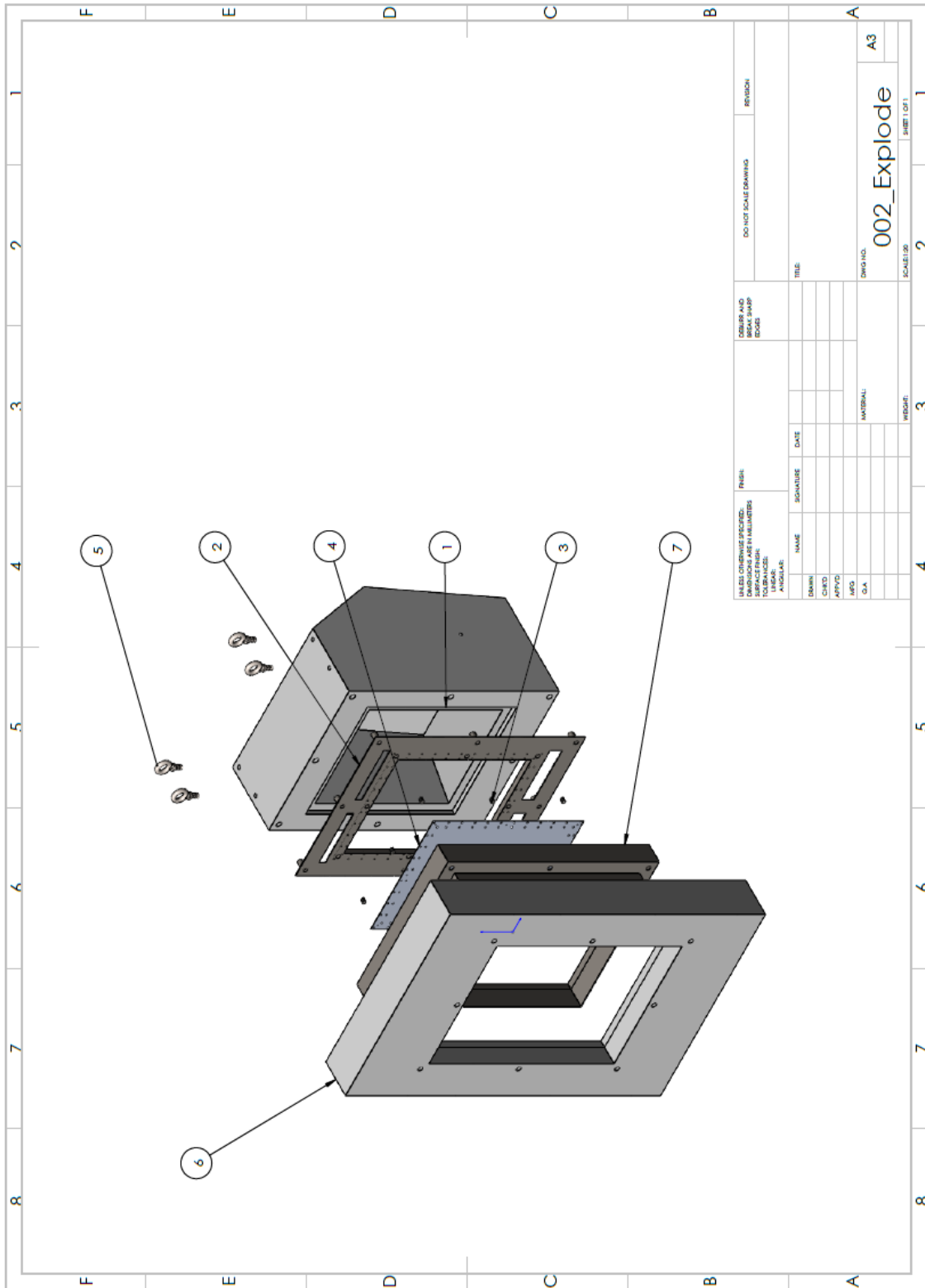
- [217] LIU L, RIPAMONTI F, CORRADI R, et al. The Modified Weighted Residual Formulation in the Wave Based Method for Plate Bending Problems: A General Formulation for Different Types of Edge Restraints (under Review)[R]. .
- [218] LE BOT A. Foundation of Statistical Energy Analysis in Vibroacoustics[M]. New York: Oxford University Press, 2015.
- [219] JOHANSSON D. Statistical Energy Analysis Software: Development and Implementation of an Open Source Code in Matlab/Octave[D]. Chalmers University of Technology, Master's Thesis 2010:130, 2010.
- [220] JOHANSSON D, COMNELL P, ANDERSSON P. SEALab - Applied Acoustics Chalmers University[EB/OL](2011)[2021-04-01]. <http://www.ta.chalmers.se/research/tools/SEALab/>.
- [221] LEPPINGTON F G, BROADBENT E G, HERON K H. Acoustic Radiation Efficiency of Rectangular Panels.[C]//Proceedings of The Royal Society of London, Series A: Mathematical and Physical Sciences. . DOI:10.1098/rspa.1982.0100.
- [222] HOPKINS C. Sound Insulation[M]. Amsterdam: Butterworth-Heinemann, 2007.
- [223] ISO 3744. Acoustics — Determination of Sound Power Levels and Sound Energy Levels of Noise Sources Using Sound Pressure — Engineering Methods for an Essentially Free Field over a Reflecting Plane[Z/OL]. Geneva: International Organization for Standardization, 2010(2010). <https://www.iso.org/standard/52055.html>.
- [224] Sound Transmission Loss Through a Concrete Wall[M/OL]. COMSOL 5.5, 2020. <https://www.comsol.com/model/sound-transmission-loss-through-a-concrete-wall-73371>.
- [225] DAVY J L. Predicting the Sound Insulation of Walls[J]. Building Acoustics, 2009, 16(1): 1–20. DOI:10.1260/135101009788066546.
- [226] SEWELL E C. Transmission of Reverberant Sound through a Single-Leaf Partition Surrounded by an Infinite Rigid Baffle[J]. Journal of Sound and Vibration, 1970, 12(1): 21–32. DOI:10.1016/0022-460X(70)90046-5.

# Appendix A: CAD drawings

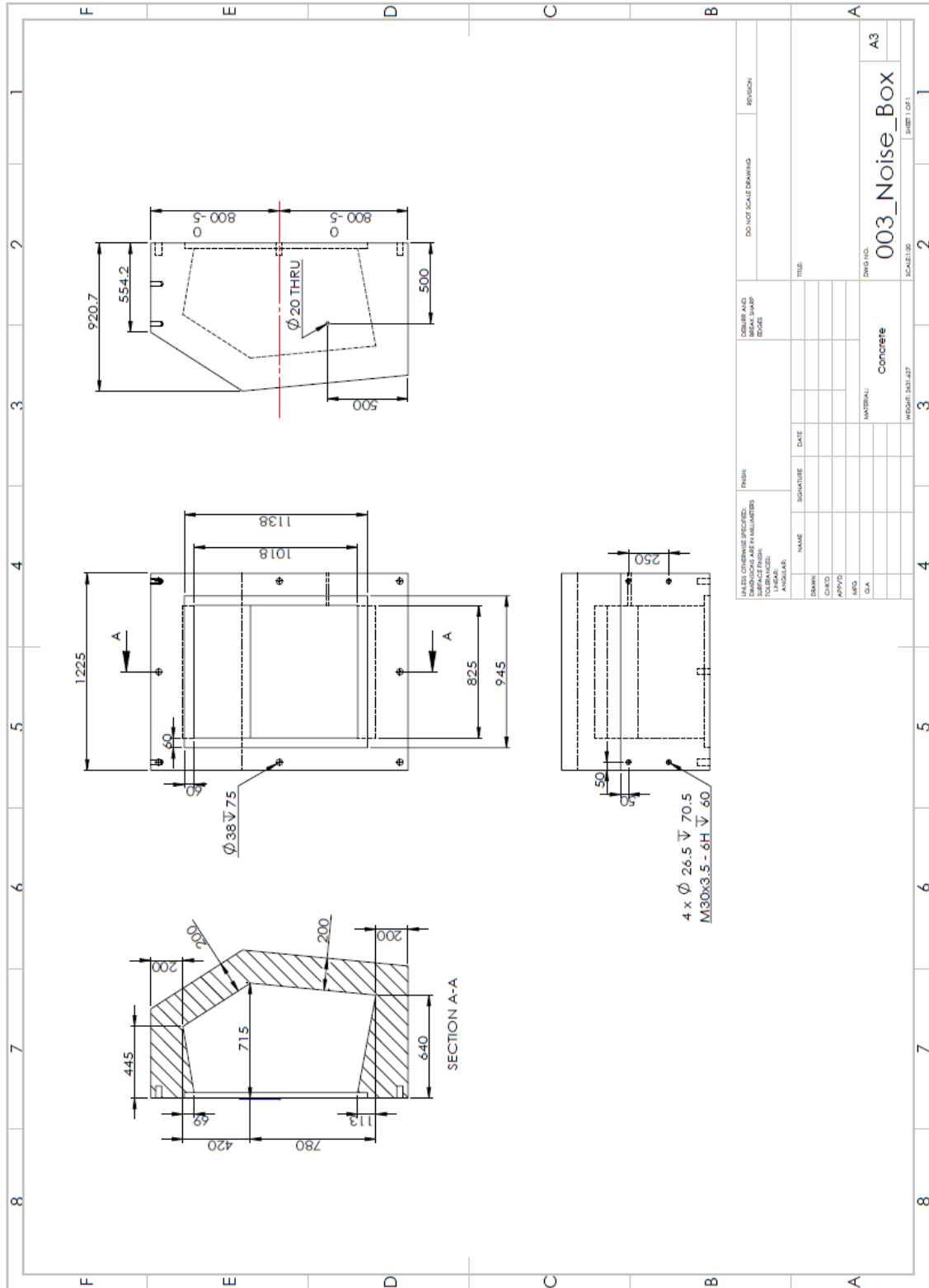
## A.1 Assembly drawing



## A.2 Exploded drawing

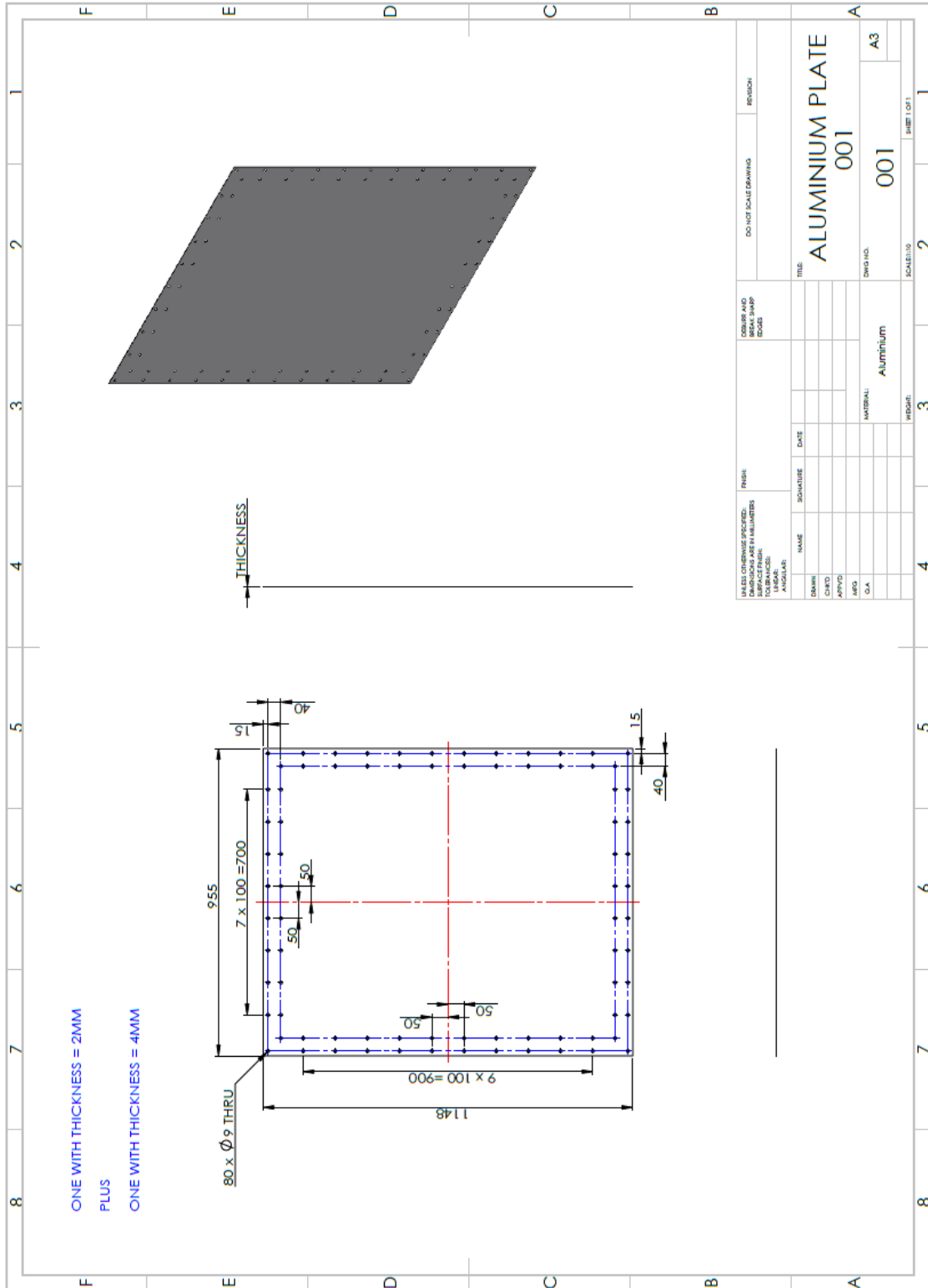


### A.3 Noise-Box concrete walls

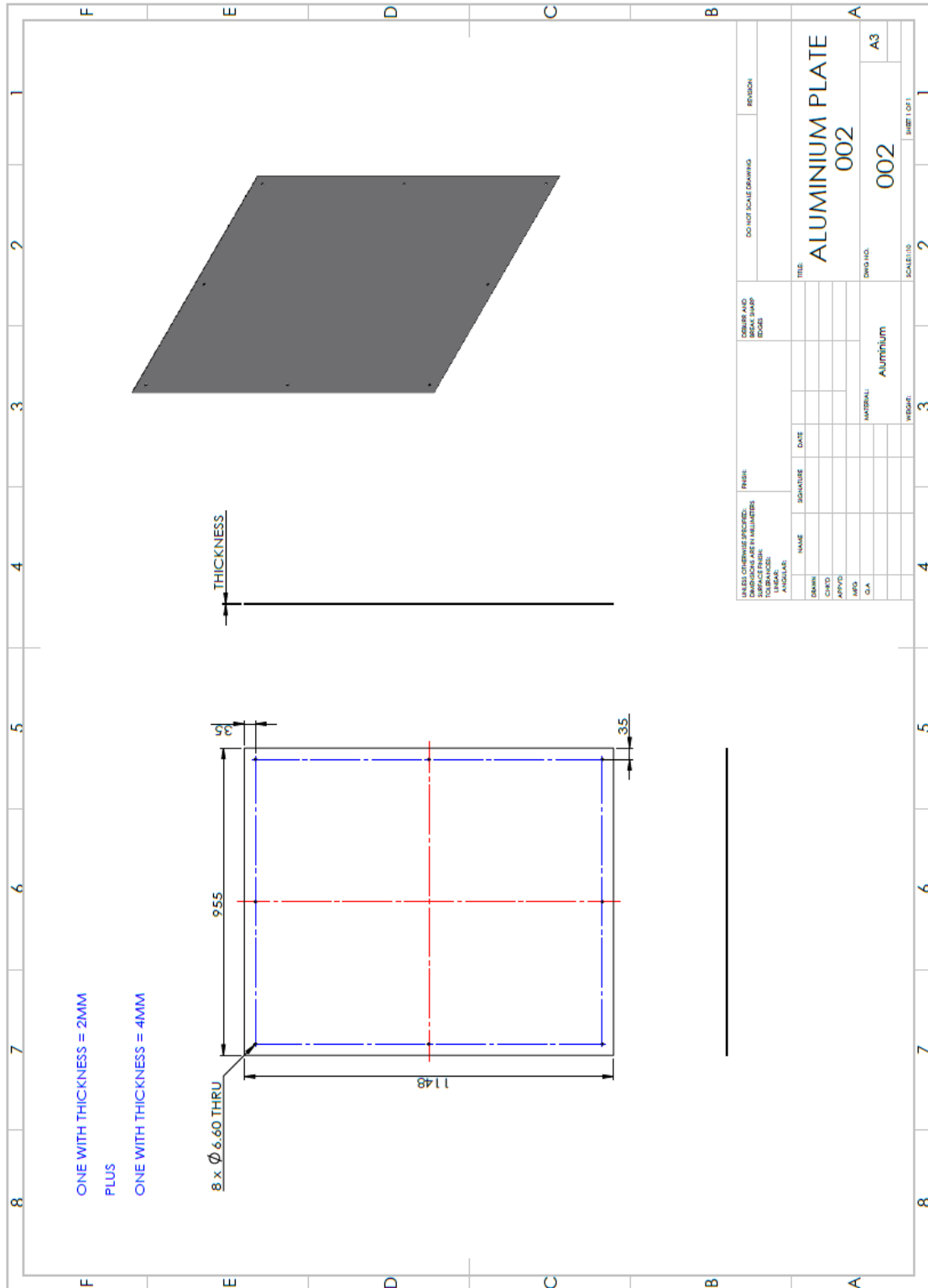




## A.5 Clamped panel

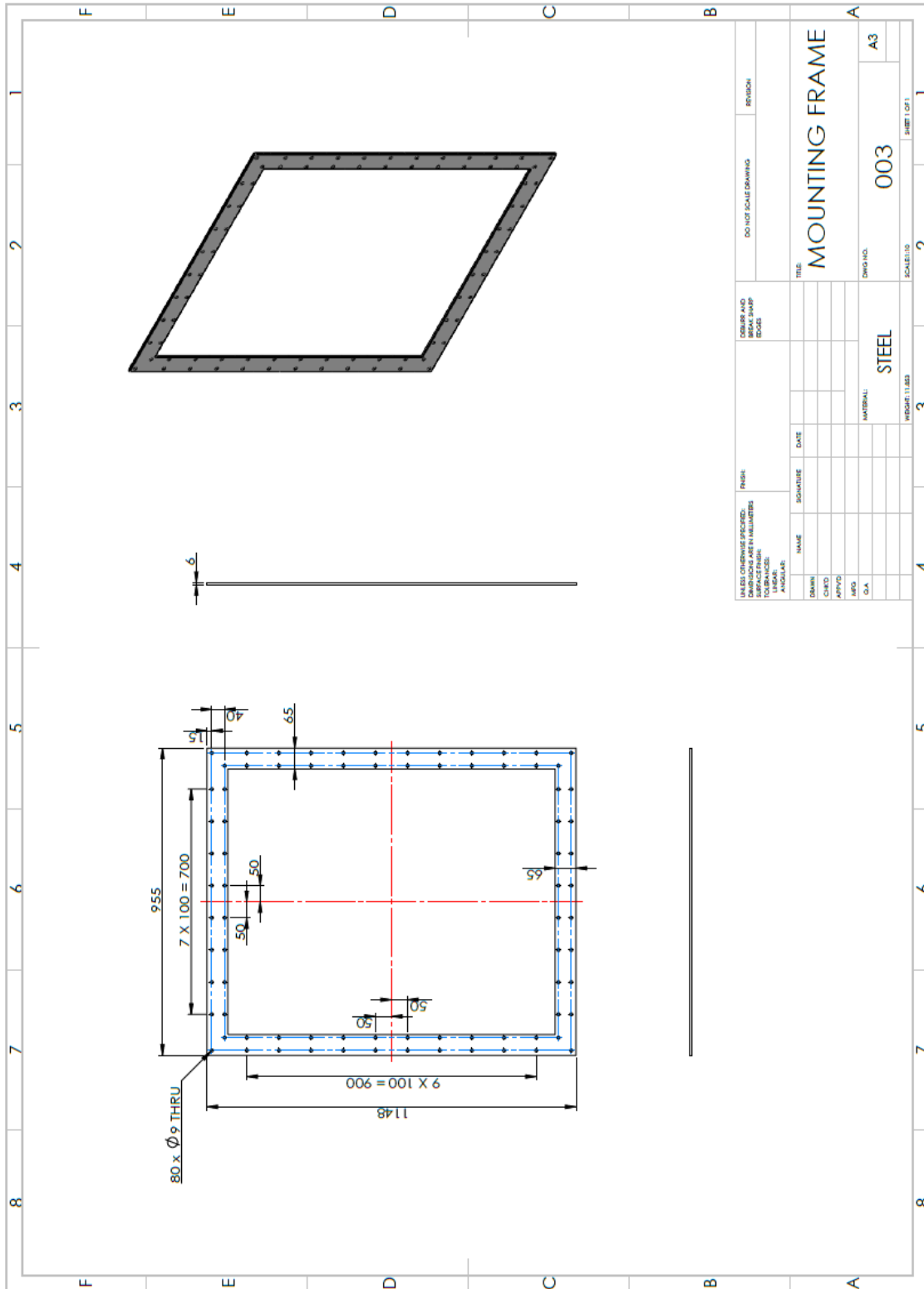


## A.6 Free panel





## A.7 Steel clamping frame





## Appendix B: Panel transmission loss approximate predictions

### B.1 Sharp's prediction scheme

In Sharp's prediction for  $f > 1.5f_1$ , the field incidence transmission loss, TL, should be calculated with  $\theta_L = 78^\circ$  in Eq. (2.37). For  $f < 1.5f_1$ , the analysis of <sup>[58]</sup> is adopted, where the panel is considered rigid but resting on flexible supports and  $s$  is the stiffness per unit area of the support. However, for a rigidly supported finite panel, the parameter  $s$  is not available from the support. The solution in this scheme is to correlate the first resonance modes. Therefore, for a simply supported panel, the stiffness is expressed as

$$s = \pi^4 D \left( \frac{1}{l_1^2} + \frac{1}{l_2^2} \right)^2, \quad (\text{B.1})$$

where  $l_1$  and  $l_2$  are panel dimensions and satisfy that  $l_1 \geq l_2$ .

Then, the formulae for different frequency ranges in 1/3 octave bands are proposed as follows <sup>[169]</sup>:

(a)  $f < f_1$

$$TL = 20 \lg s - 20 \lg f - 20 \lg(4\pi\rho_0 c) \quad (\text{B.2})$$

(b)  $0.5f_1 < f < 1.5f_1$

$$\begin{cases} \eta \gg \frac{\rho_0 c}{2\pi fm}, & TL = 20 \lg f_1 + 20 \lg m + 20 \lg \eta - 20 \lg \frac{\rho_0 c}{\pi} \\ \eta \ll \frac{\rho_0 c}{2\pi fm}, & TL = 0 \end{cases} \quad (\text{B.3})$$

(c)  $1.5f_1 < f < f_c$

$$TL = 10 \lg \left[ 1 + \left( \frac{\pi fm}{\rho_0 c} \right)^2 \right] - 5.5 \text{ dB} \quad (\text{B.4})$$

(d)  $f \approx f_c$  and  $f > f_c$

$$TL = 10 \lg \left[ 1 + \left( \frac{\pi fm}{\rho_0 c} \right)^2 \right] + 10 \lg \left( \frac{2\eta f}{\pi f_c} \right) \quad (\text{B.5})$$

## B.2 Davy's prediction scheme

In Davy's prediction, only the frequency range above  $1.5f_1$  is considered. The limiting angle  $\theta_L$  proposed by <sup>[225]</sup> is

$$\cos^2 \theta_L = \begin{cases} 0.9 & \text{if } \frac{\lambda}{2\pi\sqrt{S}} > 0.9 \\ \frac{\lambda}{2\pi\sqrt{S}} & \text{if } \frac{\lambda}{2\pi\sqrt{S}} \leq 0.9 \end{cases}, \quad (\text{B.6})$$

where,  $\lambda$  is the acoustic wavelength at corresponding frequency, and  $S$  is the area of the panel.

Then, Davy's prediction of field incidence transmission loss is provided as follows <sup>[169]</sup>:

(a)  $1.5f_1 < f \leq 0.8f_c$

$$TL = 20\lg a - 10\lg \left[ \ln \left( \frac{1+a^2}{1+a^2 \cos^2 \theta_L} \right) \right], \quad (\text{B.7})$$

with

$$a = \frac{\pi fm}{\rho_0 c} \left[ 1 - \left( \frac{f}{f_c} \right)^2 \right] \quad (\text{B.8})$$

(b)  $0.95f_c \leq f \leq 1.05f_c$

$$TL = 20\lg \left( \frac{\pi fm}{\rho_0 c} \right) + 10\lg \left( \frac{2\eta\Delta_b}{\pi} \right), \quad (\text{B.9})$$

where  $\Delta_b$  is the ratio of bandwidth with centre frequency. For 1/3-octave band,  $\Delta_b = 0.236$ .

(c)  $f > 1.7f_c$

$$TL = 10\lg \left[ 1 + \left( \frac{\pi fm}{\rho_0 c} \right)^2 \right] + 10\lg \left[ \left( \frac{2\eta}{\pi} \right) \left( \frac{f}{f_c} - 1 \right) \right] \quad (\text{B.10})$$

(d)  $0.8f_c < f < 0.95f_c$

The larger value of the two calculated by Eq. (B.7) and Eq. (B.9).

(e)  $1.05f_c < f < 1.7f_c$

The larger value of the two calculated by Eq. (B.9) and Eq. (B.10).

## B.3 BS EN ISO 12354-1 (2017) prediction scheme

In the standard <sup>[171]</sup>, the formula for estimating the sound reduction index  $R$  (equivalent to  $TL$ ) is provided. The field incidence transmission loss is calculated based on Eq. (2.36) with the field incidence transmission coefficient  $\tau$  obtained according to the following equation <sup>[171]</sup>.

$$\tau = \begin{cases} \left( \frac{2\rho_0 c}{2\pi f m} \right)^2 \left[ 2\sigma_f \left( 1 - \frac{f^2}{f_c^2} \right)^{-2} + 2 \frac{\pi f_c \sigma^2}{4f \eta_{\text{tot}}} \right] & f < f_c \\ \left( \frac{2\rho_0 c}{2\pi f m} \right)^2 \frac{\pi \sigma^2}{2\eta_{\text{tot}}} & f \approx f_c, \\ \left( \frac{2\rho_0 c}{2\pi f m} \right)^2 \frac{\pi f_c \sigma^2}{2f \eta_{\text{tot}}} & f > f_c \end{cases} \quad (\text{B.11})^1$$

where,  $\eta_{\text{tot}}$  is the total loss factor including the losses from the panel's material, radiation and mounting,  $\sigma_f$  is the radiation factor for forced transmission, and  $\sigma$  is the radiation factor for free bending waves.

The two radiation factors  $\sigma_f$  and  $\sigma$  are critical. The former related to forced waves is given by <sup>[171]</sup>:

$$\sigma_f = 0.5 \left[ \ln(k\sqrt{l_1 l_2}) - \Lambda \right]; \sigma_f \leq 2, \quad (\text{B.12})$$

with

$$\Lambda = -0.964 - \left( 0.5 + \frac{l_2}{\pi l_1} \right) \ln \frac{l_2}{l_1} + \frac{5l_2}{2\pi l_1} - \frac{1}{4\pi l_1 l_2 k^2} \quad (\text{B.13})$$

The latter radiation factor for free waves  $\sigma$  is calculated as follows <sup>[171]</sup>:

(a) determine the values of  $\sigma_1$ ,  $\sigma_2$ ,  $\sigma_3$  and  $f_{11}$ :

$$\begin{aligned} \sigma_1 &= \frac{1}{\sqrt{1 - f_c/f}}, \quad \sigma_2 = 4l_1 l_2 \left( \frac{f}{c} \right)^2, \quad \sigma_3 = \sqrt{\frac{2\pi f (l_1 + l_2)}{16c}} \\ f_{11} &= \frac{c^2}{4f_c} \left( \frac{1}{l_1^2} + \frac{1}{l_2^2} \right) \end{aligned} \quad (\text{B.14})$$

(b) if  $f_{11} \leq f_c/2$  then:

$$\begin{aligned} f \geq f_c : \sigma &= \sigma_1 \\ f < f_c : \sigma &= \frac{2(l_1 + l_2)}{l_1 l_2} \frac{c}{f_c} \delta_1 + \delta_2 \\ f < f_{11} < f_c/2 \text{ and } \sigma > \sigma_2 : \sigma &= \sigma_2 \end{aligned} \quad (\text{B.15})$$

(c) if  $f_{11} > f_c/2$  then:

$$\begin{aligned} f < f_c \text{ and } \sigma_2 < \sigma_3 : \sigma &= \sigma_2 \\ f > f_c \text{ and } \sigma_1 < \sigma_3 : \sigma &= \sigma_1 \\ \text{else} : \sigma &= \sigma_3 \end{aligned} \quad (\text{B.16})$$

(d) in all case,  $\sigma \leq 2$ .

<sup>1</sup> The expression for  $f < f_c$  in this equation is modified because it is considered that the original expression has a typical mistake, where  $\left( \frac{1-f^2}{f_c^2} \right)^{-2}$  should be  $\left( 1 - \frac{f^2}{f_c^2} \right)^{-2}$ , which is referred to <sup>[226]</sup>. Note that the expression in EN 12354-1 (2000) is given by  $\left( \frac{\rho_0 c}{\pi f m} \right)^2 \left[ 2\sigma_f + \frac{(l_1 + l_2)^2}{l_1^2 + l_2^2} \sqrt{\frac{f_c \sigma^2}{f \eta_{\text{tot}}}} \right]$ .

In Eq. (B.15), the unknowns  $\delta_1$  and  $\delta_2$  are given by

$$\delta_1 = \frac{(1-b^2)\ln\frac{1+b}{1-b} + 2b}{4\pi^2(1-b^2)^{1.5}},$$

$$\delta_2 = \begin{cases} 0 & f > f_c/2 \\ \frac{8c^2(1-2b^2)}{f_c^2\pi^4l_1l_2b\sqrt{1-b^2}} & f \leq f_c/2 \end{cases}, \quad (\text{B.17})$$

with  $b = \sqrt{f/f_c}$ .

## Acknowledgements

First of all, I would like to express my sincere gratitude to the Polimi Sound and Vibration Laboratory (PSVL) of Politecnico di Milano for the provided resources, and to the China Scholarship Council for the two-year financial support (No. 201806230718) in my study and research overseas.

Then, I would like to thank all the people who helped and supported me in this journey of completing the dissertation:

I am deeply grateful to my supervisors Prof. Roberto Corradi and Prof. Zhushi Rao. Thanks to Prof. Corradi's proposal for this interesting topic, I started to work on it about three years ago. Then, at every stage of the research, he patiently helped me to solve all the problems and kindly provided his insightful comments and suggestions. His feedback sharpened my thinking and brought my work to a higher level. At the same time, Prof. Rao generously gave me his fully support in my work and tried his best to help me and suggest me. Though we are about 9000 km away while I'm in my overseas period, he answered my questions and relived my doubts promptly. His suggestions helped me a lot and lightened my way.

I would also specially thank Prof. Francesco Ripamonti for his essential help throughout the work. He offered many useful suggestions that have adopted in the work, and also helped a lot with the experimental and technique stuff. I really appreciate for his generous help.

I would also like to thank my tutor Prof. Andrea Matta. Without him, I should have not joined this double PhD program between POLIMI and SJTU. I was also fortunate for being tutored by him during my period in Milan. He provided me with his valuable guidance that helped me complete my study and thesis.

I would like to acknowledge my colleagues in Milan: Dr. Qianqian Li, Dr. Ivano La Paglia, Dr. Cesare Lupo Ferrari, Eng. Anthony Giampa', Eng. Riccardo Giona, Eng. Gianluca Acquistapace, for their help in various things, where I would especially emphasize the experiments.

I would also like to acknowledge our group in Shanghai: Dr. Tana, Dr. Donglin Zhou, Dr. Jing Zhang, Dr. Jianbo Zhang, Dr. Chunxiao Jiao, Dr. Jianghai Xu, Eng. Fen Zou, Eng. Fengning Yu, Eng. Zijun Leng, for their willingness to help or advise me. I bothered them a lot regarding the affairs in SJTU and my desktop in the office.

I would like to extend my sincere thanks to Prof. Hui Zheng, Dr., Haosen Yang and Dr. Yongzhen Mi for sharing their work and advice.

I would also like to thank all the reviewers for their valuable suggestions that help the improvement of this work. I would like to acknowledge the internal reviews from Prof. Zhushi Rao, Prof. Roberto Corradi, Prof. Francesco Ripamonti, Prof. Hui Zheng, Prof. Zhiyi Zhang, Prof. Haijun Wu, Prof. Xinhua Long and Prof. Bintang Yang, and thank the external reviews from Prof. Marek Pawelczyk, Prof. Li Cheng and Prof. Katrin Ellermann.

Last but not the least, I would like to thank my beloved parents and friends for their endless love, understanding and support.

Thank you for reading this dissertation.

*Milan, June 2021*

*Ling Liu*



## List of publications

- [1] **L. Liu**, R. Corradi, F. Ripamonti, Z. Rao. Wave Based Method for Flexural Vibration of Thin Plate with General Elastically Restrained Edges [J]. *Journal of Sound and Vibration*, 2020, 483: 115468. DOI:10.1016/j.jsv.2020.115468. (SCI)
- [2] **L. Liu**, R. Corradi, F. Ripamonti, Z. Rao. Data on the Flexural Vibration of Thin Plate with Elastically Restrained Edges: Finite Element Method and Wave Based Method Simulations [J]. *Data in Brief*, 2020, 31: 105883. DOI:10.1016/j.dib.2020.105883. (Data Article)
- [3] **L. Liu**, M. Yang, Y. Zhang, X. Zhu, N. Ta, Z. Rao. A Miniature Four-Microphone Array for Two-Dimensional Direction-of-Arrival Estimation Based on Biomimetic Time-Delay Magnification [J]. *Journal of Vibration and Acoustics*, 2019, 141(2): 021017. DOI:10.1115/1.4042124. (SCI)
- [4] **L. Liu**, D. Zou, Z. Rao, N. Ta, Analysis of Sound Transmission through a Multi-Leaf Partition Using FEM and SEA [C]//25th International Congress on Sound and Vibration, ICSV 2018. Hiroshima: International Institute of Acoustics and Vibration, IIAV, 2018: 4654–4660. (EI)
- [5] **L. Liu**, R. Corradi, Z. Rao, Wave based method for vibro-acoustic analysis of a plate-cavity system with elastically restrained plate and irregularly shaped cavity [C]//27th International Congress on Sound and Vibration, ICSV 2021. (EI, accepted in 2020, to be held in July 2021)
- [6] **L. Liu**, F. Ripamonti, R. Corradi, Z. Rao, The modified weighted residual formulation in the wave based method for plate bending problems: a general formulation for different types of edge restraints [J], *Journal of Sound and Vibration*. (SCI, accepted)
- [7] J. Wyrwal, M. Pawelczyk, **L. Liu**, Z. Rao. Double-Panel Active Noise Reducing Casing with Noise Source Enclosed inside – Modelling and Simulation Study [J]. *Mechanical Systems and Signal Processing*, 2021, 152: 107371. DOI:10.1016/j.ymssp.2020.107371. (SCI)
- [8] K. Lu, **L. Liu**, Z. Yang, X. Gong, Z. Rao, Z. Xie. Semi-Active Dynamic Absorber of a Ship Propulsion Shafting Based on MREs [J]. *Zhendong Yu Chongji/Journal of Vibration and Shock*, 2017, 36(15): 36–42. DOI:10.13465/j.cnki.jvs.2017.15.006. (EI)
- [9] Z. Zhang, **L. Liu**, W. Wei, F. Tao, T. Li, A. Liu. A Systematic Function Recommendation Process for Data-Driven Product and Service Design [J]. *Journal*

- of Mechanical Design, Transactions of the ASME, 2017, 139(11). DOI:10.1115/1.4037610. (SCI)
- [10] D. Zou, **L. Liu**, Z. Rao, N. Ta. Coupled Longitudinal–Transverse Dynamics of a Marine Propulsion Shafting under Primary and Internal Resonances [J]. Journal of Sound and Vibration, 2016, 372: 299–316. DOI:10.1016/J.JSV.2016.03.001. (SCI)
- [11] D. Zou, **L. Liu**, Z. Rao, N. Ta. Primary Resonances of Shafts with Coupled Longitudinal-Transverse Vibration by Finite Element and Shooting Methods [J]. Zhendong Gongcheng Xuebao/Journal of Vibration Engineering, 2016, 29(1): 87–95. DOI:10.16385/j.cnki.issn.1004-4523.2016.01.012. (EI)
- [12] Z. Xie, Z. Rao, Ta-Na, **L. Liu**, R. Chen. Theoretical and Experimental Research on the Friction Coefficient of Water Lubricated Bearing with Consideration of Wall Slip Effects [J]. Mechanics and Industry, 2016, 17(1). DOI:10.1051/meca/2015039. (SCI)
- [13] Z. Xie, Z. Rao, N. Ta, **L. Liu**. Investigations on Transitions of Lubrication States for Water Lubricated Bearing. Part I: Determination of Friction Coefficients and Film Thickness Ratios[J]. Industrial Lubrication and Tribology, 2016, 68(3): 404–415. DOI:10.1108/ILT-10-2015-0146. (SCI)
- [14] Z. Xie, Z. Rao, N. Ta, **L. Liu**. Investigations on Transitions of Lubrication States for Water Lubricated Bearing. Part II: Further Insight into the Film Thickness Ratio Lambda[J]. Industrial Lubrication and Tribology, 2016, 68(3): 416–429. DOI:10.1108/ILT-10-2015-0147. (SCI)